

VU Research Portal

Molecular properties in the linear response regime and beyond with relativistic coupled-cluster

Yuan, Xiang

2024

DOI (link to publisher)

[10.5463/thesis.505](https://doi.org/10.5463/thesis.505)

document version

Publisher's PDF, also known as Version of record

[Link to publication in VU Research Portal](#)

citation for published version (APA)

Yuan, X. (2024). *Molecular properties in the linear response regime and beyond with relativistic coupled-cluster*. [PhD-Thesis - Research and graduation internal, Vrije Universiteit Amsterdam]. <https://doi.org/10.5463/thesis.505>

General rights

Copyright and moral rights for the publications made accessible in the public portal are retained by the authors and/or other copyright owners and it is a condition of accessing publications that users recognise and abide by the legal requirements associated with these rights.

- Users may download and print one copy of any publication from the public portal for the purpose of private study or research.
- You may not further distribute the material or use it for any profit-making activity or commercial gain
- You may freely distribute the URL identifying the publication in the public portal ?

Take down policy

If you believe that this document breaches copyright please contact us providing details, and we will remove access to the work immediately and investigate your claim.

E-mail address:

vuresearchportal.ub@vu.nl

VRIJE UNIVERSITEIT

**MOLECULAR PROPERTIES IN THE LINEAR RESPONSE REGIME AND BEYOND
WITH RELATIVISTIC COUPLED-CLUSTER**

ACADEMISCH PROEFSCHRIFT

ter verkrijging van de graad Doctor of Philosophy aan
de Vrije Universiteit en Université de Lille
op gezag van de rectores magnifici
prof.dr. J.J.G. Geurts en J.C. Camart, Pr,
in het openbaar te verdedigen
ten overstaan van de promotiecommissie
van de Faculteit der Bètawetenschappen
op woensdag 10 januari 2024 om 11.45 uur
in een bijeenkomst van de universiteit,
De Boelelaan 1105

door

Xiang Yuan

geboren te Zhejiang, China

promotor:

prof.dr. L. Visscher

copromotor:

dr. A. Severo Pereira Gomes

promotiecommissie:

dr. A. Borschevsky
prof.dr. T. Jagau
prof.dr. S. Coriani
dr. D.P. Geerke
dr. T. Saue
dr. V. Vallet

UNIVERSITÉ LILLE NORD DE FRANCE

Doctoral School ED 104 - Sciences de la Matière, du Rayonnement et de l'Environnement

University Department Laboratoire PhLAM

Thesis defended by Xiang YUAN

Defended on January 10, 2024

In order to become Doctor from Université Lille Nord de France

Academic Field Physics

Speciality Theoretical chemical physics

**Molecular properties in the linear
response regime and beyond with
relativistic coupled-cluster**

Thesis supervised by Andre SEVERO PEREIRA GOMES Supervisor
Lucas VISSCHER Co-Supervisor

Committee members

<i>Referees</i>	Anastasia BORSCHESKY Thomas JAGAU	Associate Professor at Rijksuniversiteit Groningen Associate Professor at Katholieke Universiteit Leuven
<i>Examiners</i>	Sonia CORIANI Daan GEERKE Trond SAUE Valérie VALLET	Professor at Technical University of Denmark Associate Professor at Vrije Universiteit Amsterdam directeur de recherche CNRS/Univ. Toulouse III-Paul Sabatier directrice de recherche CNRS/Univ. Lille
<i>Supervisors</i>	Andre SEVERO PEREIRA GOMES Lucas VISSCHER	chargé de recherche au CNRS (HDR) / Univ. Lille Professor at Vrije Universiteit Amsterdam

UNIVERSITÉ LILLE NORD DE FRANCE

Doctoral School ED 104 - Sciences de la Matière, du Rayonnement et de l'Environnement

University Department Laboratoire PhLAM

Thesis defended by Xiang YUAN

Defended on January 10, 2024

In order to become Doctor from Université Lille Nord de France

Academic Field Physics

Speciality Theoretical chemical physics

**Molecular properties in the linear
response regime and beyond with
relativistic coupled-cluster**

Thesis supervised by Andre SEVERO PEREIRA GOMES Supervisor
Lucas VISSCHER Co-Supervisor

Committee members

<i>Referees</i>	Anastasia BORSCHESKY Thomas JAGAU	Associate Professor at Rijksuniversiteit Groningen Associate Professor at Katholieke Universiteit Leuven
<i>Examiners</i>	Sonia CORIANI Daan GEERKE Trond SAUE Valérie VALLET	Professor at Technical University of Denmark Associate Professor at Vrije Universiteit Amsterdam directeur de recherche CNRS/Univ. Toulouse III-Paul Sabatier directrice de recherche CNRS/Univ. Lille
<i>Supervisors</i>	Andre SEVERO PEREIRA GOMES Lucas VISSCHER	chargé de recherche au CNRS (HDR) / Univ. Lille Professor at Vrije Universiteit Amsterdam

UNIVERSITÉ LILLE NORD DE FRANCE

École doctorale ED 104 - Sciences de la Matière, du Rayonnement et de l'Environnement

Unité de recherche **Laboratoire PhLAM**

Thèse présentée par **Xiang YUAN**

Soutenue le **10 janvier 2024**

En vue de l'obtention du grade de docteur de l'Université Lille Nord de France

Discipline **Physique**

Spécialité **Physico-Chimie Théorique**

**Propriétés moléculaires dans le
régime de réponse linéaire et au-delà
avec méthodes coupled cluster
relativistes**

Thèse dirigée par Andre SEVERO PEREIRA GOMES directeur
Lucas VISSCHER co-directeur

Composition du jury

<i>Rapporteurs</i>	Anastasia BORSHEVSKY	Associate Professor at Rijksuniversiteit Groningen
	Thomas JAGAU	Associate Professor at Katholieke Universiteit Leuven
<i>Examineurs</i>	Sonia CORIANI	professeur au Technical University of Denmark
	Daan GEERKE	Associate Professor at Vrije Universiteit Amsterdam
	Trond SAUE	directeur de recherche CNRS/Univ. Toulouse III-Paul Sabatier
	Valérie VALLET	directrice de recherche CNRS/Univ. Lille
<i>Directeurs de thèse</i>	Andre SEVERO PEREIRA GOMES	chargé de recherche au CNRS (HDR) / Univ. Lille
	Lucas VISSCHER	professeur au Vrije Universiteit Amsterdam

This thesis has been prepared at

Laboratoire PhLAM

Laboratoire PhLAM

CNRS UMR 8523

Université Lille Nord de France

Bâtiment P5

59655 Villeneuve d'Ascq

France

☎ (33)(0)3 20 43 44 84

✉ cristian.focsa@univ-lille.fr

Web Site <http://phlam.univ-lille.fr>



To my parents and friends !

À mes parents et amis !

If, in some cataclysm, all of scientific knowledge were to be destroyed, and only one sentence passed on to the next generation of creatures, what statement would contain the most information in the fewest words? I believe it is the atomic hypothesis that all things are made of atoms

Richard Feynman

MOLECULAR PROPERTIES IN THE LINEAR RESPONSE REGIME AND BEYOND WITH RELATIVISTIC COUPLED-CLUSTER**Abstract**

This thesis mainly focuses on the development and implementation of new methods to study various types of response properties for molecules containing heavy elements. We implement static and frequency-dependent linear and quadratic response properties based upon relativistic coupled cluster wave function models. The validations are done by calculating various types of molecular properties such as frequency-(in)dependent (hyper)polarizability (purely electric), indirect spin-spin coupling constant (purely magnetic), and optical rotation (mixed electric-magnetic).

Moreover, the current implementations also allow evaluation of the absorption cross-sections: the linear response code can evaluate the damped response functions, which can be used to calculate the one-photon absorption cross-sections, and the quadratic response code can evaluate the two-photon absorption cross-sections provided the wave functions of the target states exist.

In addition, we also implement the equation-of-motion (EOM) coupled cluster theory to evaluate the ionization potential, electron affinity, and excitation energy. The new EOM codes reproduce the results from the previous implementation in the program RELCCSD very well.

All the codes are implemented on the new GPU-accelerated coupled cluster module ExaCorr in DIRAC. This module is designed for dealing with large systems and performing efficiently coupled cluster calculations on modern supercomputer architectures. To further reduce the calculation cost, we implement the relativistic MP2 frozen natural orbitals (FNOs) to reduce the virtual orbital space in the correlated calculation. The pilot tests show with using FNOs, one can obtain reliable estimates for both energies and molecular properties with only half the size of the full spaces.

Apart from the development work, this thesis also contains applications of the existing relativistic quantum chemistry models to obtain the highly accurate electronic structures and transition properties of molecules containing heavy elements. We discuss the importance of the evaluation of the relativistic effect and electron correlation on an equal footing and the corresponding impact on different topics such as molecular laser cooling and plasma physics.

Keywords: response properties, coupled cluster, relativistic effects

Laboratoire PhLAM

Laboratoire PhLAM – CNRS UMR 8523 – Université Lille Nord de France –
Bâtiment P5 – 59655 Villeneuve d’Ascq – France

PROPRIÉTÉS MOLÉCULAIRES DANS LE RÉGIME DE RÉPONSE LINÉAIRE ET AU-DELÀ AVEC MÉTHODES COUPLED CLUSTER RELATIVISTES**Résumé**

Cette thèse se concentre principalement sur le développement et la mise en œuvre de nouvelles méthodes pour étudier divers types de propriétés de réponse pour les molécules contenant des éléments lourds.

Nous mettons en œuvre des propriétés de réponse linéaire et quadratique, statiques et dépendantes de la fréquence, basées sur les modèles de fonction d'onde de cluster couplé relativiste. Les validations sont effectuées en calculant divers types de propriétés moléculaires telles que la (hyper)polarisabilité (purement électrique), la constante de couplage spin-spin indirect (purement magnétique) et la rotation optique (mixte électrique-magnétique).

De plus, les implémentations actuelles permettent également d'évaluer les sections efficaces d'absorption : le code de réponse linéaire peut évaluer les fonctions de réponse amorties, qui peuvent être utilisées pour calculer les sections efficaces d'absorption à un photon, et le code de réponse quadratique peut évaluer les sections efficaces d'absorption à deux photons à condition que les fonctions d'onde des états cibles existent.

De plus, nous avons également mis en œuvre la théorie *equation-of-motion (EOM) coupled cluster* pour évaluer le potentiel d'ionisation, l'affinité électronique et l'énergie d'excitation. Les nouveaux codes EOM reproduisent très bien les résultats de l'implémentation précédente dans le programme RELCCSD.

Tous les codes sont implémentés sur le nouveau module de cluster couplé accéléré par GPU ExaCorr dans DIRAC. Ce module a été conçu pour traiter des systèmes à grand taille et effectuer de façon efficace des calculs de *coupled cluster* sur des supercalculateurs de dernière génération. Pour réduire encore le coût des calculs, nous avons mis en œuvre les orbitales naturelles gelées MP2 relativistes (FNOs) pour réduire l'espace orbital virtuel dans les calculs corrélés. Les tests pilotes montrent qu'en utilisant FNOs, on peut obtenir des estimations fiables pour les énergies et les propriétés moléculaires avec seulement la moitié de la taille des espaces complets.

Outre le travail de développement, cette thèse contient également des applications des modèles existants de chimie quantique relativiste pour obtenir les structures électroniques et les propriétés de transition très précises pour des molécules contenant des éléments lourds. Nous discutons de l'importance de l'évaluation des effets relativistes et de la corrélation électronique quand ceux-ci sont traités sur un pied d'égalité et de l'impact correspondant sur différents sujets tels que le refroidissement moléculaire au laser et la physique des plasmas.

Mots clés : propriété de réponse, coupled cluster, effet relativiste

Acknowledgements

First of all, I would like to thank my supervisor in France André Severo Pereira Gomes. I would like to mention his help not only for his advice in science and research but also for many practical things about how to live in France. This Ph.D. project to develop the program on DIRAC was a big challenge for me, but André's continuous encouragement and insightful recommendations bolstered my confidence, enabling me to bring this project to fruition.

Next, I would like to thank my supervisor in the Netherlands Lucas Visscher. I learned a lot from him what is the right way to do research. His rigor in science will always be the goal of my studies and work.

I like to thank the PCMT team at the University of Lille. Their unwavering support in both my academic journey and life was indispensable. Particularly, I like to thank Loïc Halbert. We worked on this EOM response project together, which was quite successful.

I like to thank my colleagues at VU for their camaraderie. The countless enjoyable gatherings and memorable lunches added much-needed levity to my time there. Especially, I want to thank Mauricio Rodríguez-Mayorga. Thanks to his many suggestions in theory, programming, cooking, and even climbing.

I want to thank several projects including Labex CaPPA, the I-Site ULNE, and CompRIXS for their financial support.

As a developer in DIRAC, I attended four times of annual DIRAC meetings. My appreciation goes out to the entire DIRAC community. The congenial atmosphere always reinforced my belief that research can be both fulfilling and enjoyable.

I would like to mention the names of my cooperators, short term work with whom were very enlightening - Sonia Coriani and Nicolas Sisourat.

Also, I want to thank my friends in China - especially, Shaoqing Ai, and Yue Lin for giving me memories to cherish.

To my parents, your silent support has been my bedrock. I'm eternally grateful.

Last but not least I would like to thank Ying. Even across the miles, you've remained my perennial source of joy and solace.

Outline

Abstract	xv
Acknowledgements	xvii
Outline	xix
List of publications	xxi
Introduction	1
I Methodology	7
1 Electronic Structure Theory	9
2 Response Theory	27
II ExaCorr Implementation	39
3 Implementation of Linear Response properties based on Relativistic Coupled Cluster Theory	41
4 Implementation of Quadratic Response Properties based on Relativistic Equation-of-Motion Coupled Cluster Theory	103
5 Note: Reimplementation of Ionization Potential, and Electron Affinity based upon Relativistic Equation-of-Motion Coupled Cluster	143
6 Reduced-Scaling: Relativistic MP2 Frozen Natural Orbitals	153
III Applications on molecules containing heavy elements	171

7 Papers of application works	173
Summary and Conclusion	203
Bibliography	207
A Supplemental information of Chapter 3	219
B Supplemental information of Chapter 4	241
C Supplemental information of Chapter 6	247
D Supplemental information of Chapter 7	253

List of publications

- 1. Frequency-Dependent Quadratic Response Properties and Two-photon Absorption from Relativistic Equation-of-Motion Coupled Cluster Theory**
Yuan, X; Halbert, L; Visscher, L; Gomes, A. S. P
accepted for publication in J. Chem. Theory Comput. (arXiv:2309.07295)
- 2. Formulation and Implementation of Frequency-Dependent Linear Response Properties with Relativistic Coupled Cluster Theory for GPU-accelerated Computer Architectures**
Yuan, X; Halbert, L; Pototschnig, J; Papadopoulos, A; Coriani, S; Visscher, L; Gomes, A. S. P
under review in J. Chem. Theory Comput. (arXiv:2307.14296)
- 3. Assessing MP2 frozen natural orbitals in relativistic correlated electronic structure calculations**
Yuan, X; Visscher, L; Gomes, A. S. P
J. Chem. Phys, 156, 224108, 2022
- 4. Reassessing the potential of TlCl for laser cooling experiments via four-component correlated electronic structure calculations**
Yuan, X; Gomes, A. S. P
J. Chem. Phys, 157, 074313, 2022
- 5. Final-state-resolved mutual neutralization in $I^+ - I^-$ collisions**
Poline, M; Yuan, X; Badin, S; Ji, MC; Rosén, S; Indrajith, S; Thomas, R. D; Schmidt, H. T; Zettergren, H; Gomes, A. S. P; Sisourat, N
Phys. Rev. A, 106, 012812, 2022

6. Theoretical study of the I^+ - I^- mutual neutralization reaction

Badin, S; **Yuan, X**; Bourgeois, P. L; Gomes, A. S. P; Sisourat, N

Phys. Rev. A, 107, 022808, 2023

Introduction

Molecules containing heavy elements, found in the lower rows of the periodic table, are increasingly garnering interest in both physics and chemistry. For instance, in chemistry, there are various notable applications, such as uranium chemistry[1–8] in the nuclear sector, the development of new materials leveraging the robust optical properties of Lanthanide[9–14] and Actinide[15–18] complexes, and the exploration of gold nanoparticles for cancer treatments[19, 20]. These represent just a few examples of contemporary research in this domain.

Small molecules containing heavy elements are furthermore proposed in fundamental physics to search for new physics beyond the Standard Model[21–24]. Given the precision required for such experiments, the development of slowing and trapping technologies for potential molecular candidates becomes essential. However, the inherent complexities in molecules, such as their vibrational and rotational structures, hinder the straightforward application of direct laser cooling as done on their atomic counterparts. The criteria for molecular candidates in laser cooling experiments are quite strict[25], so the laser systems designed for cooling specific molecules are both specialized and costly. In this context, advanced quantum chemistry calculations—which encompass both energy aspects (like determining the potential energy surfaces of the ground and excited electronic states) and molecular properties (like transition dipole moments and polarizabilities)—are pivotal in the domain of laser cooling molecules[26].

In experiments, molecular properties are gauged through various spectroscopic methods and their interpretation relies on theoretical models of varying degrees of sophistication. In theory, we assume that a molecule’s wave function changes when subjected to an external electromagnetic field. For most molecular spectroscopic experiments, where the field is relatively weak, one can ap-

ply time-dependent perturbation theory to assess the altered wave function and subsequently observe the molecule's response to the external field.

However, general time-dependent perturbation theory typically starts from the exact unperturbed wave function. In this framework, evaluating molecular properties requires information on all excited states. This makes programming challenging and restricts solutions to simple models. On the other hand, response theory[27–30] provides an effective way for assessing molecular properties. Because it doesn't necessitate explicit computations of all excited states and also can be constructed based on approximated models of reference states such as Hartree-Fock (HF), density functional theory (DFT), and various post-HF models. As a result, it is implementable in most contemporary quantum chemistry software.

DFT is a widely favored method in the computational chemistry community, and the combination of response theory with DFT has been the primary tool for evaluating frequency-dependent molecular properties[31–33]. However, unlike methods based on wave function theory (WFT), current density functional approximations don't allow for systematic improvements in the quality of calculations. This limitation hinders the interpretation of DFT results, especially in the absence of experimental data or other benchmarks. Furthermore, in the relativistic quantum chemistry field, DFT results may significantly diverge from experimental and other more accurate theoretical models[34–36]. Consequently, there's a pressing need to develop a response theory rooted in high-level relativistic wave function models. Such approaches will serve as a benchmark for other less precise models like DFT in molecular property calculations, similar to how benchmarks are established for energy calculations.

Among various post-HF wave function models, Coupled Cluster (CC) theory stands out as a "gold standard" due to its ability to produce results nearing chemical accuracy for both correlation energies and properties[37–46]. However, the substantial computational cost—scaling as $O(N^6)$ for CCSD, and $O(N^7)$ for CCSD(T)—restricts its applicability to larger systems. The swift advances in computing technologies have fostered the emergence of highly parallelized implementations[47–52], especially with that combined with the use of Graphics Processing Units (GPU) acceleration technology[47, 53–57], have significantly

expanded the scope of applicability of coupled cluster theory. For instance, Pototschnig et al.[58] introduced the ExaCorr code, a novel relativistic coupled cluster implementation based on ExaTENSOR[59], a distributed numerical tensor algebra library, and demonstrated the feasibility of CCSD calculations for $[(\text{UO}_2)(\text{NO}_3)_3]^-$, which involved correlating 200 electrons and approximately 1000 virtual orbitals. The efficiency of such implementations can be further enhanced through techniques like the use of localized orbitals [60–64], Cholesky decomposition[65–68], and density fitting[68–70].

Building on the work of Pototschnig et al.[58], my main objective in this thesis has been to extend the capabilities of the DIRAC program[71, 72] to study ground and excited state properties of molecular systems. This has been accomplished through the implementation in ExaCorr of relativistic coupled cluster response theory and equation of motion approaches, as well as of a method to reduce the cost of CC calculations. Moreover, I will present three application cases computed using DIRAC, illustrating the impact of correlation and relativity on electronic structures and their subsequent effects on physical processes.

Outline of the thesis

The contents of this thesis are organized into three parts.

In the first part of this thesis, in Chapter 1, I will briefly discuss the electronic structure theory including relativistic effects, and the standard models dealing with electron correlation, including configuration interaction, Møller–Plesset perturbation theory, and coupled cluster theory.

In the subsequent chapter (Chapter 2), I introduce response theory, reviewing its main concepts. Starting with the definition of time-averaged quasi-energy in sections 2.1 and in 2.2, I present the time-dependent Hellmann–Feynman theorem, which links time-dependent molecular properties to the derivatives of the time-averaged quasi-energy. Following this, section 2.3 outlines the parameterization of the time-dependent wave function, and the transformation of both quasi-energy and Lagrangian from the time domain to the frequency domain. Section 2.4 characterizes two approximated time-dependent wave function models: CC-CI and CC-CC. This characterization includes the derivation

of their associated response equations and the response functions.

In the second part, I focus on the ExaCorr implementation including linear and quadratic response properties, as well as the calculation of energies based on equation-of-motion (EOM) coupled cluster models. In Chapter 3, I discuss the implementation of the frequency-dependent linear response for both CC-CI (EOM) and CC-CC models. These two models are founded on the same reference state—the time-independent coupled cluster wave function; however they differ in their characterization of the time-evolution part. The CC-CI model utilizes linear time evolution functions, while the CC-CC model employs exponential time evolution functions. Consequently, within the linear response framework, these two models solve the same response equations but they have different response functions.

As a measure of validation for the code, we evaluate various molecular properties: electric properties such as polarizability, magnetic properties like the indirect spin-spin coupling constant, and optical rotation, which is a combined electric-magnetic property. Notably, our current approach is rooted in complex algebra, simplifying the extension to damped response theory through the use of a complex frequency representing excitation energies and its inverse lifetime. Utilizing damped response theory, we determine the absorption cross-sections and stimulate the spectrum of I_2 . Our findings align closely with experimental observations.

In Chapter 4, I will address the implementation of frequency-dependent quadratic response property based on EOM-CC models. As an initial examination, we assess the frequency-dependent hyperpolarizability of hydrogen halide molecules and Verdet constant of Xe and Rn. I also implement the EOM-based two-photon absorption (TPA) cross-sections. Both the quadratic response property outcomes and the TPA results are validated by extant experimental values and non-relativistic calculations derived from the DALTON program.

Chapter 5 centers on the execution of the EOM-CC method. I provide a succinct overview of the implementation of sigma vectors and the Davidson modules, which can be used to compute energies encompassing the ionization potential (IP), excitation energy (EE), and electron affinity (EA). Subsequently, I present test results from a few small systems, contrasting them with outcomes

from the legacy relativistic coupled cluster implementation in DIRAC, the REL-CCSD code.

In the final chapter of this section (Chapter 6), I explore a method to reduce cost for our current relativistic coupled cluster implementation. This involves compressing the virtual orbital space using MP2 frozen natural orbitals (FNOs). Through our evaluations of both correlation energy and expectation values, we found that the MP2FNO approach significantly accelerates convergence for both energy and molecular properties.

In Part III, I move into the application of relativistic quantum chemistry using DIRAC for the molecules containing heavy elements. This entails the use of four-component multi-reference configuration interaction (MRCI), Polarization Propagator (PP), and coupled cluster models. The high-precision relativistic correlated electronic structure becomes paramount in fundamental physics, as illustrated in the analysis of the transition dipole moment and its consequential impact on laser cooling dynamics, highlighted in section 7.1 of Chapter 7. In sections 7.2 and 7.3, we determine high-accuracy potential energy curves (PECs) of I_2 . Leveraging these PECs, we assess the collision cross-section and observe that our results align closely with the most recent experimental values.

Part I

Methodology

Electronic Structure Theory

In this chapter, we will give a brief summary of the electronic structure theory. It starts with the introduction of relativistic Hamiltonian for both 4-component and 2-component models. We then discuss Dirac-Hatree-Fock wave function and three correlated wave functions including configuration interaction, Møller-Plesset perturbation theory, and coupled cluster. Atomic units are used throughout unless explicitly indicated: $\hbar = e = m_e = 4\pi\epsilon_0 = 1$.

1.1 Relativistic Hamiltonian

1.1.1 Exact Hamiltonian

We start with the molecular Hamiltonian within Born–Oppenheimer approximation[73], since it provides a preferred reference framework for relativistic treatment:

$$\hat{H} = \sum_i \hat{h}_i + \sum_{i,j} \hat{V}_{i,j} + \hat{V}_{N,N} \quad (1.1)$$

where, \hat{h}_i is the one-electron operator including electronic kinetic energy and electron-nuclear attraction potential, $\hat{V}_{i,j}$ is the two-electron operator representing electron-electron interaction, and $\hat{V}_{N,N}$ represents the nuclear repulsion potential. We will discuss the molecular Hamiltonian separately in one-electron and two-electron parts.

One-electron part

In relativistic quantum mechanics, the one-electron operator can be written as[74]

$$\hat{h} = \beta mc^2 + c\vec{\alpha} \cdot \hat{\vec{\pi}} + q\phi \quad (1.2)$$

$$\hat{\vec{\pi}} = \hat{\vec{p}} - q\vec{A} \quad (1.3)$$

here, $\hat{\vec{p}}$ is the momentum operator, m is the mass of the electron, c is the speed of light, q is the particle charge (electrons: $q = -e$; positrons: $q = e$), ϕ is the scalar potential, \vec{A} is the vector potential, and α, β are 4-dimensional matrices:

$$\beta = \begin{bmatrix} I_{(2 \times 2)} & 0 \\ 0 & -I_{(2 \times 2)} \end{bmatrix} \quad (1.4)$$

$$\vec{\alpha} = \begin{bmatrix} 0 & \vec{\sigma} \\ \vec{\sigma} & 0 \end{bmatrix} \quad (1.5)$$

where $\vec{\sigma}$ is a vector whose components are the Pauli matrix.

The time-dependent Dirac equation is

$$i \frac{\partial \Psi(t, \vec{r})}{\partial t} = \hat{h} \Psi(t, \vec{r}) \quad (1.6)$$

Concerning the appearance of 4×4 matrix in the Dirac equation, the wave function has to be a 4-component vector:

$$\Psi(t, \vec{r}) = \begin{bmatrix} \phi_1(t, \vec{r}) \\ \phi_2(t, \vec{r}) \\ \phi_3(t, \vec{r}) \\ \phi_4(t, \vec{r}) \end{bmatrix} \quad (1.7)$$

In quantum chemistry, one usually starts with the time-independent equations:

$$\hat{h} \Psi(\vec{r}) = E \Psi(\vec{r}) \quad (1.8)$$

where E is the energy associated to the stationary state $\Psi(\vec{r})$

$$\Psi(\vec{r}) = \begin{bmatrix} \phi_1(\vec{r}) \\ \phi_2(\vec{r}) \\ \phi_3(\vec{r}) \\ \phi_4(\vec{r}) \end{bmatrix} \quad (1.9)$$

By evaluating the equation 1.8 for a single free particle, one can find that there are four energy solutions, and two of them are negative[75].

$$E_1 = +\sqrt{m^2c^4 + c^2p^2}; \quad \Psi_1 = Ne^{i\vec{k}\cdot\vec{r}} \begin{bmatrix} 1 \\ 0 \\ ck_z/(E + mc^2) \\ c(k_x + ik_y)/(E + mc^2) \end{bmatrix}$$

$$E_2 = +\sqrt{m^2c^4 + c^2p^2}; \quad \Psi_2 = Ne^{i\vec{k}\cdot\vec{r}} \begin{bmatrix} 0 \\ 1 \\ c(k_x - ik_y)/(E + mc^2) \\ -ck_z/(E + mc^2) \end{bmatrix}$$

$$E_3 = -\sqrt{m^2c^4 + c^2p^2}; \quad \Psi_3 = Ne^{i\vec{k}\cdot\vec{r}} \begin{bmatrix} ck_z/(E - mc^2) \\ c(k_x + ik_y)/(E - mc^2) \\ 1 \\ 0 \end{bmatrix}$$

$$E_4 = -\sqrt{m^2c^4 + c^2p^2}; \quad \Psi_4 = Ne^{i\vec{k}\cdot\vec{r}} \begin{bmatrix} c(k_x - ik_y)/(E - mc^2) \\ -ck_z/(E - mc^2) \\ 0 \\ 1 \end{bmatrix}$$

where N is the normalization constant

Since we are interested in chemistry, we consider only $q = -e$ with electronic

solutions. It is normally not necessary to explicitly take into account negative energy solutions.

The ratio between the upper two components with those of the lower two is large: when the lower two components are large, the lower two are small, and vice versa. One can then group together the upper and lower two components as 2-component spinors (Φ^L and Φ^S respectively) and write the wave function as

$$\Psi(\vec{r}) = \begin{bmatrix} \Phi^L(\vec{r}) \\ \Phi^S(\vec{r}) \end{bmatrix} \quad (1.10)$$

In the non-relativistic limit, we find that small components $\Phi^S \rightarrow 0$ and large component becomes the non-relativistic wave function in two-component form. Such behavior inspires developments to eliminate the small components and transform the equations to the 2-component form.

Two-electron part

For the two-electron operator $\hat{V}_{1,2}$, apart from the classic Coulomb electrostatic potential, we need to consider the Lorentz covariance for the electron-electron interaction, which results in the magnetic induction effects that introduce interactions beyond the static Coulomb potential[74].

$$\hat{V}_{1,2} = q_1 \phi_2 - q_1 \vec{v}_1 \cdot \vec{A}(\vec{r}_2, t) \quad (1.11)$$

$$\phi(\vec{r}_2, t) = \int \frac{\rho(\vec{r}_2, t)}{r_{12}} (d\vec{r}_2)^3; r_{12} = |\vec{r}_1 - \vec{r}_2| \quad (1.12)$$

$$\vec{A}(\vec{r}_1, t) = \frac{4\pi}{c^2} \int \frac{\vec{j}(r_2, t')}{r_{12}} d\vec{r}_2^3; t' = t - \frac{r_{12}}{c} \quad (1.13)$$

where t' is the retarded time, q_1, q_2 are the charge of the particle 1,2, respectively, and \vec{v} is the relativistic velocity operator:

$$\vec{v} = c\vec{\alpha} \quad (1.14)$$

1.1.2 Approximated Hamiltonian

Breit interaction

The exact two-electron interaction is too complex to be implemented in a practical computation, one usually takes account of the first-order relativistic correction in a similar manner to the case of the classical Darwin approximation[74]:

$$q_1\phi_2 - q_1\vec{v}_1 \cdot \vec{A}(\vec{r}_2, t) = \frac{q_1q_2}{r_{12}} - \frac{q_1\vec{v}_1 \cdot q_2\vec{v}_2}{2c^2r_{12}} - \frac{(q_1\vec{v}_1 \cdot \vec{r}_{12})(q_2\vec{v}_2 \cdot \vec{r}_{12})}{2c^2r_{12}^3} \quad (1.15)$$

Going to quantum mechanics in which the velocity operator is $c\vec{\alpha}$, the part (Breit interaction) that corrects the Coulomb potential could be written as

$$\hat{V}_B = -\left[\frac{c\vec{\alpha}_1 \cdot c\vec{\alpha}_2}{2c^2r_{12}} + \frac{(c\vec{\alpha}_1 \cdot \vec{r}_{12})(c\vec{\alpha}_2 \cdot \vec{r}_{12})}{2c^2r_{12}^3}\right] \quad (1.16)$$

The first term on the right side is known as the Gaunt term representing the current-current interaction, and the second term is a gauge-dependent term.

These magnetic interactions could be understood as the combination of various terms: spin-orbit coupling (SOC), orbit-orbit interaction, and spin-spin interaction. We can further subdivide spin-orbit coupling into spin-same-orbit (SSO) and spin-other-orbit (SOO) effects. SSO describes the coupling of magnetic moment between the spin of electron i , and its own orbital in the reference systems of electron j . SOO corresponds to the coupling between the spin of electron i and the orbital of electron j and vice versa. Particularly, the SOO solely results from the Gaunt term.

Four-Component Hamiltonian

One can combine the exact 4-component one-electron Hamiltonian \hat{h} and different terms of Breit interaction to obtain various types of 4-component Hamiltonians[74, 75]:

1. Dirac-Coulomb (DC): only consider the instantaneous Coulomb interaction $\frac{1}{r_{12}}$

2. Dirac-Coulomb-Gaunt (DCG): add to the DC Hamiltonian the Gaunt terms in two-electron interaction $\frac{\alpha_1 \cdot \alpha_2}{r_{12}}$
3. Dirac-Coulomb-Breit (DCB): add to the DC Hamiltonian the full (frequency-independent) Breit interaction.

Two-Component Hamiltonian

As we shall see in the following, performing 4-component calculations is computationally expensive, particularly for large systems containing many electrons. The idea is thus to transform the 4-component (4c) equation into the 2-component (2c) equation while maintaining only the positive energy solutions.

Here, we show only the transformation within the one-electron part. For the two-electron operator, the transformation requires the full set of two-electron integrals at the 4c level and the generation of the 2c two-electron integral is more expensive than the corresponding 4c calculation[74], and one should consider additional approximation.

The first attempt to transform Dirac Hamiltonian from 4c to 2c is called Foldy-Wouthuysen transformation[76].

$$\mathbf{U}^\dagger \begin{bmatrix} h_{LL} & h_{LS} \\ h_{SL} & h_{SS} \end{bmatrix} \mathbf{U} = \begin{bmatrix} h_{++} & 0 \\ 0 & h_{--} \end{bmatrix} \quad (1.17)$$

The general matrix form for the Foldy-Wouthuysen transformation can be written as:

$$\mathbf{U} = \begin{bmatrix} \Omega_+ & -R^\dagger \Omega_- \\ R \Omega_+ & \Omega_- \end{bmatrix} \quad (1.18)$$

with Ω_\pm being defined as

$$\Omega_+ = \frac{1}{\sqrt{1 + R^\dagger R}} \quad \text{and} \quad \Omega_- = \frac{1}{\sqrt{1 + RR^\dagger}}$$

and R is the connection factor between large and small component in 4c wave function, which is normally energy-dependent:

$$\Phi_S = R \Phi_L \quad (1.19)$$

$$R = (2mc^2 - V + E^+)^{-1} c(\vec{\sigma} \cdot \vec{p}) \quad (1.20)$$

Since the energy dependence of R and \mathbf{U} , the exact Foldy-Wouthuysen transformation is very complicated. It is necessary to find other approximated methods to carry out the 4c to 2c transformation.

Exact Two-component Hamiltonian(X2C)

There have been various ways to perform approximated 4c to 2c transformation such as Douglas-Kroll-Hess (DKH)[77–79], Zeroth Order Regular Approximation (ZORA)[80–82], and eXact two-component Hamiltonian (X2C)[83–86]. Here, we present the X2C scheme, which is the Hamiltonian used in most of calculations in this thesis.

The X2C method constructs \mathbf{R} by solving the one-electron equation directly in the corresponding matrix form[84]. The generic equation is given by

$$\mathbf{h}\mathbf{c}_i = \begin{bmatrix} \mathbf{h}^{\text{LL}} & \mathbf{h}^{\text{LS}} \\ \mathbf{h}^{\text{SL}} & \mathbf{h}^{\text{SS}} \end{bmatrix} \begin{bmatrix} \mathbf{c}_i^{\text{L}} \\ \mathbf{c}_i^{\text{S}} \end{bmatrix} = \epsilon_i \begin{bmatrix} \mathbf{c}_i^{\text{L}} \\ \mathbf{c}_i^{\text{S}} \end{bmatrix} \quad (1.21)$$

$$\mathbf{c}_i^{\text{S}} = \mathbf{R}\mathbf{c}_i^{\text{L}} \quad (1.22)$$

From this relation, one can then obtain the exact form of the transformation matrix \mathbf{U} explicitly, within the finite basis set[87, 88].

$$\mathbf{U} = \mathbf{W}_1\mathbf{W}_2 \quad (1.23)$$

$$\mathbf{W}_1 = \begin{bmatrix} \mathbf{I} & -\mathbf{R}^\dagger \\ \mathbf{R} & \mathbf{I} \end{bmatrix} \quad (1.24)$$

$$\mathbf{W}_2 = \begin{bmatrix} (\mathbf{I} + \mathbf{R}^\dagger\mathbf{R})^{-1/2} & \mathbf{0} \\ \mathbf{0} & (\mathbf{I} + \mathbf{R}\mathbf{R}^\dagger)^{-1/2} \end{bmatrix} \quad (1.25)$$

where \mathbf{I} is the unit matrix.

The key difference between X2C and other approximated two-component philosophies is that other methods derive the analytical expressions of the two-component Hamiltonian with an approximated \mathbf{U} , but X2C directly determines the matrix form of \mathbf{U} without approximation. Therefore, X2C doesn't have the

analytical expression of the Hamiltonian like Breit-Pauli but it gives the exact matrix form in the given basis set. The X2C scheme can be summarized in three steps:

1. Solve the parent 4c one-electron equation on the matrix form
2. Extract coupling factor \mathbf{R} in matrix form from the connection between the large and small component solution
3. Construct transformation matrix \mathbf{U} from \mathbf{R}

For molecular property calculations, which require the evaluation of property integrals, one needs to also transform the property operators Ω from 4-component into 2-component[74]:

$$\Omega^{2c} = [\mathbf{U}^\dagger \Omega^{4c} \mathbf{U}]_{++} \quad (1.26)$$

where we take the ++ block of the transformed 4c parent property matrix as we did for Hamiltonian in the equation 1.17.

One advantage of the X2C scheme is that one can obtain the explicit representation of matrix \mathbf{U} , and transform the property operator on the fly. For other schemes such as DKH, one may take the approximated expression

$$\Omega^{2c} \approx [\Omega^{4c}]_{LL} \quad (1.27)$$

which will lead to significant picture change errors[89].

1.2 Dirac-Hartree-Fock method

Now we turn to many-electron systems, we start from the time-independent Dirac equation with the molecular Hamiltonian defined in 1.1.

$$\left(\sum_i \hat{h}_i + \sum_{i,j} \hat{V}_{i,j} + \hat{V}_{N,N} \right) \Psi(\vec{r}) = E \Psi(\vec{r}) \quad (1.28)$$

The first approach to solving the many-body problems is to consider that each particle is moving in the mean field of others (Hartree-Fock approximation).

Mathematically, an exact many-electron wave function can always be expanded by a set of Slater determinants functions, and the most simple approximation is to use only one determinant[90]:

$$|0'\rangle = e^{-\hat{\kappa}} |0\rangle \quad (1.29)$$

here, $\hat{\kappa}$ is the orbital rotation operator, and $|0\rangle$ is an initial guess state. The $\hat{\kappa}$ can be expressed in the second quantization form:

$$\hat{\kappa} = \sum_{p>q} \kappa_{pq} (a_p^\dagger a_q - a_q^\dagger a_p) = \sum_{p>q} \kappa_{pq} A_{pq} \quad (1.30)$$

where a^\dagger , a , and A are creation, annihilation, and orbital rotation operators, respectively. p and q indicate general (occupied or virtual) spinors.

The energy of the Hartree-Fock state is the expectation value of the Hamiltonian in the rotated basis:

$$E(\kappa_{pq}) = \langle 0' | \hat{H} | 0' \rangle = \langle 0 | e^{\hat{\kappa}} \hat{H} e^{-\hat{\kappa}} | 0 \rangle \quad (1.31)$$

which can be expanded with the Baker-Campbell-Hausdorff (BCH) series:

$$E(\kappa_{pq}) = \langle 0 | \hat{H} | 0 \rangle + \langle 0 | [\hat{\kappa}, \hat{H}] | 0 \rangle + \frac{1}{2!} \langle 0 | [\hat{\kappa}, [\hat{\kappa}, \hat{H}]] | 0 \rangle + \dots \quad (1.32)$$

The coefficients κ_{pq} can be obtained with the help of the variation principle that is, by determining the stationary points of the gradient g of the energy with respect to the coefficients κ_{pq} :

$$\left. \frac{\partial E}{\partial \kappa_{pq}} \right|_{|0'\rangle=|HF\rangle} = g_{pq} = \langle 0 | [A_{pq}, \hat{H}] | 0 \rangle = 0 \quad (1.33)$$

In second quantization form g can be expressed as [75]

$$g_{pq} = f_{pq} - f_{qp}^* \quad (1.34)$$

where f is the Fock matrix:

$$f_{pq} = h_{pq} + \sum_i^{occ} \langle ip | iq \rangle \quad (1.35)$$

with the integral notation:

$$\langle pr | qs \rangle = \langle pr | \frac{1}{r_{12}} | qs \rangle - \langle pr | \frac{1}{r_{12}} | sq \rangle \quad (1.36)$$

$$\langle pr | \frac{1}{r_{12}} | qs \rangle = \int dr_1^3 \int dr_2^3 \phi_p^*(r_1) \phi_r^*(r_2) \frac{1}{r_{12}} \phi_q(r_1) \phi_s(r_2) \quad (1.37)$$

Therefore, the gradient matrix g is being zero corresponds to the Fock matrix f becoming diagonal, leading to the HF equations,

$$f_{qq} |q\rangle = \epsilon_q |q\rangle, \quad (1.38)$$

where ϵ_q are the spinor energies.

The Hartree-Fock energy can be expressed as:

$$E(HF) = \sum_i^{occ} h_{ii} + \frac{1}{2} \sum_{ij}^{occ} \langle ij | ij \rangle + V_{N,N} \quad (1.39)$$

To diagonalize the Fock matrix, we expand the molecular orbitals in terms of atomic basis functions χ :

$$|q\rangle = \sum_{\mu} C_{q\mu} \chi_{\mu} \quad (1.40)$$

and evaluate the pseudoeigenvalue equation (Roothaan equations) with self-

consistent-field (SCF) methods until the results converge[90]:

$$\mathbf{F}^{\text{AO}}\mathbf{C} = \mathbf{S}\mathbf{C}\epsilon \quad (1.41)$$

where \mathbf{F}^{AO} is the Fock matrix in the atomic basis set, and \mathbf{S} is the overlap matrix.

Unlike in the non-relativistic case, the 4-component Roothaan-type of Dirac-Hartree-Fock equation generates both positive and negative energy states. That indicates one has to pick up a suitable basis set to expand both the large and small components, otherwise, an arbitrary expansion will result in "variational collapse" because of the presence of the negative energy solutions.

In the 4c calculation, one usually uses basis sets following the kinetic balance[75, 91], that is the small component basis set has to be expressed in terms of the large component basis set:

$$\chi^{\text{S}} = N(\vec{\sigma} \cdot \vec{p})\chi^{\text{L}} \quad (1.42)$$

where N is the normalization constant.

On the other hand, in the usual X2C scheme, we transform the Hamiltonian from 4c to 2c before the SCF procedure, so in the latter, only positive energy orbitals are generated, except for the X2C molecular-mean-field (X2Cmmf) scheme[88], where we run the 4c molecular Hartree-Fock calculation first to obtain the transformation matrix.

1.3 Correlated wave functions

1.3.1 Configuration Interaction

The Hartree-Fock approximation treats electrons moving in an average potential while ignoring the instantaneous electron-electron interaction (dynamic electron correlation). To consider such influence, one can put electrons on a set of 'configurations' where electrons could occupy different orbitals.

The Hartree-Fock equation provides the orbitals to construct the ground and excited determinants, in which we then solve the equation 1.28. Considering all

possible configurations within the given basis set (Full-CI limits), we can obtain the exact wave function and energy. The electronic correlation problem can then be translated into how we evaluate the coefficients of the CI expansion.

$$|\Psi\rangle = \sum_i^{\infty} c_i |\phi_i\rangle \quad (1.43)$$

The first way is that we directly solve the many-body equation 1.28. In practice, we always truncate the CI space. For example, the well-known CISD method is to pick up all excited determinants that are singly and doubly excited from the Hartree-Fock determinant,

$$|\Psi_{CISD}\rangle = |HF\rangle + \sum_i^a c_i^a |\phi_i^a\rangle + \sum_{ij}^{ab} c_{ij}^{ab} |\phi_{ij}^{ab}\rangle \quad (1.44)$$

$$|\phi_i^a\rangle = a_a^\dagger a_i |HF\rangle \quad (1.45)$$

$$|\phi_{ij}^{ab}\rangle = a_a^\dagger a_b^\dagger a_j a_i |HF\rangle \quad (1.46)$$

To evaluate the CI coefficients, one puts Eq. 1.44 into Eq. 1.28 and left-multiplies with the corresponding determinants to obtain a matrix equation [92]

$$\mathbf{HC} = EC \quad (1.47)$$

$$\mathbf{H}_{\boxtimes\boxtimes} = \langle\phi_\nu|\hat{H}|\phi_\mu\rangle \quad (1.48)$$

where the eigenvalues and eigenvectors of the Hamiltonian matrix represent the energy and wave function of ground and excited states. The correlation energy can be defined as the difference between the exact total energy and the Hartree-Fock energy.

In the second way, we start from the variational principle, since the exact solution should be stable under any perturbations [90].

$$E(c_i) = \frac{\langle\Phi(c_i)|\hat{H}|\Phi(c_i)\rangle}{\langle\Phi(c_i)|\Phi(c_i)\rangle} \quad (1.49)$$

$$\frac{\partial E(c_i)}{\partial c_i} = 0 \quad (1.50)$$

Here the variational parameters are the CI coefficients associated with the determinants.

The variational equation 1.50 gives the same matrix form as 1.47. That means the solutions of the CI method satisfy the variational principle and the roots represent the upper bound of the exact ground and excited states.

The single reference (SR) CI method shown above is based on the dominance of the HF determinant, so the calculations become meaningless in case the HF determinant is not dominant, such as in molecular dissociation problems. To overcome these shortcomings, multi-reference (MR) CI methods are proposed. The MRCI wave functions are based on the concept of the reference space $|\psi(m)\rangle$ including more than a single determinant[93]:

$$|\psi(m)_i^a\rangle = a_a^\dagger a_i |HF\rangle; \quad (1.51)$$

$$|\psi(m)_{ij}^{ab}\rangle = a_a^\dagger a_b^\dagger a_j a_i |HF\rangle; \dots \quad (1.52)$$

$$m = 1 \dots N_{ref} \quad (1.53)$$

where N_{ref} is the number of configurations in the reference space.

The MRCI wave function is then generated by including all configurations belonging to the reference space and all excitations up to a given level from each reference configuration[93].

$$\begin{aligned} |\Psi_{MRCI}\rangle &= \sum_m c_m |\psi(m)\rangle \\ &+ \sum_m \sum_{i,a} c(m)_i^a |\psi(m)_i^a\rangle \\ &+ \sum_m \sum_{i>j,a>b} c(m)_{ij}^{ab} |\psi(m)_{ij}^{ab}\rangle \\ &+ \dots \end{aligned} \quad (1.54)$$

The MRCI model can provide very accurate results as long as the user can include all important configurations in the reference space. However, for large systems, the number of configurations in the reference space is large, resulting

in the calculation being impossible. Therefore, setting a suitable reference space is the key step in the MRCI calculation, which relies on the user's experience and patience.

Other significant issues in CI methods are the lack of size-extensivity and size-consistency. These issues exist in all truncated CI models for both SR and MR approaches. The size-consistency states that for two noninteraction molecular fragments A and B, the total energy should be additively separable[90]:

$$\hat{H}_A |\phi_A\rangle = E_A |\phi_A\rangle \quad (1.55)$$

$$\hat{H}_B |\phi_B\rangle = E_B |\phi_B\rangle \quad (1.56)$$

$$\hat{H}_{AB} |\phi_{AB}\rangle = E_{AB} |\phi_{AB}\rangle \quad (1.57)$$

$$E_{AB} = E_A + E_B \quad (1.58)$$

However, for the truncated CI models, for instance, in the CI-doubles (CID) wave function, there are double excitations in the total wave functions for the dimer, but there are quadruple excitations if we do the calculations for each subsystem, separately (double excitations on each monomer). Size-extensivity is a more mathematically formal characteristic which refers to the correct scaling of a method with the number of electrons[94]. These issues will introduce substantial errors into calculated properties such as dissociation energy. While it can be partially fixed by some approximated methods such as Davidson correction (+Q)[95], it would be better to develop a method to consider the size-extensivity exactly such as perturbation theory and coupled cluster discussed in the following.

1.3.2 Møller–Plesset Perturbation Theory

The second approach is to use the perturbation theory, which has been widely used in physics. In most situations, compared to the Hartree-Fock energy, the correlation energy is so small that can be safely treated as a perturbation. Unlike the CI method, the Møller–Plesset Perturbation Theory (MPPT) doesn't follow the variational principle, but it is the simplest method to compute the electron

correlation.

As the first strategy to derive the CI equation, we also start from the equation 1.28, but divide the total Hamiltonian into two parts: 1) the unperturbed Hamiltonian (H_0); and 2) the perturbation term V [90]:

$$H |\Psi\rangle = (H_0 + \lambda V) |\Psi\rangle = E |\Psi\rangle \quad (1.59)$$

Here, H_0 denotes the Hartree-Fock Hamiltonian, and we know the corresponding eigenfunctions and eigenvalues:

$$H_0 |\Phi_m^0\rangle = E_m^0 |\Phi_m^0\rangle \quad (1.60)$$

Then, we expand the exact wave function and energy in a Taylor series with respect to the perturbation parameter λ :

$$E = E^0 + \lambda E^1 + \lambda^2 E^2 + \dots + \lambda^n E^n + \dots \quad (1.61)$$

$$|\Psi\rangle = |\Phi^0\rangle + \lambda |\Phi^1\rangle + \lambda^2 |\Phi^2\rangle + \dots + \lambda^n |\Phi^n\rangle + \dots \quad (1.62)$$

Substituting Eq. 1.61, 1.62 into Eq. 1.59 while keeping perturbation corrections always orthogonal to the zeroth order part:

$$\langle \Phi^0 | \Phi^n \rangle = 0 \quad (1.63)$$

and collecting all terms of the same order under the perturbation. Then, we can obtain expressions for the n-th order perturbation energies and wave functions. We show the expression for the perturbation energy until the second order below:

$$E^0 = \sum_i^{occ} \epsilon_i \quad (1.64)$$

$$E^1 = \langle \Phi^0 | V | \Phi^0 \rangle = -\frac{1}{2} \sum_{i,j}^{occ} \langle ij | |ij \rangle \quad (1.65)$$

$$E^2 = \sum_m \frac{|\langle \Phi_0^0 | V | \Phi_m^0 \rangle|^2}{E_0^0 - E_m^0} = \frac{1}{4} \sum_{i,j}^{occ} \sum_{a,b}^{vir} \frac{|\langle ij || ab \rangle|^2}{\epsilon_i + \epsilon_j - \epsilon_a - \epsilon_b} \quad (1.66)$$

Compared to equation 1.39, we note that the Hartree-Fock energy is the sum of the zeroth order and the first-order energies. Therefore, the first-order correction to the Hartree-Fock energy is the second-order perturbation energy E^2 .

1.3.3 Coupled Cluster Theory

As we see in Eq.1.44, the CI type of wave functions expand the electronic correlation by a linear combination of higher order Slater determinants including double, triple, quadruple excitations, and so forth. However, it suffers from two serious disadvantages: the lack of size-extensivity and the fairly slow convergence towards the Full CI limit[37, 90]. On the other hand, in Coupled Cluster theory, the wave function is parametrized as an exponential function:

$$|\Psi_{CC}\rangle = e^{\hat{T}} |HF\rangle \quad (1.67)$$

where \hat{T} is the cluster operator:

$$\hat{T} = \hat{T}_1 + \hat{T}_2 + \hat{T}_3 + \dots \quad (1.68)$$

For example, in the well-known CCSD wave function \hat{T} is restricted to terms \hat{T}_1 and \hat{T}_2 only:

$$|\Psi_{CCSD}\rangle = e^{\hat{T}_1 + \hat{T}_2} |HF\rangle \quad (1.69)$$

in second quantization, \hat{T}_1 and \hat{T}_2 can be defined as:

$$\hat{T}_1 = \sum_i^a t_i^a \hat{a}_a^\dagger \hat{a}_i \quad (1.70)$$

$$\hat{T}_2 = \frac{1}{4} \sum_{ij}^{ab} t_{ij}^{ab} \hat{a}_a^\dagger \hat{a}_b^\dagger \hat{a}_j \hat{a}_i \quad (1.71)$$

yielding

$$|\Psi_{CCSD}\rangle = |HF\rangle + \sum_i^a t_i^a |\phi_i^a\rangle + \sum_{i>j}^{a>b} t_{ij}^{ab} |\phi_{ij}^{ab}\rangle + \sum_{i,j}^{a,b} t_i^a t_j^b |\phi_{ij}^{ab}\rangle + \sum_{i,k>l}^{a,c>d} t_i^a t_{kl}^{cd} |\phi_{ijk}^{abc}\rangle + \dots \quad (1.72)$$

Unlike the CISD wave function, the CCSD wave function contains determinants higher than double excitations by the so-called unconnected terms. For instance, the CCSD wave function has part of triple excitations by including the product of \hat{T}_1 and \hat{T}_2 , which are not present in the linear type of wave function CISD.

While there has been some progress recently in evaluating the CC wave function with the variational principle[96], such methods are still difficult to program for a classical computer. Alternatively, one uses the intermediate normalization as Eq. 1.63 in perturbation theory[90]:

$$\hat{H} |\Psi_{CC}\rangle = E e^{\hat{T}} |HF\rangle \quad (1.73)$$

$$\langle HF | \Psi_{CC} \rangle = 1, \quad (1.74)$$

we obtain the Coupled-Cluster ground state energy:

$$E = \langle HF | \hat{H} | \Psi_{CC} \rangle = \langle HF | e^{-\hat{T}} \hat{H} e^{\hat{T}} | HF \rangle = \langle HF | \hat{\hat{H}} | HF \rangle \quad (1.75)$$

where $\hat{\hat{H}}$ is called similarity-transformed Hamiltonian.

Projecting the Eq.1.73 against the excited determinants $\langle \mu |$, we obtain the set of equations for the amplitudes:

$$\langle \mu | \hat{\hat{H}} | HF \rangle = 0 \quad (1.76)$$

Another way to derive the CC amplitude equations is by introducing the Lagrangian multiplier λ_μ to construct the CC Lagrangian L [97]:

$$L = \langle HF | \hat{\hat{H}} | HF \rangle + \sum_\mu \lambda_\mu \langle \mu | \hat{\hat{H}} | HF \rangle \quad (1.77)$$

where L is orbital-unrelaxed.

Making the CC Lagrangian stationary with respect to the amplitudes t , and multipliers λ :

$$\frac{\partial L}{\partial \lambda} = 0 \quad (1.78)$$

$$\frac{\partial L}{\partial t} = 0 \quad (1.79)$$

We can recognize that equation 1.78 corresponds to the amplitude equation 1.76. Moreover, with equation 1.79, one can evaluate the multipliers λ , which can be used to construct the ground state (one-body reduced) density matrix and from it obtain ground-state expectation values for one-body operators.

The CC equations are expressed in the molecular orbital (MO) basis as other correlation models like CI and MP2, so a transformation between atomic orbitals (AO) to MO is necessary before performing the CC evaluation. A further improvement beyond the CCSD is the CCSD(T) model[98], which considers the triple excitations with a non-iterative perturbation fashion.

Response Theory

In this chapter, a brief overview of response theory is given. We start with defining static molecular properties with the help of time-independent perturbation theory. For frequency-dependent properties, while the formulation can be defined with the so-called Ehrenfest approach, we follow the formulation based upon the quasi-energy formalism. Then we discuss the parametrization of the time-dependent wave function, particularly focusing on the coupled cluster models. We note the quasi-energy formulation of coupled cluster molecular properties is extensively discussed in the articles by Christiansen et al.[27], and Pałowski et al.[92], and we refer the reader to these references for further details.

2.1 Molecular response properties

Molecular response properties describe how molecules respond to changes in the environment. For example, when we apply a static external electromagnetic field to a molecule, such a field will change the system's wave function and energy following the time-independent equations:

$$H(\epsilon) |0(\epsilon)\rangle = E(\epsilon) |0(\epsilon)\rangle \quad (2.1)$$

$$H(\epsilon) = H_0 + V(\epsilon) \quad (2.2)$$

where H and H_0 are the total and unperturbed Hamiltonian, respectively, $|0(\epsilon)\rangle$ is the total wave function, V is the time-independent external perturbation, E is the total molecular energy, and ϵ is the parameter to describe the perturbation such as field strength.

There are two primary methods to define molecular properties. The first method views molecular properties as variations (derivatives) in molecular energy due to an external perturbation. For instance, the electric dipole moment (μ), electric polarizability (α), first-order hyperpolarizability (β), and second-order hyperpolarizability (γ) can be defined as the first, second, third, and fourth-order derivatives, respectively, of E with respect to the ϵ .

$$\mu = \left. \frac{\partial E}{\partial \epsilon} \right|_{\epsilon=0} \quad (2.3)$$

$$\alpha = \left. \frac{\partial^2 E}{(\partial \epsilon)^2} \right|_{\epsilon=0} \quad (2.4)$$

$$\beta = \left. \frac{\partial^3 E}{(\partial \epsilon)^3} \right|_{\epsilon=0} \quad (2.5)$$

$$\gamma = \left. \frac{\partial^4 E}{(\partial \epsilon)^4} \right|_{\epsilon=0} \quad (2.6)$$

The second approach begins with the derivatives of expectation values (Ehrenfest approach)[30, 99], such as the dipole moment. It treats properties like polarizability and first-order hyperpolarizability as expansion coefficients of the electric dipole moment using subsequent Taylor series expansions.

$$\mu(\epsilon) = \langle 0(\epsilon) | \hat{\mu} | 0(\epsilon) \rangle \quad (2.7)$$

$$\mu(\epsilon) = \mu + \alpha\epsilon + \frac{1}{2}\beta\epsilon^2 + \frac{1}{6}\gamma\epsilon^3 + \dots \quad (2.8)$$

Both methods have their respective advantages and limitations. The first is versatile as it can connect energy with various static properties, leveraging the Hellmann–Feynman theorem.

$$\frac{dE}{d\epsilon} = \langle 0(\epsilon) | \frac{dH}{d\epsilon} | 0(\epsilon) \rangle \quad (2.9)$$

However, this approach faces challenges when studying time-dependent properties, where energy isn't clearly defined. Conversely, the method based on expectation values can be seamlessly extended to time-dependent cases, as the time-dependent expectation value can be defined as

$$\mu(\epsilon, t) = \langle 0(\epsilon, t) | \hat{\mu} | 0(\epsilon, t) \rangle \quad (2.10)$$

2.2 Quasi-energy

While the Ehrenfest approach is quite flexible for dealing with the time-dependent response properties and Koch and Jørgensen[100] derived the corresponding response functions and equations for coupled cluster wave function, in this thesis we focus on an alternative method based on the concept of quasi-energy. It is more attractive than the Ehrenfest approach in that it treats the variational and nonvariational wave functions in a unified framework as similar to time-independent theory, which can be naturally formulated in the limit of static perturbations.

The quasi-energy $Q(t)$ is defined with the expressions[92]

$$Q(t) = \langle 0(\epsilon, t) | (H(\epsilon, t) - i \frac{\partial}{\partial t}) | 0(\epsilon, t) \rangle \quad (2.11)$$

$$H(\epsilon, t) = H_0 + V(\epsilon, t) \quad (2.12)$$

where $|0(\epsilon, t)\rangle$ is the time-dependent wave function corresponding to the time-independent wave function $|0(\epsilon)\rangle$ in the static limit. $V(\epsilon, t)$ is a time-dependent perturbation, and can be expanded in a sum over Fourier components,

$$V(\epsilon, t) = \sum_i X_i \epsilon_{X_i} e^{-i\omega_{X_i} t} \quad (2.13)$$

where X_i is a Hermitian time-independent operator, and ω_{X_i} is the associated real frequency.

Consequently, $Q(t)$ has the same content as the energy in the time-independent limit. Furthermore, for periodic perturbations, it has been demonstrated that

one can compute the derivatives of the time-averaged quasi-energy to define time-dependent properties [27]:

$$\langle X \rangle = \frac{d\{Q\}_T}{d\epsilon_x(0)} \quad (2.14)$$

$$\langle\langle X; Y \rangle\rangle_{\omega_y} = \frac{d^2\{Q\}_T}{d\epsilon_x(\omega_0)d\epsilon_y(\omega_y)} \quad (2.15)$$

$$\langle\langle X; Y, Z \rangle\rangle_{\omega_y, \omega_z} = \frac{d^3\{Q\}_T}{d\epsilon_x(\omega_0)d\epsilon_y(\omega_y)d\epsilon_z(\omega_z)} \quad (2.16)$$

$$\langle\langle X; Y, Z, \dots \rangle\rangle_{\omega_y, \omega_x, \dots} = \frac{d^{n+1}\{Q\}_T}{d\epsilon_x(\omega_0)d\epsilon_y(\omega_y)d\epsilon_z(\omega_z)\dots} \quad (2.17)$$

where the time-averaged quasi-energy is defined by

$$\{Q\}_T = \frac{1}{T} \int_{-T/2}^{T/2} Q(t) dt \quad (2.18)$$

and the frequency ω should follow the relations:

$$\sum_i \omega_i + \omega_0 = 0 \quad (2.19)$$

The concept of quasi-energy significantly simplifies the process of deriving time-dependent response functions and their associated response equations, because we can apply the same procedures used for computing energy derivatives in time-independent problems. Additionally, this approach allows for the reuse of techniques such as Wigner's $2n+1$ and $2n+2$ rules[92].

The $2n+1$ rule states that from the n -th and lower-order wave function on the right-hand side of eq 2.11 one can determine the $(2n+1)$ -th order of perturbation to the energy. For non-variational wave functions such as CC, the left-hand wave-function is not merely the complex conjugate of the right-side counterpart. However, it allows for further simplifications by applying the $2n+2$ rule to the wave function on the left-hand side, as with the determination of the n -th order left-hand side wave function we can determine the $(2n+2)$ -th order of perturbation to the energy. Specifically, for the linear response, which is

the second-order perturbation to energy, we are required to evaluate the first-order and zeroth-order perturbation for the right and left wave functions, respectively. For the quadratic response, which is the third-order perturbation, we are required to calculate first-order perturbation for both left and right wave functions.

2.3 Parametrization of time-dependent wave function

The time-dependent wave function can be defined in general form via an exponential parametrization[92, 101]:

$$|0_R(t, \epsilon)\rangle = N(t, \epsilon)e^{B_0}e^{B(t)} |R\rangle \quad (2.20)$$

where, $N(t, \epsilon)$ is the normalization constant, $|R\rangle$ is the time-independent reference state such as Hartree-Fock wave function. B_0 , and $B(t)$ are time-independent and time-dependent operators, respectively.

$$B_0 = \sum_k b_k^0 \beta_k^0 \quad (2.21)$$

$$B(t) = \sum_k b_k(t) \beta_k \quad (2.22)$$

They are determined by the specific wave function forms, which are discussed in the following. Then, the time-averaged quasi-energy is defined as [92]

$$Q = \text{Re}\{\langle R| e^{-B(t)}(H^{B_0} - i\frac{\partial}{\partial t})e^{B(t)} |R\rangle\}_T \quad (2.23)$$

where H^{B_0} is the similarity-transformed Hamiltonian \hat{H} defined in 1.75.

For a non-variational wave function such as coupled cluster, one should make use of a Lagrangian with time-dependent multipliers $\bar{b}_k(t)$. Using Fourier transformation, the time-averaged Lagrangian in the frequency domain can be

expressed as

$$L = \text{Re}\{\{\langle R | e^{-B(t)}(H^{B_0} - i\frac{\partial}{\partial t})e^{B(t)} | R \rangle\}_T + \sum_{k,K} \bar{b}_k(\omega_K)\{\langle k | e^{-B(t)}(H^{B_0} - i\frac{\partial}{\partial t})e^{B(t)} | R \rangle\}_T\} \quad (2.24)$$

where, $\bar{b}_k(\omega_K)$ are the Fourier components of the time-dependent multipliers $\bar{b}_k(t)$:

$$\bar{b}_k(t) = \sum_K \bar{b}_k(\omega_K)e^{-i\omega_K t} \quad (2.25)$$

$$\begin{aligned} \bar{b}_k(\omega_K) &= \bar{b}_k^0 \delta(0 - \omega_K) + \sum_i \bar{b}_k^{X_i}(\omega_{X_i}) \epsilon_{X_i}(\omega_{X_i}) \delta(\omega_{X_i} - \omega_K) \\ &+ \frac{1}{2} \sum_i \sum_j \bar{b}_k^{X_i X_j}(\omega_{X_i}, \omega_{X_j}) \epsilon_{X_i}(\omega_{X_i}) \epsilon_{X_j}(\omega_{X_j}) \times (\omega_{X_j}) \delta(\omega_{X_i} + \omega_{X_j} - \omega_K) \\ &+ \dots \\ &+ \frac{1}{n!} \sum_i \dots \sum_n \bar{b}_k^{X_i \dots X_n}(\omega_{X_i}, \dots, \omega_{X_n}) \times \left(\prod_{m=1}^n \epsilon_{X_m}(\omega_{X_m}) \right) \delta\left(\sum_{m=1}^n \omega_{X_m} - \omega_K\right) \\ &+ \dots \end{aligned} \quad (2.26)$$

with

$$\begin{aligned} \delta(X) &= 0(x \neq 0) \\ &= 1(x = 0) \end{aligned} \quad (2.27)$$

Each molecular response property, characterized by a response function, can be derived from the Taylor expansion of the Lagrangian with respect to the field strength ϵ at different orders.

$$L = \sum_n L^n \quad (2.28)$$

$$L^n = \frac{1}{n!} \sum_i \dots \sum_n N L^{X_i \dots X_n}(\omega_{X_i}, \dots, \omega_{X_n}) \times \epsilon_{X_i}(\omega_{X_i}) \dots \epsilon_{X_n}(\omega_{X_n}) \quad (2.29)$$

$$L^{X_i \dots X_n}(\omega_{X_i}, \dots, \omega_{X_n}) = \left(\frac{d^n L}{d\epsilon_{X_i}(\omega_{X_i}) \dots d\epsilon_{X_n}(\omega_{X_n})} \right)_0 \quad (2.30)$$

The Lagrangian at each order is then determined by making it stationary with respect to the wave function parameters (b_k, \bar{b}_k), yielding the response equations

for a given order. Thus, for L^n one has:

$$\frac{\partial L^{X_i \dots X_n}(\omega_{X_i}, \dots, \omega_{X_n})}{\partial b^{X_i \dots X_n}(\omega_{X_i}, \dots, \omega_{X_n})} = 0 \quad (2.31)$$

$$\frac{\partial L^{X_i \dots X_n}(\omega_{X_i}, \dots, \omega_{X_n})}{\partial \bar{b}^{X_i \dots X_n}(\omega_{X_i}, \dots, \omega_{X_n})} = 0 \quad (2.32)$$

whose solution may be simplified, or not required at all, due to the $2n+1$ and $2n+2$ rules. Once the necessary wave function parameters have been determined, the response functions defined as

$$\langle\langle X_i; \dots, X_n \rangle\rangle_{\omega_{X_i}, \dots, \omega_{X_n}} = \frac{1}{2} \left(L^{X_i \dots X_n}(\omega_{X_i}, \dots, \omega_{X_n}) + L^{X_i \dots X_n*}(\omega_{-X_i}, \dots, \omega_{-X_n}) \right) \quad (2.33)$$

$$\omega_{X_i} + \dots + \omega_{X_n} = 0 \quad (2.34)$$

2.4 Response functions for Coupled Cluster models

There are different parametrization schemes for the time-dependent wave function [92]. In this thesis, our emphasis is on the coupled cluster model, in which, the time-independent reference state is represented by the normal coupled cluster wave function, so B_0 is the time-independent cluster operator:

$$b_k^0 = t_k^0 \quad (2.35)$$

$$\beta_k^0 = \hat{t}_k \quad (2.36)$$

$$B_0 = T_0 = \sum_k t_k^0 \hat{t}_k \quad (2.37)$$

where, \hat{t}_k denotes the excitation operator, which transforms the Hartree-Fock state to an excited Slater determinant $|k\rangle$:

$$|k\rangle = \hat{t}_k |R\rangle \quad (2.38)$$

When solving the response equations 2.31 and 2.32, it is convenient to in-

roduce the Jacobian matrix \mathbf{A} , which is defined by differentiating Q or L with respect to the independent parameters b_k , and \bar{b}_k , in the limit of the zero perturbation strength. The Jacobian matrix is equal to the similarity-transformed Hamiltonian matrix within the coupled cluster framework:

$$\mathbf{A} = \mathbf{H}^{\mathbf{B}_0} = \mathbf{H}^{T_0} = \bar{\mathbf{H}} \quad (2.39)$$

For the time evolution function $B(t)$, it can be defined as either linear or non-linear. The former corresponds to the CC-CI model, while the latter is indicative of the CC-CC model.

2.4.1 CC-CI

In the CC-CI model, the β_k in $B(t)$ of equation 2.22 is defined with the state-transfer operator

$$\beta_k = |k\rangle\langle R| \quad (2.40)$$

and we use $s(t)$ to replace the wave function coefficients $b(t)$:

$$B(t) = S(t) = \sum_k s_k(t)\beta_k \quad (2.41)$$

It follows from this definition of $S(t)$ that

$$S(t)S(t) = 0 \quad (2.42)$$

Then, the wave function is linear for the time evolution part:

$$|0_{I(t,\epsilon)}\rangle^{\text{CC-CI}} = e^{S(t)}e^{T_0}|R\rangle = e^{T_0}|R\rangle + \sum_k s_k(t)\hat{\tau}_k e^{T_0}|R\rangle \quad (2.43)$$

Following the equation 2.28, 2.30, and 2.33, the zeroth, first-order, and second-order perturbed Lagrangian in the frequency domain are:

$${}^{\text{CC-CI}}L^{(0)} = E_0 = \langle R|H_0^{T_0}|R\rangle \quad (2.44)$$

$${}^{CC-CI}L^{X_1} = \langle R | X_1^{T_0} | R \rangle + \sum_k \bar{t}_k^{(0)} \langle k | X_1^{T_0} | R \rangle \quad (2.45)$$

$$\begin{aligned} {}^{CC-CI}L^{X_1, X_2}(\omega_{X_1}, \omega_{X_2}) = & P^{X_1, X_2} \\ & \left[\sum_{km} \bar{s}_k^{X_1}(\omega_{X_1}) s_m^{X_2}(\omega_{X_2}) (A_{km} - \omega_{X_2} \delta_{km}) \right. \\ & + \sum_m s_m^{X_2}(\omega_{X_2}) \langle R | [X_1^{T_0}, |m\rangle] \langle R | | R \rangle \\ & + \sum_k \bar{s}_k^{X_2}(\omega_{X_2}) \langle k | X_1^{T_0} | R \rangle \\ & - \sum_k \bar{t}_k^0 s_k^{X_1}(\omega_{X_1}) \sum_m s_m^{X_2}(\omega_{X_2}) \langle R | H_0^{T_0} | m \rangle \\ & \left. - \sum_{km} \bar{t}_k^0 s_m^{X_2}(\omega_{X_2}) s_m^{X_2}(\omega_{X_2}) \langle k | [X_1^{T_0}, |m\rangle] \langle R | | R \rangle \right] \end{aligned} \quad (2.46)$$

where \bar{t}^0 is the ground state Lagrangian amplitudes, which can be obtained by solving the Lambda-equations of the ground state. P^{X_1, X_2} acts to permute perturbations X_1 and X_2 .

The $s_m^{X_1}$ and $\bar{s}_m^{X_1}$ are the first-order perturbed amplitudes for the right and left state, respectively. They are determined by the corresponding right and left first-order response equations:

$$\sum_m (A_{km} - \omega_{X_1} \delta_{km}) s_m^{X_1} = -\langle k | X_1^{T_0} | R \rangle \quad (2.47)$$

$$\begin{aligned} \sum_m \bar{s}_m^{X_1} (A_{mk} + \omega_{X_1} \delta_{km}) = & \left(\sum_m \bar{t}_m^{(0)} s_m^{X_1} \right) \langle R | H_0^{T_0} | k \rangle \\ & + \bar{t}_k^{(0)} \sum_m s_m^{X_1} \langle R | H_0^{T_0} | m \rangle \\ & - \langle R | [X_1^{T_0}, |k\rangle] \langle R | | R \rangle \\ & - \sum_m \bar{t}_m^{(0)} \langle m | [X_1^{T_0}, |k\rangle] \langle R | | R \rangle \end{aligned} \quad (2.48)$$

2.4.2 CC-CC

In the CC-CC model, the $B(t)$ is defined with the excitation operator \hat{t}_k , and we use $t_k(t)$ to present the coefficients $b_k(t)$

$$\beta_k = \hat{t}_k \quad (2.49)$$

$$B(t) = T(t) = \sum_k t_k(t) \hat{t}_k \quad (2.50)$$

The wave function is exponential for the time evolution part:

$$|0_{I(t,\epsilon)}\rangle^{CC-CC} = e^{T(t)} e^{T_0} |R\rangle = e^{T_0} |R\rangle + \sum_k t_k(t) \hat{t}_k e^{T_0} |R\rangle + \frac{1}{2} \sum_{k,l} t_k(t) t_l(t) \hat{t}_k \hat{t}_l e^{T_0} |R\rangle + \dots \quad (2.51)$$

The zeroth, first-order, and second-order perturbation Lagrangian are:

$${}^{CC-CC}L^{(0)} = E_0 = \langle R | H_0^{T_0} | R \rangle \quad (2.52)$$

$${}^{CC-CC}L^{X_1} = \langle R | X_1^{T_0} | R \rangle + \sum_k \bar{t}_k^{(0)} \langle k | X_1^{T_0} | R \rangle \quad (2.53)$$

$$\begin{aligned} {}^{CC-CC}L^{X_1, X_2}(\omega_{X_1}, \omega_{X_2}) = & P^{X_1, X_2} \\ & [\sum_{km} \bar{t}_k^{X_1}(\omega_{X_1}) t_m^{X_2}(\omega_{X_2}) (A_{km} - \omega_{X_2} \delta_{km}) \\ & + \sum_m t_m^{X_2}(\omega_{X_2}) \langle R | [X_1^{T_0}, \hat{t}_m] | R \rangle \\ & + \sum_k \bar{t}_k^{X_2}(\omega_{X_2}) \langle k | X_1^{T_0} | R \rangle \\ & + \sum_{km} \bar{t}_k^0 t_m^{X_2}(\omega_{X_2}) \langle k | [X_1^{T_0}, \hat{t}_m] | R \rangle \\ & + 1/2 \sum_{mn} t_m^{X_1}(\omega_{X_1}) t_n^{X_2}(\omega_{X_2}) \langle R | [[H_0^{T_0}, \hat{t}_m], \hat{t}_n] | R \rangle \\ & + 1/2 \sum_{kmn} \bar{t}_k^0 t_m^{X_1}(\omega_{X_1}) t_n^{X_2}(\omega_{X_2}) \langle k | [[H_0^{T_0}, \hat{t}_m], \hat{t}_n] | R \rangle \end{aligned} \quad (2.54)$$

The zeroth and first-order Lagrangian is the same as the CC-CI model, but the second-order is different.

The first-order perturbed amplitudes $t_m^{X_1}$ and $\bar{t}_m^{X_1}$ are determined with the right and left response equations:

$$\sum_m (A_{km} - \omega_{X_1} \delta_{km}) t_m^{X_1} = -\langle k | X_1^{T_0} | R \rangle \quad (2.55)$$

$$\begin{aligned} \sum_m \bar{t}_m^{X_1} (A_{km} + \omega_{X_1} \delta_{km}) = & - \sum_m t_m^{X_1} \langle R | [[H_0^{T_0}, \hat{t}_m], \hat{t}_k] | R \rangle \\ & + \sum_{mn} \bar{t}_m^{(0)} t_n^{X_1} \langle m | [[H_0^{T_0}, \hat{t}_m], \hat{t}_k] | R \rangle \\ & - \langle R | [X_1^{T_0}, \hat{t}_k] | R \rangle \\ & - \sum_m \bar{t}_m^{(0)} \langle m | [X_1^{T_0}, \hat{t}_k] | R \rangle \end{aligned} \quad (2.56)$$

It should be noted that the right response equation is the same for CC-CC and CC-CI models. Additionally, Coriani et al.[101] demonstrated that the response properties derived from the EOM-CC method are equivalent to those of the CC-CI model.

The first-order derivatives of the Lagrangian represent the expectation value of the ground state as shown before. The associated implementation on DIRAC has been discussed in the reference[102]. The second and third-order derivatives correspond to linear and quadratic response properties, respectively. Detailed discussions on their implementations are presented in Chapters 3 and 4.

Part II

ExaCorr Implementation

Chapter 3

Implementation of Linear Response properties based on Relativistic Coupled Cluster Theory

Paper: Formulation and Implementation of Frequency-Dependent Linear Response Properties with Relativistic Coupled Cluster Theory for GPU-accelerated Computer Architectures

I worked out the equations, implemented the code, carried out all calculations, and wrote the manuscript.

Formulation and Implementation of Frequency-Dependent Linear Response Properties with Relativistic Coupled Cluster Theory for GPU-accelerated Computer Architectures

Xiang Yuan,^{†,‡} Loïc Halbert,[†] Johann Valentin Pototschnig,[‡] Anastasios
Papadopoulos,[‡] Sonia Coriani,[¶] Lucas Visscher,[‡] and André Severo Pereira
Gomes^{*,†}

[†]*Univ. Lille, CNRS, UMR 8523 - PhLAM - Physique des Lasers Atomes et Molécules,
F-59000 Lille, France*

[‡]*Department of Chemistry and Pharmaceutical Sciences, Faculty of Science, Vrije
Universiteit Amsterdam, 1081 HV Amsterdam, The Netherlands*

[¶]*DTU Chemistry – Department of Chemistry, Technical University of Denmark, DK-2800
Kongens Lyngby, Denmark*

E-mail: andre.gomes@univ-lille.fr

Abstract

We present the development and implementation of the relativistic coupled cluster linear response theory (CC-LR) which allows the determination of molecular properties arising from time-dependent or time-independent electric, magnetic, or mixed

electric-magnetic perturbations (within a common gauge origin for the magnetic properties), as well as to take into account the finite lifetime of excited states in the framework of damped response theory. We showcase our implementation, which is capable to offload the computationally intensive tensor contractions characteristic of coupled cluster theory onto graphical processing units (GPUs), in the calculation of: *(a)* frequency-(in)dependent dipole-dipole polarizabilities of IIB atoms and selected diatomic molecules, with a particular emphasis on the calculation of valence absorption cross-sections for the I_2 molecule; *(b)* indirect spin-spin coupling constants for benchmark systems such as the hydrogen halides (HX, X = F-I) as well the H_2Se-H_2O dimer as a prototypical system containing hydrogen bonds; and *(c)* optical rotations at the sodium D line for hydrogen peroxide analogues (H_2Y_2 , Y=O, S, Se, Te). Thanks to this implementation, we are able show the similarities in performance—but often the significant discrepancies—between CC-LR and approximate methods such as density functional theory (DFT). Comparing standard CC response theory with the flavor based upon the equation of motion formalism, we find that, for valence properties such as polarizabilities, the two frameworks yield very similar results across the periodic table as found elsewhere in the literature; for properties that probe the core region such as spin-spin couplings, on the other hand, we show a progressive differentiation between the two as relativistic effects become more important. Our results also suggest that as one goes down the periodic table it may become increasingly difficult to measure pure optical rotation at the sodium D line, due to the appearance of absorbing states.

1 Introduction

The fundamental molecular properties, that are connected to the response of a system to external perturbations such as electric or magnetic fields, are central to the study of linear and non-linear optics.¹⁻⁴ It is widely acknowledged that molecules containing heavy elements, that is, those found towards the lower parts of the periodic table, have a plethora of appli-

cations. For instance, by manipulating the molecular polarizability, researchers can design materials with advanced optical properties for use in photovoltaic devices and glasses, such as bismuth oxide-based materials.⁵ Another important example is the utilization of optical activity to design Lanthanide complexes as chiral probes for biological processes.⁶ A detailed understanding of the physical phenomena behind these properties at the atomic or molecular level is very important to tune them or to provide insight for the development of new materials and novel applications.

In quantum mechanics, molecular properties can be derived via perturbation theory, or more specifically, through the response theory formalism, which in general lines identify molecular properties from the derivatives of the energy (or an equivalent quantity) with respect to the external perturbations. The genesis of modern response theory may perhaps be traced back to the introduction by Langhoff et al.⁷ in 1972, of a formalism that allowed both time-dependent and time-independent perturbations to be taken into account analytically, i.e., without employing finite-difference (finite-field) approaches, which are numerically straightforward (but computationally expensive) and only applicable to the time-independent case. Among the properties one can calculate, those related to the linear response^{8,9} of the systems are particularly interesting since they give rise to e.g. the polarizability and optical activity, and can provide us with information on electronically excited states.

The current formulations of response properties may be categorized into those employing either Ehrenfest theorem^{10,11} or quasi-energy approaches.¹²⁻¹⁴ Although response theory based on exact wave functions can provide the expressions for molecular properties directly, practical applications require the use of approximate models such as Hartree-Fock (HF) and density functional theory (DFT), and many other wave function based approaches such as multi-configuration self-consistent field (MCSCF), configuration interaction (CI), coupled cluster (CC) to name just a few (see Helgaker et al.⁹ for a comprehensive survey). To date response theory has achieved great success in dealing with a wide variety of molecular proper-

ties, and treating both small and large-scale systems.^{8,9,15–18} Here, the availability of analytic derivatives approaches has proven to be important for efficient calculations, particularly for large-scale molecule simulations.

However, while most formulations (and implementations) of response theory mentioned above are based on non-relativistic quantum mechanics, it is now widely recognized that when dealing with molecules containing heavy elements, relativistic effects must also be taken into account.^{19–22} In addition, heavy elements also have more electrons than their lighter counterparts, which can bring about subtler effects due to electron correlation that may significantly impact the molecular properties. In the domain of relativistic quantum chemistry, the linear-response function based on approximate models including HF,^{23,24} DFT,^{25,26} and Second-Order-Polarization-Propagator Approximation (SOPPA)²⁷ has been well-established. Due to its modest computational cost, DFT has become the most widely used approach for correlated electronic structure theory, even though it is not possible to systematically improve the quality of calculations with currently available density functional approximations.²⁸ Due to that, depending on the property of interest, DFT results may deviate strongly from experimental or accurate theoretical models for relativistic electronic structure calculations, even for closed-shell species around the ground-state equilibrium structure.^{29,30} An alternative to DFT is found in CC theory, which is considered as a “gold standard”^{31,32} among electronic structure methods due to its ability to yield results that approach chemical accuracy for both correlation energies and properties.

To date, there are various CC linear-response (CC-LR) implementations based on standard models such as CC2,³³ CCSD^{14,15} and CC3.³⁴ These approaches have been shown to achieve good agreement with experimental values for both electric and magnetic molecular properties.^{35–40} We also note the emergence in recent years of response theory implementations based on the equation-of-motion coupled cluster (EOM-CC) model,^{41–46} which are appealing due to their simpler programmable expressions while yielding exactly the same excitation energies as CC-LR, and nearly equivalent numerical results for response proper-

ties. In the time-dependent framework, as pointed out by Coriani et al.⁴¹, the EOM-CC response is equivalent to the combination of an exponential parametrization for the ground-state wavefunction, and a linear parametrization for the time-dependent wavefunction (which these authors refer to as a CC-CI type wave function), as opposed to the CC-LR case, which employs exponential parametrizations for both time-dependent and time-independent wavefunctions (referred to as CC-CC type wavefunctions).

A significant downside of these implementations, however, is that they are available only for non-relativistic or rather approximate relativistic Hamiltonians. As such, they are not generally suitable for treating molecular systems containing heavy elements. In this manuscript, we aim to bridge this gap and present the implementation and pilot applications of CC-LR and EOM-CC models in combination with relativistic Hamiltonians, as part of the ExaCorr⁴⁷ module of the DIRAC program.⁴⁸ One feature of ExaCorr is its ability, through the use of the ExaTENSOR⁴⁹ library, to carry out distributed tensor operations with offloading to graphical processing units (GPUs)—which have been shown to be ideally suited to accelerate coupled cluster calculations due to the latter’s substantial floating-point operation and memory-intensive nature.^{47,50–53} In the work detailed here we take advantage of GPU offloading and thread-level parallelism, and will discuss the currently ongoing work to enable large-scale parallel calculations in a subsequent publication.

Apart from discussing our implementation, we showcase its generality and versatility by examining examples of three distinct classes of molecular properties: those involving purely electrical perturbations, purely magnetic perturbations, and mixed electric and magnetic perturbations.

As an example of the first class, we take the electric dipole polarizabilities because of their significance in a wide range of applications and because they provide valuable insights into the properties and behavior of molecules. For example, materials with high dipole polarizabilities and dielectric constant are used in the polymers that are needed for high-energy-density capacitors,⁵⁴ while materials with low dipole polarizabilities⁵⁵ are used as

insulators in electrical devices. For optical spectroscopies, in the calculation of resonant processes such as electronic excitations it is important, from both a practical and physical points of view, to account for the finite excited-state lifetimes in the calculation of response functions, since these will relate to the broadening in the measured spectra. The damped coupled cluster response theory has in recent years emerged as a very effective tool for incorporating such effects in simulating the spectroscopy of complex molecules.⁵⁶⁻⁶⁰ In this manuscript, we demonstrate our ability to calculate damped response functions, as we can handle perturbing external fields with either real or complex frequencies.

We consider indirect nuclear spin-spin coupling constants as a representative of the second class. Indirect nuclear spin-spin coupling constants manifest themselves in Nuclear Magnetic Resonance (NMR) spectroscopy, which alongside optical spectroscopies is another invaluable tool in chemistry. As a substantial fraction of the atoms in the periodic table is NMR-active, the technique can very often be used to provide critical information about their chemical environment⁶¹⁻⁶³ in a non-destructive way. Regarding computational analysis, apart from the fact that theoretical calculations are extremely useful to interpret experimental signals, it has been demonstrated that it is essential to account for relativistic effects already for elements around the third row of the periodic table.⁶⁴⁻⁶⁸ Magnetic properties are often challenging to calculate, due to the dependence of the results on the gauge origin of an external magnetic field for incomplete bases sets. However, the indirect spin-spin coupling is expressed as the second derivative of the electronic energy with respect to the internal magnetic fields caused by nuclear spins, so that the gauge-origin issue does not arise.

Optical rotation is taken as an example of the third class. Studying optical rotation is of significant interest for several reasons. First and foremost, optical rotation measurements can provide information about the chiral nature of molecules. This is particularly important in the pharmaceutical industry, as many drugs are chiral and their properties can vary depending on their handedness.⁶⁹ In addition to its applications in the pharmaceutical industry, studying optical rotations can also provide insights into the electronic and structural

properties of molecules. Optical rotations are influenced by a variety of factors, including the electronic structure of the molecule, the molecular geometry, and the surrounding environment. Moreover, in materials science, the optical properties of materials can be used to design and develop new materials.⁷⁰ For this property the gauge-origin issue mentioned above also arises.⁹ In subsequent work we will explore approaches to ensure gauge-invariance for coupled-cluster calculations of optical rotation,^{71–73} but we note that for the small, symmetric molecules studied here the use of a common gauge origin yields sufficiently accurate results to allow for a comparison of different electronic structure approaches,^{74–76} which is our goal here.

The manuscript is organized as follows: In Section 2, response theory and its corresponding parametrization for time-dependent coupled cluster wave-function are summarized. In Section 3, we described the details of the implementation. Section 4 is devoted to the details of the computations we used to test the implementation. The calculations are presented and discussed in Section 5. Finally, a brief summary is given in Section 6.

2 Theory

We base the theory on the time-averaged quasienergy formalism, which we briefly summarize below, and refer the reader to the landmark paper by Christiansen et al.¹⁴ for a detailed discussion on it, as well as other more recent works.^{15,41,77}

2.1 Response functions based on time-average quasienergy

We aim to solve the time-dependent wave equation

$$i \frac{\partial}{\partial t} |\Psi(t)\rangle = H |\Psi(t)\rangle \quad (1)$$

where H is the total electronic Hamiltonian

$$H = H_0 + V(t), \quad (2)$$

composed of H_0 , which represents the time-independent electronic Hamiltonian (e.g. the Dirac-Coulomb Hamiltonian, the eXact 2-component Hamiltonian (X2C), the Levy-Leblond Hamiltonian, etc., see^{20,48} and references therein), and $V(t)$ representing a sum of N perturbations that are periodic in time with frequencies ω_k

$$V(t) = \sum_{k=1}^N \left[(e^{i\omega_k t} + e^{-i\omega_k t}) \sum_x \epsilon_x(\omega_k) X \right] \quad (3)$$

expressed in terms of a one-body operator X and the associated frequency-dependent perturbation strength $\epsilon_x(\omega_k)$. In the present study, X corresponds, for instance, to the x -component of the electric dipole operator $\hat{\mu}_x$, or to the y -component of the magnetic dipole operator, \hat{m}_y , etc.

According to the time-averaged time-dependent Hellmann-Feynman theorem,^{7,14} by defining a time-averaged quasienergy $\{Q\}_T$ (over the period T)

$$\{Q\}_T = \frac{1}{T} \int_{-T/2}^{T/2} \langle 0(t) | (\hat{H} - i \frac{\partial}{\partial t}) | 0(t) \rangle dt, \quad (4)$$

and making it stationary to changes in $|0(t)\rangle$, we arrive at a definition of time-dependent response properties as derivatives of $\{Q\}_T$

$$\{Q\}_T = E_0 + \sum_x \langle X \rangle \epsilon_x(0) + \frac{1}{2} \sum_{x,y,k} \langle \langle X; Y \rangle \rangle_{\omega_k} \epsilon_y(\omega_k) \delta(\omega_0 + \omega_k) \quad (5)$$

where

$$\langle X \rangle = \frac{d\{Q\}_T}{d\epsilon_x(0)} \quad (6)$$

corresponds to an expectation value and

$$\langle\langle X; Y \rangle\rangle_{\omega_k} = \frac{d^2\{Q\}_T}{d\epsilon_x(\omega_0)d\epsilon_y(\omega_k)}, \quad \omega_0 = -\omega_k \quad (7)$$

to linear response properties.

2.2 Parametrization of the time-dependent wave-function

In the following, we shall be concerned with wavefunctions based on an exponential parametrization of the ground state wavefunction such as the coupled cluster expansion,

$$|0\rangle = e^{T_0} |R\rangle = |\text{CC}\rangle \quad (8)$$

in which $|R\rangle$ denotes the reference state, typically the Hartree-Fock wavefunction, and T_0 is the time-independent cluster operator, here restricted to single (ν_1) and double (ν_2) excitations

$$T_0 = T_1 + T_2 = \sum_{\nu_1} t_{\nu_1} \hat{\tau}_{\nu_1} + \sum_{\nu_2} t_{\nu_2} \hat{\tau}_{\nu_2} = \sum_{ai} t_i^a \{a_a^\dagger a_i\} + \frac{1}{4} \sum_{abij} t_{ij}^{ab} \{a_a^\dagger a_b^\dagger a_j a_i\} \quad (9)$$

with a, b indicating particle lines and i, j hole lines, respectively,³¹ and ν_1, ν_2 representing excited configurations with respect to the reference ($\nu_1 \leftrightarrow |\nu_i^a\rangle = \{a_a^\dagger a_i\} |R\rangle, \nu_2 \leftrightarrow |\nu_{ij}^{ab}\rangle = \{a_a^\dagger a_b^\dagger a_j a_i\} |R\rangle$); in the following, we shall sometimes omit explicit excitation ranks and particle/hole labels and instead employ the shorthand notation μ, ν to denote excited determinants.

As suggested by Pawłowski et al.¹⁵, the time-dependent wave-function $|0(t)\rangle$ can be parametrized in a general manner as :

$$|0(t, \epsilon_x)\rangle = e^{B_0} e^{B(t, \epsilon_x)} |R\rangle, \quad (10)$$

where e^{B_0} and $e^{B(t, \epsilon_x)}$ define the parametrization of the time-independent and time-dependent wavefunctions associated with perturbation X with perturbation strength ϵ_x , respectively. In the case of coupled cluster wavefunctions, $B_0 = T_0$, and the choice to be made is that of the parametrization of the time-dependent part. If the exponential parametrization is retained, we have the CC-CC model (more commonly known as LR-CC), whereas for a linearized version we have the CC-CI model (also referred to as EOM-CC)

$$e^{B(t, X)} \simeq 1 + B(t, \epsilon_x) = 1 + \sum_{ai} t_i^a(t, \epsilon_x) \{a_a^\dagger a_i\} + \frac{1}{4} \sum_{abij} t_{ij}^{ab}(t, \epsilon_x) \{a_a^\dagger a_b^\dagger a_j a_i\}. \quad (11)$$

2.3 The coupled cluster linear response function

As in the time-independent case, the non-variational nature of the coupled cluster method requires that we define a second-order quasienergy Lagrangian

$$\{L\}_T = \{Q\}_T + \sum_{\mu} \bar{t}_{\mu}^{(0)} \{ \langle \bar{\mu} | e^{-B^{(1)}(t, \epsilon_x)} (H - i \frac{\partial}{\partial t}) e^{B^{(1)}(t, \epsilon_x)} | \text{CC} \rangle \}_T \quad (12)$$

in order to obtain the linear response functions. Here, $\langle \bar{\mu} | \equiv \langle \mu | e^{-T_0}$ and $\bar{t}_{\mu}^{(0)}$ are the Lagrange multipliers for the ground-state, obtained solving the linear system

$$\bar{\mathbf{t}}^{(0)} \mathbf{A} = -\boldsymbol{\eta}, \quad (13)$$

in which the matrix \mathbf{A} is the Jacobian matrix. We note that \mathbf{A} is strictly equivalent to the normal-ordered similarly transformed Hamiltonian \bar{H}_N

$$A_{\mu\nu} \equiv (\bar{H}_N)_{\mu\nu} = \left[\exp(-\hat{T}_0) \hat{H}_0 \exp(\hat{T}_0) - \langle \text{HF} | \hat{H}_0 | \text{HF} \rangle \right]. \quad (14)$$

In the following, we shall use the two terms interchangeably, and for brevity drop the subscript N in \bar{H}_N .

The linear response functions are expressed as

$${}^{\text{CC-CC}}\langle\langle X; Y \rangle\rangle_{\omega_k} = \frac{1}{2} C^{\pm\omega} P(X(\omega_0), Y(\omega_k)) \left[\boldsymbol{\eta}^X + \frac{1}{2} \mathbf{F} \mathbf{t}^X(\omega_0) \right] \mathbf{t}^Y(\omega_k) \quad (15)$$

for CC-CC^{14,15,41} and

$${}^{\text{CC-CI}}\langle\langle X; Y \rangle\rangle_{\omega_k} = \frac{1}{2} C^{\pm\omega} P(X(\omega_0), Y(\omega_k)) \left[{}^{EOM} \boldsymbol{\eta}^X \mathbf{t}^Y(\omega_k) - \sum_{\mu} \bar{t}_{\mu}^{(0)} t_{\mu}^X(\omega_0) \sum_{\nu} \bar{t}_{\nu}^{(0)} \xi_{\nu}^Y \right] \quad (16)$$

for CC-CI.^{15,41,46} In the equations above, $P(X(\omega_0), Y(\omega_k))$ acts to permute perturbations X and Y , and

$$C^{\pm\omega} f^{XY}(\omega_0, \omega_k) = f^{XY}(\omega_0, \omega_k) + f^{XY}(-\omega_0, -\omega_k)^* \quad (17)$$

symmetrizes the response functions with respect to simultaneous complex conjugation and inversion of the sign of the frequencies.¹⁴

We have also implemented an alternative expression for the response function, that can be rewritten in an asymmetric form:¹⁴

$${}^{\text{CC-CC}}\langle\langle X; Y \rangle\rangle_{\omega_k} = \frac{1}{2} [\boldsymbol{\eta}^X \mathbf{t}^Y(\omega_k) + \bar{\mathbf{t}}^Y(\omega_k) \boldsymbol{\xi}^X] \quad (18)$$

where $\bar{\mathbf{t}}^Y$ collect the derivatives of Lagrange multipliers with respect to one perturbation. The asymmetric form gives the same results as the symmetric form and has advantages in some cases such as NMR calculations⁷⁸ as one needs to solve response equations for one operator (e.g. Y), but at the cost of having to solve response equations for both perturbed amplitudes and multipliers. In the properties investigated in this manuscript, the asymmetric form does not offer a clear advantage, and as such we focus on the symmetric form in the following.

To evaluate the linear response function, we need to obtain the frequency (in-)dependent first-order perturbed amplitudes \mathbf{t}^Y by solving the corresponding first-order right-hand side

response equations:¹⁴

$$(\bar{\mathbf{H}} - \omega_k \mathbf{I}) \mathbf{t}^Y = -\boldsymbol{\xi}^Y. \quad (19)$$

with \mathbf{I} as the identity matrix.

Because of the equivalence between \mathbf{A} and $\bar{\mathbf{H}}$, Eq. (19) is the same for the CC-CC and CC-CI models, and the poles of the response functions will occur at the same places in the two formulations. This is in line with the fact that excitation energies for CC-LR and EOM-CC are the eigenvalues of \mathbf{A} or $\bar{\mathbf{H}}$ respectively.

Here, we use the same definitions for matrices $\boldsymbol{\eta}^Y$, $\boldsymbol{\xi}^Y$ and \mathbf{F} (the coupled cluster Hessian) as done by Christiansen et al.¹⁴, which are listed in Table 1, and note that in the case of CC-CI, $\boldsymbol{\eta}^Y$ is replaced by $^{\text{EOM}}\boldsymbol{\eta}^Y$ as defined by Faber and Coriani⁴⁶. The detailed working equations used in our implementation are listed in the supplementary material.

Table 1: Vectors and matrices for CC linear response function^a

$\boldsymbol{\eta}^Y$	$\langle \Lambda [Y, \hat{\tau}_\mu] CC \rangle$
$\boldsymbol{\xi}^Y$	$\langle \bar{\mu} Y CC \rangle$
\mathbf{F}	$\langle \Lambda [[H_0, \hat{\tau}_\mu], \hat{\tau}_\nu] CC \rangle$
\mathbf{A}	$\langle \bar{\mu} [H_0, \hat{\tau}_\mu] CC \rangle$

^a $|CC\rangle = e^{T_0} |R\rangle$ denote the regular CC reference wavefunction, and $|R\rangle$ is the reference state for the CC parametrization such as Hartree-Fock state. $\langle \Lambda | = \langle R | + \sum_\mu \bar{r}_\mu^0 \langle \bar{\mu} |$. $\langle \bar{\mu} | = \langle R | \hat{\tau}_\mu^\dagger e^{-T_0} \equiv \langle \mu | e^{-T_0}$, where $\hat{\tau}_\mu^\dagger$ is the deexcitation operator, which is biorthogonal to excitation operator $\hat{\tau}_\mu$, satisfying $\langle R | \hat{\tau}_\mu^\dagger \hat{\tau}_\nu | R \rangle = \delta_{\mu\nu}$.

Finally, due to the fact that ExaCorr was originally designed for treating systems without symmetry and that in such a case the relativistic wave functions are complex-valued, complex algebra is used throughout. This makes the implementation of damped coupled cluster response theory relatively straightforward; it suffices, in the computation of the response function of interest (for instance the yy component of the electric dipole polarizability, $\alpha_{yy}(\omega_0; \omega_k)$), to set the imaginary component of the perturbing frequency ω_k to a particular

inverse lifetime γ

$$\omega_k \equiv \omega_k + i0 \rightarrow \omega_k + i\gamma \quad (20)$$

when solving the response equation:⁵⁶⁻⁵⁸

$$(\bar{\mathbf{H}} - (\omega_k + i\gamma)\mathbf{I})\mathbf{t}^Y(\omega_k + i\gamma) = -\boldsymbol{\xi}^Y, \quad (21)$$

subject to the condition that $(\omega_k + i\gamma) + (-\omega_0 - i\gamma) = 0$. We note that, while we can in principle use a different value of γ for each ω_k , in practice we will follow common usage and keep this value constant for a range of frequencies for which we shall calculate a particular response function. With that, the absorption cross-section for dipole transitions can be determined by the imaginary part of the complex electric dipole polarizability⁷⁹ :

$$\sigma(\omega) = \frac{4\pi\omega}{c} \text{Im}[\bar{\alpha}(\omega)] \quad (22)$$

3 Implementation

The above-mentioned algorithm has been implemented in the development version of the relativistic quantum chemistry package DIRAC⁴⁸ as a part of the ExaCorr code.⁴⁷ Currently, the implementation allows for calculations to be carried out only using a single-node configuration. The implementation of multi-node is currently in progress and will be reported in forthcoming works. We can summarize the main computational tasks in the following four steps :

1. Solve closed-shell ground state CCSD equations to obtain the $\mathbf{t}_1, \mathbf{t}_2$ amplitudes.
2. With $\mathbf{t}_1, \mathbf{t}_2$, construct the one and two-body intermediates, that are necessary for building the $\bar{\mathbf{H}}$ and linear response functions.
3. Solve the linear response equation in the full single-double excitation space to obtain

the first-order perturbed amplitudes for each operator-frequency combination. To avoid the explicit construction of large matrix $\bar{\mathbf{H}}$, an iterative solver is employed.

4. Construct the response function by combining the first-order perturbed amplitudes and the property integrals in the molecular orbital (MO) basis.

The first step is carried out within a Kramers-unrestricted formalism⁸⁰ and has been extensively discussed in prior work.⁴⁷

The intermediates in the second step consist of two sets: The first set is property-independent and is utilized to construct the σ -vectors, which are the projection of $\bar{\mathbf{H}}$ in the trial vector space. These intermediates were previously discussed in the literature^{81,82} and an implementation of relativistic EOM-CC is available in the RelCCSD module⁸³ as well. We have included a rewritten version of the σ -vectors for EOM-CC for excitation energies (EOM-EE) in the supplementary material (for completeness, expressions for the left EOM-EE σ -vectors are also given), due to our use of full tensors in this implementation. We have also corrected misprints identified in the expressions given by Shee et al.⁸³ (the previously implemented expressions were verified and found to be correct).

In deriving the working equations, we note that for the matrix \mathbf{F} it is not possible to obtain its matrix elements diagrammatically,⁸⁴ due to the number of unconnected hole/particle-lines. However, \mathbf{F} is never used by itself but rather as the vector-matrix product $\mathbf{t}^X \mathbf{F}$, in analogy to the σ -vector expressions for the eigenvalue and response equations. Apart from being readily expressed diagrammatically, dealing with the vector-matrix product is computationally advantageous as it reduces storage requirements.

Moreover, as Faber and Coriani⁴⁶ suggested, we can avoid computing the \mathbf{F} matrix in CC-CI implementation by computing the ${}^{\text{EOM}}\boldsymbol{\eta}^X$, which is easily accomplished by modifying the existing $\boldsymbol{\eta}^X$ routine (see working equation in the supplementary material).

In the current implementation, the set of all property-related intermediates is computed on the MO basis, but as the property integrals are first generated in the atomic orbital (AO) basis in DIRAC, it is necessary to transform all desired property integrals from AO to

MO prior to the response calculations. All the intermediates and the property integrals in MO basis are therefore stored as tensor objects according to the definition of the TAL-SH library,⁸⁵ so that they can be efficiently employed in constructing the elements of $\boldsymbol{\xi}^X$, $\boldsymbol{\eta}^X$ and ${}^{\text{EOM}}\boldsymbol{\eta}^X$.

In the supplemental information, we will focus on discussing the third step, which involves solving the first-order response equation. There are different algorithms to solve linear equations such as direct inversion of the iterative subspace (DIIS),^{86–88} as well as the Lanczos-chain^{89,90} and Davidson⁹¹ schemes. In the current work, we utilized the latter, which required minor modifications with respect to evaluating the eigenvalues and eigenvectors of $\bar{\mathbf{H}}$ in our EOM-CC implementation. We also note that the default algorithm in ExaCorr to solve for the unperturbed amplitudes \mathbf{t} was recently changed to Conjugate Residual with OPTimal trial vectors (CROP)^{92,93} as this reduces the memory requirements in this stage of the calculation.

One particular difference between our implementation and the one by Shee et al.⁸³ is that the ExaTENSOR and TAL-SH libraries, for reasons of scalability and generality, do not enforce triangularity or the (anti)symmetry of tensors with respect to exchange of pairs of indices. Consequently, and in contrast to the prior implementation, beyond rank-2 tensors antisymmetry needs to be enforced in order to ensure that at all times we satisfy the underlying fermionic nature of the problem.

For example, in the generation of trial vectors for the \mathbf{t}_2^x amplitudes (or \mathbf{r}_2 in EOM-CC), this means that we pick out a unique element $|_{ij}^{ab}\rangle$, where $a > b$ and $i > j$, generate the permutations and antisymmetrize them. During Davidson iterations we also ensure that the trial vectors remain antisymmetric during the Gram-Schmidt orthonormalization process, as we found that if explicit antisymmetrization is not carried out, numerical noise may lead to loss of the antisymmetry in new vectors during iterations.

With respect to the choice of starting vectors, differently from the eigenvalue case in which the pivoting was done on the basis of the value of the diagonal of $\bar{\mathbf{H}}$ (see Shee et al.⁸³ for details), for linear systems, the pivoting is done on the basis of the magnitude of the

property gradient ξ^X vector elements (from highest to lowest), in order to avoid selecting initial vectors with zero norm.

4 Computational details

All coupled cluster linear-response calculations were carried out with a development version of the DIRAC code,^{48,94} employing the uncontracted singly-augmented valence double zeta Dyall basis set s-aug-dyall.v2z for the heavy elements (Zn,⁹⁵ Cd,⁹⁵ Hg,⁹⁵ Cs,⁹⁵ I,^{96,97} Tl^{96,97}), and a similar uncontracted Dunning basis set aug-cc-pVDZ for the light elements (H,⁹⁸ Li,⁹⁹ Na,⁹⁹ K,¹⁰⁰ F,⁹⁸ Cl,¹⁰¹ O,⁹⁸ S,¹⁰¹ Se,¹⁰² Br¹⁰²). In most calculations, we utilized the exact two-component (X2C)¹⁰³ relativistic Hamiltonian, where the spin-orbit operator takes the form of an effective one-electron operator. The screening of the nuclear charges is in the version that we used approximated by an atomic mean field.¹⁰⁴ To show the effect of relativity explicitly we also provide results using the non-relativistic Hamiltonian.^{105,106} We furthermore show some results with the spin-free X2C Hamiltonian in which spin-orbit coupling terms are identified by transforming to the modified Dirac representation¹⁰⁷ and eliminated prior to defining the X2C transformation and Hamiltonian. To study the effect of electron correlation, we performed linear-response calculations based on mean-field methods like Hartree-Fock (HF)¹⁰⁸ as well as density-functional theory¹⁰⁹ (especially with the B3LYP¹¹⁰ density functional approximation). The relativistic and non-relativistic calculations have been carried out with the Gaussian type¹¹¹ and point charge nucleus model, respectively.

In our calculations, we have profited from the components of an ongoing implementation in ExaCorr of the Cholesky-decomposition¹¹²⁻¹¹⁴ approach to reduce the memory footprint of our calculations in the step to transform two-electron integrals from AO to MO basis, by avoiding the storage in memory of the whole AO basis two-electron integral tensor. The Cholesky vectors (generated with a conservative threshold of 10^{-9} , as to retain most of them)

are then used to explicitly form all six two-electron integral classes needed by the coupled cluster method. In a subsequent publication¹¹⁵ we shall address the use of Cholesky vectors directly in the coupled cluster implementation of ground and excited state properties.

The molecular structures employed in all calculations are taken from the literature: In case of the diatomic molecules, from Huber¹¹⁶ for HX(X=F, Cl, Br, I), I₂, ICl, from Hessel¹¹⁷ for NaLi, and from Ferber et al.¹¹⁸ for CsK. The internuclear distances employed are thus H-F(0.91680 Å), H-Cl(1.27455 Å), H-Br(1.41443 Å), H-I(1.60916 Å), Cl-I(2.32087 Å), I-I(2.6663 Å), Li-Na(2.81 Å), and K-Cs(4.285 Å). For the chiral molecules H₂Y₂(Y=O, S, Se, Te), the Y-Y bond length, H-Y bond length, and H-Y-Y bond angle are taken from Table I of Laerdahl and Schwerdtfeger¹¹⁹ and the dihedral angle is kept fixed at 45 degrees.

The size of the correlated virtual spinor spaces in the coupled cluster calculations is truncated by discarding spinors with energies above 5 a.u. For the IIB atoms, we correlate both semi-core and valence electrons for Zn(3d,4s), Cd(4d,5s), Hg(5d,6s), respectively. In the polarizability and optical rotation calculations of molecular systems, we correlate only valence electrons. In the spin-spin coupling calculations, which are known to be more sensitive to core relaxation and correlation, we correlate all occupied and virtual orbitals.

All optical rotation calculations (HF, DFT, CC) employed a common gauge origin, set to the origin of the coordinate system, chosen at the midpoint of the bond between the two chalcogen atoms, which nearly coincides with the systems' center of mass. The atomic coordinates for each system under consideration as well as further details on the calculations (position of center of mass etc.) are provided respectively as XYZ and output files in the dataset associated with this manuscript (see "Supporting Information Available").

5 Sample applications

5.1 Polarizability of IIB atoms

We begin the discussion by analyzing the obtained results for the polarizability of the Zn, Cd, and Hg atoms and present in Table 2 the static polarizability of these atoms, calculated by different methods. A comparison of the first three rows of this Table shows the growing influence of relativity on the static polarizability from Zn to Hg. For example, the relativistic HF value for Hg (44.82 a.u.) is nearly half of its nonrelativistic counterpart (81.05 a.u.). This is mainly due to the strong relativistic contraction of the 6s-shell.

In contrast, the effect of electron correlation at CCSD level is rather constant for these elements (-10.15 a.u. for Zn, -15.39 a.u, and -9.57 a.u, for Hg).

For Zn, electron correlation primarily accounts for the discrepancy between HF and the experimental results. However, for Cd and especially Hg, the inclusion of relativity is crucial. The above-mentioned contraction of the valence s-shell reduces the magnitude of the polarizability, whereas spin-orbit coupling (SOC) becomes increasingly important by enabling spin-forbidden transitions. We will discuss this consequence of relativity in greater depth when looking at the frequency-dependence of the polarizability in the next section.

An error of approximately 1-2 a.u. remains between our relativistic CCSD results and the experimental values. To locate the source of this error, we performed CCSD(T) calculations using the finite-field method, since the analytic gradient is not yet available for CCSD(T) in DIRAC. In these CCSD(T) finite-field calculations, we used an external electric strength of 0.005 a.u, which is sufficiently large to avoid numerical issues and small enough to remain in the linear regime.

From a comparison between the results of CCSD and CCSD(T), it is evident that the inclusion of the triple excitations indeed enhances the accuracy: from 95.99% to 99.84% for Zn, from 98.44% to 99.71% for Cd, and from 96.20% to 97.95% for Hg, respectively. In the results of CCSD(T), we also performed a calculation in which all virtual orbitals were used

(so without energy truncation), but this did not significantly affect the results. Upon using the valence triple-zeta basis set s-aug-dyall.v3z, the Hg results improve and come close to the experimental error bar.

Table 2: Static polarizability (a.u.) of IIB atoms calculated with the X2C Hamiltonian

	Zn	Cd	Hg
NR-HF ^a	53.88	76.01	81.05
SF-HF ^b	50.58	63.65	44.90
HF	50.57	63.64	44.82
SF-CCSD ^b	40.42	48.28	35.35
CCSD	40.42	48.25	35.25
CCSD(T)	38.86	47.64	34.62
CCSD(T) (all virtual dz)	38.80	47.69	34.66
CCSD(T) (tz)	38.86	46.64	34.27
Exp	38.8±0.80 ¹²⁰	47.5±2 ¹²¹	33.91±0.34 ¹²²

^a Nonrelativistic calculation with the Levy-Leblond Hamiltonian

^b Scalar relativistic calculation with the spin-free¹⁰⁷ X2C Hamiltonian

We now turn to the frequency-dependence of the polarizability and look at the effect of SOC. In Figure 1, the frequency-range from 0.0 to 0.30 a.u. is displayed. The singularities at the frequencies of spin-allowed transition $^1S_0 \rightarrow ^1P_1(ns \rightarrow np)$ dominate these curves, while the non-relativistically spin-forbidden transition to the 3P state is clearly visible for Hg and, after zooming in on the transition energy, also already for Zn. Calculating and plotting the polarizability⁶⁰

$$\alpha_{\alpha\beta}(\omega) = - \sum_n \left[\frac{\langle 0 | \hat{\mu}_\alpha | n \rangle \langle n | \hat{\mu}_\beta | 0 \rangle}{E_n - \omega} + \frac{\langle 0 | \hat{\mu}_\beta | n \rangle \langle n | \hat{\mu}_\alpha | 0 \rangle}{E_n + \omega} \right] \quad (23)$$

over a range of frequencies $\{\omega\}$ implicitly shows all excitation energies E_n in the associated energy range. However, when interested in the values of these energies it is of course more efficient to directly solve for the poles by diagonalizing $\bar{\mathbf{H}}$. To check the correctness of the implemented solvers, we therefore compared the linear response and EOM-EE results employing the same Hamiltonian and basis set. The resulting excitation energies are depicted in Fig 1 with red lines and do indeed precisely align with the pole locations in the polarizability

curves.

Looking at the low-lying parity-allowed ($ns \rightarrow mp$) transitions in the studied frequency-range, for Zn and Cd we find two $ns \rightarrow (n)p$ transitions (A and B, respectively spin-forbidden $^1S_0 \rightarrow ^3P_1^o$ and spin-allowed $^1S_0 \rightarrow ^1P_1^o$ transitions) and two $ns \rightarrow (n+1)p$ transitions (C and D, similarly spin-forbidden and spin-allowed transitions). For Hg on the other hand, only A and B are within the studied frequency-range, with C and D coming at higher energies and therefore not observed.

On the right side of Fig 1, we also show a simulated spectrum of the first spin-allowed transition $^1S_0 \rightarrow ^1P_1^o$ by calculating the damped linear response function for both CC-CC and CC-CI models. While CC-CI is an approximation of the CC-CC model, we note that the CC-CI curve exhibits a shape very similar to that of CC-CC curves, in that both are Lorentzian-type line shapes and share the exact same peak location since they solve the same response equation as demonstrated in the Eq. (19). The CC-CI model spectrum shows only a minor difference in the peak height with a relative error of about 1%. To verify the implementation of the complex polarizability, we pay particular attention to the peak value of the spectrum of B atomic transition. Around the pole of the transitions we are investigating, the stationary point in the curves should be well approximated by the norm of the transition dipole moment divided by γ ,

$$\begin{aligned} \text{Im}(\alpha_{\alpha\beta}(\omega)) &= \text{Im} \left(- \sum_n \left[\frac{\langle 0 | \hat{\mu}_\alpha | n \rangle \langle n | \hat{\mu}_\beta | 0 \rangle}{E_n - \omega - i\gamma} + \frac{\langle 0 | \hat{\mu}_\beta | n \rangle \langle n | \hat{\mu}_\alpha | 0 \rangle}{E_n + \omega + i\gamma} \right] \right) \\ &\approx \text{Im} \left(\frac{\langle 0 | \hat{\mu}_\alpha | n \rangle \langle n | \hat{\mu}_\beta | 0 \rangle}{i\gamma} \right) \end{aligned} \quad (24)$$

In the current work, we set the imaginary component of the frequency γ as 0.01 a.u. for all three atoms. Even though the EOMCC transition dipole moment is not yet available in DIRAC, we can still compare the intensity ratios (Zn:Cd:Hg) between our results (1.39:1.55:1.0) and the values derived from the experimental lifetimes^{123–125} (1.48:1.54:1.0). It is noteworthy that our results qualitatively mirror the experimental trend. The small dif-

ference in ratios likely stems from the omission of higher-order correlation and the quality of the basis set used. In supplementary information, we simulate the spectrum of BH molecules with damped CC-CC and find our results exactly reproduce the DALTON results.

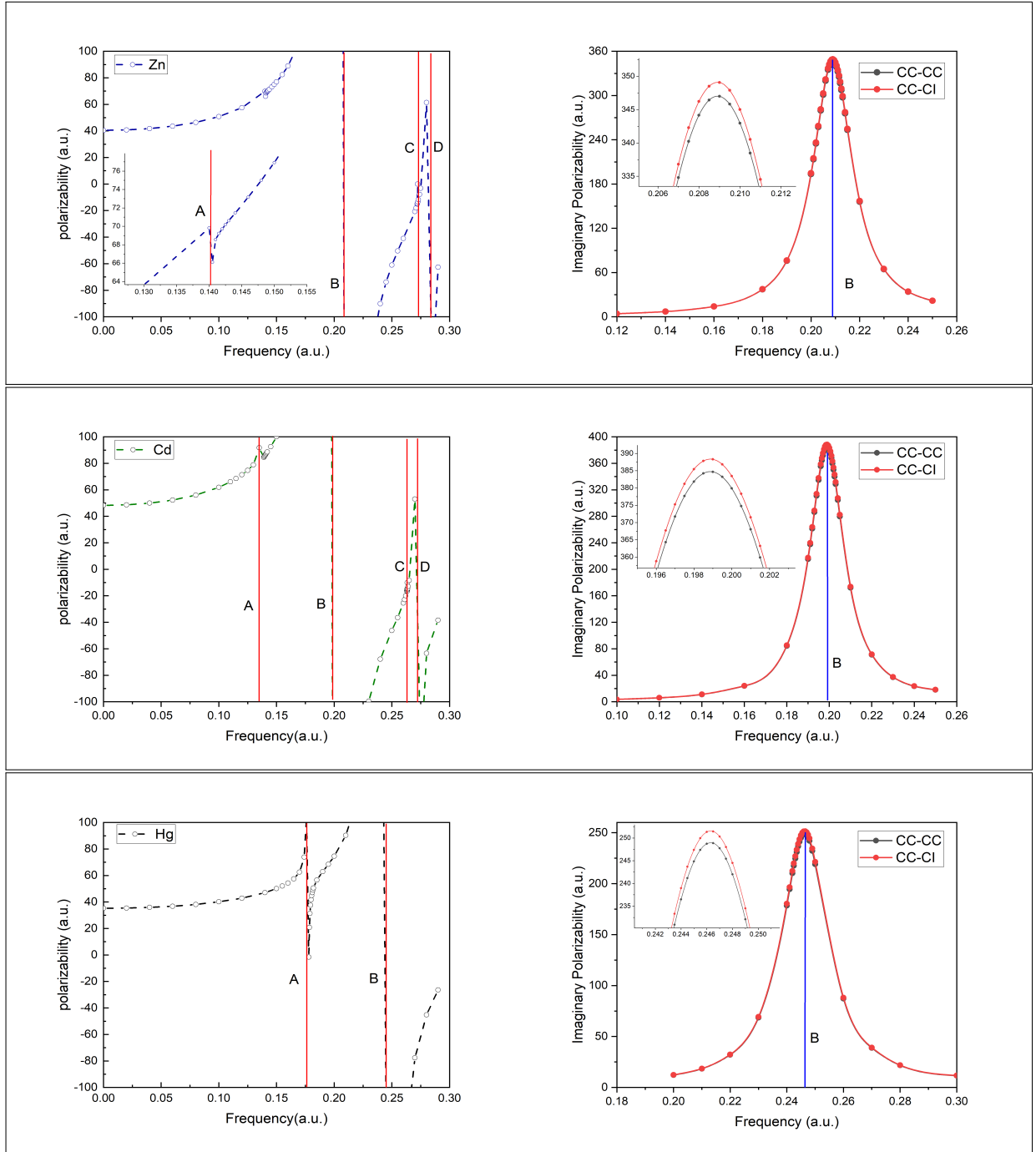


Figure 1: Frequency dependent polarizability of Zn(top), Cd(middle), and Hg (bottom). The left figures show the real (undamped) polarizability with frequency ranging from 0.0 to 0.30 a.u. The right figures, with insets to zoom in on the peak maxima, show the simulated spectra focusing on the **B** transition, and are obtained from the imaginary part of the complex (damped) polarizability with an imaginary component of the frequency $\gamma = 0.01$ a.u. The red vertical lines are the EOM excitation energy: For **Zn**: A(${}^3P_1^o(4s^14p^1)$)0.1403 a.u.); B(${}^1P_1^o(4s^14p^1)$)0.2089 a.u.); C(${}^3P_1^o(4s^15p^1)$)0.2723 a.u.); D(${}^1P_1^o(4s^15p^1)$)0.2828 a.u.). For **Cd**: A(${}^3P_1^o(5s^15p^1)$)0.1356 a.u.); B(${}^1P_1^o(5s^15p^1)$)0.1989 a.u.); C(${}^3P_1^o(5s^16p^1)$)0.2634 a.u.); D(${}^1P_1^o(5s^16p^1)$)0.2728 a.u.). For **Hg**: A(${}^3P_1^o(6s^16p^1)$)0.1771 a.u.); B(${}^1P_1^o(6s^16p^1)$)0.2463 a.u.).

5.2 Polarizability of Molecules

As our implementation is mainly intended for molecular systems, we will now look at results for molecular polarizabilities which may have up to three distinct values upon diagonalizing the polarizability tensor. For diatomic and other symmetric molecules it is sufficient to consider the mean dipole polarizability $\alpha(\omega)$ and the anisotropy $\Delta\alpha(\omega)$:

$$\alpha(\omega) = \frac{1}{3} (\alpha_{zz}(\omega) + \alpha_{xx}(\omega) + \alpha_{yy}(\omega)) \quad (25)$$

$$\Delta\alpha(\omega) = \alpha_{zz}(\omega) - \frac{1}{2} (\alpha_{xx}(\omega) + \alpha_{yy}(\omega)), \quad (26)$$

where z is the molecular symmetry axis. In Table 3, we list the static mean and anisotropic polarizability of hydrogen halides and alkali-metal diatomic molecules assessed by HF, B3LYP, and CC models with both relativistic (X2C) and nonrelativistic Hamiltonians, and the corresponding experimental values as well. Unless otherwise specified, 'CC' refers to 'CC-CC-LR'.

The HF results deviate from the experimental value for both the mean and anisotropic polarizability and the impact of the relativistic effect increases as we move from lighter to heavier molecules. For example, the relativistic correction is nearly zero for hydrogen fluoride but amounts to 1.3 a.u. for I_2 . In the case of the CsK molecule, the relativistic correction at the HF level is 31 a.u., emphasizing the necessity of considering the relativistic effect in the calculation of heavy elements. For this molecule, the effect of relativity may again be rationalized in terms of contraction of the outermost valence s -orbitals, in particular that of Cs, which reduces the polarizability, similar to what we observed in the Hg atom.

Apart from relativity, another source of discrepancy between HF and experiment lies in the importance of electron correlation. Electron correlation is modeled in DFT by the B3LYP functional, and explicitly calculated in the CC models. From the results, it is evident that in both cases the electron correlation and the relativistic correction are not strictly additive. For example, computed with CC the relativistic corrections for I_2 and CsK are 0.91 a.u. and -26 a.u., respectively, while they are 1.30 a.u. and -31 a.u. when computed with HF.

The B3LYP calculations yield much better values than HF for both the relativistic and nonrelativistic Hamiltonian. The relativistic correction on the B3LYP model is similar in magnitude as found for HF, but with a different sign. For instance, the relativistic correction of anisotropic polarizability for CsK for HF is +9 a.u. while it is -11 a.u. in B3LYP. For the halides, the B3LYP calculations yield values that are close to the CC results and are within or only slightly outside the experimental error bars for both isotropic and anisotropic polarizability. However, for the alkali-metal diatomic molecules NaLi and CsK, the B3LYP values significantly deviate from the experimental value.

The CC results are close to the experimental data for both halide and alkali-metal molecules. We have also tried using the triple-zeta basis set for CC on three light hydrogen halide molecules (HF, HCl, HBr) to reduce the error and indeed observe an improvement of CC values which then fall within the experiment error bar for the isotropic polarizability. Getting the smaller anisotropic polarizability agree with experimental data is more demanding on the model and may require addition of more diffuse functions and/or the inclusion of the triple excitations.

One may note for the anisotropic polarizability of HI the considerable deviation of all three theoretical values (around 2 a.u.) from the experimental value of 11.4 a.u. that was determined in 1940 by Denbigh.¹²⁶ Curiously, this value appears to have not been re-evaluated since then, while the isotropic polarizabilities of HCl and HBr, that were also reported by Denbigh, were later estimated to be significantly lower by Kumar and Meath.¹²⁷ The anisotropy of HBr that was given as 6.14 a.u. by Denbigh was adjusted to just 1.7 a.u. by Pinkham and Jones,¹²⁸ but we could not find a similar re-evaluation of the anisotropic polarizability of HI on basis of experimental data in the literature. This discrepancy between theory and the old experimental value for the anisotropy was also noted in theoretical work of Maroulis¹²⁹ and Iliáš et al.¹³⁰ Iliáš et al. used relativistic CCSD(T) and included vibrational corrections on both dipole moment and static polarizability and found their results to be significantly lower than the experimental value: their anisotropic polarizability

was 2.33 ± 0.05 a.u., which agrees well with the current relativistic CC linear response value of 2.51 a.u. While their suggestion that also the experimental value of the dipole moment could be inaccurate could not be not sustained^{131,132} we agree that the discrepancy between theory and experiment for the anisotropic polarizability is likely due to an inaccuracy in the experimental value. Nonetheless, it would be nice to put more firm error bars on the theoretical value as well by employing a larger basis set, including g and h functions. This was not feasible with our current implementation due to memory constraints related to the use of a single compute node.

Table 3: Static dipole polarizability (a.u.) of diatomic molecules

	HF ^a	HF ^b	B3LYP ^a	B3LYP ^b	B3LYP ^c	CC ^a	CC ^b	CC ^c	Exp
Mean dipole polarizability									
HF	4.40	4.40	5.11	5.12	5.57	5.04	5.05	5.52	5.60 ± 0.10 ¹²⁷
HCl	15.51	15.54	16.34	16.38	17.53	16.06	16.09	17.14	17.39 ± 0.20 ¹²⁷
HBr	21.86	21.90	22.85	22.94	24.43	22.52	22.58	24.02	23.74 ± 0.50 ¹²⁷
HI	33.62	33.50	34.63	34.69	36.71	34.36	34.30		35.30 ± 0.50 ¹³³
ICl	46.48	46.52	47.53	47.66	49.80	47.48	47.59		43.8 ± 4.4 ¹³⁴
I ₂	67.90	69.20	68.72	69.92	72.55	68.81	69.72		69.7 ± 1.8 ¹³⁵
NaLi	231	230	210	209	210	240	240	239	263 ± 20 ¹³⁶
CsK	723	692	581	548	549	637 ^d	611 ^d		601 ± 44 ¹³⁷
Anisotropic dipole polarizability									
HF	1.79	1.79	1.91	1.91	1.46	1.96	1.96	1.45	1.62 ¹³⁸
HCl	2.35	2.34	2.18	2.16	1.66	2.39	2.38	1.85	2.10 ¹³⁹
HBr	2.43	2.45	1.98	1.92	1.65	2.35	2.30	2.02	1.7 ¹²⁸
HI	2.66	2.81	2.09	2.00	1.87	2.60	2.51		11.4 ¹²⁶
ICl	26.14	26.96	24.27	24.63	24.50	25.30	25.82		
I ₂	44.92	49.01	41.31	43.75	42.88	44.00	45.87		45.1 ± 2.3 ¹³⁵
NaLi	92	92	109	109	108	154	154	149	
CsK	353	362	400	389	390	510 ^d	499 ^d		

^a Nonrelativistic calculation using the Levy-Leblond Hamiltonian

^b Relativistic calculation using the X2C Hamiltonian

^c Using diffuse Triple-zeta basis set

^d Correlate both 6s and 5p electrons of Cs

We now turn our attention to the frequency-dependent polarizability and focus on the I₂ molecule given the extensive experimental research on this molecule and the abundance of experimental spectral data that can be used to validate theoretical models. Relevant in

the frequency region that we consider are the lowest electronically excited states, that arise from the $\sigma_g^2\pi_u^4\pi_g^3\sigma_u^1$ and $\sigma_g^1\pi_u^4\pi_g^4\sigma_u^1$ configurations. These are primarily triplet states that are denoted in the literature¹⁴⁰ as $A^3\Pi_u$, $B^3\Pi_u$ and $C^3\Sigma_u$, with the latter originating from the second configuration. The lowest singlet state is from the first configuration and is indicated as $^1B''$. In Table 4, we present the computed frequency-dependent polarizability for three theoretical methods alongside the experimental values¹³⁵ measured by Maroulis et al. at three frequencies. Like the experimental values, the values computed with CC at these three frequencies are quite close to each other and we find reasonable agreement with the CC values slightly underestimating the experimental data. The HF and B3LYP results deviate rather strongly from the experimental results for the first two frequencies which can be rationalized as being caused by an error in the position of the pole close to the first two laser frequencies, that is computed at a too low energy with HF and DFT(B3LYP). Due to the selection rules for this transition to the $B^3\Pi_{0+u}$ state, this then leads to a negative value of the parallel (zz-)component of the polarizability for HF and B3LYP, while the perpendicular (xx-)component is not affected and has a similar value for HF, B3LYP and CC.

Table 4: Frequency dependent polarizability (a.u.) of I₂ molecule

	$\alpha_{zz}(\omega)$	$\alpha_{xx}(\omega)$	$\alpha(\omega)$
$\omega_1=15798 \text{ cm}^{-1}$			
HF	152.0	55.0	87.4
B3LYP	-10.7	58.7	35.6
CC	114.8	55.8	75.5
Exp ¹³⁵			86.8±2.2
$\omega_1=16832.3 \text{ cm}^{-1}$			
HF	-97.3	56.0	4.9
B3LYP	75.4	62.0	66.5
CC	124.0	56.8	79.2
Exp ¹³⁵			93.6±3.4
$\omega_1=30756.9 \text{ cm}^{-1}$			
HF	117.9	55.3	76.2
B3LYP	114.5	61.0	78.8
CC	113.9	59.9	77.9
Exp ¹³⁵			95.3±1.9

Rather than looking at the values for just these three frequencies, two of which are close to the X→B transition, it is more illustrative to apply Eq. (22) and plot simulated absorption cross-section curves. We scan the wavelength ranging from 400 nm to 700 nm and set the imaginary component of the complex frequency (γ) to 0.005 a.u, which corresponds to the experimental lifetime of the B³Π₀₊ state. As selection rules are different for the transitions to the B³Π₀₊ and C¹Π₁ states we may thereby identify the *zz*-component of the complex dipole electric polarizability as being (primarily) due to the B³Π₀₊ state, while the *xx*-component is due to the C¹Π₁ state. This facilitates the comparison to the experimental analysis that was carried out by Tellinghuisen.¹⁴¹ The resulting curves for three models, NR-HF (green lines), X2C-HF (red lines), and X2C-CC (blue lines), are depicted in Fig. 2 and clearly show the effect of SOC. The NR computed curves are entirely due to the weaker transition X¹Σ₀₊ to C¹Π₁ and severely underestimate the absorption cross-section. With SOC, this transition becomes a shoulder on the dominant X¹Σ₀₊ to B³Π₀₊ transition. Comparison with the measured curves (black lines) from the work of Tellinghuisen¹⁴¹ shows a quite good agreement for the height of the dominant peak that is slightly red-shifted compared to the experimental transition.

The dominant peak in the X2C-HF exhibits a severe red-shift, which clarifies the error seen in the frequency-dependent polarizability in Table 4. For the peak values, the X2C-HF result $2.95 \cdot 10^{-18} \text{cm}^{-2}$ is, however, quite close to the X2C-CC value $2.98 \cdot 10^{-18} \text{cm}^{-2}$ suggesting that the value of the transition dipole moment is similar in both models under the current calculation conditions. This suggests that the relativistic HF model does describe this excited state qualitatively well, albeit at a wrong energy.

Regarding the spin-allowed transition from X¹Σ₀₊ to C¹Π₁ state, displayed by the dotted line in Fig 2, we observe the X2C-CC model to agree well with the experimental analysis of Tellinghuisen.¹⁴¹ The discrepancy in pole location is around 20 nm and the difference in the peak value is minor at $0.02 \cdot 10^{-18} \text{cm}^{-2}$.

To further analyze the results, we calculate and present the excitation energy of B³Π₀₊

and $C^1\Pi_1$ states in Table 5. We note that HF underestimates the excitation energy of $B^3\Pi_{0+}$ compared to the CC values no matter what relativistic effects are included. This can be attributed to the triplet instability of the TDHF model.^{142–150} On the other hand, such underestimation can be largely avoided by using the simpler configuration interaction singles (CIS) approach. Thus, we perform nonrelativistic CIS calculations by DALTON and find that the CIS value indeed is higher by about 0.011 a.u. for the $B^3\Pi_{0+}$ state.

For the singlet state $C^1\Pi_1$, HF excitation energies are larger than the CC values in both nonrelativistic and spin-free calculations. However, when spin-orbit coupling is introduced via X2C, HF energies become lower. While SOC raises the excitation energy in CC, it reduces the excitation energy in HF, implying that SOC effects and correlation are again not additive.

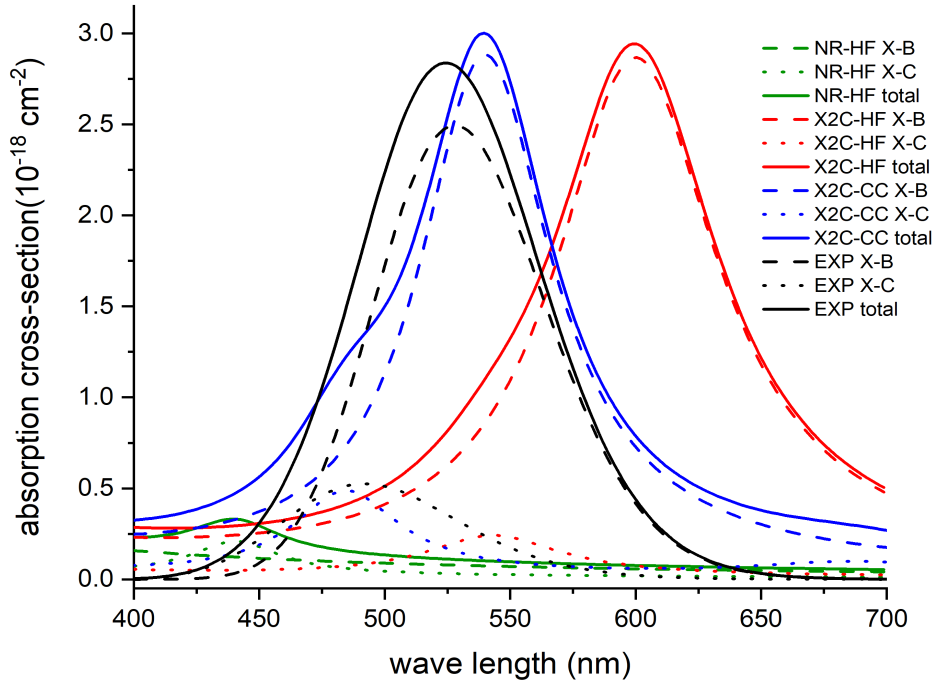


Figure 2: Simulated Spectrum of I_2 . The green lines are non-relativistic HF, the red lines are X2C-HF, the blue lines are X2C-CC, and the black lines are experimental value from work of Tellinghuisen.¹⁴¹ The dashed lines represent the contribution of transition from ground state $X^1\Sigma_{0+}$ to the $B^3\Pi_{0+}$ state. The dot lines are contributions of transition from $X^1\Sigma_{0+}$ state to $C^1\Pi_1$ state. The solid lines are total absorption cross-section.

Table 5: Excitation energy (a.u.) for I_2

States	NR-HF	NR-CIS ^a	NR-CC	SF-HF	SF-CC	X2C-HF	X2C-CC
$B^3\Pi_{0+}$	0.065	0.076	0.076	0.060	0.070	0.076	0.084
$C^1\Pi_1$	0.103	0.107	0.098	0.097	0.092	0.084	0.094

^a Calculations were performed using the DALTON program

In the supplemental materials, we provide a calculation of the spectrum of BH molecule which was used to verify the correctness of our implementation. We compare our damped CC-LR calculation with the broadening of coupled cluster transition dipole moment computed by the DALTON program.^{151,152} and find good agreement.

5.3 Spin-spin coupling

In the previous section, we investigated electric properties. In the current section, we show a calculation of the indirect nuclear spin-spin coupling constant as an illustrative example of the use of our implementation for a magnetic property. The coupling constant K_{KL} can be related to the experimentally observed coupling J_{KL} between the nuclear spins of atoms K and L via

$$J_{KL} = \frac{1}{2\pi} \gamma_K \gamma_L K_{KL} \quad (27)$$

where γ_K is the gyromagnetic ratio of nucleus K . The K_{KL} tensor can in a relativistic framework be expressed in terms of linear response functions with respect to the hyperfine operator \hat{h}_K^{hfs} :⁹

$$K_{KL,\mu\nu} = \frac{\partial^2}{\partial m_{K;\mu} \partial m_{L;\nu}} \langle \langle \hat{h}_K^{\text{hfs}}; \hat{h}_L^{\text{hfs}} \rangle \rangle_{\omega_{k1}, \omega_{k2}} \quad (28)$$

$$\hat{h}_K^{\text{hfs}} = \frac{1}{c} \sum_i \mathbf{m}_K \cdot \frac{\mathbf{r}_{iK} \times \boldsymbol{\alpha}}{r_{iK}^3} \quad (29)$$

In the non-relativistic framework, it is common to formulate K in terms of three distinct contributions: diamagnetic spin-orbit coupling (DSO), paramagnetic spin-orbit (PSO), and the Fermi contact-Spin dipolar (FC-SD) term. Of these, the first term can be computed as an expectation value, whereas the second and third require the use of response theory. Moreover, the PSO term involves only singlet excitations, whereas the FC-SD term couples a singlet ground state to triplet excited states due to the triplet nature of the Fermi contact and spin-dipolar operators. An explicit sum-over-states form of the contributions to K_{KL} in the nonrelativistic framework is:^{9,153}

$$\begin{aligned} K_{KL} = & \frac{1}{2c^4} \langle 0 | \frac{\mathbf{r}_K^T \mathbf{r}_L I - \mathbf{r}_K \mathbf{r}_L^T}{r_K^3 r_L^3} | 0 \rangle - \frac{2}{c^4} \sum_{n_S} \frac{\langle 0 | r_K^{-3} I_K | n_S \rangle \langle n_S | r_L^{-3} I_L | 0 \rangle}{E_{n_S} - E_0} \\ & - \frac{2}{c^4} \sum_{n_T} \frac{\langle 0 | \frac{8\pi}{3} \delta(r_L) \mathbf{s} + \frac{3\mathbf{r}_L \mathbf{r}_L^T - r_L^2 I_3}{r_L^5} \mathbf{s} | n_T \rangle \langle n_T | \frac{8\pi}{3} \delta(r_L) \mathbf{s}^T + \frac{3\mathbf{r}_L \mathbf{r}_L^T - r_L^2 I_3}{r_L^5} \mathbf{s}^T | 0 \rangle}{E_{n_T} - E_0} \end{aligned} \quad (30)$$

As discussed in Reference 154, the PSO and FC-SD response functions can in the relativistic framework of Eq. (28) be identified as orbital responses involving rotations amongst positive energy orbitals. The DSO contribution, on the other hand, comes from the rotations between positive and negative energy orbitals and can in a sequence of approximations be brought into an expectation value form that is identical to the non-relativistic expression and is then called the Sternheim approximation.¹⁵⁵ Therefore, in relativistic calculations, there are two ways to obtain the diamagnetic terms: one by including electron-positron rotations explicitly in the response calculation or by making use of the Sternheim approximation.

In contrast to the Sternheim approximation, in which a numerically very stable expectation value is computed, the formally more rigorous response approach is quite sensitive to the quality of sampling of the positronic orbital space in a finite basis.^{64,154} This is why in the current study, we compute the diamagnetic terms as an expectation value. An important modification as compared to the original application in 4-component theory is the use of the X2C transformation, in which all operators are first transformed to a 2C representation. The generic expression is:

$$\mathbf{X}^{X2C} = \mathbf{X}^{++} = \sum_{V,W}^{L,S} [\mathbf{U}^{V+}]^\dagger \mathbf{X}^{VW} \mathbf{U}^{W+} \quad (31)$$

in which \mathbf{U}^{L+} and \mathbf{U}^{S+} are blocks of the X2C transformation matrix that block-diagonalizes the matrix representation of a reference Hamiltonian operator (usually and also in this work taken as the molecular Hamiltonian without 2-electron interactions) and allows to solve only for positive (+) energy solutions. In case of magnetic properties, the original 4C matrix representation of operator (29) is off-diagonal with respect to the Large (L) and (S) Small parts of the 4C basis so that

$$\mathbf{h}_K^{hfs,X2C} = \frac{1}{c} [\mathbf{U}^{L+}]^\dagger [\mathbf{m}_K \cdot \frac{\boldsymbol{\sigma} \times \mathbf{r}_{iK}}{r_{iK}^3}]^{LS} \mathbf{U}^{S+} + h.c. \quad (32)$$

This matrix representation can be interpreted as providing the X2C equivalent of the sin-

plet PSO and triplet FC-SD operators that are used in nonrelativistic response calculations. The Sternheim approximation yields a diagonal 4C DSO operator \mathbf{k}_{KL} that is transformed as

$$\mathbf{k}_{KL}^{X2C} = [\mathbf{U}^{L+}]^\dagger \mathbf{k}_{KL}^{LL} \mathbf{U}^{L+} + [\mathbf{U}^{S+}]^\dagger \mathbf{k}_{KL}^{SS} \mathbf{U}^{S+} \quad (33)$$

$$\mathbf{k}_{KL}^{VW} = \frac{1}{2c^4} \left[\frac{\mathbf{r}_K^T \mathbf{r}_L I - \mathbf{r}_K \mathbf{r}_L^T}{r_K^3 r_L^3} \right]^{VW} \delta_{VW} \quad (34)$$

and contracted with the unperturbed density matrix to obtain the DSO contribution to the spin-spin coupling.

In Table 6, we list the resulting reduced isotropic and anisotropic spin-spin coupling constants of HX(X=F, Cl, Br, I) computed by HF, B3LYP, CC-CI, and CC-CC models with both nonrelativistic and relativistic Hamiltonians. As is well-known, relativistic effects are very important for magnetic properties and we see the expected increase of their magnitude upon descending the periodic table from hydrogen fluoride to hydrogen iodide. To benchmark the quality of the X2C transformation, we also carried out four-component Dirac-Coulomb(DC) HF calculations with default approximation for the all small two-electron integrals¹⁵⁶ and see that the X2C values match the DC results very well for all molecules.

At the Hartree-Fock level, the isotropic constants generally exhibit a downward trend from HF to HI, while the anisotropic values typically show an upward trend for both relativistic and nonrelativistic calculations. After including electron correlation, these trends are qualitatively the same although the precise values change considerably, especially for HBr. To verify our CC implementation, we also utilize the CFOUR program¹⁵⁷ for nonrelativistic CC response and find our CC-CC models with the nonrelativistic Hamiltonian to reproduce the CFOUR values for all three light molecules.

Although the nonrelativistic calculation is useful for analysis, we cannot ignore relativistic effects for heavy molecules. For example, the relativistic correction at the coupled cluster level for HBr is around 25% and slightly smaller than that with Hartree-Fock. We also

performed DFT calculations, the results obtained with B3LYP functionals are quite far from both the HF and the CC results. As there are no suitable experimental values to compare with one cannot assess rigorously the performance of the methods, but the large discrepancy between the commonly used B3LYP DFT and CC makes these systems of interest for future benchmarking with converged CC expansion (we deem both our employed basis set as well as excitation level not yet suitable for this purpose).

Looking at the two ways of carrying out CC response calculations, we observe minor variances between the CC-CI and CC-CC, which appear to become more pronounced for the heavier elements. It is known that LR-CC transition moments are size-extensive whereas EOM-CC ones are not,^{41,46,158–164} though in these comparisons it was found the numerical differences between LR-CC and EOM-CC were rather small for a single molecule. Numerical studies have been primarily concerned with light molecules and properties within the valence domain, like the electric transition dipole moment,^{46,162,164} and the dipole polarizability,^{158,161} and our results for polarizabilities are in line with these findings. A notable exception is the work of Sekino and Bartlett¹⁶¹, which have investigated spin-spin couplings for ethane and found a difference of 0.05% between EOM-CC and LR-CC for J_{CC} . This value is comparable to our difference of about 0.19% for the HF molecule.

If the lack of size extensivity in EOM-CC transition moments is a significant source of discrepancies, one would expect the difference between CC-CI and CC-CC to grow as the number of electrons correlated increases across the HX series, but the difference per correlated electron to remain roughly constant. Our analysis of the zz, xx and yy components of the linear response contribution to K_{HX} (see supplementary information) provides some evidence this is the case, as differences (in absolute value) for each component fall between 0.004 and 0.02 a.u. for all molecules. There are some differences between Hamiltonians for HBr and HI, but these are of smaller magnitude than those due to non-extensivity. However, we believe the sample size is not large enough for definitive conclusions, and in future investigations we intent to revisit this issue for a broader range of molecules.

Table 6: Isotropic and anisotropic reduced spin-spin coupling $K(10^{19} \text{ m}^{-2} \text{ kg s}^{-2} \text{ A}^{-2})$ for $\text{HX}(\text{X}=\text{F}, \text{Cl}, \text{Br}, \text{I})$

Models	$^1\text{HF}^{19}$	$^1\text{HCl}^{35}$	$^1\text{HBr}^{79}$	$^1\text{HI}^{127}$
Isotropic				
NR-HF	49.5486	28.1528	10.8253	-0.8979
NR-B3LYP	33.3898	19.7146	-1.8769	
NR-CC-CI	40.5554	31.3181	30.7926	
NR-CC-CC	40.4794	31.0971	29.9730	
NR-CC-CC ^a	40.4778	31.0970	29.9729	
X2C-HF	49.5023	27.2261	-4.5338	-83.1522
X2C-B3LYP	33.2367	18.9409	-11.6914	-57.3316
X2C-CC-CI	40.4834	30.9008	23.8246	3.4887
X2C-CC-CC	40.4047	30.6448	22.7588	0.7481
DC-HF	49.4725	27.1494	-4.8396	-84.0079
Anisotropic				
NR-HF	2.5499	59.6666	161.9806	277.7237
NR-B3LYP	6.3484	50.1075	130.4249	
NR-CC-CI	-3.7566	36.3828	100.9785	
NR-CC-CC	-3.4931	37.1193	102.9362	
X2C-HF	2.5858	60.2375	168.5425	305.7204
X2C-B3LYP	6.4477	50.3990	130.5655	201.0597
X2C-CC-CI	-3.6579	36.8838	106.6559	192.8454
X2C-CC-CC	-3.3929	37.6281	108.7226	196.3474
DC-HF	2.5978	60.2822	168.7214	306.1280

^a Calculations were performed using the CFOUR program

As most experimental work is carried out in the condensed phase, we wanted to go beyond isolated diatomic molecules, and provide a sample investigation of solvent effects. For this purpose we chose the solvent shift on the spin-spin coupling constant $^1\text{H}_b\text{-}^{34}\text{Se}$ in the the $\text{H}_2\text{Se-H}_2\text{O}$ dimer. The supermolecular structure is taken from the work of Olejniczak et al.¹⁶⁵ and displayed on Fig.3. It can readily be seen from Table 7 that all calculations show the solvent effect on the Se-H_b coupling for the bond involved in the hydrogen bond to be quite substantial. However, the shifts ΔJ in the correlated models have a different magnitude than that at the HF level. For example, the shifts of Se-H_b are 19.5403 Hz and 19.0648 Hz for CC-CC and B3LYP, respectively, while they are almost twice as large at 40.0220 Hz for HF. Although, the shifts of DFT are quite close to those computed with CC, the absolute J_{iso}^{super}

and J_{iso} deviate a lot. Comparing with BLYP and B3LYP values, we find the addition of exact exchange to the DFT to have a significant effect, with the hybrid DFT B3LYP results being closer to the CC values.

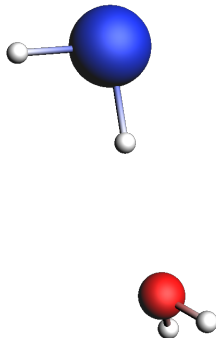


Figure 3: $\text{H}_2\text{Se}-\text{H}_2\text{O}$ complex system. Color of atoms: Se (blue), O(red), H(white), H_b is the Hydrogen atom that belongs to Se and is close to O.

Table 7: Isotropic and anisotropic indirect spin-spin coupling (J_{iso} and J_{aniso} in Hz) for isolated H_2Se subsystem, (J_{iso}^{super} and J_{aniso}^{super} in Hz) for H_2Se subsystem in $\text{H}_2\text{Se}-\text{H}_2\text{O}$, and the shifts (ΔJ , in Hz) for the isolated ("ME") H_2Se molecules in the presence of H_2O

Models	J_{iso}	J_{iso}^{super}	ΔJ_{iso}^{ME} $^1\text{H}_b-\text{Se}^{34}$	J_{aniso}	J_{aniso}^{super}	ΔJ_{ianso}^{ME}
HF ^a	90.4949	128.2837	36.7888	305.8746	302.1583	-3.7163
HF	52.7369	92.7589	40.0220	353.6191	353.4049	-0.2142
BLYP	-26.8400	-11.0675	15.7725	265.5061	271.8454	6.3393
B3LYP	-9.1404	9.9244	19.0648	269.7740	275.2143	5.4403
CC-CI	66.6432	85.8755	19.2303	215.4586	218.7408	3.2821
CC-CC	65.9553	85.4956	19.5403	219.8036	223.0023	3.1987

^a Nonrelativistic calculation with the Levy-Leblond Hamiltonian

5.4 Optical rotation

Finally, we consider both electric and magnetic fields, by looking at optical rotation (in the length gauge and for a common gauge origin) for the archetypical chiral molecules H_2Y_2 ($\text{Y}=\text{O}, \text{S}, \text{Se}, \text{Te}$). At the frequency of the sodium D-line (in 589.29 nm), which is the most common experimental setup, the specific optical rotation $[\alpha]_D^{25}$ in unit $[\text{dm}^{-1}(\text{g}/\text{mol})^{-1}]$ is given by the equations⁷⁴

$$[\alpha]_D^{25} = -228 \cdot 10^{-30} \frac{\pi^2 N a_0^4 \omega}{3M} \sum_{\alpha} G'_{\alpha\alpha} \quad (35)$$

$$G'_{\alpha\beta}(-\omega; \omega) = -\text{Im}\langle\langle \hat{\mu}_{\alpha}; \hat{m}_{\beta} \rangle\rangle_{\omega} \quad (36)$$

where M is the molecular mass in g mol^{-1} , N is the number density, and μ_{α} and m_{β} are the electric and magnetic dipole operator, respectively.

In Fig 4, we display the results for HF, B3LYP, and CC for both the nonrelativistic and X2C Hamiltonian. First, to verify our implementation, we performed the calculation on H_2S_2 with the DALTON program with the same basis set. The resulting data are available in the supplemental information and show good agreement, confirming the correctness of the implementation. To benchmark the influence of the truncation on the virtual orbital space, we furthermore performed a calculation in which we truncated the virtual orbital space with an energy threshold of 100 a.u. instead of the otherwise used value on 5 a.u. and found that results match up to 99%. This is similar to the tendency observed in the electric dipole polarizability, as expected as both optical rotation and electric dipole polarizability are predominantly determined by the valence electrons and do not require core-like high-energy virtuals.

Fig 4 shows that for the lighter molecules, H_2O_2 and H_2S_2 , the B3LYP and CC values are nearly twice as large than those of the HF. While the relativistic effect is negligible for H_2O_2 , with a correction of less than 1%, it cannot be neglected for H_2S_2 , where it rises to 10%. The impact of the relativistic effect is present for all models, but correlation and relativistic effects are again not additive. For instance, we find a relativistic HF correction of -12 [$^{\circ} \text{ dm}^{-1}(\text{g/mol})^{-1}$], while for B3LYP and CC, these corrections are -26 [$^{\circ} \text{ dm}^{-1}(\text{g/mol})^{-1}$] and -18 [$^{\circ} \text{ dm}^{-1}(\text{g/mol})^{-1}$], respectively. For the heavier molecules H_2Se_2 and H_2Te_2 , values computed for the sodium D-line frequency become exceedingly large as these molecules have an excitation that is almost at resonance with this frequency. To better understand

this phenomenon, we have therefore calculated the excitation energy of the first eleven microstates for these two molecules. The resulting values are compiled and presented in Table 8. Note that we display all degenerate components of triplet states for better comparison to relativistic states.

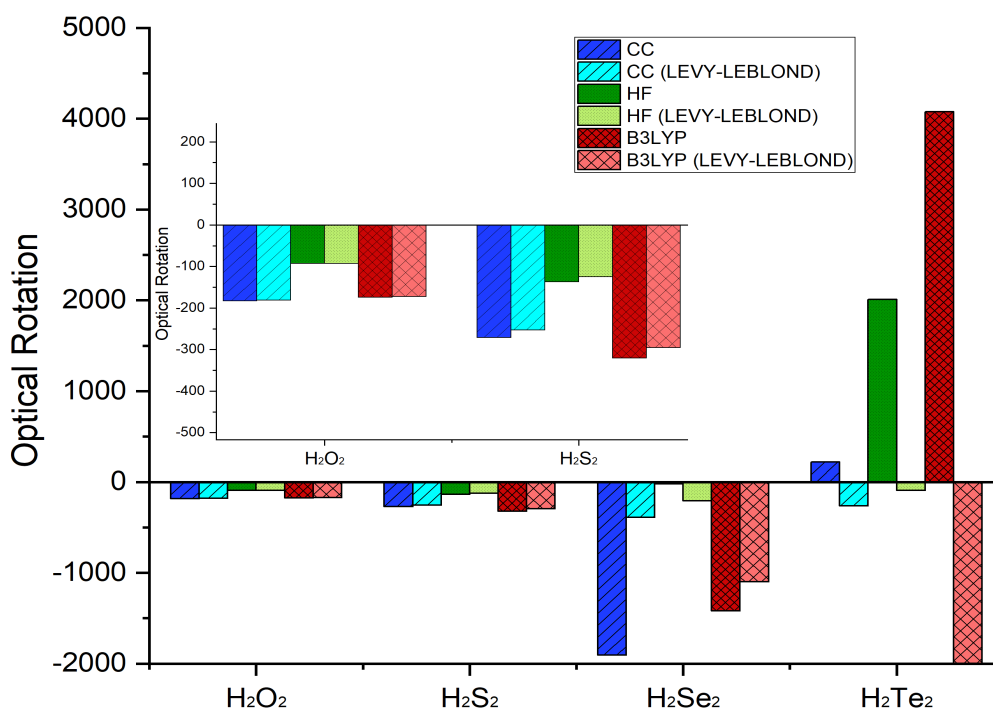


Figure 4: Optical rotation of Hydrogen peroxide series (H_2Y_2) in $[\text{° dm}^{-1}(\text{g/mol})^{-1}]$ with a frequency corresponding to the sodium D-line (589.29 nm, 0.077319 a.u.) calculated with the X2C and Levy-Leblond Hamiltonians

The computed excitation values show that in case of H_2Se_2 , the relativistic CC value is significantly larger than the nonrelativistic CC because the employed frequency is quite close to the resonance frequency of the second excited state in the relativistic calculation (0.0789 a.u.), whereas it is distant from all excited states in the nonrelativistic CC calculation. For the B3LYP computations, we see that the frequency is close to the fourth excited state in both relativistic and nonrelativistic scenarios (0.0863 and 0.0889 respectively). This proximity

results in large values being obtained from both calculations.

When we examine the H_2Te_2 molecule, we find the relativistic effect to be substantial for all three models and even reversing the sign of the optical rotation. For example, the nonrelativistic CC value is -263.59 [$^\circ \text{ dm}^{-1}(\text{g/mol})^{-1}$], but the relativistic CC is 218.83 [$^\circ \text{ dm}^{-1}(\text{g/mol})^{-1}$]. Besides reversing the sign, with HF also the magnitude of the optical rotation is very different in the relativistic and nonrelativistic cases. This is because the first six excited states, while being close to transitions, are triplets and hence do not contribute to the optical rotation that is in the nonrelativistic case. In the relativistic case, SOC makes these transitions allowed, which combined with their proximity to the sodium D-line leads to a much larger optical rotation of opposite sign than computed non-relativistically. The B3LYP values are large in both the relativistic and the NR case because the frequency is then close to the singlet state (0.0721 a.u. and 0.0777 a.u. respectively). To avoid artifacts due to the proximity of poles and the associated infinity of the real frequency-dependent response function, it is probably opportune to consider the lifetime of the excited state and use damped response theory like shown for the complex polarizability for I_2 .

In addition, we observe the triplet instability in HF results as well, similar to what we observed for I_2 . For example, we note the excitation energy of HF's first triplet is larger than that in CC. In HF calculations, the second triplet state lies below the first singlet state. However, in both the correlation models B3LYP and CC, the first singlet state is positioned above the second triplet. To address this issue, we perform nonrelativistic calculations for ten lowest states including five triplets and five singlets. Detailed results are provided in the supplementary information. Similar to I_2 , we note the CIS largely overcomes the triplet instability seen in HF and yields a more systematic error pattern when compared to B3LYP and CC.

Table 8: Excitation energy (a.u.) of the first eleven microstates for H_2Se_2 and H_2Te_2

	State	HF	HF ^a	B3LYP	B3LYP ^a	CC	CC ^b	CC ^a
H_2Se_2	1	0.0671	0.0719	0.0639	0.0661	0.0789	0.0785	0.0812
	2	0.0672	0.0719	0.0639	0.0661	0.0789	0.0785	0.0812
	3	0.0699	0.0719	0.0642	0.0661	0.0792	0.0788	0.0812
	4	0.0860	0.0954	0.0863	0.0889	0.0988	0.0984	0.1016
	5	0.0911	0.0954	0.1098	0.1121	0.1285	0.1282	0.1309
	6	0.0913	0.0954	0.1099	0.1121	0.1286	0.1282	0.1309
	7	0.1082	0.1083	0.1100	0.1121	0.1288	0.1284	0.1309
	8	0.1289	0.1315	0.1314	0.1343	0.1443	0.1440	0.1478
	9	0.1293	0.1315	0.1497	0.1510	0.1541	0.1541	0.1561
	10	0.1295	0.1315	0.1499	0.1510	0.1543	0.1542	0.1561
	11	0.1600	0.1624	0.1500	0.1510	0.1545	0.1544	0.1561
H_2Te_2	1	0.0517	0.0635	0.0542	0.0584	0.0672	0.0672	0.0721
	2	0.0517	0.0635	0.0543	0.0584	0.0673	0.0673	0.0721
	3	0.0605	0.0635	0.0558	0.0584	0.0689	0.0686	0.0721
	4	0.0697	0.0924	0.0721	0.0777	0.0835	0.0835	0.0898
	5	0.0873	0.0924	0.0931	0.0968	0.1098	0.1097	0.1143
	6	0.0888	0.0924	0.0935	0.0968	0.1101	0.1100	0.1143
	7	0.0993	0.0957	0.0940	0.0968	0.1109	0.1108	0.1143
	8	0.1098	0.1138	0.1102	0.1158	0.1220	0.1220	0.1292
	9	0.1123	0.1138	0.1316	0.1320	0.1349	0.1349	0.1367
	10	0.1139	0.1138	0.1324	0.1320	0.1357	0.1356	0.1367
	11	0.1370	0.1402	0.1324	0.1320	0.1360	0.1359	0.1367

^a Nonrelativistic calculation with the Levy-Leblond Hamiltonian

^b With truncation of virtual orbitals on 100 a.u. done by RELCCSD.

6 Conclusion

In this work, we describe the formulation and implementation of the relativistic coupled cluster linear response method for static and frequency-dependent molecular property calculations, which can accurately treat both relativistic and electronic correlation effects. This implementation was accomplished in the GPU-accelerated coupled cluster module of the DIRAC program leveraging a framework designed to handle similar transformed Hamiltonian in subspace. This framework aids in solving both eigenvalue and linear system problems. The current code is capable of calculating excitation energies within the EOM-CCSD

framework and computing the linear response function for both CC-CI and CC-CC type wave-function models.

We have validated the implementation by assessing purely electric properties such as static and frequency-dependent polarizability for Group IIB atoms (Zn, Cd, Hg) and several diatomic molecules. Compared to previous Hartree-Fock linear response calculations, our current linear response calculation based on the relativistic coupled cluster approach offers a notably improved accuracy. This enhancement is particularly evident in terms of relativistic corrections and correlation, bringing our results closer to the experimental data.

In this study, we also tested the indirect spin-spin coupling constant—a purely magnetic property—for the hydrogen halide series HX ($\text{X}=\text{F}, \text{Cl}, \text{Br}, \text{I}$). Validation was done by reproducing the results obtained by other programs such as DALTON and CFOUR using a nonrelativistic Hamiltonian. We extended our study to explore the impact of solvent effect on the $\text{H}_2\text{Se}-\text{H}_2\text{O}$ complex systems. Both correlation and relativistic corrections were found to have pronounced effects on the solvent shift. While CC and DFT gave similar magnitudes for the shifts in solvent effect, the absolute spin-spin coupling constants differed significantly. This finding calls for caution when employing DFT for such calculations.

Lastly, we computed the optical rotation—an electric and magnetic mixed property—for chiral molecules H_2Y_2 ($\text{Y}=\text{O}, \text{S}, \text{Se}, \text{Te}$) at the wave-length of sodium D-line (589.29 nm). Our exploration revealed potential challenges when using this frequency for heavy molecules. We analyzed the poles of the response function by calculating the excitation energy, and advise caution when using sodium D-line for these heavier molecules in future investigations.

A distinguishing aspect of our implementation is its use of complex algebra, which facilitates a straightforward extension of real to complex frequencies for the evaluation of the damped linear response function. We used this feature to simulate the spectrum of I_2 through the assessment of the absorption cross-section.

As a final point and perspective, it is worth noting that our current implementation

relies on the single-code tensor operation library TAL-SH. While efficient, this library is limited to using the memory capacity of a single node. Therefore, a natural development is to extend the current code for the EOM-CCSD energy and linear response to use a library suited for distributed memory computing architectures, such as the ExaTENSOR library already employed for the CC energy evaluation, but still lacks some features needed in the Davidson diagonalization procedure. After resolving these issues we are optimistic that we can eliminate the limitations caused by the library being able to use the memory of only a single compute node and enable treatment of larger systems.

Acknowledgement

This research used resources of the Oak Ridge Leadership Computing Facility, which is a DOE Office of Science User Facility supported under Contract DE-AC05-00OR22725 (allocations CHM160, CHM191 and CHP109). XY, LH and ASPG acknowledge funding from projects Labex CaPPA (Grant No. ANR-11-LABX-0005-01) and ComprIXS (Grant Nos. ANR-19CE29-0019 and DFG JA 2329/6-1), the I-SITE ULNE project OVERSEE and MESONM International Associated Laboratory (LAI) (Grant No. ANR-16-IDEX-0004), as well support from the French national supercomputing facilities (Grant Nos. DARI A0130801859, A0110801859, project grand challenge AdAstra GDA2210). SC acknowledges funding from the Independent Research Fund Denmark–Natural Sciences, Research Project 2 - grant no. 7014-00258B.

Supporting Information Available

The data (input/output) corresponding to the calculations of this paper are available at the Zenodo repository under DOI: 10.5281/zenodo.8136133.

The Supporting Information is available free of charge on the ACS Publications website at DOI: XXX. Working equations for CCSD linear response theory and EOM-EE sigma

vectors and intermediates, comparison for the BH molecule of the damped response LR-CC results obtained with DIRAC and standard LR-CC results obtained with DALTON, Indirect spin-spin coupling constants (J) for the hydrogen halide molecule, additional comparisons of methods for optical rotation.

References

- (1) Barron, L. D. *Molecular light scattering and optical activity*; Cambridge University Press, 2009.
- (2) Bishop, D. M. Molecular vibrational and rotational motion in static and dynamic electric fields. *Rev. Mod. Phys.* **1990**, *62*, 343–374.
- (3) Papadopoulos, M. G., Sadlej, A. J., Leszczynski, J., Eds. *Non-linear optical properties of matter: from molecules to condensed phases*; Springer, 2006.
- (4) Cronstrand, P.; Luo, Y.; Ågren, H. Multi-Photon Absorption of Molecules. *Adv. Quantum. Chem.* **2005**, *50*, 1–21.
- (5) Komatsu, T.; Dimitrov, V.; Tasheva, T.; Honma, T. A review: a new insight for electronic polarizability and chemical bond strength in Bi₂O₃-based glasses. *J. Non-Cryst. Solids* **2020**, *550*, 120365.
- (6) Carr, R.; Evans, N. H.; Parker, D. Lanthanide complexes as chiral probes exploiting circularly polarized luminescence. *Chem. Soc. Rev.* **2012**, *41*, 7673–7686.
- (7) Langhoff, P.; Epstein, S.; Karplus, M. Aspects of time-dependent perturbation theory. *Rev. Mod. Phys.* **1972**, *44*, 602.
- (8) Norman, P. A perspective on nonresonant and resonant electronic response theory for time-dependent molecular properties. *Phys. Chem. Chem. Phys.* **2011**, *13*, 20519.

- (9) Helgaker, T.; Coriani, S.; Jørgensen, P.; Kristensen, K.; Olsen, J.; Ruud, K. Recent Advances in Wave Function-Based Methods of Molecular-Property Calculations. *Chem. Rev.* **2012**, *112*, 543–631.
- (10) Dalgaard, E. Time-dependent multiconfigurational Hartree–Fock theory. *J. Chem. Phys* **1980**, *72*, 816–823.
- (11) Olsen, J.; Jørgensen, P. Linear and nonlinear response functions for an exact state and for an MCSCF state. *J. Chem. Phys* **1985**, *82*, 3235–3264.
- (12) Rice, J. E.; Handy, N. C. The calculation of frequency-dependent polarizabilities as pseudo-energy derivatives. *J. Chem. Phys* **1991**, *94*, 4959–4971.
- (13) Sasagane, K.; Aiga, F.; Itoh, R. Higher-order response theory based on the quasienergy derivatives: The derivation of the frequency-dependent polarizabilities and hyperpolarizabilities. *J. Chem. Phys* **1993**, *99*, 3738–3778.
- (14) Christiansen, O.; Jørgensen, P.; Hättig, C. Response functions from Fourier component variational perturbation theory applied to a time-averaged quasienergy. *Int. J. Quantum. Chem* **1998**, *68*, 1–52.
- (15) Pawłowski, F.; Olsen, J.; Jørgensen, P. Molecular response properties from a Hermitian eigenvalue equation for a time-periodic Hamiltonian. *J. Chem. Phys* **2015**, *142*, 114109.
- (16) Norman, P.; Ruud, K.; Saue, T. *Principles and practices of molecular properties: theory, modeling, and simulations*; Wiley: Hoboken, NJ, 2018.
- (17) Albota, M.; Beljonne, D.; Brédas, J.-L.; Ehrlich, J. E.; Fu, J.-Y.; Heikal, A. A.; Hess, S. E.; Kogej, T.; Levin, M. D.; Marder, S. R., et al. Design of organic molecules with large two-photon absorption cross sections. *Science* **1998**, *281*, 1653–1656.

- (18) Macak, P.; Luo, Y.; Norman, P.; Ågren, H. Electronic and vibronic contributions to two-photon absorption of molecules with multi-branched structures. *J. Chem. Phys* **2000**, *113*, 7055–7061.
- (19) Shee, A.; Visscher, L.; Saue, T. Analytic one-electron properties at the 4-component relativistic coupled cluster level with inclusion of spin-orbit coupling. *J. Chem. Phys* **2016**, *145*, 184107.
- (20) Saue, T. Relativistic Hamiltonians for Chemistry: A Primer. *ChemPhysChem* **2011**, *12*, 3077–3094.
- (21) Vícha, J.; Novotný, J.; Komorovsky, S.; Straka, M.; Kaupp, M.; Marek, R. Relativistic Heavy-Neighbor-Atom Effects on NMR Shifts: Concepts and Trends Across the Periodic Table. *Chem. Rev.* **2020**, *120*, 7065–7103.
- (22) Bolvin, H. An Alternative Approach to the g-Matrix: Theory and Applications. *Chem. Eur. J. of Chem. Phys.* **2006**, *7*, 1575–1589.
- (23) Saue, T.; Jensen, H. J. A. Linear response at the 4-component relativistic level: Application to the frequency-dependent dipole polarizabilities of the coinage metal dimers. *J. Chem. Phys* **2003**, *118*, 522–536.
- (24) Visscher, L.; Saue, T.; Oddershede, J. The 4-component random phase approximation method applied to the calculation of frequency-dependent dipole polarizabilities. *Chem. Phys. Lett* **1997**, *274*, 181–188.
- (25) Saue, T.; Helgaker, T. Four-component relativistic Kohn–Sham theory. *J. Comput. Chem* **2002**, *23*, 814–823.
- (26) Aquino, F.; Govind, N.; Autschbach, J. Electric Field Gradients Calculated from Two-Component Hybrid Density Functional Theory Including Spin-Orbit Coupling. *J. Chem. Theory Comput.* **2010**, *6*, 2669–2686.

- (27) Schnack-Petersen, A. K.; Simmermacher, M.; Fasshauer, E.; Jensen, H. J. A.; Sauer, S. P. A. The Second-Order-Polarization-Propagator-Approximation (SOPPA) in a four-component spinor basis. *J. Chem. Phys.* **2020**, *152*, 134113.
- (28) Burke, K. Perspective on density functional theory. *J. Chem. Phys.* **2012**, *136*, 150901.
- (29) Kervazo, S.; Réal, F.; Viot, F.; Severo Pereira Gomes, A.; Vallet, V. Accurate Predictions of Volatile Plutonium Thermodynamic Properties. *Inorg. Chem.* **2019**, *58*, 14507–14521.
- (30) Sunaga, A.; Saue, T. Towards highly accurate calculations of parity violation in chiral molecules: relativistic coupled-cluster theory including QED-effects. *Mol. Phys* **2021**, e1974592.
- (31) Crawford, T. D.; Schaefer III, H. F. An introduction to coupled cluster theory for computational chemists. *Rev. comp. chem* **2007**, *14*, 33–136.
- (32) Bartlett, R. J.; Musiał, M. Coupled-cluster theory in quantum chemistry. *Rev. Mod. Phys* **2007**, *79*, 291.
- (33) Christiansen, O.; Koch, H.; Jørgensen, P. The second-order approximate coupled cluster singles and doubles model CC2. *Chem. Phys. Lett* **1995**, *243*, 409–418.
- (34) Hald, K.; Pawłowski, F.; Jørgensen, P.; Hättig, C. Calculation of frequency-dependent polarizabilities using the approximate coupled-cluster triples model CC3. *J. Chem. Phys* **2003**, *118*, 1292–1300.
- (35) Crawford, T. D.; Kumar, A.; Bazanté, A. P.; Di Remigio, R. Reduced-scaling coupled cluster response theory: Challenges and opportunities. *WIREs. Comput. Mol. Sci* **2019**, *9*, e1406.

- (36) Krylov, A. I. Equation-of-motion coupled-cluster methods for open-shell and electronically excited species: The hitchhiker’s guide to Fock space. *Annu. Rev. Phys. Chem.* **2008**, *59*, 433–462.
- (37) Khani, S. K.; Faber, R.; Santoro, F.; Hättig, C.; Coriani, S. UV Absorption and Magnetic Circular Dichroism Spectra of Purine, Adenine, and Guanine: A Coupled Cluster Study in Vacuo and in Aqueous Solution. *J. Chem. Theory Comput.* **2019**, *15*, 1242–1254.
- (38) Gauss, J.; Stanton, J. F. Coupled-cluster calculations of nuclear magnetic resonance chemical shifts. *J. Chem. Phys* **1995**, *103*, 3561–3577.
- (39) Christiansen, O.; Halkier, A.; Koch, H.; Jørgensen, P.; Helgaker, T. Integral-direct coupled cluster calculations of frequency-dependent polarizabilities, transition probabilities and excited-state properties. *J. Chem. Phys* **1998**, *108*, 2801–2816.
- (40) Ruud, K.; Helgaker, T. Optical rotation studied by density-functional and coupled-cluster methods. *Chem. Phys. Lett* **2002**, *352*, 533–539.
- (41) Coriani, S.; Pawłowski, F.; Olsen, J.; Jørgensen, P. Molecular response properties in equation of motion coupled cluster theory: A time-dependent perspective. *J. Chem. Phys* **2016**, *144*, 024102.
- (42) Nanda, K. D.; Krylov, A. I.; Gauss, J. Communication: The pole structure of the dynamical polarizability tensor in equation-of-motion coupled-cluster theory. *J. Chem. Phys* **2018**, *149*, 141101.
- (43) Alessio, M.; Krylov, A. I. Equation-of-Motion Coupled-Cluster Protocol for Calculating Magnetic Properties: Theory and Applications to Single-Molecule Magnets. *J. Chem. Theory Comput.* **2021**, *17*, 4225–4241.

- (44) Andersen, J. H.; Nanda, K. D.; Krylov, A. I.; Coriani, S. Cherry-picking resolvents: Recovering the valence contribution in X-ray two-photon absorption within the core-valence-separated equation-of-motion coupled-cluster response theory. *J. Chem. Theory. Comput* **2022**, *18*, 6189–6202.
- (45) Andersen, J. H.; Nanda, K. D.; Krylov, A. I.; Coriani, S. Probing Molecular Chirality of Ground and Electronically Excited States in the UV-vis and X-ray Regimes: An EOM-CCSD Study. *J. Chem. Theory. Comput* **2022**, *18*, 1748–1764.
- (46) Faber, R.; Coriani, S. Resonant inelastic X-ray scattering and nonresonant X-ray emission spectra from coupled-cluster (damped) response theory. *J. Chem. Theory. Comput* **2018**, *15*, 520–528.
- (47) Pototschnig, J. V.; Papadopoulos, A.; Lyakh, D. I.; Repisky, M.; Halbert, L.; Severo Pereira Gomes, A.; Jensen, H. J. A.; Visscher, L. Implementation of Relativistic Coupled Cluster Theory for Massively Parallel GPU-Accelerated Computing Architectures. *J. Chem. Theory Comput.* **2021**, acs.jctc.1c00260.
- (48) Saue, T.; Bast, R.; Gomes, A. S. P.; Jensen, H. J. A.; Visscher, L.; Aucar, I. A.; Di Remigio, R.; Dyall, K. G.; Eliav, E.; Fasshauer, E., et al. The DIRAC code for relativistic molecular calculations. *J. Chem. Phys* **2020**, *152*, 204104.
- (49) Lyakh, D. I. Domain-specific virtual processors as a portable programming and execution model for parallel computational workloads on modern heterogeneous high-performance computing architectures. *Int J Quantum Chem* **2019**, *119*, e25926.
- (50) DePrince III, A. E.; Hammond, J. R. Coupled cluster theory on graphics processing units I. The coupled cluster doubles method. *J. Chem. Theory. Comput* **2011**, *7*, 1287–1295.
- (51) Calvin, J. A.; Peng, C.; Rishi, V.; Kumar, A.; Valeev, E. F. Many-body quantum chemistry on massively parallel computers. *Chem. Rev* **2020**, *121*, 1203–1231.

- (52) Hohenstein, E. G.; Martínez, T. J. GPU acceleration of rank-reduced coupled-cluster singles and doubles. *J. Chem. Phys* **2021**, *155*, 184110.
- (53) Hillers-Bendtsen, A. E.; Bykov, D.; Barnes, A. L.; Liakh, D.; Hernandez-Corzo, H.; Olsen, J.; Jørgensen, P.; Mikkelsen, K. V. Massively Parallel GPU Enabled Third Order Cluster Perturbation Excitation Energies for Cost-Effective Large Scale Excitation Energy Calculations. *J. Chem. Phys* **2023**, *158*, 144111.
- (54) Thakur, V. K.; Gupta, R. K. Recent progress on ferroelectric polymer-based nanocomposites for high energy density capacitors: synthesis, dielectric properties, and future aspects. *Chem. Rev* **2016**, *116*, 4260–4317.
- (55) Volksen, W.; Miller, R. D.; Dubois, G. Low dielectric constant materials. *Chem. Rev* **2010**, *110*, 56–110.
- (56) Norman, P.; Bishop, D. M.; Jørgen Aa. Jensen, H.; Oddershede, J. Near-resonant absorption in the time-dependent self-consistent field and multiconfigurational self-consistent field approximations. *J. Chem. Phys* **2001**, *115*, 10323–10334.
- (57) Norman, P.; Bishop, D. M.; Jensen, H. J. A.; Oddershede, J. Nonlinear response theory with relaxation: The first-order hyperpolarizability. *J. Chem. Phys* **2005**, *123*, 194103.
- (58) Coriani, S.; Christiansen, O.; Fransson, T.; Norman, P. Coupled-cluster response theory for near-edge x-ray-absorption fine structure of atoms and molecules. *Phys. Rev. A* **2012**, *85*, 022507.
- (59) Coriani, S.; Fransson, T.; Christiansen, O.; Norman, P. Asymmetric-Lanczos-Chain-Driven Implementation of Electronic Resonance Convergent Coupled-Cluster Linear Response Theory. *J. Chem. Theory Comput.* **2012**, *8*, 1616–1628.

- (60) Kauczor, J.; Norman, P.; Christiansen, O.; Coriani, S. Communication: A reduced-space algorithm for the solution of the complex linear response equations used in coupled cluster damped response theory. *J. Chem. Phys* **2013**, *139*, 211102.
- (61) Helgaker, T.; Jaszunski, M.; Ruud, K. Ab initio methods for the calculation of NMR shielding and indirect spin-spin coupling constants. *Chem. Rev* **1999**, *99*, 293–352.
- (62) Helgaker, T.; Jaszunski, M.; Pecul, M. The quantum-chemical calculation of NMR indirect spin–spin coupling constants. *Prog. Nucl. Mag. Res. Sp* **2008**, *53*, 249.
- (63) Vaara, J. Theory and computation of nuclear magnetic resonance parameters. *Phys. Chem. Chem. Phys* **2007**, *9*, 5399–5418.
- (64) Visscher, L.; Enevoldsen, T.; Saue, T.; Jensen, H. J. A.; Oddershede, J. Full four-component relativistic calculations of NMR shielding and indirect spin–spin coupling tensors in hydrogen halides. *J. Comput. Chem* **1999**, *20*, 1262–1273.
- (65) Franzke, Y. J.; Mack, F.; Weigend, F. NMR Indirect Spin–Spin Coupling Constants in a Modern Quasi-Relativistic Density Functional Framework. *J. Chem. Theory. Comput* **2021**, *17*, 3974–3994.
- (66) Franzke, Y. J. Reducing Exact Two-Component Theory for NMR Couplings to a One-Component Approach: Efficiency and Accuracy. *J. Chem. Theory. Comput* **2023**, *19*, 2010–2028.
- (67) Aucar, G. A.; Melo, J. I.; Aucar, I. A.; Maldonado, A. F. Foundations of the LRESC model for response properties and some applications. *Int. J. Quantum. Chem* **2018**, *118*, e25487.
- (68) Liu, W. *Handbook of relativistic quantum chemistry*; Springer Berlin Heidelberg Berlin, Heidelberg, 2017.

- (69) Nguyen, L. A.; He, H.; Pham-Huy, C. Chiral drugs: an overview. *Int. J. Biol. Sci* **2006**, *2*, 85.
- (70) He, G. S.; Tan, L.-S.; Zheng, Q.; Prasad, P. N. Multiphoton absorbing materials: molecular designs, characterizations, and applications. *Chem. Rev* **2008**, *108*, 1245–1330.
- (71) Pedersen, T. B.; Koch, H.; Boman, L.; de Merás, A. M. S. Origin invariant calculation of optical rotation without recourse to London orbitals. *Chem. Phys. Lett* **2004**, *393*, 319–326.
- (72) Caricato, M. Origin invariant optical rotation in the length dipole gauge without London atomic orbitals. *J. Chem. Phys* **2020**, *153*.
- (73) Parsons, T.; Balduf, T.; Caricato, M. On the choice of coordinate origin in length gauge optical rotation calculations. *Chirality* **2023**,
- (74) Ruud, K.; Helgaker, T. Optical rotation studied by density-functional and coupled-cluster methods. *Chem. Phys. Lett* **2002**, *352*, 533–539.
- (75) Ruud, K.; Stephens, P. J.; Devlin, F. J.; Taylor, P. R.; Cheeseman, J. R.; Frisch, M. J. Coupled-cluster calculations of optical rotation. *Chem. Phys. Lett* **2003**, *373*, 606–614.
- (76) Crawford, T. D.; Sekino, H. *Advances in the Theory of Atomic and Molecular Systems*; Springer Netherlands, 2009; pp 225–239.
- (77) Norman, P.; Ruud, K.; Saue, T. *Principles and practices of molecular properties: Theory, modeling, and simulations*; John Wiley & Sons, 2018.
- (78) von Ragué Schleyer, P.; Allinger, N. L.; Clark, T.; Gasteiger, J.; Kollman, P.; Schaefer, H. F.; Schreiner, P. R. *Encyclopedia of computational chemistry*; Wiley Online Library, 1998.

- (79) Boyd, R. W. *Nonlinear optics*; Academic press, 2020.
- (80) Visscher, L.; Lee, T. J.; Dyall, K. G. Formulation and implementation of a relativistic unrestricted coupled-cluster method including noniterative connected triples. *J. Chem. Phys* **1996**, *105*, 8769–8776.
- (81) Asthana, A.; Liu, J.; Cheng, L. Exact two-component equation-of-motion coupled-cluster singles and doubles method using atomic mean-field spin-orbit integrals. *J. Chem. Phys* **2019**, *150*, 074102.
- (82) Peng, B.; Lestrangle, P. J.; Goings, J. J.; Caricato, M.; Li, X. Energy-Specific Equation-of-Motion Coupled-Cluster Methods for High-Energy Excited States: Application to *K* -edge X-ray Absorption Spectroscopy. *J. Chem. Theory Comput.* **2015**, *11*, 4146–4153.
- (83) Shee, A.; Saue, T.; Visscher, L.; Severo Pereira Gomes, A. Equation-of-motion coupled-cluster theory based on the 4-component Dirac–Coulomb (–Gaunt) Hamiltonian. Energies for single electron detachment, attachment, and electronically excited states. *J. Chem. Phys* **2018**, *149*, 174113.
- (84) Shavitt, I.; Bartlett, R. *Many-Body Methods in Chemistry and Physics: MBPT and Coupled-Cluster Theory*; Cambridge Molecular Science; Cambridge University Press, 2009.
- (85) Lyakh, D. I. TAL-SH: Tensor Algebra Library for Shared Memory Computers. [github.com/https://DmitryLyakh/TAL_SH](https://github.com/DmitryLyakh/TAL_SH), 2023.
- (86) Scuseria, G. E.; Lee, T. J.; Schaefer, H. F. Accelerating the convergence of the coupled-cluster approach. *Chem. Phys. Lett* **1986**, *130*, 236–239.
- (87) Hättig, C.; Weigend, F. CC2 excitation energy calculations on large molecules using the resolution of the identity approximation. *J. Chem. Phys* **2000**, *113*, 5154–5161.

- (88) Nanda, K. D.; Krylov, A. I. Static polarizabilities for excited states within the spin-conserving and spin-flipping equation-of-motion coupled-cluster singles and doubles formalism: Theory, implementation, and benchmarks. *J. Chem. Phys* **2016**, *145*, 204116.
- (89) Hansen, M. B.; Seidler, P.; Gyórfy, W.; Christiansen, O. A Lanczos-chain driven approach for calculating damped vibrational configuration interaction response functions. *J. Chem. Phys* **2010**, *133*, 114102.
- (90) Coriani, S.; Fransson, T.; Christiansen, O.; Norman, P. Asymmetric-Lanczos-Chain-Driven Implementation of Electronic Resonance Convergent Coupled-Cluster Linear Response Theory. *J. Chem. Theory Comput.* **2012**, *8*, 1616–1628.
- (91) Olsen, J.; Jensen, H. J. A.; Jørgensen, P. Solution of the large matrix equations which occur in response theory. *J. Comput. Phys* **1988**, *74*, 265–282.
- (92) Ziólkowski, M.; Weijo, V.; Jorgensen, P.; Olsen, J. An efficient algorithm for solving nonlinear equations with a minimal number of trial vectors: applications to atomic-orbital based coupled-cluster theory. *The Journal of chemical physics* **2008**, *128*, 204105.
- (93) Ettenhuber, P.; Jørgensen, P. Discarding Information from Previous Iterations in an Optimal Way To Solve the Coupled Cluster Amplitude Equations. *Journal Of Chemical Theory And Computation* **2015**, 150403071611007.
- (94) DIRAC, a relativistic ab initio electronic structure program, Release DIRAC23 (2023), written by R. Bast, A. S. P. Gomes, T. Saue and L. Visscher and H. J. Aa. Jensen, with contributions from I. A. Aucar, V. Bakken, C. Chibueze, J. Creutzberg, K. G. Dyall, S. Dubillard, U. Ekström, E. Eliav, T. Enevoldsen, E. Faßhauer, T. Fleig, O. Fossgaard, L. Halbert, E. D. Hedegård, T. Helgaker, B. Helmich–Paris, J. Henriksen, M. van Horn, M. Iliáš, Ch. R. Jacob, S. Knecht, S. Komorovský, O. Kullie,

- J. K. Lærdahl, C. V. Larsen, Y. S. Lee, N. H. List, H. S. Nataraj, M. K. Nayak, P. Norman, A. Nyvang, G. Olejniczak, J. Olsen, J. M. H. Olsen, A. Papadopoulos, Y. C. Park, J. K. Pedersen, M. Pernpointner, J. V. Pototschnig, R. di Remigio, M. Repisky, K. Ruud, P. Salek, B. Schimmelpfennig, B. Senjean, A. Shee, J. Sikkema, A. Sunaga, A. J. Thorvaldsen, J. Thyssen, J. van Stralen, M. L. Vidal, S. Villaume, O. Visser, T. Winther, S. Yamamoto and X. Yuan (available at <https://doi.org/10.5281/zenodo.7670749>, see also <https://www.diracprogram.org>).
- (95) Dyllal, K. G. Relativistic double-zeta, triple-zeta, and quadruple-zeta basis sets for the 4s, 5s, 6s, and 7s elements. *J. Phys. Chem. A* **2009**, *113*, 12638–12644.
- (96) Dyllal, K. G.; Tecmer, P.; Sunaga, A. Diffuse Basis Functions for Relativistic s and d Block Gaussian Basis Sets. *J. Chem. Theory. Comput* **2022**,
- (97) Dyllal, K. G. Relativistic quadruple-zeta and revised triple-zeta and double-zeta basis sets for the 4p, 5p, and 6p elements. *Theor. Chem. Acc* **2006**, *115*, 441–447.
- (98) Kendall, R. A.; Dunning Jr, T. H.; Harrison, R. J. Electron affinities of the first-row atoms revisited. Systematic basis sets and wave functions. *J. Chem. Phys* **1992**, *96*, 6796–6806.
- (99) Prascher, B. P.; Woon, D. E.; Peterson, K. A.; Dunning, T. H.; Wilson, A. K. Gaussian basis sets for use in correlated molecular calculations. VII. Valence, core-valence, and scalar relativistic basis sets for Li, Be, Na, and Mg. *Theor. Chem. Acc* **2011**, *128*, 69–82.
- (100) Hill, J. G.; Peterson, K. A. Gaussian basis sets for use in correlated molecular calculations. XI. Pseudopotential-based and all-electron relativistic basis sets for alkali metal (K–Fr) and alkaline earth (Ca–Ra) elements. *J. Chem. Phys* **2017**, *147*, 244106.
- (101) Woon, D. E.; Dunning Jr, T. H. Gaussian basis sets for use in correlated molecular

- calculations. III. The atoms aluminum through argon. *J. Chem. Phys* **1993**, *98*, 1358–1371.
- (102) Wilson, A. K.; Woon, D. E.; Peterson, K. A.; Dunning Jr, T. H. Gaussian basis sets for use in correlated molecular calculations. IX. The atoms gallium through krypton. *J. Chem. Phys* **1999**, *110*, 7667–7676.
- (103) Iliáš, M.; Saue, T. An infinite-order two-component relativistic Hamiltonian by a simple one-step transformation. *J. Chem. Phys* **2007**, *126*, 064102.
- (104) Schimmelpfennig, B.; Maron, L.; Wahlgren, U.; Teichteil, C.; Fagerli, H.; Gropen, O. On the combination of ECP-based CI calculations with all-electron spin-orbit mean-field integrals. *Chem. Phys. Lett* **1998**, *286*, 267 – 271.
- (105) Lévy-Leblond, J.-M. Nonrelativistic particles and wave equations. *Commun. Math. Phys* **1967**, *6*, 286–311.
- (106) Visscher, L.; Saue, T. Approximate relativistic electronic structure methods based on the quaternion modified Dirac equation. *J. Chem. Phys* **2000**, *113*, 3996–4002.
- (107) Dyall, K. G. An exact separation of the spin-free and spin-dependent terms of the Dirac–Coulomb–Breit Hamiltonian. *J. Chem. Phys* **1994**, *100*, 2118–2127.
- (108) Saue, T.; Jensen, H. A. Linear response at the 4-component relativistic level: Application to the frequency-dependent dipole polarizabilities of the coinage metal dimers. *J. Chem. Phys* **2003**, *118*, 522–536.
- (109) Salek, P.; Helgaker, T.; Saue, T. Linear response at the 4-component relativistic density-functional level: application to the frequency-dependent dipole polarizability of Hg, AuH and PtH₂. *Chem. Phys* **2005**, *311*, 187–201.
- (110) Becke, A. D. A new mixing of Hartree–Fock and local density-functional theories. *J. Chem. Phys* **1993**, *98*, 1372–1377.

- (111) Visscher, L.; Dyall, K. G. Dirac–Fock atomic electronic structure calculations using different nuclear charge distributions. *Atom. Data. Nucl. Data* **1997**, *67*, 207–224.
- (112) Beebe, N. H.; Linderberg, J. Simplifications in the generation and transformation of two-electron integrals in molecular calculations. *Int. J. Quantum. Chem* **1977**, *12*, 683–705.
- (113) Koch, H.; Sánchez de Merás, A.; Pedersen, T. B. Reduced scaling in electronic structure calculations using Cholesky decompositions. *J. Chem. Phys* **2003**, *118*, 9481–9484.
- (114) Aquilante, F.; Pedersen, T. B.; Lindh, R. Low-cost evaluation of the exchange Fock matrix from Cholesky and density fitting representations of the electron repulsion integrals. *J. Chem. Phys* **2007**, *126*, 194106.
- (115) Pototschnig, J.; Yuan, X.; Halbert, L.; Visscher, L.; Gomes, A. S. P. Ground and excited state properties with Cholesky decomposition relativistic coupled cluster theory. *in preparation* **2023**,
- (116) Huber, K.-P. *Molecular spectra and molecular structure* **1979**,
- (117) Hessel, M. Experimental observation of the NaLi molecule. *Phys. Rev. Lett* **1971**, *26*, 215.
- (118) Ferber, R.; Klincare, I.; Nikolayeva, O.; Tamanis, M.; Knöckel, H.; Tiemann, E.; Pashov, A. The ground electronic state of KCs studied by Fourier transform spectroscopy. *J. Chem. Phys* **2008**, *128*, 244316.
- (119) Laerdahl, J. K.; Schwerdtfeger, P. Fully relativistic ab initio calculations of the energies of chiral molecules including parity-violating weak interactions. *Phys. Rev. A* **1999**, *60*, 4439.

- (120) Goebel, D.; Hohm, U.; Maroulis, G. Theoretical and experimental determination of the polarizabilities of the zinc 1S_0 state. *Phys. Rev. A* **1996**, *54*, 1973.
- (121) Hohm, U. Dipole–Dipole Polarizability of the Cadmium 1S_0 State Revisited. *Opt. Spectrosc* **2022**, *130*, 290–294.
- (122) Goebel, D.; Hohm, U. Dipole polarizability, Cauchy moments, and related properties of Hg. *J. Phys. Chem* **1996**, *100*, 7710–7712.
- (123) Lurio, A.; DeZafra, R.; Goshen, R. J. Lifetime of the First P 1 1 State of Zinc, Calcium, and Strontium. *Phys. Rev* **1964**, *134*, A1198.
- (124) Lurio, A.; Novick, R. Lifetime and hfs of the (5 s 5 p) P 1 1 State of Cadmium. *Phys. Rev* **1964**, *134*, A608.
- (125) Pinnington, E.; Ansbacher, W.; Kernahan, J.; Ahmad, T.; Ge, Z.-Q. Lifetime measurements for low-lying levels in Hg I and Hg II using the beam-foil technique. *Can. J. Phys* **1988**, *66*, 960–962.
- (126) Denbigh, K. The polarisabilities of bonds—I. *Transactions of the Faraday Society* **1940**, *36*, 936–948.
- (127) Kumar, A.; Meath, W. J. Integrated dipole oscillator strengths and dipole properties for Ne, Ar, Kr, Xe, HF, HCl, and HBr. *Can. J. Chem* **1985**, *63*, 1616–1630.
- (128) Pinkham, D.; Vogt, T.; Jones, R. Extracting the polarizability anisotropy from the transient alignment of HBr. *J. Chem. Phys* **2008**, *129*, 064307.
- (129) Maroulis, G. Is the dipole polarizability of hydrogen iodide accurately known? *Chem. Phys. Lett* **2000**, *318*, 181–189.
- (130) Iliáš, M.; Kellö, V.; Fleig, T.; Urban, M. Electric properties of hydrogen iodide: Reexamination of correlation and relativistic effects. *Theor. Chem. Acc* **2003**, *110*, 176–184.

- (131) van Stralen, J. N.; Visscher, L.; Ogilvie, J. Theoretical and experimental evaluation of the radial function for electric dipole moment of hydrogen iodide. *Phys. Chem. Chem. Phys.* **2004**, *6*, 3779–3785.
- (132) Li, G.; Gordon, I. E.; Roy, R. J. L.; Hajigeorgiou, P. G.; Coxon, J. A.; Bernath, P. F.; Rothman, L. S. Reference spectroscopic data for hydrogen halides. Part I: Construction and validation of the ro-vibrational dipole moment functions. *J. Quant. Spectrosc. Ra* **2013**, *121*, 78–90.
- (133) Cuthbertson, C.; Cuthbertson, M. info getting lost lost in the gutter on page 219-I. On the refraction and dispersion of the halogens, halogen acids, ozone, steam, oxides of nitrogen and ammonia. *Philosophical Transactions of the Royal Society of London. Series A, Containing Papers of a Mathematical or Physical Character* **1914**, *213*, 1–26.
- (134) Swift, K.; Schlie, L.; Rathge, R. Dispersion of gases in atomic iodine lasers at 1.315 μm . *Applied optics* **1988**, *27*, 4377–4384.
- (135) Maroulis, G.; Makris, C.; Hohm, U.; Goebel, D. Electrooptical properties and molecular polarization of iodine, I_2 . *J. Phys. Chem. A* **1997**, *101*, 953–956.
- (136) Antoine, R.; Rayane, D.; Allouche, A.-R.; Aubert-Frécon, M.; Benichou, E.; Dalby, F.; Dugourd, P.; Broyer, M.; Guet, C. Static dipole polarizability of small mixed sodium–lithium clusters. *J. Chem. Phys* **1999**, *110*, 5568–5577.
- (137) Tarnovsky, V.; Bunimovicz, M.; Vušković, L.; Stumpf, B.; Bederson, B. Measurements of the dc electric dipole polarizabilities of the alkali dimer molecules, homonuclear and heteronuclear. *J. Chem. Phys* **1993**, *98*, 3894–3904.
- (138) Muentzer, J. Polarizability anisotropy of hydrogen fluoride. *J. Chem. Phys* **1972**, *56*, 5409–5412.

- (139) Bridge, N.-J.; Buckingham, A. D. The polarization of laser light scattered by gases. *Proceedings of the Royal Society of London. Series A. Mathematical and Physical Sciences* **1966**, *295*, 334–349.
- (140) Huber, K. P.; Herzberg, G. H. *NIST Chemistry WebBook, NIST Standard Reference Database Number 69*; National Institute of Standards and Technology, 2023.
- (141) Tellinghuisen, J. Least-squares analysis of overlapped bound-free absorption spectra and predissociation data in diatomics: The C ($1\Pi_u$) state of I₂. *J. Chem. Phys* **2011**, *135*, 054301.
- (142) Dreuw, A.; Head-Gordon, M. Single-Reference ab Initio Methods for the Calculation of Excited States of Large Molecules. *Chem. Rev.* **2005**, *105*, 4009–4037.
- (143) Seeger, R.; Pople, J. A. Self-consistent molecular orbital methods. XVIII. Constraints and stability in Hartree–Fock theory. *J. Chem. Phys* **1977**, *66*, 3045–3050.
- (144) Bauernschmitt, R.; Ahlrichs, R. Stability analysis for solutions of the closed shell Kohn–Sham equation. *J. Chem. Phys* **1996**, *104*, 9047–9052.
- (145) Sears, J. S.; Koerzdoerfer, T.; Zhang, C.-R.; Brédas, J.-L. Communication: Orbital instabilities and triplet states from time-dependent density functional theory and long-range corrected functionals. *J. Chem. Phys* **2011**, *135*, 151103.
- (146) Peach, M. J. G.; Williamson, M. J.; Tozer, D. J. Influence of Triplet Instabilities in TDDFT. *J. Chem. Theory Comput.* **2011**, *7*, 3578–3585.
- (147) Peach, M. J.; Warner, N.; Tozer, D. J. On the triplet instability in TDDFT. *Mol. Phys* **2013**, *111*, 1271–1274.
- (148) Lutnæs, O. B.; Helgaker, T.; Jaszuński, M. Spin–spin coupling constants and triplet instabilities in Kohn–Sham theory. *Mol. Phys* **2010**, *108*, 2579–2590.

- (149) Foresman, J. B.; Head-Gordon, M.; Pople, J. A.; Frisch, M. J. Toward a systematic molecular orbital theory for excited states. *J. Phys. Chem.* **1992**, *96*, 135–149.
- (150) Rishi, V.; Perera, A.; Bartlett, R. J. A route to improving RPA excitation energies through its connection to equation-of-motion coupled cluster theory. *J. Chem. Phys* **2020**, *153*.
- (151) Aidas, K.; Angeli, C.; Bak, K. L.; Bakken, V.; Bast, R.; Boman, L.; Christiansen, O.; Cimiraglia, R.; Coriani, S.; Dahle, P., et al. The Dalton quantum chemistry program system. *WIREs. Comput. Mol. Sci* **2014**, *4*, 269–284.
- (152) Christiansen, O.; Halkier, A.; Koch, H.; Jørgensen, P.; Helgaker, T. Integral-direct coupled cluster calculations of frequency-dependent polarizabilities, transition probabilities and excited-state properties. *J. Chem. Phys* **1998**, *108*, 2801–2816.
- (153) Ramsey, N. F. Electron coupled interactions between nuclear spins in molecules. *Phys. Rev* **1953**, *91*, 303.
- (154) Aucar, G.; Saue, T.; Visscher, L.; Jensen, H. A. On the origin and contribution of the diamagnetic term in four-component relativistic calculations of magnetic properties. *J. Chem. Phys* **1999**, *110*, 6208–6218.
- (155) Sternheim, M. M. Second-order effects of nuclear magnetic fields. *Phys. Rev* **1962**, *128*, 676.
- (156) Visscher, L. Approximate molecular relativistic Dirac-Coulomb calculations using a simple Coulombic correction. *Theor. Chem. Acc* **1997**, *98*, 68–70.
- (157) Matthews, D. A.; Cheng, L.; Harding, M. E.; Lipparini, F.; Stopkowitz, S.; Jagau, T.-C.; Szalay, P. G.; Gauss, J.; Stanton, J. F. Coupled-cluster techniques for computational chemistry: The CFOUR program package. *J. Chem. Phys* **2020**, *152*, 214108.

- (158) Kobayashi, R.; Koch, H.; Jørgen, P. Calculation of frequency-dependent polarizabilities using coupled-cluster response theory. *Chem. Phys. Lett* **1994**, *219*, 30–35.
- (159) Koch, H.; Kobayashi, R.; de Merás, A. S.; Jørgensen, P. Calculation of size-intensive transition moments from the coupled cluster singles and doubles linear response function. *J. Chem. Phys* **1994**, *100*, 4393–4400.
- (160) Sekino, H.; Bartlett, R. J. Nuclear coupling constants obtained by the equation-of-motion coupled cluster theory. *Chem. Phys. Lett* **1994**, *225*, 486–493.
- (161) Sekino, H.; Bartlett, R. J. *Advances in Quantum Chemistry*; Elsevier, 1999; pp 149–173.
- (162) Caricato, M.; Trucks, G. W.; Frisch, M. J. On the difference between the transition properties calculated with linear response- and equation of motion-CCSD approaches. *J. Chem. Phys* **2009**, *131*, 174104.
- (163) Perera, A. What made possible the accurate calculations of NMR spin–spin coupling constants? *Mol. Phys* **2010**, *108*, 3017–3025.
- (164) Nanda, K. D.; Krylov, A. I. Two-photon absorption cross sections within equation-of-motion coupled-cluster formalism using resolution-of-the-identity and Cholesky decomposition representations: Theory, implementation, and benchmarks. *J. Chem. Phys* **2015**, *142*.
- (165) Olejniczak, M.; Bast, R.; Gomes, A. S. P. On the calculation of second-order magnetic properties using subsystem approaches in a relativistic framework. *Phys. Chem. Chem. Phys* **2017**, *19*, 8400–8415.

Chapter 4

Implementation of Quadratic Response Properties based on Relativistic Equation-of-Motion Coupled Cluster Theory

Paper: Frequency-Dependent Quadratic Response Properties and Two-photon Absorption from Relativistic Equation-of-Motion Coupled Cluster Theory

I worked out the equations, implemented the code, carried out all calculations, and wrote the manuscript.

Frequency-Dependent Quadratic Response Properties and Two-photon Absorption from Relativistic Equation-of-Motion Coupled Cluster Theory

Xiang Yuan,^{†,‡} Loïc Halbert,[†] Lucas Visscher,^{*,‡} and André Severo Pereira
Gomes^{*,†}

[†]*Physique des Lasers Atomes et Molecules, Universite de Lille, F-59000 Lille, France*

[‡]*Department of Chemistry and Pharmaceutical Sciences, Faculty of Science, Vrije
Universiteit Amsterdam, 1081 HV Amsterdam, The Netherlands*

E-mail: l.visscher@vu.nl; andre.gomes@univ-lille.fr

Abstract

We present the implementation of quadratic response theory based upon the relativistic equation-of-motion coupled cluster method. We showcase our implementation, whose generality allows us to consider both time-dependent and time-independent electric and magnetic perturbations, by considering the static and frequency-dependent hyperpolarizability of hydrogen halides (HX, X = F-At), providing a comprehensive insight into their electronic response characteristics. Additionally, we evaluated the Verdet constant for noble gases Xe and Rn, and discussed the relative importance of relativistic and electron correlation effects for these magneto-optical properties. Finally, we calculate the two-photon absorption cross-sections of transition ($ns^1S_0 \rightarrow (n+1)s^1S_0$) of Ga⁺, and In⁺, which are suggested as candidates for new

ion clocks. As our implementation allows for the use of non-relativistic Hamiltonians as well, we have compared our EOM-QRCC results to the QR-CC implementation in the DALTON code, and show that the differences between CC and EOMCC response are in general smaller than 5% for the properties considered. Collectively, the results underscore the versatility of our implementation and its potential as a benchmark tool for other approximated models such as density functional theory for higher-order properties.

Introduction

Nonlinear optical properties (NLO) of matter provide a wealth of information on intra- and inter-molecular interactions and are therefore widely studied in science and engineering.¹⁻³ NLO properties are also central to materials and device design, with numerous important applications such as optical devices for data transfer and storage. Among the materials being considered, there is a growing interest in NLO properties of molecules containing heavier elements, particularly in Lanthanide⁴⁻⁹ and Actinide¹⁰⁻¹² complexes, as they can offer a superior performance compared to molecules that contain only light elements.

In order to compute and analyze molecular properties in the linear and non-linear regime, one typically resorts to response theory.¹³⁻¹⁶ Within this theory, the first-order nonlinear response is characterized by the quadratic response function. Quadratic response functions have been implemented for Hartree-Fock (HF) wave-functions^{17,18} as well as at the electron correlated level employing second-order Møller-Plesset perturbation (MP2),¹⁹ multiconfigurational self-consistent field (MCSCF),^{20,21} coupled cluster (CC),²²⁻²⁴ and density functional theory (DFT)^{25,26} reference states. The common starting point of these developments has been the non-relativistic molecular Hamiltonian.

For property calculations, the spin-orbit coupling operator can be added as one of the perturbing properties. That will provide accurate results for lighter elements, at the expense of needing to go one order higher in the responses that are considered. As we move down

the periodic table, we reach a point where relativistic effects are too strong to be reliably treated as perturbations. In this domain, it is therefore necessary to refine these methods, ensuring relativistic effects are intrinsically accounted for by employing a variationally stable relativistic Hamiltonian.

In the domain of relativistic quantum chemistry, to date, quadratic response function derivations and implementations are primarily based on mean-field models, such as HF²⁷ and DFT.²⁸ To improve precision and establish benchmarks for other models, in this manuscript we discuss the development of quadratic response theory based on a relativistic equation-of-motion (EOM)²⁹⁻³⁵ coupled cluster formulation (EOM-QRCC).

We showcase the generality and versatility of our implementation by examining two molecular properties. First, we study the frequency-(in)dependent electric first hyperpolarizability (β) as it can describe the nonlinear response of a molecule to an applied electric field, which is significant for second-harmonic generation³⁶ associated with the design of optoelectronic devices and can provide valuable insights into the intermolecular interaction.³⁷ For instance, as discussed by Datta and Pati³⁸ β is related to the weak intermolecular forces such as dipolar interactions and hydrogen-bonding, thus it is possible to control β by modifying the interactions and accurate calculations would be instrumental to provide insight into designing NLO materials like π -conjugated molecular assemblies.

We consider magnetic circular birefringence, also known as the Faraday effect, as the second property. One example of the interest in studying the Faraday effect can be found in the observation by Savukov et al.³⁹ of the inverse Faraday effect in the nuclear magnetic resonance (NMR) sample of liquid water and liquid ¹²⁹Xe, which has led to the suggestion that the nuclear spin-induced optical rotation (NSOR) can provide a viable and potentially more informative analog to the NMR chemical shift of traditional NMR detection. There have been only a handful of theoretical investigations of this property, however. For ¹²⁹Xe, Ikäläinen et al.⁴⁰ performed non-relativistic (NR) time-dependent Hartree-Fock (TDHF), time-dependent Density Functional Theory (TDDFT), coupled cluster response, and rela-

tivistic TDHF, TDDFT calculations on the Verdet constant and NSOR. In subsequent work, Cadène et al.⁴¹ investigated the Verdet constant of ^{129}Xe in both gas-phase experiments and calculations derived from non-relativistic coupled cluster quadratic response calculations (QR-CC), in which the relativistic effects were approximately accounted for by employing relativistic effective core potentials (ECPs). With our implementation, we shall complement these studies and in particular investigate the relative importance of relativistic (scalar and spin-orbit coupling) effects and electron correlation to these properties.

The characterization of Two-Photon Absorption (TPA) cross-sections, which can be related to quadratic response theory, has also gained considerable attention in different domains and is the third focus of our applications. TPA was first predicted, using perturbation theory, by Göppert-Mayer⁴² in 1931, but not observed in experiments until the advent of the lasers that are capable of delivering sufficiently high intensity. The main feature of TPA is that it occurs with a probability depending quadratically on the incident light intensity, which results in the TPA-based techniques offering better spatial resolution than those based on one-photon absorption (OPA). In materials science, materials with large TPA cross-sections enable applications including drug delivery, photodynamic therapy, high-resolution, and optical storage.⁴³ Moreover, TPA spectroscopy is also very useful as a research tool. Concerning the different selection rules of TPA compared to OPA, TPA can characterize the excited state in the spectrum in the case of OPA spectrum has been large dispersions, particularly for complex molecules containing f-elements.^{44,45}

TPA is proportional to the imaginary part of the second-order hyperpolarizability γ , which requires evaluation of the cubic response function. However, under resonant conditions, it becomes possible to express the TPA cross-sections in terms of the two-photon matrix,⁴⁶ which can be obtained from the quadratic response of the reference state wave function. With this strategy, the TPA cross-sections have been evaluated in various standard models in quantum chemistry including Hartree-Fock,²¹ MCSCF,²¹ DFT,⁴⁷⁻⁴⁹ and CC.⁵⁰⁻⁵² Moreover, in the last decades resonant inelastic X-ray Scattering (RIXS),^{53,54} a two-photon

scattering process involving core electrons, received considerable attention because of the corresponding improvements in sensitivity and energy resolution,^{55–58} which provides valuable information on the electronic structure of both occupied and virtual states that are not easily accessible by the traditional spectroscopies. Several approaches aimed at the description of RIXS spectra for molecular systems based on non-relativistic or approximate relativistic Hamiltonians have been proposed including algebraic diagrammatic construction (ADC),⁵⁹ MCSCF,⁶⁰ DFT,⁶¹ and EOM-CC.^{62–67} However, in the relativistic quantum chemistry field, the implementations of TPA cross-sections are still scarce, owing to the additional complexity of handling spin-orbit effects. An implementation in the DIRAC program by Henriksson et al.⁶⁸ enabled pioneering calculations of TPA cross-sections from the four-component Hartree-Fock quadratic response theory. In this manuscript, we will focus on TPA for valence processes and will investigate processes involving core electrons such as RIXS in a subsequent publication.

Finally, we pay attention to methods that can lower computational costs. This is of practical importance here since we utilize uncontracted basis sets with adding many diffuse functions, which generate a large virtual orbital space in CC calculations. The simplest and most often used method is the utilization of the MP2 frozen natural orbitals (FNOs).^{69–71} While some authors have pointed out the shortcomings of MP2FNOs for the calculation of linear response properties,^{71,72} Surjuse et al.⁷³ recently suggested using MP2FNOs in EOM-CC calculations can bring about reduce computational cost while retaining sufficient accuracy for ionization energies. On the other hand, to the best of our knowledge, there is no reference yet reporting the performance of MP2FNOs on TPA calculations.

This manuscript is organized as follows: In Sec. 2, the EOM-CC quadratic response theory and the corresponding two-photon absorption matrix formulation are summarized. Section 3 is devoted to the details of the computations we used to test the implementation. The calculations are presented and discussed in Secs. 4. Finally, a brief summary of our findings is given in Sec. 5.

Theory

We base the theory on the time-averaged quasi-energy formalism, which has been summarized in the landmark paper by Christiansen et al.¹³. As the significant part of the formalism to obtain the quadratic response functions is common to that of linear response functions, and we have recently provided an extensive discussion of the implementation details for linear response properties,⁷⁴ in the current manuscript, we only focus on the equations related to quadratic response.

The CC quadratic response function is expressed below:

$$\begin{aligned} \langle\langle X; Y, Z \rangle\rangle_{\omega_Y, \omega_Z} = & \frac{1}{2} C^\omega P^{X,Y,Z} \\ & \left[\left[\frac{1}{2} \mathbf{F}^X + \frac{1}{6} \mathbf{G} \mathbf{t}^X(\omega_X) \right] \mathbf{t}^Y(\omega_Y) \right. \\ & \left. + \bar{\mathbf{t}}^X(\omega_X) \left[\mathbf{A}^Y + \frac{1}{2} \mathbf{B} \mathbf{t}^Y(\omega_Y) \right] \right] \mathbf{t}^Z(\omega_Z) \end{aligned} \quad (1)$$

in which the wave function is parametrized by the CC amplitudes \mathbf{t} and $P^{X,Y,Z}$ is a permutation operator interchanging the perturbations X, Y, and Z. The tensors appearing in this equation are defined in Table 1, with their dimensions determined by the number of excitations considered in the model (in this work CCSD, so single and double excitations relative to the reference state). These definitions are consistent with the ones given by Christiansen et al.¹³, the main difference is that in our case these tensors require use of complex algebra whereas in non-relativistic implementations it is typically assumed that matrix representations are either real or fully imaginary. This difference is caused by the intrinsic inclusion of spin-orbit coupling effects.

Table 1: Tensors required for the CC quadratic response function^a

$\boldsymbol{\eta}^Y$	$\langle \Lambda [Y, \hat{\tau}_\mu] \text{CC} \rangle$
$\boldsymbol{\xi}^Y$	$\langle \bar{\mu} Y \text{CC} \rangle$
\mathbf{F}	$\langle \Lambda [[H_0, \hat{\tau}_\mu], \hat{\tau}_\nu] \text{CC} \rangle$
\mathbf{F}^Y	$\langle \Lambda [[Y, \hat{\tau}_\mu], \hat{\tau}_\nu] \text{CC} \rangle$
\mathbf{G}	$\langle \Lambda [[[H_0, \hat{\tau}_\mu], \hat{\tau}_\nu], \hat{\tau}_\sigma] \text{CC} \rangle$
\mathbf{B}	$\langle \bar{\mu} [[H_0, \hat{\tau}_\nu], \hat{\tau}_\sigma] \text{CC} \rangle$
\mathbf{A}^Y	$\langle \bar{\mu} [Y, \hat{\tau}_\mu] \text{CC} \rangle$

^a $|CC\rangle = e^{T_0} |R\rangle$ denote the regular CC reference wavefunction, and $|R\rangle$ is the reference state for the CC parametrization such as Hartree-Fock state. $\langle \Lambda | = \langle R | + \sum_\mu \bar{t}_\mu^0 \langle \bar{\mu} |$. $\langle \bar{\mu} | = \langle R | \hat{\tau}_\mu^\dagger e^{-T_0} \equiv \langle \mu | e^{-T_0}$, where $\hat{\tau}_\mu^\dagger$ is the deexcitation operator, which is biorthogonal to excitation operator $\hat{\tau}_\mu$, satisfying $\langle R | \hat{\tau}_\mu^\dagger \hat{\tau}_\nu | R \rangle = \delta_{\mu\nu}$. μ, ν and σ indicate excited Slater determinants (comprising single and double excitations for the CCSD model).

In CC theory, the similarity transformed Hamiltonian, $\bar{H} = e^{-\hat{T}} \hat{H} e^{\hat{T}}$, plays an important role in obtaining the amplitudes and their responses to external perturbations. Since \bar{H} and its matrix representation $\bar{\mathbf{H}}$ are not Hermitian, the left response amplitudes are not just the complex conjugate of their right counterparts. According to the 2n+1 and 2n+2 rules in perturbation theory,¹³ for obtaining the quadratic response, it is necessary to solve both the left and right first-order response equations, given respectively by:

$$(\bar{\mathbf{H}} - \omega_X \mathbf{I}) \mathbf{t}^X = -\boldsymbol{\xi}^X \quad (2)$$

and

$$\bar{\mathbf{t}}^X (\bar{\mathbf{H}} + \omega_X \mathbf{I}) = -\boldsymbol{\eta}^X - \mathbf{F} \mathbf{t}^X \quad (3)$$

Within the EOM-CC approximation, the quadratic response function is expressed below:^{62,75,76}

$$\begin{aligned}
{}^{EOM}\langle\langle X; Y, Z \rangle\rangle_{\omega_Y, \omega_Z} &= \frac{1}{2} C^\omega P^{X, Y, Z} \\
&[-{}^{EOM}\bar{\mathbf{t}}^X(\omega_X) \mathbf{t}^Y(\omega_Y) \bar{\mathbf{t}}^0 \boldsymbol{\xi}^Z \\
&+ {}^{EOM}\bar{\mathbf{t}}^X(\omega_X) {}^{EOM}\mathbf{A}^Y \mathbf{t}^Z(\omega_Z) \\
&- \bar{\mathbf{t}}^0 \mathbf{t}^Y(\omega_Y) {}^{EOM}\bar{\mathbf{t}}^Z(\omega_Z) \boldsymbol{\xi}^X]
\end{aligned} \tag{4}$$

where $\bar{\mathbf{t}}^0$ indicates the zeroth-order multipliers, which can be obtained by solving the ground state Lambda equations,⁷⁷ and ${}^{EOM}\mathbf{A}^X$ is the EOM-CC property Jacobian matrix

$${}^{EOM}\mathbf{A}_{\mu\nu}^X = \langle \mu | \left[\bar{X}, |\nu\rangle \langle HF| \right] | HF \rangle \tag{5}$$

$$\bar{X} = e^{-\hat{T}} \hat{X} e^{\hat{T}} \tag{6}$$

The EOM-CC response is known to have an identical right response equation, as indicated in equation 2, when compared to linear response theory. On the other hand, EOM-CC left response equation is different from equation 3 due to an approximation of the \mathbf{F} matrix leading to the expression:

$${}^{EOM}\bar{\mathbf{t}}^X(\bar{\mathbf{H}} + \omega_X \mathbf{I}) = -\boldsymbol{\eta}^X - \bar{\mathbf{t}}_D^0 \boldsymbol{\xi}_S^X + (\bar{\mathbf{t}}^0 \boldsymbol{\xi}^X) \bar{\mathbf{t}}^0. \tag{7}$$

The detailed working equations for the matrix elements of the different terms in Eqs. 2 and 7 are given in our previous linear response work,⁷⁴ including those for $\boldsymbol{\sigma}$ vectors (the products $\bar{\mathbf{H}}\mathbf{t}^X$ and $\bar{\mathbf{t}}^X\bar{\mathbf{H}}$) and property gradients $\boldsymbol{\xi}^X$. The working equations for new terms appearing in the quadratic response functions, such as the ${}^{EOM}\mathbf{A}^X$ matrix are presented in the supplementary information.

To define a two-photon absorption cross-section, we first consider the sum-over states expression for the two-photon transition matrix elements between the reference state $|0\rangle$ and

the target excited state $|f\rangle$:¹

$$T_{XY}^{f0}(\omega) = \sum_n \left[\frac{\langle f | \hat{X} | n \rangle \langle n | \hat{Y} | 0 \rangle}{\omega_n - (\omega + i\gamma)} + \frac{\langle f | \hat{Y} | n \rangle \langle n | \hat{X} | 0 \rangle}{\omega_n - (\omega' + i\gamma)} \right] \quad (8)$$

where γ is the damping factor representing the inverse lifetime. The frequencies ω and ω' represent the two external photons, while ω_f corresponds to the excitation energy between reference state $|0\rangle$ and the final excited state $|f\rangle$. For TPA the relation:

$$\omega + \omega' - \omega_f = 0 \quad (9)$$

should be satisfied which means that for a given final state there is only one independent variable, whether for the most commonly studied case¹ of $\omega' = \omega = \omega_f/2$ or for cases in which $\omega' \neq \omega$ such as in resonant inelastic X-Ray scattering (RIXS).^{59,62} Within a response formulation, the EOM-CC right and left frequency-dependent transition moments are written as⁶²

$$\begin{aligned} \mathbf{Right:} \quad {}^{EOM}T_{XY}^{f0}(\omega) = & -\mathbf{L}_f [{}^{EOM}\mathbf{A}^X \mathbf{t}^Y(\omega + i\gamma) + {}^{EOM}\mathbf{A}^Y \mathbf{t}^X(\omega' - i\gamma) \\ & - (\bar{\mathbf{t}}_0 \boldsymbol{\xi}^X) \mathbf{t}^Y(\omega + i\gamma) - (\bar{\mathbf{t}}_0 \boldsymbol{\xi}^Y) \mathbf{t}^X(\omega' - i\gamma) \\ & - (\bar{\mathbf{t}}_0 \mathbf{t}^Y(\omega + i\gamma)) \boldsymbol{\xi}^X - (\bar{\mathbf{t}}_0 \mathbf{t}^X(\omega' - i\gamma))] \end{aligned} \quad (10)$$

$$\begin{aligned} \mathbf{Left:} \quad {}^{EOM}T_{XY}^{0f}(\omega) = & -[{}^{EOM}\bar{\mathbf{t}}^X(-\omega' - i\gamma) {}^{EOM}\mathbf{A}^Y + {}^{EOM}\bar{\mathbf{t}}^Y(-\omega + i\gamma) {}^{EOM}\mathbf{A}^X \\ & - (\bar{\mathbf{t}}_0 \boldsymbol{\xi}^X) {}^{EOM}\bar{\mathbf{t}}^Y(-\omega + i\gamma) - (\bar{\mathbf{t}}_0 \boldsymbol{\xi}^Y) {}^{EOM}\bar{\mathbf{t}}^X(-\omega' - i\gamma)] \mathbf{R}_f \\ & + (\bar{\mathbf{t}}_0 \mathbf{R}_f) [{}^{EOM}\bar{\mathbf{t}}^Y(-\omega + i\gamma) \boldsymbol{\xi}^X + {}^{EOM}\bar{\mathbf{t}}(-\omega' - i\gamma) \boldsymbol{\xi}^Y] \end{aligned} \quad (11)$$

where \mathbf{R}_f and \mathbf{L}_f are right and left target excited states, respectively, obtained by solving

¹Note that in these references the frequencies of the absorbed and emitted photon are both defined as positive, while we define the frequencies of absorbed photons as positive and also take the frequency ω_f corresponding to the excitation energy as positive. Scattering can in our implementation be studied by defining ω' as negative in the input.

EOM excitation energy (EOM-EE) equations:

$$\bar{\mathbf{H}}\mathbf{R}_f = E_f\mathbf{R}_f \quad (12)$$

$$\mathbf{L}_f\bar{\mathbf{H}} = \mathbf{L}_fE_f \quad (13)$$

where the operators \hat{R}^f and \hat{L}^f are given by in terms of the electron-creation (a_a^\dagger and a_b^\dagger) and electron-annihilation operators (a_i and a_j)

$$\hat{R}^f = r_0 + \sum_{ia} r_i^a a_a^\dagger a_i + \sum_{i>j,a>b} r_{ij}^{ab} a_a^\dagger a_b^\dagger a_i a_j \quad (14)$$

$$\hat{L}^f = l_0 + \sum_{ia} l_a^i a_i^\dagger a_a + \sum_{i>j,a>b} l_{ab}^{ij} a_i^\dagger a_j^\dagger a_a a_b \quad (15)$$

With these left and right transition moments available, the total scattering amplitudes can then be evaluated by the equation:^{13,62}

$$S_{XY,ZU} = T_{XY}^{0f}(\omega)T_{ZU}^{f0}(\omega) = \frac{1}{2}[T_{XY}^{0f}(\omega)T_{ZU}^{f0}(\omega) + (T_{ZU}^{0f}(\omega)T_{XY}^{f0}(\omega))^*] \quad (16)$$

Finally, the TPA cross-section, δ_{TPA} , is determined by the components of scattering amplitudes matrix \mathbf{S} :⁷⁸

$$\delta_{TPA} = \frac{1}{15}\{F \sum_{X,Y} S_{XX,YY} + G \sum_{X,Y} S_{XY,XY} + H \sum_{X,Y} S_{XY,YX}\} \quad (17)$$

The constants F , G , and H depend on the polarization of the incident light. In this work, $F = G = H = 1$ is selected to represent parallel linearly polarized light. Moreover, we set up the frequency of the external field as half of the excitation energy of the target state ($\omega' = \omega = \omega_f/2$).

Computational details

All EOM-CC quadratic response and two-photon absorption calculations were carried out with development versions (see revision number in SI) of the DIRAC code,^{79,80} employing the uncontracted triply-augmented valence triple zeta Dyall basis set (defined as t-aug-dyall.v3z in inputs) for heavy elements (In, I, At, Xe, Rn),^{81,82} and an equivalent triply-augmented uncontracted Dunning basis set (defined as t-aug-cc-pVTZ in inputs) for light elements (H, F, Cl, Ga, Br).⁸³⁻⁸⁵ We utilized the exact two-component (X2C)⁸⁶ relativistic Hamiltonian, and in some cases, to show the effect of relativity explicitly, we also provide results using the non-relativistic Hamiltonian^{87,88} (as activated by the `.Levy-Leblond` keyword). To study the effect of electron correlation, we performed quadratic-response and two-photon absorption calculations based on mean-field methods such as Hartree-Fock (HF) and density-functional theory (employing the B3LYP⁸⁹ density functional approximation). The relativistic and non-relativistic calculations have been carried out with the Gaussian type⁹⁰ and point charge nucleus model, respectively.

In what follows, we shall use the term orbital as shorthand for both spinors and spin-orbitals, depending on the Hamiltonian used in the calculation.

In our calculations for heavy elements (HI, HAt, Xe, and Rn), we have profited from the components of an ongoing implementation in ExaCorr of the Cholesky-decomposition approach⁹¹⁻⁹³ to reduce the memory footprint of our calculations in the step to transform two-electron integrals from AO to MO basis, with thresholds of 10^{-9} (Xe and Rn), and 10^{-4} (HI and HAt), the latter is looser than the one employed in our previous work; we have carried out benchmark calculations on selected systems to verify this change did not significantly alter our results.

The molecular structures employed in all calculations have been taken from the literature: from Huber⁹⁴ for HX (X=F, Cl, Br, I), and from Gomes and Visscher⁹⁵ for HAt. The internuclear distances employed are thus H-F (0.91680 Å), H-Cl (1.27455 Å), H-Br (1.41443 Å), H-I (1.60916 Å), and H-At (1.722 Å).

In the calculations, the size of the correlated virtual spaces in the coupled cluster is truncated by discarding orbitals with energies above 5 a.u. For the occupied orbitals, we correlate only valence electrons.

Results and discussion

First hyperpolarizability of HX(X=F, Cl, Br, I, At)

To demonstrate our implementation we first apply it to calculate the parallel component of the static first hyperpolarizability (β_{\parallel})³⁷ of the hydrogen halide molecules.

$$\beta_{\parallel} = \frac{1}{5} \sum_{i=x,y,z} (\beta_{iiz} + \beta_{izi} + \beta_{zii}) \quad (18)$$

Each component is defined by the equation:¹⁶

$$\beta_{ijk}(-\omega_{\sigma}; \omega_1, \omega_2) = \sum P_{-\sigma,1,2} \sum_{n,m} \frac{\langle 0 | \hat{\mu}_i | n \rangle \langle n | \hat{\mu}_j | m \rangle \langle m | \hat{\mu}_k | 0 \rangle}{(\omega_{n0} - \omega_{\sigma})(\omega_{m0} - \omega_2)} \quad (19)$$

where $\hat{\mu}_i$ are Cartesian components of the electric dipole operators, and $\sum P_{-\sigma,1,2}$ indicates the sum of six terms by permuting the pairs $(i, -\omega_{\sigma})$, (j, ω_1) , (k, ω_2) .

Before proceeding with the calculation, it is crucial to select an appropriate basis set and establish the correlation space. Our study evaluates the impact of the basis set and correlation space on the hyperpolarizability of HF molecules. The results are presented in Table 2 where they are compared with results from the DALTON program^{23,96} and experimental data.

An analysis of the first three rows reveals that both diffuse functions and polarization functions significantly influence the calculation of hyperpolarizability, as is well-known in the literature.^{23,97} For example, when utilizing the doubly-augmented d-aug-cc-pVDZ basis set, the result is only 58% of the value obtained with the augmented s-aug-cc-pVDZ basis set.

Conversely, the effect of the correlation space is relatively minor. By comparing the results of the third and fourth rows, it is evident that correlating all virtual orbitals enhances the value by merely around 1%.

In the fourth row, we observe that our calculation, when using the non-relativistic Hamiltonian, matches the DALTON value (-7.3385 a.u.) precisely and this serves as a validation of our implementation. Furthermore, based on the DALTON results, the disparity between EOM-QRCC and QR-CC is approximately 4.5%. This deviation stems from the absence of size extensivity in the transition moments of the EOM model. This inconsistency between EOM and CC was previously highlighted in research on linear response properties (see Yuan et al.⁷⁴ and references therein), and we plan to delve deeper into this topic by studying a wider array of molecules for both linear and quadratic response properties in follow-up work.

To compare with experimental data we need to account for the fact that the available value (-10.88±0.95 a.u.) concerns a value measured for a frequency corresponding to 0.0656 a.u. rather than to the static limit. Taking this into account increases $\beta_{||}$ by almost 1 a.u. to -8.79 a.u. which is still outside the experimental error bar. Beyond the limitations of the basis set, which could still be further improved, also vibrational effects will contribute to this observed discrepancy. These effects can amount to -1.24 a.u. as discussed by Hansen et al.⁹⁸ who treated these with the vibrational configuration interaction method.

Comparison between the fourth, fifth, and sixth rows of the QR-CC calculations reveals that adding more diffuse functions (from d-aug-cc-pVTZ to t-aug-cc-pVTZ) improves accuracy more significantly than incorporating additional polarization functions (from d-aug-cc-pVTZ to d-aug-cc-pVQZ). Given that the QZ calculations are notably more resource-intensive than TZ ones, we will employ the t-aug-cc-pVTZ basis set for the subsequent calculations on heavier elements.

Table 2: Benchmark of basis sets and correlation virtual orbital space for QR-CC calculations of the static $\beta_{||}$ (a.u.) of the HF molecule

Basis	NR-EOM	NR-EOM ^a	NR-QR-CC ^a	Exp ⁹⁹
s-aug-ccpVDZ ^b	-9.4232			
d-aug-ccpVDZ ^b	-5.5463			
d-aug-ccpVTZ ^b	-7.2677			
d-aug-ccpVTZ ^c	-7.3385	-7.3385	-7.6718	
d-aug-ccpVQZ ^{c,d}			-8.5816	
t-aug-ccpVTZ ^{c,d}			-8.7930	
				-10.88±0.95 ^d

^a Calculations were performed using the DALTON program

^b Truncating the virtual orbital space at 5 a.u.

^c Correlating all virtual orbitals

^d $\beta_{||}$ at frequency of 0.0656 a.u.

In Table 3, the static hyperpolarizability of hydrogen halides molecules (from F to At) is displayed, in which we show the Hartree-Fock, B3LYP, and EOM-CC results for both the non-relativistic and the X2C Hamiltonian.

At Hartree-Fock level, β_{zxx} , β_{zzz} , and $\beta_{||}$ all generally exhibit an upward trend from HF to HAt in both relativistic and non-relativistic calculations. This pattern is also discernible in the correlated calculations, though the exact values vary slightly. Both CC and B3LYP results indicate that electron correlation tends to decrease the value of β_{zxx} for all species on the series. Nevertheless, for the β_{zzz} , CC results indicate an increase in value due to electron correlation for all molecules except HF, whereas B3LYP shows the opposite pattern. This divergence between CC and B3LYP leads to discrepancies in the final $\beta_{||}$ value. For the heavier molecules, B3LYP values deviate considerably from both the Hartree-Fock and the CC ones.

Accounting for relativistic effects is, as expected, absolutely essential for systems containing heavier elements. For instance, both Hartree-Fock and CC models reveal that for HAt, the non-relativistic outcomes are approximately half of their relativistic counterparts. With the exception of HF, all three models consistently suggest that relativistic effects increase the $\beta_{||}$ values for all molecules. Furthermore, the effects of relativity on β_{zxx} are much larger

than that of β_{zzz} .

To understand the different magnitude of relativistic correction for β_{zxx} and β_{zzz} , we can look at equation 19. Through spin-orbit coupling (SOC), relativity modifies the response function by shifting the location of the poles of the response functions and by introducing additional transition channels. Without SOC, the ground state is in all cases of pure $^1\Sigma_0^+$ symmetry. When introducing SOC, the $^1\Sigma$ designation is no longer strictly valid, and allowed transitions are only characterized by the remaining quantum numbers, thereby yielding $0^+ \rightarrow 0^+$, and $0^+ \rightarrow 1$ transitions. The former is evidently connected to the z -component of the transition dipole moment, while the latter corresponds to the x and y -components. Specifically, the β_{zzz} component only permits contributions from transitions to 0^+ states, originating from $^3\Pi_{0+}$, and $^3\Sigma_{0+}$ states. On the other hand, for the β_{zxx} component, transitions to the 1 state, potentially emerging from $^3\Pi_1$, $^3\Sigma_1$ and $^1\Pi_1$ states, are also allowed, with an enhanced contribution from the singlet states $^1\Pi$.

Table 3: Static hyperpolarizability (a.u.) of hydrogen halides HX(X=F, Cl, Br, I, At)

	HF ^a	HF ^b	B3LYP ^a	B3LYP ^b	CC ^a	CC ^b
	β_{zxx}					
HF	-0.5091	-0.5100	-1.4916	-1.5565	-1.5276	-1.5286
HCl	2.3017	2.3672	-0.1127	0.0117	-0.0858	-0.0157
HBr	5.2994	5.9155	2.8120	3.8513	2.6604	3.4213
HI	10.7728	13.6493	4.8719	10.2006	6.7316	9.8900
HAt	16.0854	38.3140	8.7719	42.5584	11.1347	32.2297
	β_{zzz}					
HF	-8.3950	-8.4157	-9.8253	-9.8476	-9.4973	-9.4983
HCl	-11.4505	-11.4435	-13.1441	-13.0321	-10.2439	-10.1522
HBr	-11.0481	-11.1427	-11.4062	-10.8785	-6.4784	-5.9790
HI	-2.9448	-3.9634	-6.0444	-5.3245	5.1093	4.9752
HAt	5.3664	5.5476	1.3711	5.2236	16.9624	11.4539
	$\beta_{ }$					
HF	-5.6479	-5.6614	-7.6852	-7.7763	-7.5315	-7.5333
HCl	-4.1082	-4.0255	-8.0218	-7.8052	-6.2493	-6.1101
HBr	-0.2696	0.4130	-3.4693	-1.9055	-0.6946	0.5181
HI	11.1606	14.0011	2.2196	9.0460	11.1434	14.8531
HAt	22.5224	49.3054	11.3490	54.2043	23.5391	45.5480

^a non-relativistic calculation using the Levy-Leblond Hamiltonian

^b Relativistic calculation using the X2C Hamiltonian

We now turn to the frequency-dependence of the hyperpolarizability, focusing on the impacts of relativistic and electron correlation effects. Using both CC and Hartree-Fock methods, we assess the hyperpolarizability of the single-frequency optical processes -the second harmonic generation (SHG) of HI, in which we have $\omega_\sigma = 2\omega_1 = 2\omega_2 = 2\omega$. Figure 1 displays the result of frequency ranging from 0.0 to 0.115 a.u. To further interpret these curves, we also calculate the excitation energy for the lowest five electronic states by diagonalizing $\bar{\mathbf{H}}$. These results are summarized in Table 4.

Overall the dispersion curves for CC and HF are qualitatively similar for both non-relativistic and relativistic calculations, though the values for CC values are larger than the HF ones, which is due to larger excitation energy of the lowest lying dipole allowed states, that can be observed in Table 4.

One can clearly find singularities in the relativistic results, located at 0.0958 a.u for HF,

and located at 0.1000 a.u. for CC. According to equation 19, in SHG, a singularity should appear twice on the curve: the first pole corresponds to half of the excitation energy, while the second aligns with the full excitation energy. Observing this pattern, we pinpoint the singularities in our curves to the first pole associated with the $a^3\Pi_{0+}$ state (with excitation energies for HF and CC being 0.1916 a.u. and 0.2001 a.u., respectively).

In the absence of SOC, the transition to $a^3\Pi_{0+}$ is spin-forbidden. This observation aligns with the singularities appearing exclusively in the relativistic calculations. On the other hand, the pole related to the transition to $a^3\Pi_1$, is not observed, despite its permissibility with SOC. This is attributed to our focus on the β_{zxx} and β_{zzz} components. One can find that in equation 19, the transition dipole moment $\langle 0 | \hat{\mu}_z | n \rangle$ is zero for all $|n\rangle=|1\rangle$ states.

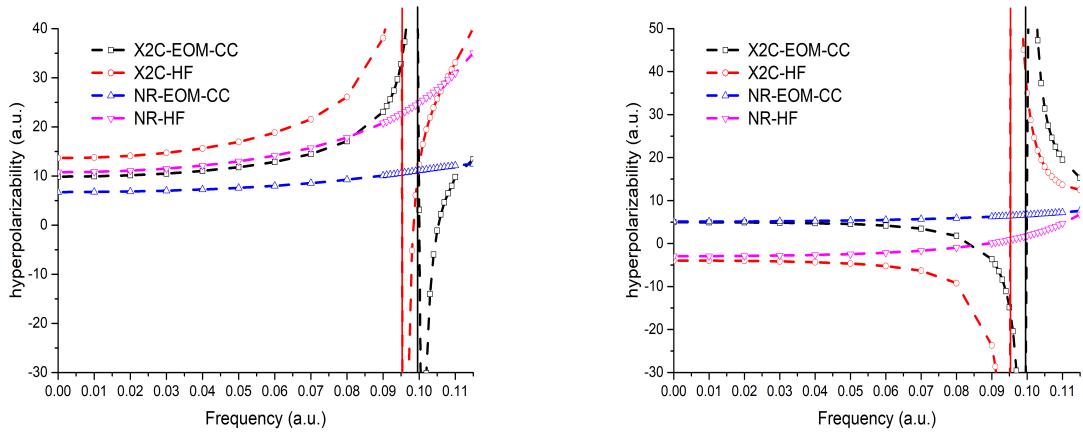


Figure 1: Frequency-dependent hyperpolarizability of HI (Left: β_{zxx} , Right: β_{zzz}). The red and black vertical lines are half of the excitation energy of $a^3\Pi_{0+}$ state for HF(0.0958 a.u.) and EOM-CC (0.1001 a.u.), respectively.

Table 4: Excitation energy (a.u.) of HI for the lowest five states

State	X2C-EOM-CC	X2C-HF	NR-EOM-CC	NR-HF
$a^3\Pi_2$	0.1773	0.1670	0.1894	0.1775
$a^3\Pi_1$	0.1831	0.1743	0.1894	0.1775
$a^3\Pi_{0-}$	0.1979	0.1861	0.1894	0.1775
$a^3\Pi_{0+}$	0.2001	0.1916	0.1894	0.1775
$A^1\Pi_1$	0.2108	0.2120	0.2111	0.2189

Verdet constant of Xe and Rn

In the current section, we show a calculation of the Verdet constant as an illustrative example of the use of our implementation for a mixed electric-magnetic property. The Verdet constant is evaluated with the following frequency-dependent quadratic response function:^{27,100}

$$V(\omega) = \omega \frac{eN\epsilon_{xyz}}{24c_0\epsilon_0m_e} \text{Im}\langle\langle\hat{\mu}_x; \hat{\mu}_y, \hat{m}_z\rangle\rangle_{\omega,0} \quad (20)$$

with N the number density of the gas, e the elementary charge, m_e the electron mass, c_0 the speed of light in vacuo, and \hat{m}_z is magnetic dipole moment operator.

We calculate the Verdet constant at three different laser wavelengths (589 nm, 694.3 nm, and 1064 nm) for Xe and Rn and list the results in Table 5. For Xe, compared to the experiment, the HF value shows sizeable relative errors of about 10%. The relativistic effect increases the value and reduces the error to 5% at the HF level. It is evident that the scalar relativistic results (with the SFDC Hamiltonian) closely align with the NR-HF values, but deviate significantly from the DC and X2C results. One can note the scalar relativistic effects decrease the Verdet constant value while SOC moves the results in the opposite direction, but more strongly. This suggests that a major portion of the relativistic correction originates from the spin-orbit coupling, and considering only scalar relativistic effects may lead to an underestimation of results. Additionally, upon investigating the influence of the Gaunt interaction, we determine it to further increase the value of the Verdet constant, but much more modestly (0.5%).

The effect of electron correlation is also to increase the Verdet constant, but the higher the degree of electron correlation recovered, the less important the increase. If we compare the DALTON NR-CCSD results obtained with a truncated correlation in space with those in which all occupied and virtual orbitals are included in the calculation, we observe a 2% difference, with the latter calculation showing smaller values. On the other hand, com-

paring CCSD and CC3¹⁰¹ results with the truncated correlation space, we observe a small increase in the Verdet constant for CC3. Relative to the QR-CC results, our non-relativistic EOM calculation seems to overestimate the correlation effect by about 1%, due to the non-extensivity issue discussed for the hyperpolarizabilities (and in ref⁷⁴). Even though this overestimation causes the X2C-EOM value to be significantly larger than experimental results, we anticipate that, given the downward trend in the QR-CC results upon improving the correlation space discussed above (approximately -0.08 (10^{-3} rad/(T m)) at the 1064 nm wavelength), the X2C-EOM value with a complete orbital space are expected to come closer to the experimental values.

When we examine the Rn, we find the relativistic effect to be substantial for both HF and CC. For example, at wavelength 589 nm, the non-relativistic EOM value is 18.90 (10^{-3} rad/(T m)), but the relativistic EOM value is 25.91 (10^{-3} rad/(T m)). Even in the absence of experimental data for reference, such a pronounced correction underscores the importance of accounting for relativistic effects. Beyond this amplified relativistic effect, other observations for Rn align with those for Xe. This includes the dominance of the relativistic effect by spin-orbit coupling, the marginal influence of the Gaunt interaction, and a comparable magnitude of difference between EOM and QR-CC.

It is also worth noting, as reported in the supplementary material of Ref,⁴⁰ that the performance of B3LYP is somewhat poor. It tends to overestimate the values in both non-relativistic and relativistic calculations, with errors approaching 18% for Xe compared to the experiment.

Table 5: Verdet Constant $V(\omega)$ [in 10^{-3} rad/(T m)] for Gaseous Xe and Rn at Different Laser Wavelengths

Method	$\lambda(589 \text{ nm})$	$\lambda(694.3 \text{ nm})$	$\lambda(1064 \text{ nm})$
Xe			
NR-HF	11.18	7.88	3.26
SFDC-HF ^d	11.12	7.83	3.24
X2C-HF	11.61	8.17	3.37
DC-HF ^b	11.61	8.17	3.37
DCG-HF ^c	11.66	8.20	3.39
NR-B3LYP	13.62	9.56	3.93
X2C-B3LYP	14.60	10.21	4.18
NR-EOM	12.55	8.83	3.65
X2C-EOM	13.10	9.21	3.79
NR-CCSD ^a	12.39	8.72	3.60
NR-CCSD ^{a*}	12.11	8.53	3.52
NR-CC3 ^a	12.46	8.77	3.62
Exp	12.30 ^e		3.56 \pm 0.10 ^f
Rn			
NR-HF	16.80	11.80	4.86
SFDC-HF ^d	16.56	11.60	4.76
X2C-HF	23.13	16.02	6.48
DC-HF ^b	23.14	16.03	6.48
DCG-HF ^c	23.25	16.10	6.51
NR-B3LYP	20.08	14.04	5.74
X2C-B3LYP	30.38	20.83	8.31
NR-EOM	18.90	13.26	5.44
X2C-EOM	25.91	17.92	7.22
NR-CCSD ^a	18.65	13.08	5.37

^a Calculations were performed using the DALTON program

* Include all occupied and virtual orbitals

^b Dirac-Coulomb Hamiltonian¹⁰²

^c Dirac-Coulomb plus Gaunt interaction Hamiltonian

^d Dirac-Coulomb without spin-orbit coupling Hamiltonian¹⁰³

^e Reference¹⁰⁴

^f Reference⁴¹

Two-photon absorption cross-sections

Finally, we consider the two-photon absorption cross-sections. As a showcase for our implementation, we highlight the two-photon transitions for group IIIB divalent ions, namely Ga^+ and In^+ . Such systems have been discussed in the literature^{105,106} for their potential use

as an atomic clock. As an initial step in this exploration, we focus on spin-allowed transitions, allowing for comparative analyses with other non-relativistic programs. We intend to address spin-forbidden transitions in subsequent work.

In Table 6, we calculate the TPA cross-sections and the corresponding excitation energy of the target states for Ga^+ , and In^+ by HF and CC. Both methods indicate that relativistic effects reduce TPA cross-sections. Notably for In^+ , the X2C value is roughly 60% of its non-relativistic counterpart. When comparing HF and CC, we find that electron correlation further diminishes the TPA cross-sections. For Ga^+ , the electron correlation effect is slightly larger than that of relativity, whereas, in the case of In^+ , relativistic effects show larger contributions to the final TPA cross-sections than electron correlation.

The observed trend, wherein both electron correlation and relativistic effects reduce the TPA, can be understood by examining their effect on the excitation energies. We find that both factors increase the excitation energy of the target state ($(4s5s)^1S_0$ for Ga^+ , $(5s6s)^1S_0$ for In^+) and from equation 8, a higher excitation energy in the denominator usually results in a smaller transition amplitude.

In non-relativistic calculations, our EOM results closely match the TPA results derived from QR-CC in DALTON, with only about a 3% discrepancy, in line with the discrepancies observed for the hyperpolarizabilities.

Table 6: Two-photon absorption cross-sections δ (a.u.) and excitation energy (a.u.) of the target states for Ga^+ , and In^+

Systems(transitions)	NR-HF	X2C-HF	DC-HF	NR-EOM ^a	X2C-EOM ^a	NR-CC ^b
Two-photon absorption cross-sections						
$\text{Ga}^+(4s-5s)$	3211.01	2710.27	2704.53	2535.17	2128.33	2455.97
$\text{In}^+(5s-6s)$	7964.78	4851.59	4831.34	6203.59	3745.02	6022.11
Excitation energy						
$\text{Ga}^+(4s-5s)$	0.4382	0.4472	0.4473	0.4718	0.4812	0.4718
$\text{In}^+(5s-6s)$	0.3760	0.3983	0.3986	0.4042	0.4269	0.4042

^a Correlate both (n-1)d and (n)s shell of total 12 electrons

^b Calculations were performed using the DALTON program

We test MP2FNO-based EOM-CC energy and TPA for Ga^+ and display the results in

Table 7. The relativistic MP2FNOs are generated based upon our previous implementation in DIRAC.¹⁰⁷ From the first three columns, it becomes apparent that when using standard selection schemes, we cannot achieve reasonable TPA values in comparison to the original canonical orbital results, even with a threshold of $1.0d^{-6}$ for the occupation number where we retrieve more than 99.99% correlation energy for the ground state. We find the excitation energy of the TPA target state $(4s5s)^1S_0$ is markedly overestimated in FNO calculations, especially when using threshold of $1.0d^{-4}$ and $1.0d^{-5}$.

At the MP2 level, the 5s orbital has a small contribution to the correlation energy in the ground state. As a result, when we obtain the MP2 density matrix and natural orbitals, the occupation numbers for natural orbitals primarily influenced by 5s orbitals are exceedingly small. These orbitals are therefore omitted by the selection scheme based purely on the threshold of occupation numbers. But while the 5s orbital is not particularly important for the ground state, it plays a significant role in the excited state under consideration.

Recognizing this, we've adjusted the selection scheme in the MP2FNO implementation. Besides selecting natural orbitals with occupation numbers exceeding the threshold, we also incorporate all doubly-degenerate orbitals with occupation numbers below the threshold (in atomic systems, that corresponds to $s_{1/2}$ and $p_{1/2}$ orbitals). We provide a more in-depth discussion on this point in the supplementary information, where we include the excitation energy for the eight lowest states and the energy of virtual orbitals.

With this expanded natural orbital space, we revisit the CC and TPA calculations, presenting the outcomes in the 4th to 6th columns of Table 7. We note a marked improvement in the excitation energy of the target state. Even at a threshold of $1.0d^{-4}$, the discrepancy when compared to full canonical results is around 1%. For the TPA, we also see more accurate results. For example, at a threshold of $1.0d^{-6}$, the error drops from 57% to 30% by correlating only two additional doubly-degenerate orbitals. We also detect a consistent trend of approaching the canonical orbitals results when going from $1.0d^{-4}$ to $1.0d^{-6}$.

There remains a 30% discrepancy between truncated FNOs and canonical orbital results.

From equation 8, to achieve precise scattering amplitudes, we cannot overlook the impact on the transition dipole moment, which is highly sensitive to diffuse orbitals. Conversely, these diffuse orbitals will have low occupation numbers in the MP2 calculations for the ground state and will therefore be removed from the correlating space, even with the slightly modified procedure we used.

Table 7: Performance of MP2FNOs on Two-photon absorption cross-sections δ (a.u.) and excitation energy (a.u.) of the target states for Ga^+

FNO ^a	FNO ^b	FNO ^c	FNO ^d	FNO ^e	FNO ^f	Canonical	Exp ^g
Number of correlated virtual orbitals							
25	35	48	29	38	50	82	
CCSD ground state correlation energy							
-0.2371	-0.2396	-0.2399	-0.2373	-0.2397	-0.2399	-0.2399	
Excitation energy of the target state $(4s5s)^1S$							
0.5864	0.6414	0.5192	0.4861	0.4838	0.4835	0.4812	0.4860
Two-photon absorption cross-sections							
0.19976	$<1.0\text{d}^{-15}$	3353.67	200.06	1300.01	1491.51	2128.33	

^a FNOs with the threshold of occupation number 1.0d^{-4}

^b FNOs with the threshold of occupation number 1.0d^{-5}

^c FNOs with the threshold of occupation number 1.0d^{-6}

^d FNOs with the threshold of occupation number 1.0d^{-4} plus doubly-degenerate orbitals

^e FNOs with the threshold of occupation number 1.0d^{-5} plus doubly-degenerate orbitals

^f FNOs with the threshold of occupation number 1.0d^{-6} plus doubly-degenerate orbitals

^g Results from NIST

Conclusion

In this work, we implement the relativistic Equation-of-Motion Coupled Cluster method to study the molecular quadratic response properties and two-photon absorption cross-sections. This implementation is accomplished in the GPU-accelerated coupled cluster module of DIRAC (ExaCorr), extending our previous linear response coupled cluster code⁷⁴ to solve both left and right response equations.

We have validated the implementation by assessing the purely electric properties such as static and frequency-dependent first hyperpolarizability of six hydrogen halide molecules

from HF to HAt. Using a non-relativistic Hamiltonian, our code exactly reproduces the EOM-based quadratic response properties implemented in the DALTON code. Compared to Hartree-Fock and B3LYP response calculations, our relativistic EOM quadratic response calculation shows the significance of both relativistic effect and electron correlation.

We have also investigated the Verdet constant, a mixed electric-magnetic property, for Xe and Rn with different Hamiltonian and correlation models. Both correlation and spin-orbit coupling are found to have pronounced effects. Compared to NR-QR-CC, our NR-EOM calculation overestimated the results by roughly 1%. While the X2C-EOM calculation deviates from the experimental value more than its non-relativistic counterpart, we find this to be due to error cancellation in the treatment of electron correlation, and we estimate that using larger correlating spaces should bring our X2C results more in line with experiment. We note such calculations are currently not feasible with our single-node code due to memory limits in computational resources at our disposal.

On the other hand, as consistent with previous works, we also observe the performance of B3LYP on the Verdet constant is poor with an error of 18% compared to the experiment for Xe. Such large deviations suggest it is important to investigate these properties with the more reliable coupled cluster method.

At last, in our study of the two-photon absorption in Ga^+ , and In^+ , we find relativistic and electron correlation effects both decrease the corresponding TPA cross-sections. We analyzed the results by evaluating the excitation energy of the target state and found that both effects increase the excitation energies.

It is worth noting that most calculations are limited in size since the quadratic response properties usually require more diffuse functions, which is challenging for the memory requirement in the current single-node implementation. There is an imperative to develop algorithms that can lower computational costs. In the current work, we utilize the MP2FNOs to reduce the virtual orbital space in TPA calculations and we find for the low-lying states, MP2FNO can effectively decrease the calculation cost while maintaining accuracy.

For higher states such as the target state in the two-photon transition considered, the bias of MP2FNOs towards the ground state may remove diffuse orbitals which will be important for excited states. A better way to consider the influence of these diffuse orbitals is to take account of the excited state in a more sophisticated manner, such as introducing the corresponding natural transition orbitals.¹⁰⁸ Exploring this further is among our future research objectives. Another natural development is to extend the current code to use libraries tailored for distributed memory computing architectures, such as the ExaTENSOR library, something which we are currently pursuing.

Acknowledgement

This research used resources of the Oak Ridge Leadership Computing Facility, which is a DOE Office of Science User Facility supported under Contract DE-AC05-00OR22725 (allocations CHM160, CHM191 and CHP109). XY, LH and ASPG acknowledge funding from projects Labex CaPPA (Grant No. ANR-11-LABX-0005-01) and ComprIXS (Grant Nos. ANR-19CE29-0019 and DFG JA 2329/6-1), the I-SITE ULNE project OVERSEE and MESONM International Associated Laboratory (LAI) (Grant No. ANR-16-IDEX-0004), as well support from the French national supercomputing facilities (Grant Nos. DARI A0130801859, A0110801859, project grand challenge AdAstra GDA2210).

Supporting Information Available

The data (input/output) corresponding to the calculations of this paper are available at the Zenodo repository under DOI: 10.5281/zenodo.8341323.

The Supporting Information is available free of charge on the ACS Publications website at DOI: XXX. Working equations for CCSD EOM quadratic response theory, MP2FNO performance on excitation energies of the lowest eight excited states, and virtual orbital energies of Ga⁺.

References

- (1) Cronstrand, P.; Luo, Y.; Ågren, H. *Advances in Quantum Chemistry*; Elsevier, 2005; Vol. 50; pp 1–21.
- (2) Papadopoulos, M. G., Sadlej, A. J., Leszczynski, J., Eds. *Non-linear optical properties of matter: from molecules to condensed phases*; Challenges and advances in computational chemistry and physics 1; Springer: Dordrecht, 2006; OCLC: 72145327.
- (3) Barron, L. D. *Molecular light scattering and optical activity*; Cambridge University Press, 2009.
- (4) Sénéchal, K.; Toupet, L.; Ledoux, I.; Zyss, J.; Le Bozec, H.; Maury, O. First lanthanide dipolar complexes for second-order nonlinear optics. *Chem. Commun.* **2004**, 2180–2181.
- (5) Law, G.-L.; Wong, K.-L.; Lau, K.-K.; Lap, S.-t.; Tanner, P. A.; Kuo, F.; Wong, W.-T. Nonlinear optical activity in dipolar organic–lanthanide complexes. *J. Mater. Chem.* **2010**, *20*, 4074.
- (6) Andraud, C.; Maury, O. Lanthanide Complexes for Nonlinear Optics: From Fundamental Aspects to Applications. *Eur. J. Inorg. Chem.* **2009**, *2009*, 4357–4371.
- (7) Tancrez, N.; Feuvrie, C.; Ledoux, I.; Zyss, J.; Toupet, L.; Le Bozec, H.; Maury, O. Lanthanide Complexes for Second Order Nonlinear Optics: Evidence for the Direct Contribution of f Electrons to the Quadratic Hyperpolarizability. *J. Am. Chem. Soc.* **2005**, *127*, 13474–13475.
- (8) Sénéchal-David, K.; Hemeryck, A.; Tancrez, N.; Toupet, L.; Williams, J. A. G.; Ledoux, I.; Zyss, J.; Boucekkine, A.; Guégan, J.-P.; Le Bozec, H.; Maury, O. Synthesis, Structural Studies, Theoretical Calculations, and Linear and Nonlinear Optical

- Properties of Terpyridyl Lanthanide Complexes: New Evidence for the Contribution of f Electrons to the NLO Activity. *J. Am. Chem. Soc.* **2006**, *128*, 12243–12255.
- (9) Valore, A.; Cariati, E.; Righetto, S.; Roberto, D.; Tessore, F.; Ugo, R.; Fragalà, I. L.; Fragalà, M. E.; Malandrino, G.; De Angelis, F.; Belpassi, L.; Ledoux-Rak, I.; Thi, K. H.; Zyss, J. Fluorinated β -Diketonate Diglyme Lanthanide Complexes as New Second-Order Nonlinear Optical Chromophores: The Role of f Electrons in the Dipolar and Octupolar Contribution to Quadratic Hyperpolarizability. *J. Am. Chem. Soc.* **2010**, *132*, 4966–4970.
- (10) Klepov, V. V.; Serezhkina, L. B.; Vologzhanina, A. V.; Pushkin, D. V.; Sergeeva, O. A.; Stefanovich, S. Y.; Serezhkin, V. N. Tris(acrylato)uranylates as a scaffold for NLO materials. *Inorg. Chem. Commun* **2014**, *46*, 5–8.
- (11) Wang, S.; Alekseev, E. V.; Ling, J.; Liu, G.; Depmeier, W.; Albrecht-Schmitt, T. E. Polarity and Chirality in Uranyl Borates: Insights into Understanding the Vitrification of Nuclear Waste and the Development of Nonlinear Optical Materials. *Chem. Mater.* **2010**, *22*, 2155–2163.
- (12) Serezhkin, V. N.; Grigoriev, M. S.; Abdulmyanov, A. R.; Fedoseev, A. M.; Savchenkov, A. V.; Stefanovich, S. Y.; Serezhkina, L. B. Syntheses, Crystal Structures, and Nonlinear Optical Activity of $\text{Cs}_2\text{Ba}[\text{AnO}_2(\text{C}_2\text{H}_5\text{COO})_3]_4$ ($\text{An} = \text{U, Np, Pu}$) and Unprecedented Octanuclear Complex Units in $\text{KR}_2(\text{H}_2\text{O})_8[\text{UO}_2(\text{C}_2\text{H}_5\text{COO})_3]_5$ ($\text{R} = \text{Sr, Ba}$). *Inorg. Chem.* **2017**, *56*, 7151–7160.
- (13) Christiansen, O.; Jørgensen, P.; Hättig, C. Response functions from Fourier component variational perturbation theory applied to a time-averaged quasienergy. *Int. J. Quantum Chem.* **1998**, *68*, 1–52.
- (14) Helgaker, T.; Coriani, S.; Jørgensen, P.; Kristensen, K.; Olsen, J.; Ruud, K. Re-

- cent Advances in Wave Function-Based Methods of Molecular-Property Calculations. *Chem. Rev.* **2012**, *112*, 543–631.
- (15) Norman, P. A perspective on nonresonant and resonant electronic response theory for time-dependent molecular properties. *Phys. Chem. Chem. Phys.* **2011**, *13*, 20519.
- (16) Norman, P.; Ruud, K.; Saue, T. *Principles and practices of molecular properties: theory, modeling, and simulations*; Wiley: Hoboken, NJ, 2018.
- (17) Sekino, H.; Bartlett, R. J. Frequency dependent nonlinear optical properties of molecules. *J. Chem. Phys.* **1986**, *85*, 976–989.
- (18) Rice, J. E.; Amos, R. D.; Colwell, S. M.; Handy, N. C.; Sanz, J. Frequency dependent hyperpolarizabilities with application to formaldehyde and methyl fluoride. *J. Chem. Phys.* **1990**, *93*, 8828–8839.
- (19) Rice, J. E.; Handy, N. C. The calculation of frequency-dependent hyperpolarizabilities including electron correlation effects. *Int. J. Quantum Chem.* **1992**, *43*, 91–118.
- (20) Olsen, J.; Jørgensen, P. Linear and nonlinear response functions for an exact state and for an MCSCF state. *J. Chem. Phys.* **1985**, *82*, 3235–3264.
- (21) Hettema, H.; Jensen, H. J. A.; Jørgensen, P.; Olsen, J. Quadratic response functions for a multiconfigurational self-consistent field wave function. *J. Chem. Phys.* **1992**, *97*, 1174–1190.
- (22) Rozyczko, P.; Bartlett, R. J. Frequency dependent equation-of-motion coupled cluster hyperpolarizabilities: Resolution of the discrepancy between theory and experiment for HF? *J. Chem. Phys.* **1997**, *107*, 10823–10826.
- (23) Hättig, C.; Christiansen, O.; Koch, H.; Jørgensen, P. Frequency-dependent first hyperpolarizabilities using coupled cluster quadratic response theory. *Chem. Phys. Lett* **1997**, *269*, 428–434.

- (24) Gauss, J.; Christiansen, O.; Stanton, J. F. Triple excitation effects in coupled-cluster calculations of frequency-dependent hyperpolarizabilities. *Chem. Phys. Lett* **1998**, *296*, 117–124.
- (25) Sałek, P.; Vahtras, O.; Helgaker, T.; Ågren, H. Density-functional theory of linear and nonlinear time-dependent molecular properties. *J. Chem. Phys.* **2002**, *117*, 9630–9645.
- (26) Schipper, P. R. T.; Gritsenko, O. V.; Van Gisbergen, S. J. A.; Baerends, E. J. Molecular calculations of excitation energies and (hyper)polarizabilities with a statistical average of orbital model exchange-correlation potentials. *J. Chem. Phys.* **2000**, *112*, 1344–1352.
- (27) Norman, P.; Jensen, H. J. A. Quadratic response functions in the time-dependent four-component Hartree-Fock approximation. *J. Chem. Phys.* **2004**, *121*, 6145–6154.
- (28) Henriksson, J.; Saue, T.; Norman, P. Quadratic response functions in the relativistic four-component Kohn-Sham approximation. *J. Chem. Phys.* **2008**, *128*, 024105.
- (29) Stanton, J. F.; Bartlett, R. J. The equation of motion coupled-cluster method. A systematic biorthogonal approach to molecular excitation energies, transition probabilities, and excited state properties. *J. Chem. Phys.* **1993**, *98*, 7029–7039.
- (30) Wang, F. In *Handbook of Relativistic Quantum Chemistry*; Liu, W., Ed.; Springer Berlin Heidelberg: Berlin, Heidelberg, 2017; pp 797–823.
- (31) Shee, A.; Saue, T.; Visscher, L.; Severo Pereira Gomes, A. Equation-of-motion coupled-cluster theory based on the 4-component Dirac–Coulomb(–Gaunt) Hamiltonian. Energies for single electron detachment, attachment, and electronically excited states. *J. Chem. Phys.* **2018**, *149*, 174113.
- (32) Krylov, A. I. Equation-of-Motion Coupled-Cluster Methods for Open-Shell and Elec-

- tronically Excited Species: The Hitchhiker’s Guide to Fock Space. *Annu. Rev. Phys. Chem.* **2008**, *59*, 433–462.
- (33) Bartlett, R. J. Coupled-cluster theory and its equation-of-motion extensions. *WIREs Comput Mol Sci* **2012**, *2*, 126–138.
- (34) Sneskov, K.; Christiansen, O. Excited state coupled cluster methods: Excited state coupled cluster methods. *WIREs Comput Mol Sci* **2012**, *2*, 566–584.
- (35) Liu, J.; Cheng, L. Relativistic coupled-cluster and equation-of-motion coupled-cluster methods. *WIREs Comput Mol Sci* **2021**, *11*.
- (36) Burland, D. M.; Miller, R. D.; Walsh, C. A. Second-order nonlinearity in poled-polymer systems. *Chem. Rev.* **1994**, *94*, 31–75.
- (37) Shelton, D. P.; Rice, J. E. Measurements and calculations of the hyperpolarizabilities of atoms and small molecules in the gas phase. *Chem. Rev.* **1994**, *94*, 3–29.
- (38) Datta, A.; Pati, S. K. Dipolar interactions and hydrogen bonding in supramolecular aggregates: understanding cooperative phenomena for 1st hyperpolarizability. *Chem. Soc. Rev.* **2006**, *35*, 1305.
- (39) Savukov, I. M.; Lee, S.-K.; Romalis, M. V. Optical detection of liquid-state NMR. *Nature* **2006**, *442*, 1021–1024.
- (40) Ikäläinen, S.; Lantto, P.; Vaara, J. Fully Relativistic Calculations of Faraday and Nuclear Spin-Induced Optical Rotation in Xenon. *J. Chem. Theory Comput.* **2012**, *8*, 91–98.
- (41) Cadène, A.; Fouché, M.; Rivère, A.; Battesti, R.; Coriani, S.; Rizzo, A.; Rizzo, C. Circular and linear magnetic birefringences in xenon at $\lambda = 1064$ nm. *J. Chem. Phys.* **2015**, *142*, 124313.

- (42) Göppert-Mayer, M. Über Elementarakte mit zwei Quantensprüngen. *Ann. Phys.* **1931**, *401*, 273–294.
- (43) Lee, C.; Xu, E. Z.; Liu, Y.; Teitelboim, A.; Yao, K.; Fernandez-Bravo, A.; Kotulska, A. M.; Nam, S. H.; Suh, Y. D.; Bednarkiewicz, A.; Cohen, B. E.; Chan, E. M.; Schuck, P. J. Giant nonlinear optical responses from photon-avalanching nanoparticles. *Nature* **2021**, *589*, 230–235.
- (44) Barker, T. J.; Denning, R. G.; Thorne, J. R. G. Applications of two-photon spectroscopy to inorganic compounds. 1. Spectrum and electronic structure of dicesium tetrachlorodioxouranate. *Inorg. Chem.* **1987**, *26*, 1721–1732.
- (45) Barker, T. J.; Denning, R. G.; Thorne, J. R. G. Applications of two-photon spectroscopy to inorganic compounds. 2. Spectrum and electronic structure of cesium uranyl nitrate, $\text{CsUO}_2(\text{NO}_3)_3$. *Inorg. Chem.* **1992**, *31*, 1344–1353.
- (46) Hättig, C.; Christiansen, O.; Jørgensen, P. Multiphoton transition moments and absorption cross sections in coupled cluster response theory employing variational transition moment functionals. *J. Chem. Phys.* **1998**, *108*, 8331–8354.
- (47) Salek, P.; Vahtras, O.; Guo, J.; Luo, Y.; Helgaker, T.; Ågren, H. Calculations of two-photon absorption cross sections by means of density-functional theory. *Chem. Phys. Lett* **2003**, *374*, 446–452.
- (48) Frediani, L.; Rinkevicius, Z.; Ågren, H. Two-photon absorption in solution by means of time-dependent density-functional theory and the polarizable continuum model. *J. Chem. Phys.* **2005**, *122*, 244104.
- (49) Nayyar, I. H.; Masunov, A. E.; Tretiak, S. Comparison of TD-DFT Methods for the Calculation of Two-Photon Absorption Spectra of Oligophenylvinylenes. *J. Phys. Chem. C* **2013**, *117*, 18170–18189.

- (50) Hättig, C.; Christiansen, O.; Jørgensen, P. Coupled cluster response calculations of two-photon transition probability rate constants for helium, neon and argon. *J. Chem. Phys.* **1998**, *108*, 8355–8359.
- (51) Friese, D. H.; Hättig, C.; Ruud, K. Calculation of two-photon absorption strengths with the approximate coupled cluster singles and doubles model CC2 using the resolution-of-identity approximation. *Phys. Chem. Chem. Phys.* **2012**, *14*, 1175–1184.
- (52) Nanda, K. D.; Krylov, A. I. Two-photon absorption cross sections within equation-of-motion coupled-cluster formalism using resolution-of-the-identity and Cholesky decomposition representations: Theory, implementation, and benchmarks. *J. Chem. Phys.* **2015**, *142*, 064118.
- (53) De Groot, F. High-Resolution X-ray Emission and X-ray Absorption Spectroscopy. *Chem. Rev.* **2001**, *101*, 1779–1808.
- (54) Ament, L. J. P.; van Veenendaal, M.; Devereaux, T. P.; Hill, J. P.; van den Brink, J. Resonant inelastic x-ray scattering studies of elementary excitations. *Rev. Mod. Phys.* **2011**, *83*, 705–767.
- (55) Fuchs, O.; Zharnikov, M.; Weinhardt, L.; Blum, M.; Weigand, M.; Zubavichus, Y.; Bär, M.; Maier, F.; Denlinger, J. D.; Heske, C.; Grunze, M.; Umbach, E. Isotope and Temperature Effects in Liquid Water Probed by X-Ray Absorption and Resonant X-Ray Emission Spectroscopy. *Phys. Rev. Lett.* **2008**, *100*, 027801.
- (56) Hennies, F.; Pietzsch, A.; Berglund, M.; Föhlich, A.; Schmitt, T.; Strocov, V.; Karlsson, H. O.; Andersson, J.; Rubensson, J.-E. Resonant Inelastic Scattering Spectra of Free Molecules with Vibrational Resolution. *Phys. Rev. Lett.* **2010**, *104*, 193002.
- (57) Kunnus, K.; Zhang, W.; Delcey, M. G.; Pinjari, R. V.; Miedema, P. S.; Schreck, S.; Quevedo, W.; Schröder, H.; Föhlich, A.; Gaffney, K. J.; Lundberg, M.; Odelius, M.;

- Wernet, P. Viewing the Valence Electronic Structure of Ferric and Ferrous Hexacyanide in Solution from the Fe and Cyanide Perspectives. *J. Phys. Chem. B* **2016**, *120*, 7182–7194.
- (58) Kjellsson, L. et al. Resonant Inelastic X-Ray Scattering Reveals Hidden Local Transitions of the Aqueous OH Radical. *Phys. Rev. Lett.* **2020**, *124*, 236001.
- (59) Rehn, D. R.; Dreuw, A.; Norman, P. Resonant Inelastic X-ray Scattering Amplitudes and Cross Sections in the Algebraic Diagrammatic Construction/Intermediate State Representation (ADC/ISR) Approach. *J. Chem. Theory Comput.* **2017**, *13*, 5552–5559.
- (60) Josefsson, I.; Kunnus, K.; Schreck, S.; Föhlich, A.; De Groot, F.; Wernet, P.; Odellius, M. Ab Initio Calculations of X-ray Spectra: Atomic Multiplet and Molecular Orbital Effects in a Multiconfigurational SCF Approach to the L-Edge Spectra of Transition Metal Complexes. *J. Phys. Chem. Lett.* **2012**, *3*, 3565–3570.
- (61) Nascimento, D. R.; Biasin, E.; Poulter, B. I.; Khalil, M.; Sokaras, D.; Govind, N. Resonant Inelastic X-ray Scattering Calculations of Transition Metal Complexes Within a Simplified Time-Dependent Density Functional Theory Framework. *J. Chem. Theory Comput.* **2021**, *17*, 3031–3038.
- (62) Faber, R.; Coriani, S. Resonant Inelastic X-ray Scattering and Nonesonant X-ray Emission Spectra from Coupled-Cluster (Damped) Response Theory. *J. Chem. Theory Comput.* **2019**, *15*, 520–528.
- (63) Schnack-Petersen, A. K.; Moitra, T.; Folkestad, S. D.; Coriani, S. New Implementation of an Equation-of-Motion Coupled-Cluster Damped-Response Framework with Illustrative Applications to Resonant Inelastic X-ray Scattering. *J. Phys. Chem. A* **2023**, *127*, 1775–1793, arXiv:2211.12215 [physics].

- (64) Skomorowski, W.; Krylov, A. I. Feshbach–Fano approach for calculation of Auger decay rates using equation-of-motion coupled-cluster wave functions. I. Theory and implementation. *J. Chem. Phys.* **2021**, *154*, 084124.
- (65) Skomorowski, W.; Krylov, A. I. Feshbach–Fano approach for calculation of Auger decay rates using equation-of-motion coupled-cluster wave functions. II. Numerical examples and benchmarks. *J. Chem. Phys.* **2021**, *154*, 084125.
- (66) Skeidsvoll, A. S.; Moitra, T.; Balbi, A.; Paul, A. C.; Coriani, S.; Koch, H. Simulating weak-field attosecond processes with a Lanczos reduced basis approach to time-dependent equation-of-motion coupled-cluster theory. *Phys. Rev. A* **2022**, *105*, 023103.
- (67) Ranga, S.; Dutta, A. K. A Core–Valence Separated Similarity Transformed EOM-CCSD Method for Core-Excitation Spectra. *J. Chem. Theory Comput.* **2021**, *17*, 7428–7446.
- (68) Henriksson, J.; Norman, P.; Jensen, H. J. A. Two-photon absorption in the relativistic four-component Hartree–Fock approximation. *J. Chem. Phys.* **2005**, *122*, 114106.
- (69) Taube, A. G.; Bartlett, R. J. Frozen Natural Orbitals: Systematic Basis Set Truncation for Coupled-Cluster Theory. *Collect. Czech. Chem. Commun.* **2005**, *70*, 837–850.
- (70) Taube, A. G.; Bartlett, R. J. Frozen natural orbital coupled-cluster theory: Forces and application to decomposition of nitroethane. *J. Chem. Phys.* **2008**, *128*, 164101.
- (71) Crawford, T. D.; Kumar, A.; Bazanté, A. P.; Di Remigio, R. Reduced-scaling coupled cluster response theory: Challenges and opportunities. *WIREs Comput Mol Sci* **2019**, *9*.
- (72) Kumar, A.; Crawford, T. D. Frozen Virtual Natural Orbitals for Coupled-Cluster Linear-Response Theory. *J. Phys. Chem. A* **2017**, *121*, 708–716.

- (73) Surjuse, K.; Chamoli, S.; Nayak, M. K.; Dutta, A. K. A low-cost four-component relativistic equation of motion coupled cluster method based on frozen natural spinors: Theory, implementation, and benchmark. *J. Chem. Phys.* **2022**, *157*, 204106.
- (74) Yuan, X.; Halbert, L.; Pototschnig, J.; Papadopoulos, A.; Coriani, S.; Visscher, L.; Gomes, A. S. P. Formulation and Implementation of Frequency-Dependent Linear Response Properties with Relativistic Coupled Cluster Theory for GPU-accelerated Computer Architectures. 2023; <http://arxiv.org/abs/2307.14296>, arXiv:2307.14296 [physics].
- (75) Pawłowski, F.; Olsen, J.; Jørgensen, P. Molecular response properties from a Hermitian eigenvalue equation for a time-periodic Hamiltonian. *J. Chem. Phys.* **2015**, *142*, 114109.
- (76) Coriani, S.; Pawłowski, F.; Olsen, J.; Jørgensen, P. Molecular response properties in equation of motion coupled cluster theory: A time-dependent perspective. *J. Chem. Phys.* **2016**, *144*, 024102.
- (77) Shee, A.; Visscher, L.; Saue, T. Analytic one-electron properties at the 4-component relativistic coupled cluster level with inclusion of spin-orbit coupling. *The Journal of Chemical Physics* **2016**, *145*.
- (78) McClain, W. M. Excited State Symmetry Assignment Through Polarized Two-Photon Absorption Studies of Fluids. *J. Chem. Phys.* **1971**, *55*, 2789–2796.
- (79) Saue, T.; Bast, R.; Gomes, A. S. P.; Jensen, H. J. A.; Visscher, L.; Aucar, I. A.; Di Remigio, R.; Dyall, K. G.; Eliav, E.; Fasshauer, E., et al. The DIRAC code for relativistic molecular calculations. *J. Chem. Phys.* **2020**, *152*, 204104.
- (80) DIRAC, a relativistic ab initio electronic structure program, Release DIRAC23 (2023), written by R. Bast, A. S. P. Gomes, T. Saue and L. Visscher and H. J. Aa. Jensen, with

contributions from I. A. Aucar, V. Bakken, C. Chibueze, J. Creutzberg, K. G. Dyall, S. Dubillard, U. Ekström, E. Eliav, T. Enevoldsen, E. Faßhauer, T. Fleig, O. Fossgaard, L. Halbert, E. D. Hedegård, T. Helgaker, B. Helmich–Paris, J. Henriksen, M. van Horn, M. Iliáš, Ch. R. Jacob, S. Knecht, S. Komorovský, O. Kullie, J. K. Lærdahl, C. V. Larsen, Y. S. Lee, N. H. List, H. S. Nataraj, M. K. Nayak, P. Norman, A. Nyvang, G. Olejniczak, J. Olsen, J. M. H. Olsen, A. Papadopoulos, Y. C. Park, J. K. Pedersen, M. Pernpointner, J. V. Pototschnig, R. di Remigio, M. Repisky, K. Ruud, P. Salek, B. Schimmelpfennig, B. Senjean, A. Shee, J. Sikkema, A. Sunaga, A. J. Thorvaldsen, J. Thyssen, J. van Stralen, M. L. Vidal, S. Villaume, O. Visser, T. Winther, S. Yamamoto and X. Yuan (available at <https://doi.org/10.5281/zenodo.7670749>, see also <https://www.diracprogram.org>).

- (81) Dyall, K. G.; Tecmer, P.; Sunaga, A. Diffuse Basis Functions for Relativistic s and d Block Gaussian Basis Sets. *J. Chem. Theory. Comput* **2022**,
- (82) Dyall, K. G. Relativistic quadruple-zeta and revised triple-zeta and double-zeta basis sets for the 4p, 5p, and 6p elements. *Theor. Chem. Acc* **2006**, *115*, 441–447.
- (83) Kendall, R. A.; Dunning Jr, T. H.; Harrison, R. J. Electron affinities of the first-row atoms revisited. Systematic basis sets and wave functions. *J. Chem. Phys* **1992**, *96*, 6796–6806.
- (84) Woon, D. E.; Dunning Jr, T. H. Gaussian basis sets for use in correlated molecular calculations. III. The atoms aluminum through argon. *J. Chem. Phys* **1993**, *98*, 1358–1371.
- (85) Wilson, A. K.; Woon, D. E.; Peterson, K. A.; Dunning Jr, T. H. Gaussian basis sets for use in correlated molecular calculations. IX. The atoms gallium through krypton. *J. Chem. Phys* **1999**, *110*, 7667–7676.

- (86) Iliáš, M.; Saue, T. An infinite-order two-component relativistic Hamiltonian by a simple one-step transformation. *J. Chem. Phys* **2007**, *126*, 064102.
- (87) Lévy-Leblond, J.-M. Nonrelativistic particles and wave equations. *Commun. Math. Phys* **1967**, *6*, 286–311.
- (88) Visscher, L.; Saue, T. Approximate relativistic electronic structure methods based on the quaternion modified Dirac equation. *J. Chem. Phys* **2000**, *113*, 3996–4002.
- (89) Becke, A. D. A new mixing of Hartree–Fock and local density-functional theories. *J. Chem. Phys* **1993**, *98*, 1372–1377.
- (90) Visscher, L.; Dylla, K. G. Dirac–Fock atomic electronic structure calculations using different nuclear charge distributions. *Atom. Data. Nucl. Data* **1997**, *67*, 207–224.
- (91) Beebe, N. H.; Linderberg, J. Simplifications in the generation and transformation of two-electron integrals in molecular calculations. *Int. J. Quantum. Chem* **1977**, *12*, 683–705.
- (92) Koch, H.; Sánchez de Merás, A.; Pedersen, T. B. Reduced scaling in electronic structure calculations using Cholesky decompositions. *J. Chem. Phys* **2003**, *118*, 9481–9484.
- (93) Aquilante, F.; Pedersen, T. B.; Lindh, R. Low-cost evaluation of the exchange Fock matrix from Cholesky and density fitting representations of the electron repulsion integrals. *J. Chem. Phys* **2007**, *126*, 194106.
- (94) Huber, K.-P. *Molecular spectra and molecular structure* **1979**,
- (95) Gomes, A. S. P.; Visscher, L. The influence of core correlation on the spectroscopic constants of HAt. *Chem. Phys. Lett.* **2004**, *399*, 1.
- (96) Aidas, K. et al. The Dalton quantum chemistry program system: The Dalton program. *WIREs Comput Mol Sci* **2014**, *4*, 269–284.

- (97) Rizzo, A.; Coriani, S.; Fernández, B.; Christiansen, O. A coupled cluster response study of the electric dipole polarizability, first and second hyperpolarizabilities of HCl. *Phys. Chem. Chem. Phys.* **2002**, *4*, 2884–2890.
- (98) Hansen, M. B.; Christiansen, O.; Hättig, C. Automated calculation of anharmonic vibrational contributions to first hyperpolarizabilities: Quadratic response functions from vibrational configuration interaction wave functions. *J. Chem. Phys.* **2009**, *131*, 154101.
- (99) Dudley, J.; Ward, J. Measurements of second- and third-order nonlinear polarizabilities for HF and HCl. *J. Chem. Phys.* **1985**, *82*, 4673–3677.
- (100) Coriani, S.; Hättig, C.; Jørgensen, P.; Halkier, A.; Rizzo, A. Coupled cluster calculations of Verdet constants. *Chem. Phys. Lett* **1997**, *281*, 445–451.
- (101) Pecul, M.; Pawłowski, F.; Jørgensen, P.; Köhn, A.; Hättig, C. High-order correlation effects on dynamic hyperpolarizabilities and their geometric derivatives: A comparison with density functional results. *J. Chem. Phys.* **2006**, *124*, 114101.
- (102) Visscher, L. Approximate molecular relativistic Dirac-Coulomb calculations using a simple Coulombic correction. *Theor. Chem. Acc.* **1997**, *98*, 68–70.
- (103) Dylla, K. G. An exact separation of the spin-free and spin-dependent terms of the Dirac-Coulomb-Breit Hamiltonian. *J. Chem. Phys.* **1994**, *100*, 2118–2127.
- (104) Ingersoll, L. R.; Liebenberg, D. H. Faraday Effect in Gases and Vapors. II*. *J. Opt. Soc. Am.* **1956**, *46*, 538–542.
- (105) Zuhrianda, Z.; Safronova, M. S.; Kozlov, M. G. Anomalously small blackbody radiation shift in the Tl + frequency standard. *Phys. Rev. A* **2012**, *85*, 022513.
- (106) Safronova, M. S.; Kozlov, M. G.; Clark, C. W. Precision Calculation of Blackbody Radiation Shifts for Optical Frequency Metrology. *Phys. Rev. Lett.* **2011**, *107*, 143006.

- (107) Yuan, X.; Visscher, L.; Gomes, A. S. P. Assessing MP2 frozen natural orbitals in relativistic correlated electronic structure calculations. *J. Chem. Phys.* **2022**, *156*, 224108.
- (108) Höfener, S.; Klopper, W. Natural transition orbitals for the calculation of correlation and excitation energies. *Chem. Phys. Lett* **2017**, *679*, 52–59.

Note: Reimplementation of Ionization Potential, and Electron Affinity based upon Relativistic Equation-of-Motion Coupled Cluster

In this chapter, I will briefly discuss the implementation of the equation-of-motion (EOM) coupled cluster for evaluating the ionization potential (IP), electron affinity (EA), and excitation energy (EE).

The EOM-CC is a robust and accurate method to evaluate the energies and properties of electronically excited states within the CC framework. In relativistic quantum chemistry, the EOM-CC method serves as a good tool to simulate spectroscopy and construct the potential energy surface of molecules containing heavy elements. Readers can refer to the review of Liu and Cheng[45] to find the recent progress of the relativistic EOM-CC methods. In DIRAC, the EOM-CC has been implemented and discussed for RELCCSD[103]. To extend its ability for large systems, we reimplement the codes on ExaCorr.

Concerning the EOM-EE-related equations that have been used and discussed in Chapters 3 and 4, In this chapter, we will focus on the IP and EA implementation and show some pilot tests compared to RELCCSD.

5.1 Theory

The excitation energies and excited states in the EOM-CC framework are defined as the eigenvalues and eigenvectors of the similarity-transformed Hamiltonian \hat{H} , respectively.

$$\hat{H} = e^{-\hat{T}} \hat{H} e^{\hat{T}} \quad (5.1)$$

Due to the fact that \hat{H} is non-Hermitian, the right-handed ($|R\rangle$) and left-handed ($\langle L|$) eigenvectors are not the same, and we have to separately solve the corresponding eigenvalue equation for a given state n with energy E_n :

$$\hat{H} |R_n\rangle = E_n |R_n\rangle \quad (5.2)$$

$$\langle L_n | \hat{H} = \langle L_n | E_n \quad (5.3)$$

While $|R_n\rangle$ and $\langle L_n|$ are not simple adjoints of each other, they obey the biorthogonality:

$$\langle L_n | R_m \rangle = \delta_{nm} \quad (5.4)$$

The right-hand and left-hand states are parametrized as CI-type wavefunctions, where the reference state of a single-determinant wave function has been replaced by the exponential-type wave function of the coupled cluster ground state, so the single-reference method EOM-CC can partially consider the multi-reference effects for excited states[43].

$$|R_n\rangle = \hat{R}_n e^{\hat{T}} |\Phi_0\rangle \quad (5.5)$$

$$\langle L_n | = \langle \Phi_0 | e^{-\hat{T}} \hat{L}_n \quad (5.6)$$

The \hat{R}_n and \hat{L}_n operators are defined in the following for ionization potential (IP), and electron affinity (EA) states with truncation at single and doubles level as the same as truncation used for the \hat{T} operator in the coupled cluster ground state:

Ionized states (IP):

$$\hat{R}^{IP} = r_0 + \sum_i r_i a_i + \sum_{i>j,a} r_{ij}^a a_a^\dagger a_j a_i \quad (5.7)$$

$$\hat{L}^{IP} = l_0 + \sum_i l^i a_i^\dagger + \sum_{i>j,a} l_a^{ij} a_i^\dagger a_j^\dagger a_a \quad (5.8)$$

Electron-attached states (EA):

$$\hat{R}^{EA} = r_0 + \sum_a r^a a_a^\dagger + \sum_{i,a>b} r_i^{ab} a_a^\dagger a_b^\dagger a_i \quad (5.9)$$

$$\hat{L}^{EA} = l_0 + \sum_a l_a a_a + \sum_{i,a>b} l_{ab}^i a_i^\dagger a_b a_a \quad (5.10)$$

The key step for obtaining the excited state in EOM-CC is solving the equation 5.2 and 5.3, that is the diagonalization of the \bar{H} matrix. As discussed in the case of solving response equations in Chapter 3 and Chapter 4, we cannot store and diagonalize \bar{H} matrix in the full single and double excitation space and have to project it into a subspace and solve the equation with an iterative algorithm such as the Davidson method.

The Davidson procedure[104, 105] has been extensively discussed elsewhere. Additionally, there's an extensive discussion of the RELCCSD code in DIRAC in reference[103], and in Chapter 3 on ExaCorr. Therefore, here we skip the discussion of the constructing error vectors and preconditioner and focus on the formation of the left (${}^L\sigma$) or right (${}^R\sigma$) vectors:

$${}^R\sigma = \hat{H}b \quad (5.11)$$

$${}^L\sigma = b^\dagger \hat{H} \quad (5.12)$$

where $\mathbf{b}(\mathbf{b}^\dagger)$ (complex conjugate) are the trial vectors. The corresponding working equations of σ vectors are outlined in section 5.5 (The related intermediates including \bar{F} , \bar{W} , W , and G are collected in the supplementary information (SI) of Chapter 3, so they are not repeated here.).

5.2 Implementation

The iterative solver workflow for diagonalization of \tilde{H} matrix is similar to the workflow in Chapter 3, which is summarized in Figure 5.1. Variables which have been shown in Figure 1 of Chapter 3 have the same meaning here. For convenience to read, I repeat the corresponding definition below:

- **b**: trial vectors
- σ vectors: see the working equations in SI of Chapter 3, and Section 5.5 of the current chapter.
- G' : the representation of \tilde{H} in the subspace spanned by a set of trial vectors
- β' : the eigenvectors of G' , which are the Fortran arrays
- β : the eigenvectors of G' , which are TAL-SH tensors
- $\tilde{H}_{||}$: diagonal elements of \tilde{H}
- g : eigenvalues associated β' and β .
- **r**: residual vectors
- ϵ : correction vectors

There are still some differences between the scheme of solving linear systems in Chapter 3 and the diagonalization procedure used in the current workflow. First, for the diagonalization, we normally solve several roots at the same time, which requires to selection of multiple trial vectors at the beginning of the Davidson procedure.

Second, in Chapter 3, to avoid obtaining zero solution in the linear system, we select the initial trial vectors, which are associated with nonzero elements of property gradient vectors, but in the current workflow, we construct the initial vectors based on the large diagonal elements of \tilde{H} matrix.

In addition, the formula of precondition used in the current workflow is different, where we replace the frequency ω in Chapter 3 with the eigenvalue g .

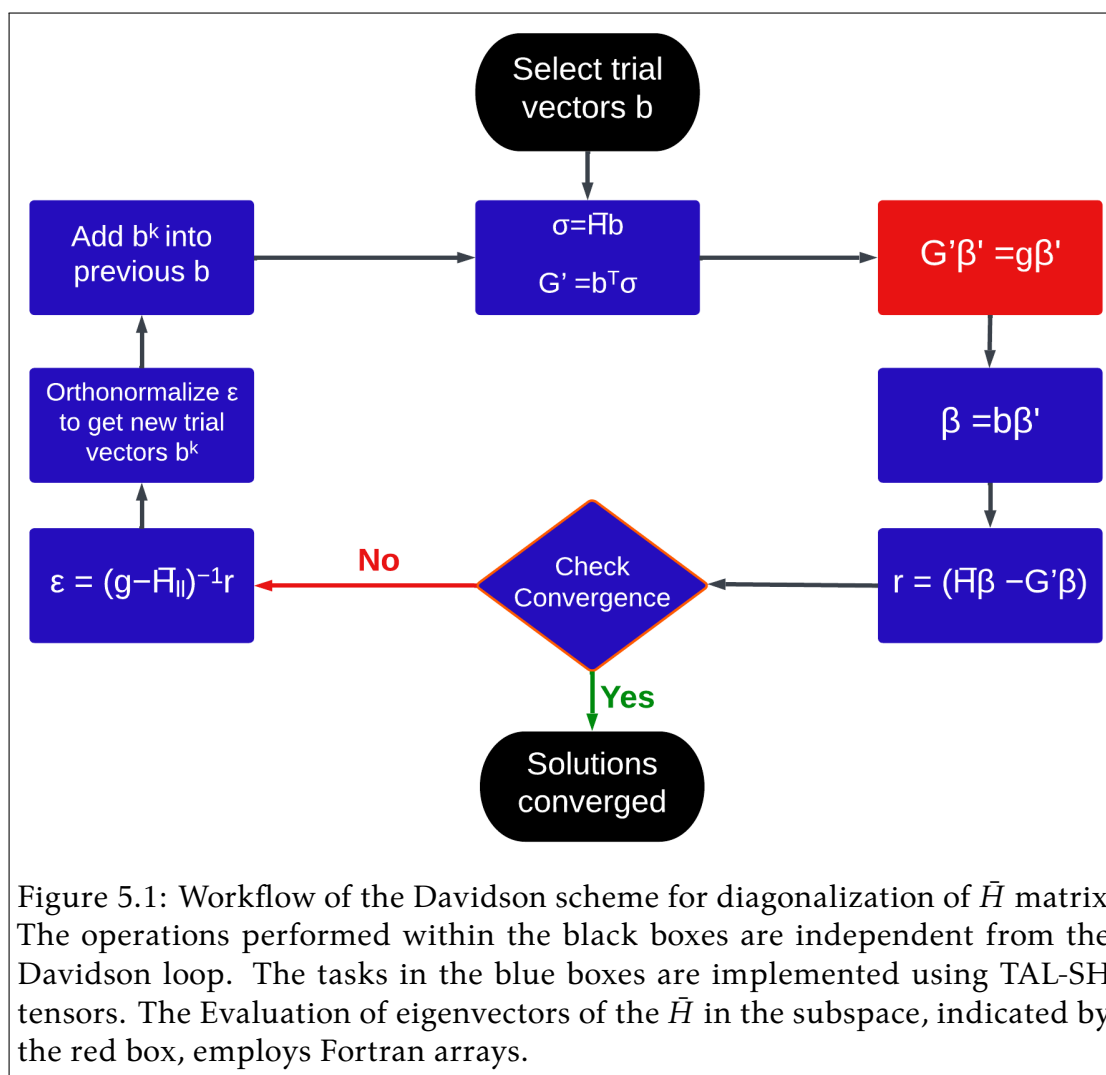


Figure 5.1: Workflow of the Davidson scheme for diagonalization of \bar{H} matrix. The operations performed within the black boxes are independent from the Davidson loop. The tasks in the blue boxes are implemented using TAL-SH tensors. The Evaluation of eigenvectors of the \bar{H} in the subspace, indicated by the red box, employs Fortran arrays.

5.3 Pilot tests

We calculate the IP and EA for the low-lying states of selected systems: noble gas atoms (Ar, Kr, Xe, Rn), and water molecules with ExaCorr and RELCCSD. While this implementation allows us to evaluate both left and right hand equations, here we only compute the right equations since both left and right equations give the same eigenvalues.

In the current calculations, we employed the X2C Hamiltonian and double zeta basis sets (cc-pVDZ for H, O, Ar, Kr, and dyall.v2z for Xe, and Rn). For the

sake of completeness, we also provide the results of the excitation energy (EOM-EE), an EOM flavor that has been discussed and validated in the linear response calculation of Chapter 3. The results are listed in Table 5.1, 5.2, and 5.3. The cc-pVDZ basis set is unsuitable for obtaining accurate results particularly, for the electron affinity as it should be zero for all noble gases and water molecules. To achieve accurate electron affinity values, it is necessary to incorporate more diffuse functions (see Table 5.4 for electron affinity of Ar using different basis sets). However, in this chapter, we focus on checking the correctness of the new implementation and observe ExaCorr reproduces the RELCCSD results very well, with errors smaller than $1.0d^{-8}$. This agreement validates the correctness of our implementation for EOM-IP, EA, and EE.

Table 5.1: Comparison of ionization potential (a.u.) obtained with the ExaCorr and RELCCSD codes for selected systems

System	State	ExaCorr	RELCCSD
Ar	1	0.561506896	0.561506902
Kr	1	0.496662989	0.496662988
Xe	1	0.429982648	0.429982648
Rn	1	0.380111009	0.380111008
H ₂ O	1	0.427987553	0.427987555
	2	0.503417732	0.503417729

Table 5.2: Comparison of electron affinity (a.u.) obtained with the ExaCorr and RELCCSD codes for selected systems

System	State	ExaCorr	RELCCSD
Ar	1	0.706922719	0.706922716
	2	0.711475587	0.711475588
Kr	1	0.637684818	0.637684819
	2	0.693815292	0.693815294
Xe	1	0.491917812	0.491917814
	2	0.567921598	0.567921598
Rn	1	0.460641679	0.460641680
	2	0.465545332	0.465545340
H ₂ O	1	0.161140032	0.161140035
	2	0.233359689	0.233359692

Table 5.3: Comparison of excitation energies (a.u.) obtained with the ExaCorr and RELCCSD codes for selected systems

System	State	ExaCorr	RELCCSD
Ar	1	0.834364752	0.834364766
	2	0.898702008	0.898701993
Kr	1	0.780823595	0.780823596
Xe	1	0.616406736	0.616406747
Rn	1	0.561813836	0.561813854
H ₂ O	1	0.264890174	0.264890177
	2	0.264890301	0.264890304
	3	0.264890679	0.264890683
	4	0.290344237	0.290344239

Table 5.4: Electron affinity (a.u.) of Ar obtained with different basis sets

Basis set	Energy
cc-PVDZ	0.7069
cc-PVTZ	0.5182
s-aug-cc-PVTZ	0.1230
d-aug-cc-PVTZ	0.0351
t-aug-cc-PVTZ	0.0110
q-aug-cc-PVTZ	0.0035
5-aug-cc-PVTZ	0.0011
6-aug-cc-PVTZ	0.0003

5.4 Perspectives

As already mentioned in Chapters 3 and 4, the current implementation of EOM-CC energy is also based on the single-node tensor operation library TAL-SH, which has limitations on the capacity of a single node, particularly for memory. It seems for small systems with high symmetry tested above such as atoms and small molecules, the advantage of using ExaCorr instead of RELCCSD may not be evident. Here one should keep in mind first that if ExaCorr has been designed with the goal of treating significantly larger systems that are beyond the reach of RELCCSD, even for small systems it is sometimes necessary to carry out calculations in lower symmetry (or without any symmetry), such as when considering the effects of the environment. In this case, even the current single-node implementation in ExaCorr can become competitive with RELCCSD, with the advantage of efficiency, that it requires next to no disk space, which can save time in Input/output (I/O).

In any case, it is clear that once we complete the extension of the current code to use the ExaTENSOR library, which is suited for distributed memory computing architectures, we will significantly widen the range of applications both EOM and response theory codes can handle. For example, prior work in our group evaluated the effect of the environment (solvent, etc) on the ionization energy of valence[106] and core electrons[107] of the halide ions by comb-

5.5. EOM-CCSD IP and EA sigma vectors were not given in SI of Chapter 3151

ing the relativistic EOM-IP and frozen density embedding (FDE) methods[108–110]. While such simulations were still doable with RELCCSD, for slightly more complex systems, such as IO_3^- , and $\text{UO}_2\text{Cl}_4^{2-}$ [111], this is no longer the case and our new implementation will be the way forward.

Apart from the utilization of the ExaTENSOR library, for the single-node version code, another strategy to enable larger calculations involves the implementation of reduced-scaling methods before performing CC calculations, to reduce the memory requirements. One strategy is to replace the normal Hartree-Fock orbitals with more compacted orbitals such as MP2 frozen natural orbitals (FNOs). For instance, Surjuse et al.[112] demonstrated using MP2FNO can gain on reducing the virtual orbital space in the EOM ionization energy.

The relativistic MP2FNO method will be discussed for implementation details and the corresponding performance on the CC ground state energy and property in Chapter 6. Also, we have employed the MP2FNOs to reduce the costs of evaluation of EOM excitation energy and two-photon absorption (TPA) cross-sections in Chapter 4 and find that the MP2FNO scheme is reliable for the low-lying excited states but has challenges for higher states, and TPA. To solve this issue, we are working on incorporating the natural transition orbitals, which is potentially a more reliable, generally applicable approach.

5.5 EOM-CCSD IP and EA sigma vectors were not given in SI of Chapter 3

EOM-CCSD-IP σ -VECTOR RIGHT EQUATIONS:

$$\sigma_i = -\bar{F}_i^m r_m + \bar{F}_e^m r_{im}^e - \frac{1}{2} W_{ie}^{mn} r_{mn}^e \quad (5.13)$$

$$\sigma_{ij}^a = -W_{ij}^{ma} r_m - P_{-ij} \bar{F}_i^m r_{mj}^a + \frac{1}{2} W_{ij}^{mn} r_{mn}^a - P_{-ij} W_{ie}^{ma} r_{mj}^e + \bar{F}_e^a r_{ij}^e + \frac{1}{2} (V_{ef}^{mn} r_{mn}^f) t_{ij}^{ea} \quad (5.14)$$

EOM-CCSD-EA σ -VECTOR RIGHT EQUATIONS:

$$R_{\sigma}^a = \bar{F}_e^a r^e + \bar{F}_e^m r_m^{ea} + \frac{1}{2} W_{fe}^{am} r_m^{ef} \quad (5.15)$$

$$R_{\sigma_i}^{ab} = -W_{ei}^{ab} r^e + P_{-ab} \bar{F}_e^a r_i^{eb} + \frac{1}{2} W_{ef}^{ab} r_i^{ef} - P_{-ab} W_{ei}^{am} r_m^{eb} - \bar{F}_i^m r_m^{ab} - \frac{1}{2} (V_{ef}^{mn} r_n^{ef}) t_{mi}^{ab} \quad (5.16)$$

Chapter 6

Reduced-Scaling: Relativistic MP2 Frozen Natural Orbitals

Paper: Assessing MP2 frozen natural orbitals in relativistic correlated electronic structure calculations

I implemented the code, carried out all calculations, and wrote the manuscript.

Journal of Chemical Physics, 156, 224108, 2022

Reproduced from *Journal of Chemical Physics* with the permission of AIP Publishing.

Copyright 2022 AIP Publishing LLC.

Assessing MP2 frozen natural orbitals in relativistic correlated electronic structure calculations

Cite as: J. Chem. Phys. 156, 224108 (2022); doi: 10.1063/5.0087243

Submitted: 3 February 2022 • Accepted: 22 May 2022 •

Published Online: 9 June 2022



View Online



Export Citation



CrossMark

Xiang Yuan,^{1,2,a)}  Lucas Visscher,^{2,b)}  and André Severo Pereira Gomes^{1,c)} 

AFFILIATIONS

¹ Univ. Lille, CNRS, UMR 8523 - PhLAM - Physique des Lasers Atomes et Molécules, F-59000 Lille, France

² Department of Chemistry and Pharmaceutical Sciences, Faculty of Science, Vrije Universiteit Amsterdam, de Boelelaan 1083, 1081 HV Amsterdam, The Netherlands

^{a)} Electronic mail: xiang.yuan@univ-lille.fr

^{b)} Electronic mail: l.visscher@vu.nl

^{c)} Author to whom correspondence should be addressed: andre.gomes@univ-lille.fr

ABSTRACT

The high computational scaling with the basis set size and the number of correlated electrons is a bottleneck limiting applications of coupled cluster algorithms, in particular for calculations based on two- or four-component relativistic Hamiltonians, which often employ uncontracted basis sets. This problem may be alleviated by replacing canonical Hartree–Fock virtual orbitals by natural orbitals (NOs). In this paper, we describe the implementation of a module for generating NOs for correlated wavefunctions and, in particular, second order Møller–Plesset perturbation frozen natural orbitals (MP2FNOs) as a component of our novel implementation of relativistic coupled cluster theory for massively parallel architectures [Pototschnig *et al.* J. Chem. Theory Comput. 17, 5509, (2021)]. Our implementation can manipulate complex or quaternion density matrices, thus allowing for the generation of both Kramers-restricted and Kramers-unrestricted MP2FNOs. Furthermore, NOs are re-expressed in the parent atomic orbital (AO) basis, allowing for generating coupled cluster singles and doubles NOs in the AO basis for further analysis. By investigating the truncation errors of MP2FNOs for both the correlation energy and molecular properties—electric field gradients at the nuclei, electric dipole and quadrupole moments for hydrogen halides HX (X = F–Ts), and parity-violating energy differences for H₂Z₂ (Z = O–Se)—we find MP2FNOs accelerate the convergence of the correlation energy in a roughly uniform manner across the Periodic Table. It is possible to obtain reliable estimates for both energies and the molecular properties considered with virtual molecular orbital spaces truncated to about half the size of the full spaces.

Published under an exclusive license by AIP Publishing. <https://doi.org/10.1063/5.0087243>

I. INTRODUCTION

Understanding the electronic structure of large molecules or complexes containing heavy elements, such as lanthanides or actinides, is a problem of relevance for many technological applications. Examples are the nuclear fuel cycle, such as in the development of new extractants for separation processes,^{1–6} and the use of lanthanides as exceptionally strong single molecule magnets.⁷ To model such materials, Density Functional Theory (DFT) has become the most widely used correlated electronic structure theory approach⁸ even though it is difficult to systematically approach exact results with the currently available density functional

approximations.^{8,9} In the particular case of relativistic electronic structure calculations, DFT energies may even for closed-shell species strongly deviate from experimental or accurate theoretical results.^{10–12}

This also holds for molecular properties; recently, Sunaga and Saue¹³ reported that the performance of DFT for parity violation energy shift (PV) calculations—a property requiring a very accurate description of the electronic wave function near the nuclei—is somewhat disappointing with deviations to coupled cluster singles and doubles (CCSD) being as large as 10%. These uncertainties in the performance of DFT for heavy elements, especially for cases in which experimental values are absent or difficult to generate, call for

the use of state-of-the-art wavefunction methods to either provide accurate reference data or be applied directly if the model sizes are small enough.

Among currently available approaches, CC theory serves as a “gold standard”^{14,15} for its ability to give results approaching chemical accuracy for both correlation energies and properties. However, the main difficulty in employing CC theory in large-scale applications (such as molecules containing several hundred electrons) is its high computational scaling with respect to the size of the system (N). For example, without approximations, CCSD and CCSD with perturbative triples corrections [CCSD(T)] approaches scale with $O(N^6)$ and $O(N^7)$, respectively, and also with approximations such as Laplace transforms,¹⁶ distance screening,¹⁷ and density fitting,^{18,19} the scaling and prefactors are still significantly higher than in a mean-field approach, such as DFT.

Another key ingredient in modeling heavy element species is the treatment of relativistic effects.^{20–22} For cases in which a given molecular property is not particularly sensitive to effects such as spin–orbit coupling (SOC) (which is often so for molecular structural parameters, such as bond lengths and angles) or to contributions from electrons other than those in the valence (e.g., dipole moments), approximate treatments of relativity can be employed through pseudopotential approaches^{23,24} or by including only scalar relativistic effects. For more challenging applications or higher precision, a more general framework can be based on the solution of the four-component (4C) molecular Dirac equation.^{25–28} At the present time, this approach is often made more tractable by solving the exact two-component (X2C) equation that can be derived from the Dirac equation after a basis set discretization.^{29–39} Both the original 4C approach and its X2C approximation can deliver accurate molecular properties across the Periodic Table and also for properties involving core electrons.^{10,13,40–45}

The one-electron functions (molecular spinors, for simplicity, also referred to in the following as molecular orbitals) obtained from solving the 4C or X2C matrix equations serve then as a basis for a correlation treatment in the so-called no-pair approximation in which contributions to the correlation energy due to admixture of states with explicit electron–positron pairs are neglected.⁴⁶ As the computational cost of 2C approaches is lower than 4C ones, the choice between which treatment to use prior to the correlated treatment will depend on a case-by-case analysis of whether the additional cost of the latter will be offset by improvements in accuracy over the former.

Recently, Pototschnig *et al.*⁴⁷ described a new, efficient relativistic coupled cluster implementation based on ExaTENSOR,⁴⁸ a distributed numerical tensor algebra library for graphical processing unit (GPU)-accelerated high-performance computing (HPC) platforms. This code enabled the calculation of molecular properties with CCSD wave functions for systems such as $[(\text{UO}_2)(\text{NO}_3)_3]^-$ for which 200 electrons and around 1000 virtual molecular orbitals (VMOs) were included in the correlated treatment. Compared to nonrelativistic implementations, it is, in particular, the introduction of SOC that increases the computational cost (although not altering the overall scaling).⁴⁹ Not only does this necessitate the use of complex algebra, it also makes use of contracted basis sets more difficult as one needs to be able to describe the differences in radial extent of spin–orbit split orbitals. This effectively doubles the number of functions that is needed to describe

the p -, d -, and f -type core orbitals⁵⁰ in the case of implementations based on expressing spinors in scalar basis sets.^{26,28,50} In this framework, another complication arises in how to define contractions for the small component part of the spinors that would respect the kinetic balance condition. We note that these problems do not arise in implementations capable of directly evaluating two-electron integrals over 2C spinor basis functions.^{27,51}

The lack of efficient contraction schemes for scalar basis-derived implementations combined with the fact that in many potential applications it may be required that all or a significant part of core electrons (e.g., in core spectroscopies⁴⁵) are treated explicitly, including the deep core orbitals that require many Gaussian type functions to be described correctly, leading to calculations having large virtual spaces. This directly affects the performance of CC-based approaches as these scale with the fourth power of the number of virtuals ($O(V^4)$). In practice, one therefore often alleviates the computational effort to some extent by leaving out high energy virtuals that are mostly localized in the core, but convergence with respect to such an energy cut-off threshold is slow, especially when semi-core or core correlation needs to be described as well.

In non-relativistic electronic structure theory, it has long been recognized that in contrast to canonical Hartree–Fock molecular orbitals (CMOs), natural orbitals (NOs)—the eigenvectors of the one-body reduced density matrix (1RDM)^{52,53}—provide a more compact and quickly converging orbital representation for describing post Hartree–Fock wavefunctions. Based on this observation, the idea of replacing the CMOs by NOs to reduce the size of the virtual space and thereby computational cost was introduced.⁵⁴

Rather than using an energy threshold as is performed by CMOs, one may instead omit NOs, which are likely to not strongly contribute to the total correlation energy from the virtual space. This is performed by considering the magnitude of natural occupation numbers of approximate NOs, obtained from a method that quickly gives access to a reasonable approximation of the 1RDM of the correlated wave function. For this purpose, second order Møller–Plesset perturbation theory (MP2) is a particularly appealing approach to obtain the 1RDM and the approximate NOs because of its low scaling, non-iterative $O(N^5)$, and the ability to recover most of correlation effects. Within the natural orbital family of methods, the virtual frozen natural orbital (FNO) approach^{54–56} has therefore become popular because of its clear concept and simple implementation. FNO theory has been thoroughly discussed for non-relativistic models, such as configuration interaction (CI),⁵⁴ multi-configuration self-consistent field (MCSCF),^{57,58} and coupled cluster.^{56,59} Recently, Verma *et al.*⁶⁰ furthermore extended the FNOs algorithm to quantum computers.

The ability of virtual FNOs to reduce computational cost compared to CMOs is even more appealing in relativistic electronic structure calculations, in particular in the case of contracted basis sets or when correlating sub-valence electrons. The main goal of this paper is therefore to describe and showcase the implementation of MP2-based FNOs (MP2FNOs) within the framework of the new relativistic coupled cluster implementation for massively parallel, GPU-accelerated platforms.⁴⁷ While our code primarily aims at describing cases in which spin–orbit coupling is taken into account, we also demonstrate its use with a non-relativistic Hamiltonian.

Our second aim is to discuss the performance of MP2FNOs across the Periodic Table by treating model systems containing

elements ranging from first-row such as fluorine to superheavy elements such as tennessine. Here, we shall focus in how well truncated FNO spaces describe both correlation energies and first-order properties, such as the electric field gradient at the nuclei (EFGs), parity-violation energy shifts, and electric multipoles (dipole and quadrupole). The first two properties are chosen as representatives of properties for which a good description of wavefunctions in the region close to the nuclei is important (even if only valence electrons are correlated), while the electric dipole and quadrupole moments are an example of properties for which the major contributions arise from valence electrons.

Besides being able to improve the efficiency of a calculation, natural orbitals are also interesting as tools for analysis, such as in estimating the multi-reference character of a system.⁶¹ Their visualization in real space can furthermore provide insight into correlation effects since by their one-particle nature they are easier to interpret than the wavefunction itself. Thus, another aim of our implementation was to provide a tool for obtaining natural orbitals for any correlated wavefunction from a 1RDM. In this paper, we shall make use of the analysis of the CCSD natural orbitals, and in subsequent work, we plan to further explore the use of natural orbitals in visualization.

This article is organized as follows: In Sec. II, the background of MP2FNO theory is summarized. In Sec. III, we described the details of the implementation. All the sample calculations are presented and discussed in Secs. IV and V. In addition, finally, a brief summary is given in Sec. VI.

We note that upon completing this paper, we have become aware of another implementation of the MP2FNO approach for relativistic correlated methods in the BAGH code.⁶² While the main features of the MP2FNOs method are the same in both implementations, we first note that our implementation fully exploits ExaTENSOR's single-node or distributed memory (multi-node) and GPU acceleration capabilities and as such can be efficiently employed in systems ranging from local clusters to latest-generation supercomputers. Second, as it will be outlined in the following, our implementation is capable of manipulating both complex and quaternion density matrices, thus allowing for the generation of both Kramers-restricted and Kramers-unrestricted MP2FNOs. Finally, it allows for re-expressing NOs in the atomic orbital (AO) basis for further analysis.

II. THEORY

As the MP2FNO approach is well-known in a non-relativistic context and requires essentially no modification for application in a no-pair relativistic context, we will only provide a brief description. We apply the orbital-unrelaxed MP2 approximation (for working equations for the orbital-relaxed formalism in a relativistic context, see Ref. 63). The second-order contribution to the occupied-virtual block of the density matrix from single excitations is zero for canonical orbitals⁵³ while the relaxation contributions to this block are ignored in orbital-unrelaxed MP2. This approximation thus decouples the occupied and virtual spaces and allows us to focus only on obtaining the virtual-virtual block of the density matrix. We want to keep occupied orbitals in their canonical form and therefore will not determine the occupied-occupied part of the density matrix for

which we simply retain the diagonal Hartree-Fock form $D_{oo}^{(0)} = I_{oo}$. With these approximations, the second-order FNO density matrix is given as

$$D^{FNO} = \begin{bmatrix} I_{oo} & \mathbf{0}_{ov} \\ \mathbf{0}_{ov} & D_{vv}^{(2)} \end{bmatrix}, \quad (1)$$

with the relevant matrix elements given as

$$D_{AB}^{(2)} = \frac{1}{2} \sum_{C,I,J} \frac{\langle AC||IJ \rangle \langle IJ||BC \rangle}{\epsilon_{IJ}^{AC} \epsilon_{IJ}^{BC}}. \quad (2)$$

Here, following usual conventions, I and J denote the occupied spinors, A and B denote the virtual spinors, and $\epsilon_{IJ}^{AB} = \epsilon_I + \epsilon_J - \epsilon_A - \epsilon_B$ is the energy difference between the canonical Hartree-Fock spinors. In our implementation, these matrices are obtained without imposing any time-reversal symmetry on the spinor set and are thus valid for both Kramers-restricted and Kramers-unrestricted Hartree-Fock procedures. If time-reversal⁶⁴ and spatial symmetry⁶⁵ are not present, these matrices are, in general, to be represented in complex algebra.

The simplest procedure to obtain natural spinors is to apply a diagonalization in complex algebra after $D_{vv}^{(2)}$ is formed. However, for closed shell systems in which time-reversal symmetry is enforced for the orbitals at the mean-field level as is the case in the DIRAC code, one would like to retain such Kramers pairing also for the natural spinors. This requires careful attention when degeneracies beyond the twofold Kramers degeneracy are present as complex diagonalization will arbitrarily mix the degenerate solutions such that Kramers pairing is not guaranteed.

In such cases, Kramers pairing of the natural spinors can be enforced by first transforming $D_{vv}^{(2)}$ from complex to quaternion algebra $D_{vv}^{(Q)}$,

$$D_{vv}^{(Q)} = U^\dagger D_{vv}^{(2)} U, \quad (3)$$

where the transformation matrix U is given by⁶⁶

$$U = \begin{pmatrix} \mathbb{I} & \check{J}\mathbb{I} \\ \check{J}\mathbb{I} & \mathbb{I} \end{pmatrix} \quad (4)$$

and \mathbb{I} is a unit matrix of dimension $n \times n$, with n being the number of Kramers pairs. This transformation will block diagonalize $D_{vv}^{(2)}$, leading to two decoupled matrix problems of half the original dimension in quaternion algebra,

$$D_{vv}^{(Q)} V = O V. \quad (5)$$

Diagonalization of one of the two blocks provides a unique set (V) of quaternion FNOs in the MO basis and their respective occupation numbers (O) from which the solutions for the other block can be generated via Kramers symmetry.

At this stage, we can employ the information from the occupation numbers to reduce the original virtual space V to \tilde{V} by removing from V orbitals with occupation numbers lower than a user-defined threshold. The larger the threshold the smaller the remaining set. In

the numerical examples presented in the following, we will try to find the optimal balance between efficiency (smaller sets) and accuracy (recovering more of the correlation energy and better reproducing first order properties).

After the basis is truncated, it is convenient to re-canonicalize the remaining orbitals. To this end, we perform two operations: first, we transform the virtual–virtual block of the Fock matrix (F_{vv}) into the truncated FNO basis (\tilde{F}_{vv}) and then do a (quaternion re)diagonalization to obtain a new set of canonical orbitals \tilde{W} and orbital energies $\tilde{\epsilon}$,

$$\tilde{F} = \tilde{V}^\dagger F \tilde{V}, \quad (6)$$

$$\tilde{F} \tilde{W} = \tilde{W} \tilde{\epsilon}. \quad (7)$$

The product $\tilde{V} \tilde{W}$ of these two transformation matrices gives the transformation that expresses the re-canonicalized truncated natural orbital set in the atomic orbital (AO) basis. These orbitals can then be used in any subsequent correlated calculation as replacement to the original Hartree–Fock orbitals. In summary, the transformation of the original Hartree–Fock orbitals U to the new set \tilde{U} is thus given by

$$U_{new} = [U_{occ}, \tilde{U}_{vir}], \quad (8)$$

where

$$\tilde{U}_{vir} = U_{vir}(\tilde{V} \tilde{W}), \quad (9)$$

$$\tilde{U}_{occ} = U_{occ}, \quad (10)$$

and the dimension of the rectangular matrix \tilde{V} and that of the square matrix \tilde{U} depend on the truncation threshold.

III. IMPLEMENTATION

The aforementioned algorithm has been implemented in the relativistic quantum chemistry package DIRAC,²⁶ as part of the ExaCorr code.⁴⁷ Our implementation allows for calculations to be carried out either using a single-node configuration (for which ExaTENSOR provides OpenMP parallelization on top of GPU offloading) or employing distributed memory in the case of multi-node runs.

Our implementation is structured following its three main tasks: one module deals with the construction of density matrices in the MO basis, another carries out the complex or quaternion diagonalization of density matrices, and the final module takes care of the construction of the re-canonicalized MP2FNOs. The final step should be repeated if the truncation threshold is changed; the first two are independent of this threshold.

A. Density matrix construction

In ExaCorr, all computationally expensive operations, such as the tensor contractions used in the determination of amplitudes or the construction of density matrices, are offloaded to ExaTENSOR library.

In the case of MP2FNOs, we have created a dedicated driver for MP2 calculations in which we (i) calculate and store in memory two electron repulsion integrals (ERIs) in the AO basis

with the aid of the InteRest library⁶⁷ and (ii) employ the standard Yoshimine scheme⁶⁸ [which scales as $O(N^5)$] to transform the AO integrals to the MO basis. Only the direct and exchange contributions to the $\langle ij||ab \rangle$ (OOVV-type) integrals are calculated, which makes the integral transformation step much faster than the generation of a complete set of MO integrals as is normally performed in ExaCorr. After antisymmetrization, the $\langle ij||ab \rangle$ integrals are stored (in memory) as ExaTENSOR tensors, which may reside on a single node or be distributed over several nodes. Finally, (iii) the MP2 amplitude tensor and the MP2 energy are determined, and the density matrix $D_{vv}^{(2)}$ is constructed according to Eq. (2).

B. Complex-quaternion transformation and diagonalization

The density matrix computed in ExaCorr is generated in complex algebra. The complex-quaternion transformation is carried out following Eq. (27) in Ref. 69,

$${}^Q\gamma_{pq} = \text{Re}(\gamma_{pq}) + \check{i}\text{Im}(\gamma_{pq}) + \check{j}\text{Re}(\gamma_{p\check{q}}) + \check{k}\text{Im}(\gamma_{p\check{q}}), \quad (11)$$

in which lowercase symbols with (without) bars indicate the Kramers pairing of the original MO basis and the one-particle reduced density matrix (1RDM) is now indicated by γ for consistency of the notation with that of Ref. 69. This quaternion form can be diagonalized using the quaternion diagonalization routine provided by DIRAC and be back-transformed to the complex representation by the routines provided in this module. If the original basis did not possess Kramers symmetry, the diagonalization is directly carried out in complex algebra. The resulting full set of FNOs is then stored on a file for analysis and processing by the module (C) described in the following. The module responsible for the quaternion transformation and diagonalization is constructed in such a way that it can also be used with wave function models other than MP2.

C. Selection and re-canonicalization

The third module retrieves FNOs that have occupation numbers above threshold and transforms the original Fock matrix to the truncated virtual space. After re-canonicalization [Eq. (7)] and transformation to AO-basis [Eq. (10)], the final reduced set of FNOs is stored on file. As this step takes virtually no time compared to the other steps in the procedure, this may be easily repeated to test out the effect of varying the threshold value on the generated re-canonicalized orbitals and their energies.

D. Summary of the MP2FNO algorithm

The MP2FNO workflow is schematically represented in Fig. 1 and consists of the following steps:

1. A calculation in the full basis set is performed to get a set of occupied and virtual molecular orbitals.
2. The virtual–virtual block of MP2 density matrix is generated. We note that in this step, it is possible to either consider the full virtual set or already employ a preliminary screening in which, for instance, very high-energy virtuals are neglected.
3. Optional, only for restricted starting orbitals: Transform the complex $D_{vv}^{(2)}$ into the quaternion representation, $D_{vv}^{(Q)}$.

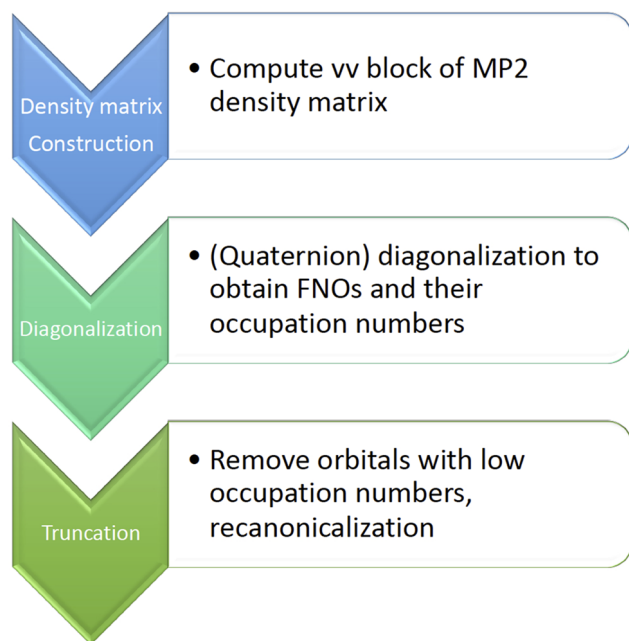


FIG. 1. Work flow of a MP2 frozen natural orbital calculation.

4. Diagonalize D_{vv} or $D_{vv}^{(Q)}$ to determine FNOs and occupation numbers.
5. For a given threshold, truncate the FNO space and transform the Fock matrix to recanonicalize and write the orbitals out in the AO basis.
6. Use the recanonicalized FNOs in higher level wave-function models, such as coupled cluster.

IV. COMPUTATIONAL DETAILS

All MP2 and CC calculations are carried out with development versions (revisions 2e659d7, 0f8e9f2, 9e10bc667, 8b81f8a, e7d2d4d, ec415a5, 0ff0d6f, and d70bbe2) of the DIRAC code^{26,70,71} and of the ExaTENSOR^{48,72} library (revision d304c03b7), employing Dyall basis sets of triple-zeta quality (dyall.av3z)^{73–75} for the heavy elements (Br, I, At, Ts, and Se), and Dunning aug-cc-pVTZ sets^{76–78} for (H, F, Cl, O, and S), all of which are left uncontracted unless otherwise noted. The aug-cc-pCVTZ basis set was also employed in the HCl case^{79,80} for investigating how the additional core correlating functions in aug-cc-pCVTZ affect the results. Finally, for investigating the convergence of expectation values for HI, we employed double-zeta quality Dyall^{73,74} (dyall.av2z) and Dunning^{76–78} (aug-cc-pVDZ) basis sets for I and H, respectively.

Here, we make use in all calculations of the exact two component Hamiltonian (X2C)³² in which we include two-electron spin-orbit contributions to the untransformed two-electron potential via atomic mean-field contributions calculated with the AMFI code.^{81–83} In our calculations, we have made use of Kramers symmetry in the generation of the molecular spinors.²⁶ As part of

the [supplementary material](#), we provide in Table S2 results with different Hamiltonians (Dirac-Coulomb, X2C, spinfree X2C, and non-relativistic) for expectation values for the HTs molecule. We note the code is equally capable of handling orbitals obtained with the so-called molecular-mean-field approach in which the transformation to 2C is carried out after a 4C mean-field calculation.³⁹ In the case of the HCl molecule, we have also employed the non-relativistic Hamiltonian (as specified by the .NONREL keyword), both with contracted and uncontracted bases sets.

The molecular structures employed in all calculations have been taken from the literature: In the case of hydrogen halides, from Huber⁸⁴ for HF to HI, from Gomes and Visscher⁴¹ for HAt, and from Thierfelder *et al.*⁴² for HTs, the internuclear distances employed are thus H-F(0.9168 Å), H-Cl(1.274 55 Å), H-Br(1.414 43 Å), H-I(1.609 Å), H-At(1.722 Å), and H-Ts(1.941 Å). For the chiral molecules H₂Z₂, the Z-Z bond length, H-Z bond length, and H-Z-Z bond angle are taken from Table I of Laerdahl and Schwerdtfeger,⁸⁵ and the dihedral angle is fixed at 45° throughout the computation. All calculations have been carried out with a point charge nucleus model.

Besides calculating MP2, CCSD, and CCSD(T) energies, we have obtained electric dipole moment (EDM), electric quadrupole moment (EQM), and electric field gradient (EFG) for the HX systems and parity violation energy differences (PV) for H₂Z₂ systems. These properties have been obtained analytically for CCSD wavefunctions using the implementation described in Ref. 69.

In the calculations, the size of the complete virtual spinor spaces is 156 (HF), 182 (HCl), 310 (HBr), 382 (HI), 544 (HAt) and 588 (HTs), 314 (H₂O₂), 366 (H₂S₂), and 622 (H₂Se₂). Unless otherwise noted, all electrons were correlated in the calculations. For the smaller systems HF, HCl, HBr, H₂O₂, and H₂S₂ we were able to perform calculations on a single node of the laboratory compute cluster in Lille. For HI, HAt, H₂Se₂, and HTs we employed, respectively, 32, 32, 49, and 64 nodes of the Summit supercomputer. For HI calculations with double-zeta quality basis sets, we were able to perform single-node calculations on the Jean Zay supercomputer.

The data presented in this paper are available at the Zenodo repository of Ref. 86.

V. RESULTS AND DISCUSSION

In this section, we discuss the performance of the MP2FNO approach for the CCSD correlation energy and molecular properties and the impact of employing different occupation number thresholds on the results. In order to minimize computational cost on our systematic studies, we carried out CCSD(T) calculations only when discussing the effect of FNO and CMO truncation on HCl bond lengths.

For minimizing the bias in the CMO and FNO comparison, we report results in which we employ the closest possible number of CMO to that of FNO such that for CMO we avoid truncations that would remove close-lying orbitals, such as those belonging to the same atomic shell. In practice, this means CMO calculations generally contain a few more orbitals than FNO ones.

In Fig. S1 in the [supplementary material](#), we present for the EFG of HI the difference between the approach taken here for CMO and that of strictly considering the same number of CMO and FNO.

We can see that arbitrarily truncating the virtual space for CMO can lead to large oscillations in the expectation values, a point that will be addressed in detail in the following. Additionally, from the comparison of Hamiltonians for HTs in Table S2 in the [supplementary material](#), we see that our choice of the X2C Hamiltonian is a suitable one for our purposes; while total energies obviously are very different between Hamiltonians, we see that for those taking into account SOC, relative energies (HOMO–LUMO gap) and expectation values are very close to each other. This is in stark contrast with scalar relativistic and non-relativistic calculations, which still show fairly good agreement with 2C/4C approaches for the quadrupole moment and even the HOMO–LUMO gap but are completely off the mark for the EFG and dipole moment. This is due to the very strong spin–orbit splitting in the valence p-shell of the superheavy tennesse.

A. Correlation energy

CCSD correlation energies obtained with CMO and FNOs are displayed in [Fig. 2](#) for the hydrogen halides. In these, we show values computed for four values of natural occupation number

threshold (1.0×10^{-3} , 1.0×10^{-4} , 1.0×10^{-5} , 1.0×10^{-6}) as well as the two extrema: a point without any virtual orbitals (corresponding to the Hartree–Fock solution) and another without any truncation of the virtual space. Since the number of virtuals varies for each system, we provide relative measures in terms of the percentage of the virtual space included in the calculations for each point and likewise for the amount of correlation energy recovered at each point.

From the plots, it is clearly the case that FNOs show a more rapid convergence than CMO across the Periodic Table, as could be expected from the non-relativistic literature.^{56,59,87} For example, to recover only 50% correlation energy, already 40%–50% of the virtual CMO space is required while only 20% of the FNO space suffices. In addition, for the more realistic goal of attaining at least 90% of the correlation energy, the use of FNOs can reduce the required space by 10 s of %, thereby introducing significant savings in (memory) storage of tensors with virtual indices as well as in operation counts for contractions involving virtual indices in the CCSD equations.

An interesting finding is that the area enclosed by two lines slightly decreases as we go down the Periodic Table from F to Ts. This means that the FNO approach recovers less correlation for a

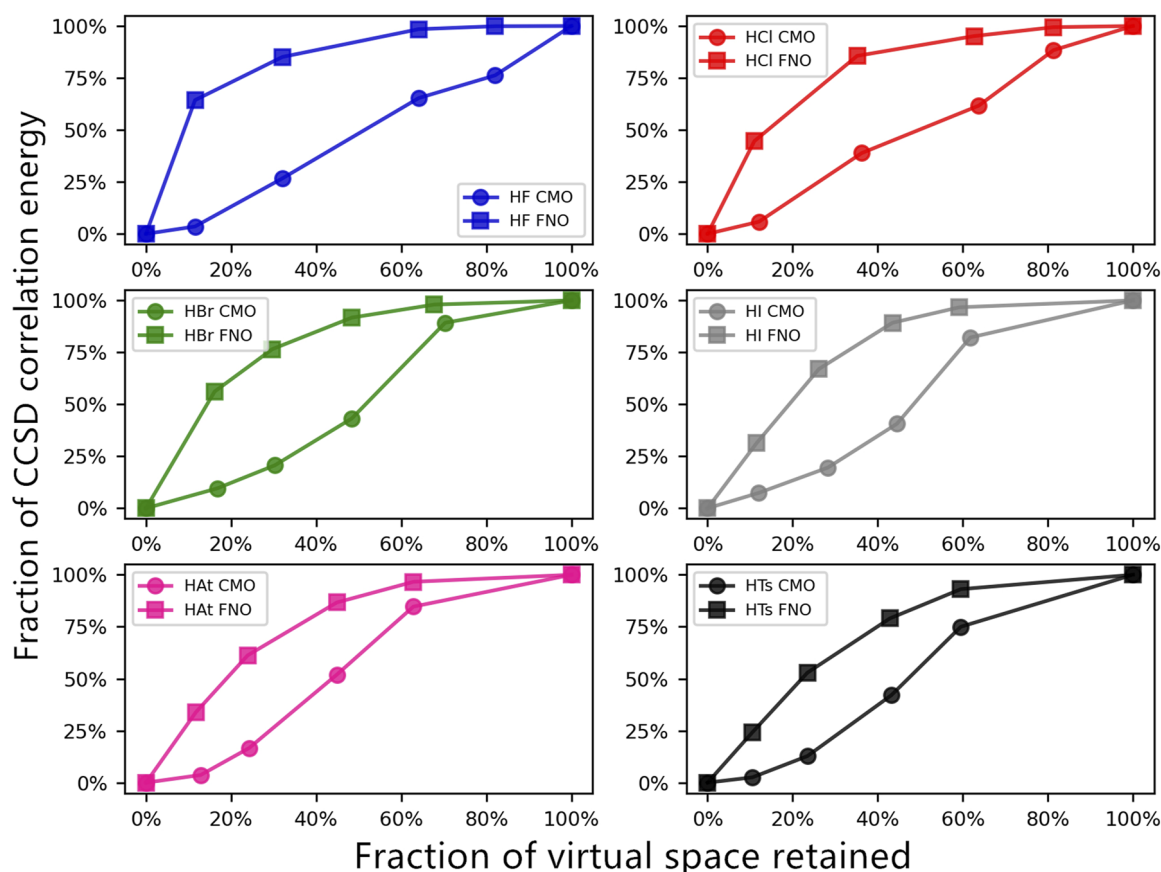


FIG. 2. Convergence of the CCSD correlation energy with respect to the size of the virtual orbital space for the X2C Hamiltonian. The X axis indicates the fraction of the virtual space retained, while the Y axis gives the fraction of the correlation energy recovered with respect to the value obtained with the untruncated virtual space.

given truncation as the number of electrons increases. For example, a threshold of 1.0×10^{-5} (the fourth point in Fig. 2) means, for HF and HCl, that more than 60% of the virtual space is included in the calculation, whereas for HTs, the same threshold only includes 43%; this means that for HTs, virtual orbitals with low occupation numbers are still important for the correlation treatment.

Apart from testing the performance for a single point at the potential energy surface, it is also important to verify the performance of FNOs at different geometric structures. To this end, in Fig. 3, we present the potential energy curves around equilibrium for HCl at the CCSD(T) level, comparing sets of FNOs and CMO virtuals that are truncated to the same number of virtuals (corresponding to about 50% of the complete virtual space). We see that except for a global energy shift, the FNOs follow the curvature of the full virtual space potential energy curve more closely than the CMO curve does.

The better agreement of FNOs relative to CMOs can be quantified by a comparison of spectroscopic constants for the three curves, shown in Table I. There, we report the equilibrium distance (R_e) and vibrational constant (ω_e) calculated with the LEVEL program.⁸⁸ Taking the full valence space result as a reference, the truncated orbitals overestimate R_e but underestimate ω_e . However, the error of truncated FNOs is 0.0037 \AA (R_e) and 17 cm^{-1} (ω_e), which is only half that of truncated CMOs.

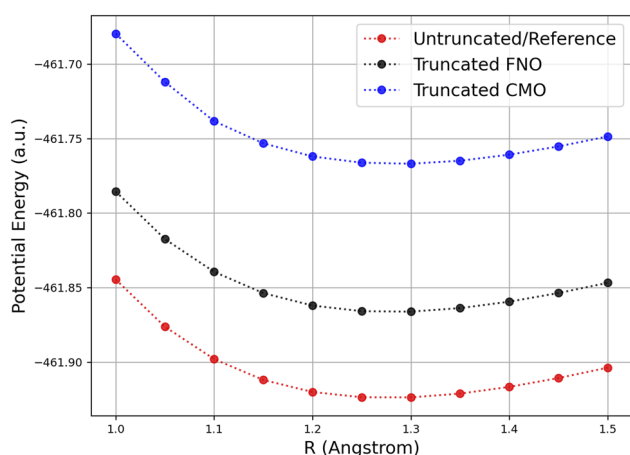


FIG. 3. Potential energy curves of HCl at the CCSD(T) level using untruncated orbitals (red) as the reference, truncated FNO (black), and truncated CMO (blue). The X axis is the internuclear distance, and the Y axis is the total energy in hartrees.

TABLE I. Spectroscopic constants of the ground state of HCl.

	R_e (\AA)	ω_e (cm^{-1})
Exp	1.2746	2991
Untruncated orbitals	1.2756	2986
Truncated CMO	1.2859	2942
Truncated FNO	1.2793	2969

As we correlated all electrons but employed basis sets without specific core correlating functions, one may ask what would be the effect of including such functions. In Table S1 of the supplementary material, we provide a comparison of correlation energies and expectation values between the uncontracted aug-pVTZ and aug-pCVTZ basis sets for the HCl molecule without using virtual space truncation. These results clearly indicate that although the additional high angular momentum core correlating functions are quite important for increasing the amount of correlation energy for the core and core-valence interactions, the two types of uncontracted basis sets agree well for the computed property values. Another interesting point to note is that as can be seen from Table S3 of the supplementary material, the percentage of correlation energy recovered at each virtual space truncation point is nearly the same for MP2 and CCSD. This indicates that the information obtained from the full virtual space MP2 calculation preceding the truncation can potentially be used to correct the CCSD correlation energy for the effect of truncation. While going beyond the scope of this paper, this point merits further investigation in which also correction for truncation errors in higher order methods, such as CCSD(T), could be investigated.

B. Molecular properties

1. Electric dipole and quadrupole moments

To assess performance of FNOs for molecular properties, we first considered the molecular EDM and EQM because these do well characterize the overall electronic charge distribution within molecules. These properties sample the regions away from the nuclei as is clear from their operator forms in Eqs. (12) and (13), respectively,

$$D_\mu = e \sum_i (\vec{r}_i)_\mu, \quad (12)$$

$$Q_{\mu\nu} = e \sum_i ((\vec{r}_i)_\mu (\vec{r}_i)_\nu - r_i^2 \delta_{\mu\nu}). \quad (13)$$

Figure 4 shows how the EDM and EQM correlation correction varies with the truncation of the virtual orbital spaces with dotted and solid lines representing EDM and EQM, respectively. As before, FNO results are plotted with square markers. For these properties, the convergence is non-monotonic, unlike energy that we considered before. For both CMO and FNO truncation, the use of a high truncation value and consequently small virtual space (less than 30% virtual orbitals) may lead to a strong overestimation or even a wrong sign of the correlation correction to the molecular property. Especially, for CMO truncation, it is almost impossible to estimate the truncation error from a sequence of results for small virtual spaces. For FNO truncation, oscillations are much less pronounced than for CMO, which indicates that also for these properties it is advantageous to use FNO truncation rather than CMO truncation. The similar performance for the correlation energy could thereby be used as a guideline. Taking the HF molecule as an example, we note that with a threshold of 1.0×10^{-4} , the FNOs recover 72% of the correlation contribution to EDM while recovering 85% of the correlation energy. This indicates that the simplification of using a common cutoff for both properties could be a suitable strategy. In addition, we note that the performance of FNOs in EDM also

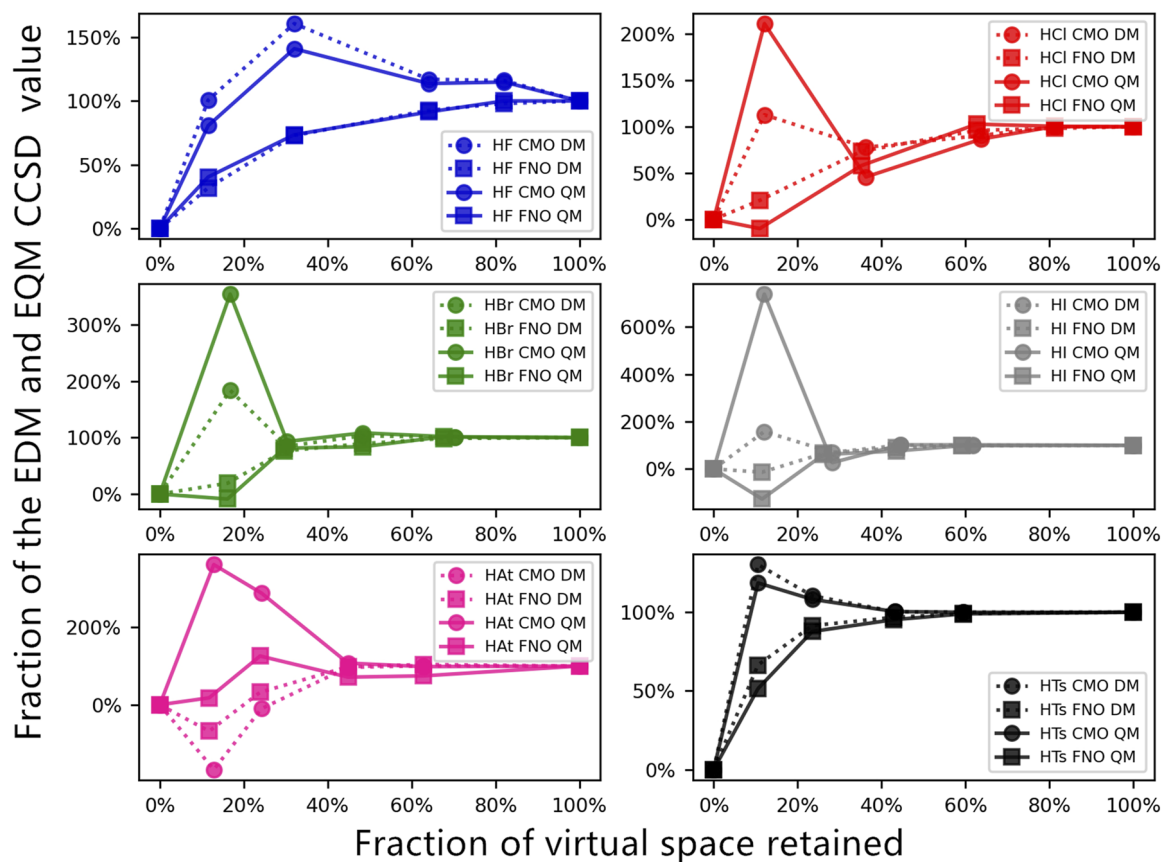


FIG. 4. Convergence of the CCSD electric dipole and quadrupole moments with respect to the size of the virtual orbital space for the X2C Hamiltonian. The X axis indicates the fraction of the virtual space retained, while the Y axis gives the fraction of the expectation values recovered with respect to the value obtained with the untruncated virtual space.

applies to the heavier elements in the studied series. Even for HTs, setting the truncation threshold to 1.0×10^{-4} (using only 23% of the orbital space) already recovers 91% of the correlation contribution to the EDM.

The EQM shows a similar behavior as the EDM, albeit with stronger oscillations. The largest oscillations for the EQM occur at the same position as for the EDM, but the amplitude thereof is much larger. This is again most pronounced in the CMO case. Taking HI as an example, retaining 12% of the CMO virtual space overestimates the correlation contribution to EDM by 150%, while the EQM contribution is even seven times too large. As for the EDMs, the oscillations resulting from FNO truncation are smaller and convergence is more smooth, which should make it possible to use a more aggressive cut-off strategy than is possible with CMOs.

2. Electric field gradient

To also consider the effect of truncation on properties that probe the regions close to atomic nuclei, we now turn to the electric field gradients (EFGs) at the halogen nuclei. EFGs couple with nuclear quadrupole moments⁸⁹ for nuclei with spin greater or equal to one and are important in the analysis of nuclear magnetic

resonance (NMR) experiments.⁹⁰ For EFGs, both (semicore) correlation and SOC effects are known to be of importance,⁹¹ and they form therefore a good second test for the applicability of FNO truncation in relativistic calculations. The EFG is defined as the second derivative of the electric potential $V(\mathbf{R})$ with respect to the nuclear position vector, taken at the nuclear position \mathbf{R}_N ,

$$q_{\mu\nu}(\mathbf{R}_N) = -\frac{\partial^2 V(\mathbf{R})}{\partial R_\mu \partial R_\nu} \Big|_{\mathbf{R}=\mathbf{R}_N}. \quad (14)$$

By introducing the EFG tensor operator,⁹²

$$\hat{q}_{\mu\nu}^e = \frac{3(\vec{r} - \vec{R}_N)_\mu(\vec{r} - \vec{R}_N)_\nu - |\vec{r} - \vec{R}_N|^2 \delta_{\mu\nu}}{|\vec{r} - \vec{R}_N|^5}, \quad (15)$$

the EFG can be expressed as the expectation value of a one-body operator, which makes evaluating its value similar to computing the EDM and EQM.

For linear molecules, it suffices to compute only the zz -component (with the z axis chosen along the molecular bond) as the other non-zero parts of the tensor can then be determined by symmetry. Figure 5 plots this zz component of the EFG and

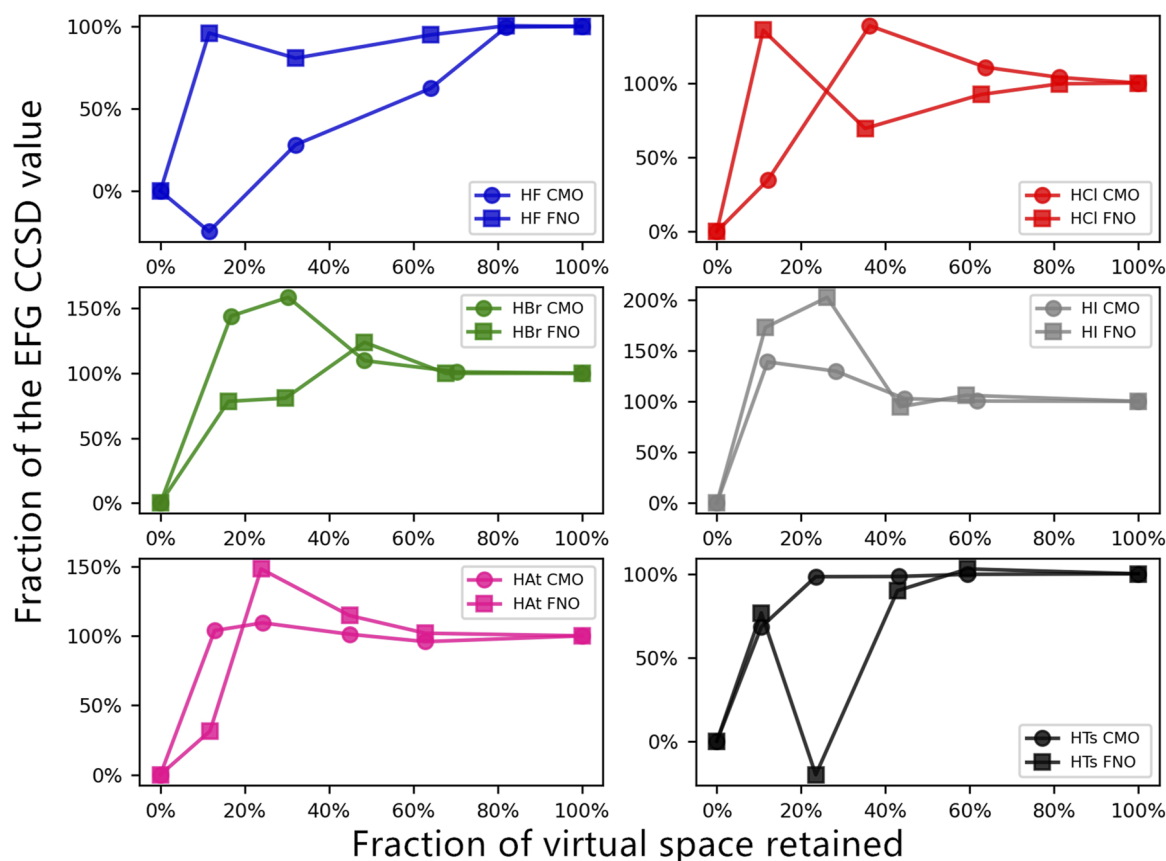


FIG. 5. Convergence of the CCSD electric field gradient at the halogen nucleus with respect to the size of the virtual orbital space for the X2C Hamiltonian. The X axis indicates the fraction of the virtual space retained, while the Y axis gives the fraction of the expectation value recovered with respect to the value obtained with the untruncated virtual space.

shows for both FNO and CMO oscillations upon truncating the orbital spaces. In the case of correlating all electrons, we see that FNO truncation leads to worse performance than CMO truncation due to even more rapid oscillations. Recalling that the only difference between computing the EFG and EDM properties is in the operators used, it is of interest to consider their differences. The EFG tensor operator scales as r^{-3} in contrast to the r^1 and r^2 scaling of the EDM and EQM operators. Density changes in the core region due to correlation are thus magnified by the EFG operator while they are hardly of influence for the EDM and EQM. Such changes may both come from core correlation as well as from correlating the valence electrons (through the tails of the valence orbitals in the core region). As core correlation may be harder to converge than valence correlation, we will separate the two effects by comparing all-electron and valence-only electron calculations in Subsec. V B 3.

3. Convergence analysis for HCl and HI

The issue of oscillating convergence can be conveniently analyzed for the HCl molecule as chlorine is large enough to investigate

the effect of core correlation yet small enough to allow for quick calculations. Rather than taking only a few truncation values, we now systematically extend the size of the virtual space by adding individual FNOs and show the effect thereof on the EDM, EQM, and EFG of HCl in Fig. 6 for both all-electron and valence-only correlation calculations.

For the all-electron case, we see in the EDM and EQM plots for CMO truncation peaks when 13 and 23 orbitals are used. This is probably due to quasi-degeneracies as the orbital energies of the 12th, 13th, and 14th orbital are 0.424 18, 0.436 57, and 0.436 73 hartree, respectively. This set of virtual orbitals is primarily a diffuse chlorine p-type orbital shell that is split due to the formation of the hydrogen–chlorine bond as well as due to spin–orbit coupling. Taking only one of the two almost degenerate π -type orbitals in the correlation space gives an unbalanced description and impacts these valence properties significantly. For the EFG, this particular set of three CMOs is less important because diffuse orbitals only contribute indirectly to this property. For the EFG, one may notice (Fig. 6, lower left panel, blue line) a large oscillation around virtual orbital number 70 in the all-electron calculation.

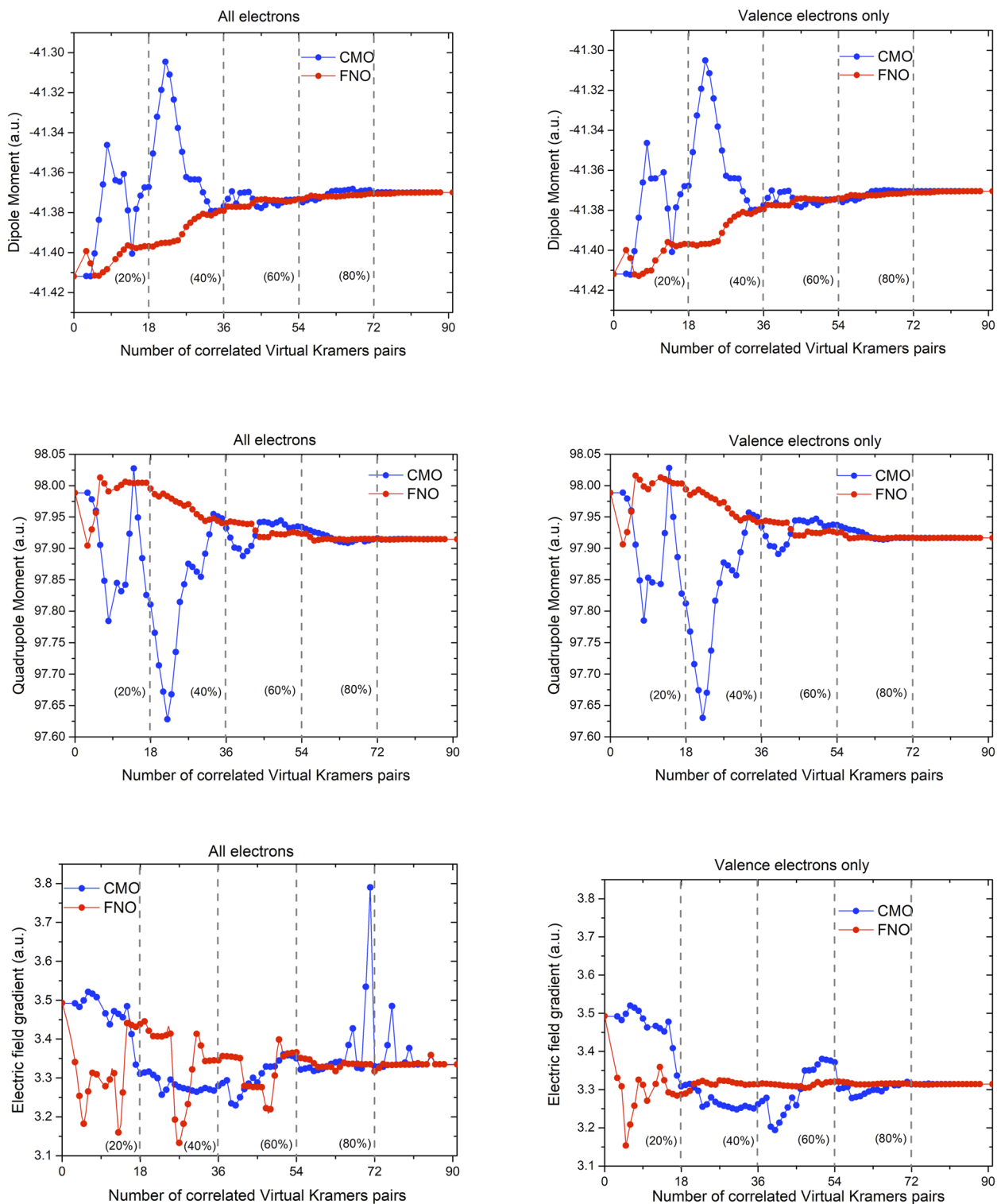


FIG. 6. Effect of virtual space truncation on the expectation values (top panel: EDM, middle panel: EQM, bottom panel: EFG) of HCl for the X2C Hamiltonian. The X axis gives the number of correlated virtual Kramers pairs up to and including the full virtual space (the rightmost points in the graphs correspond to calculations with the full virtual space). Figures to the left correspond to calculations correlating all electrons and to the right correlating valence electrons only.

This is due to the more core-like p -orbitals 70, 71, and 72 with energies of, respectively, 35.63, 35.73, and 36.10 hartree, which are impacting the correlation of core electrons. Restricting the correlation treatment to valence electrons only strongly reduces the effect of these virtuals (Fig. 6, lower right panel).

The FNO curves for the EDM and EQM show only an initial oscillation that is followed by rather smooth convergence. This initial oscillation can also be traced to quasi-degenerate orbitals (but now in terms of occupation numbers). For the FNOs, the occupation numbers of the 2nd, 3rd, 4th, and 5th orbital are 0.008 692, 0.008 676, 0.008 508, and 0.008 491, respectively, and like with near-degenerate CMOs, it appears recommendable to either include all or none of a degenerate set. For the EFG, the situation is unfortunately more complicated, also with FNOs.

In the all-electron calculation, values only stabilize after inclusion of about 50 orbitals, while in the valence-only calculation, stable convergence is reached after addition of about 20 FNOs. Compared to the CMO truncation scheme, the advantage of FNO truncation appears to be the absence of “late” oscillations (at low threshold values) that could cause artifacts in the CMO truncation schemes. Such oscillations are typical for EFGs for which an individual orbital may provide a significant contribution but where the contribution of full, spherically symmetric shells of orbitals adds up to zero due to symmetry. This is well-known for CMOs but also holds for FNOs. An example is the EFG integrals of the 13th, 14th, and 15th FNOs, which evaluate to -78 , 44 , and 26 a.u. These large values get multiplied by very similar occupation numbers (respectively, 7.9×10^{-4} , 7.0×10^{-4} , and 7.0×10^{-4}) so that their contributions to the total EFG nearly cancel.

A similar argument can be used to rationalize the difference between the valence and all-electron calculations. In the correlation of core orbitals, one effectively changes the relative occupation of the three $2p$ orbitals in the chlorine core by making their occupations slightly smaller than two. Imbalances in the correlation get thereby for the EFG multiplied by large integral values (about 80 au for the $2p_{3/2}$ orbitals), which creates the large oscillation seen in these calculations. For EDMs and EQMs, the integral values are much more alike and smaller in the magnitude, leading to the observed smoother convergence.

To check if such oscillation problems are particular for the relativistic domain or can also be found in the non-relativistic case, we have carried out the same analysis as above by employing a non-relativistic Hamiltonian, employing both contracted and uncontracted (valence) basis sets and correlating both valence and all electrons. The results are shown in Fig. 7.

From these, it can be seen that for the electric dipole and quadrupole moments, the non-relativistic calculations basically show the same oscillations as for X2C, and results for contracted and uncontracted basis sets are nearly indistinguishable from each other. For the EFG, there is also no noticeable difference for the convergence patterns between X2C and non-relativistic results for uncontracted basis sets.

On the other hand, we observe significant differences between EFG calculations employing contracted and uncontracted basis sets. The first one is that already at the Hartree–Fock level, there is a significant difference (nearly 10%) on the absolute value of the EFG with contracted values underestimating uncontracted ones. Second,

we note that with contracted basis sets, there are very few oscillations in FNO EFG values (even when correlating all electrons), and FNO results are already quite stable for a much lower number of virtuals than CMO results (CMO EFG values are still not completely converged at nearly full virtual spaces for the contracted sets).

This can be understood as a manifestation of the degree of atomic symmetry that is imposed by the contraction for the different orbital shells, particularly for the occupied core orbitals. In the contracted sets, these are forced to maintain their atomic-like nature during the molecular calculation because electron correlation cannot as easily deform the orbitals as is possible when the basis set is uncontracted. This is underscored by the nearly identical behavior of the contracted all electron and valence calculations as in the latter core orbitals are kept frozen.

To check if the convergence behavior mentioned above is also found for a heavier system, we carried out similar calculations for HI but using an uncontracted double zeta basis set. It can be seen from Fig. 8 that although HI has many more electrons, it still shows a very similar convergence as observed for HCl. For instance, to get a converged EFG value of HI, in the valence only computation, one just needs to correlate 20 FNOs.

Looking at these tests, we may conclude that for properties such as EDM and EQM, which are dominated by valence electron contributions, one can safely use FNOs and their occupation numbers to cut off the orbital space, both in valence-only and all-electron correlation calculations. For sensitive properties for which core electrons may give large and nearly canceling contributions, it is also with FNOs numerically more stable to correlate only the valence electrons.

C. Parity violation

Detection of parity violation (PV) effects associated with weak force in atoms and molecules is an active field of research.^{13,93,94} While this property can also be computed with perturbation theory starting from nonrelativistic theory,⁹⁵ it is advantageous to use a relativistic quantum chemistry framework because the PV energy can then be formulated as an expectation value of an effective one-body operator,⁸⁵

$$E_{PV} = \sum_A \langle \Psi | \hat{H}_{PV}^A | \Psi \rangle, \quad (16)$$

with

$$\hat{H}_{PV}^A = \frac{G_F}{2\sqrt{2}} Q_W^A \sum_i \gamma_i^5 \rho^A(r_i) \quad (17)$$

and $G_F = 1.166\ 37 \times 10^{-11}$ MeV $^{-2}$ being the Fermi coupling constant. The A and i label nuclei and electrons, respectively. The weak charge $Q_W^A = -N_A + Z_A(1 - 4 \sin^2 \theta_w)$, where N_A and Z_A is the number of neutrons and protons in each nucleus, respectively. θ_w is Weinberg mixing angle, which is set to 0.2319 for $\sin^2 \theta_w$. ρ^A and γ_i^5 are normalized nucleon density and 4-dimensional chirality operator, respectively,

$$\gamma^5 = \begin{pmatrix} \mathbb{O} & \mathbb{I} \\ \mathbb{I} & \mathbb{O} \end{pmatrix}. \quad (18)$$

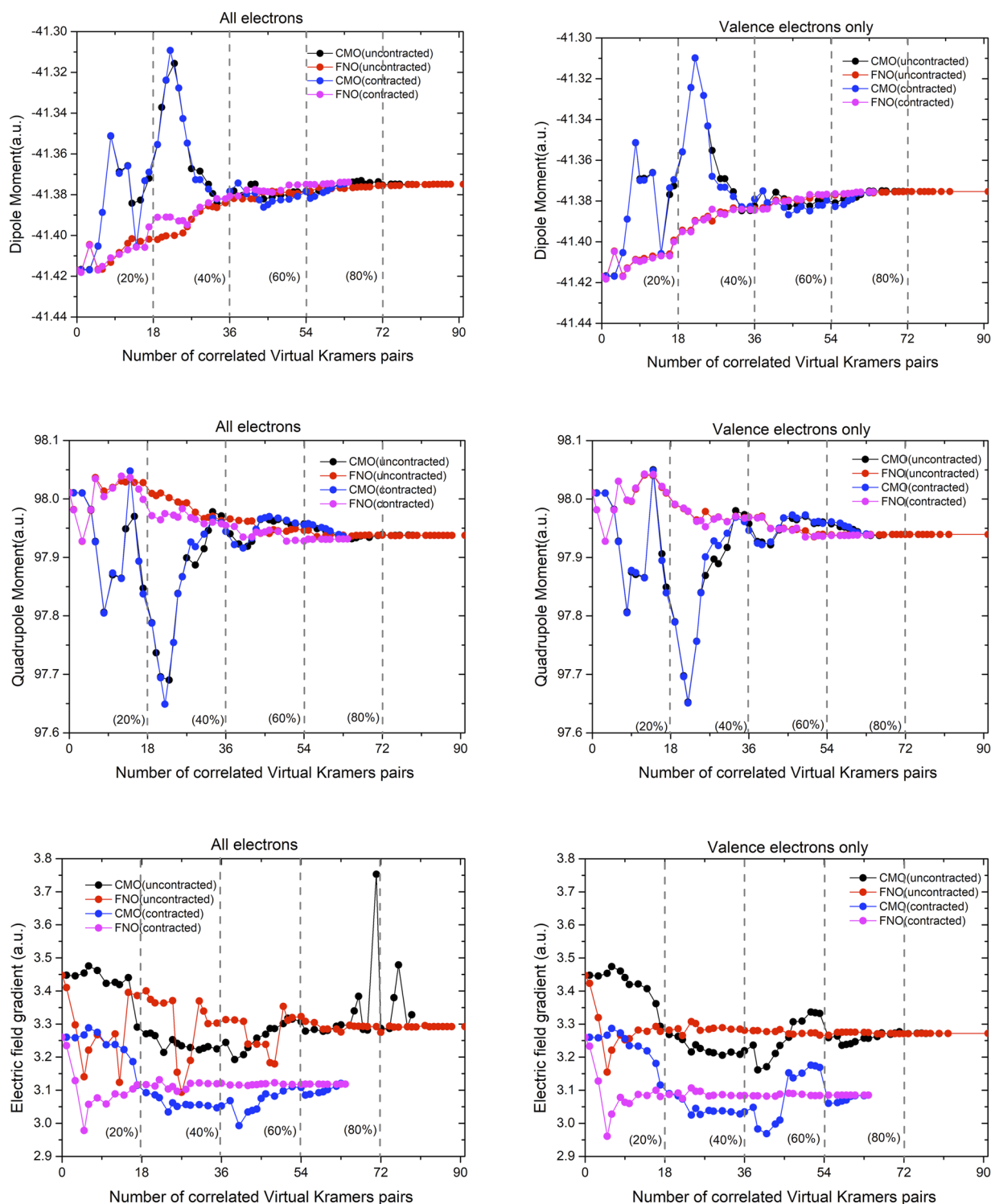


FIG. 7. Effect of virtual space truncation on the expectation values (top panel: EDM, middle panel: EQM, bottom panel: EFG) of HCl for the non-relativistic Hamiltonian and employing contracted and uncontracted Dunning basis sets. The X axis gives the number of correlated virtual Kramers pairs up to and including the full virtual space (the rightmost points in the graphs correspond to calculations with the full virtual space). Figures to the left correspond to calculations correlating all electrons and to the right correlating valence electrons only.

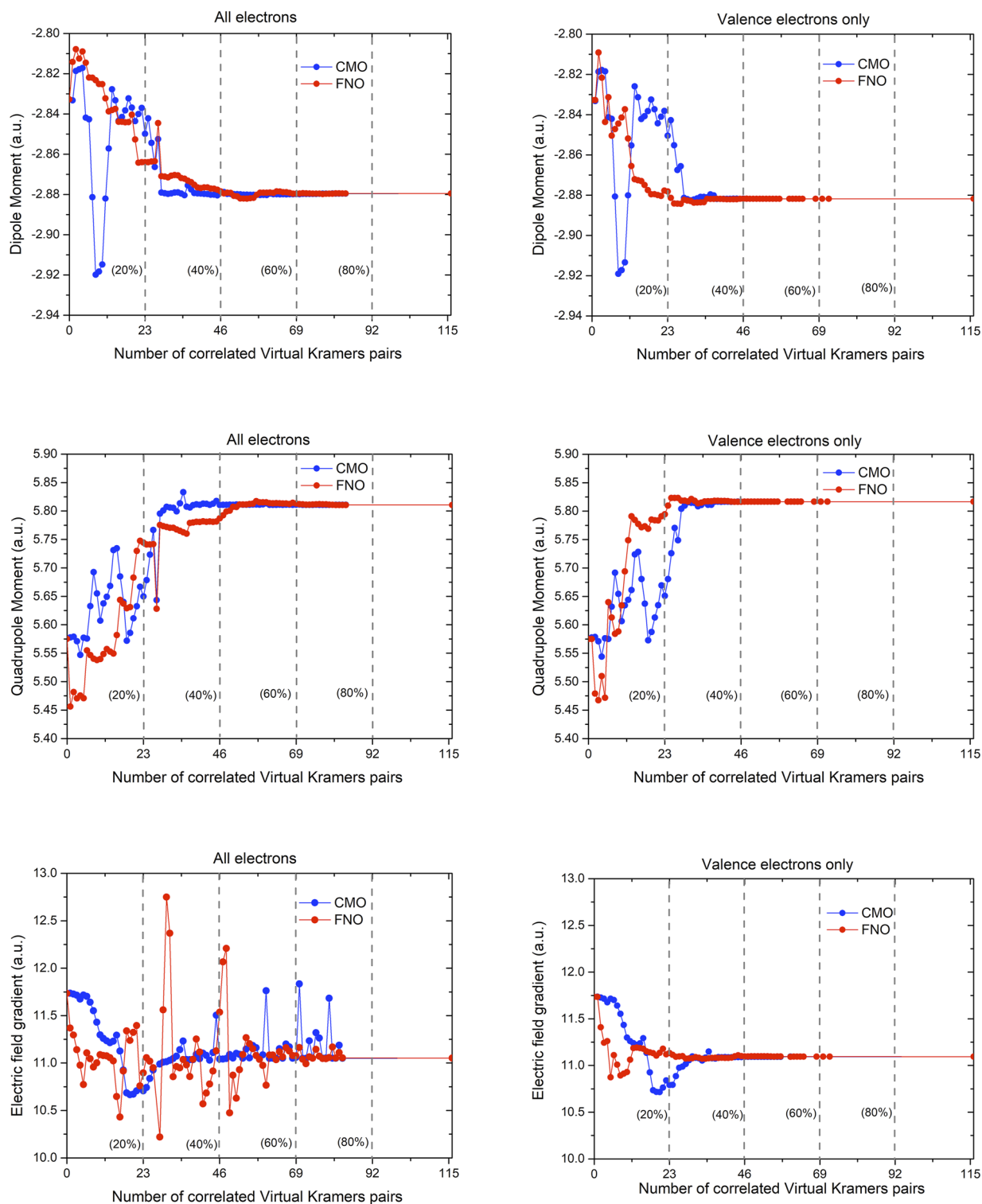


FIG. 8. Effect of virtual space truncation on the expectation values (top panel: EDM, middle panel: EQM, bottom panel: EFG) of HI for the X2C Hamiltonian. The X axis gives the number of correlated virtual Kramers pairs up to and including the full virtual space (the rightmost points in the graphs correspond to calculations with the full virtual space). Figures to the left correspond to calculations correlating all electrons and to the right correlating valence electrons only.

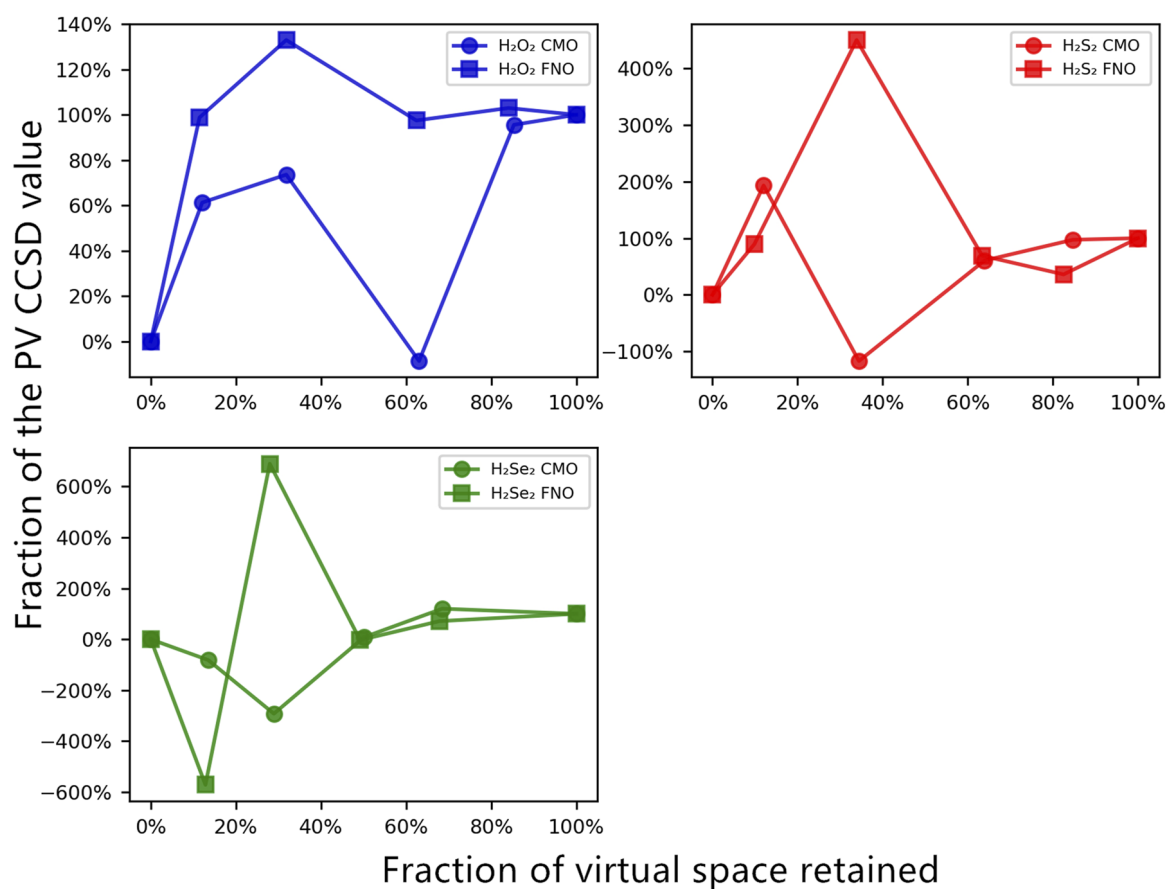


FIG. 9. Convergence of the CCSD PV energy with respect to the size of the virtual orbital space for the X2C Hamiltonian. The X axis indicates the fraction of the virtual space retained, while the Y axis gives the fraction of the expectation value recovered with respect to the value obtained with the untruncated virtual space.

Sunaga and Saue¹³ already investigated the use of CMO truncation at the CCSD level with two different threshold values and showed that truncation is well possible for this property. In current work, we also employ FNO truncation and test more thresholds for CMO truncation and its effect on the PV value.

The results of the two truncation schemes for the H₂Z₂ (Z = O, S, Se) molecules are displayed in Fig. 9. We find that both FNO and CMO truncation lead to strong oscillations such as those observed in the EFG case. Again, these are most pronounced for aggressive truncation in which more than 50% of the virtual orbital space is removed. Looking more closely at these systems, we find that orbital energies (for CMO) or occupation numbers (for FNO) show a number of near-degeneracies. These orbitals give individually large but partially canceling contributions. We have not investigated valence-only correlation explicitly for this property as core contributions are probably more important than for the EFG, and it is more difficult to define a representative small test case. For our current tests, we note that the convergence behavior is consistent with results of Ref. 13 in which rather conservative CMO truncation thresholds of 100 and 500 Hartree were used for H₂Se₂. With both CMO

and FNO truncation, a 50% reduction appears realistic, leading to a significant reduction in the computational effort. For instance, in the current test, the H₂Se₂ calculation on 49 nodes of Summit with the full orbital space took 100 min while the 50% reduced calculation took only 20 min.

Nevertheless, for the particular case of PV energy evaluation, FNO truncation does not appear to give a significant advantage over the simpler CMO truncation scheme. Apart from the sensitivity of the PV operator on core correlation already observed in the EFG evaluation, another possible reason is our use of the unrelaxed MP2 density matrix. Shee *et al.*⁶⁹ found for H₂S₂ that the contribution of orbital relaxation to the density matrix is significant when used to evaluate this property. It would be interesting to investigate how these contributions impact the generated FNOs are thereby the convergence of the FNO truncation scheme.

VI. CONCLUSIONS

In this work, we describe the formulation and implementation of the MP2 frozen natural orbital (MP2FNO) method for relativistic

electronic structure calculations, which is an appealing approach for truncating the large virtual orbital spaces typically associated with relativistic calculations while retaining the high accuracy expected of wavefunction-based approaches, such as coupled cluster.

This implementation was carried out in the massively parallel coupled cluster module of the DIRAC program with the help of a framework to manipulate 1RDMs obtained from correlated wavefunction calculations. A particularity of our code is its ability to generate a set of canonical occupied and truncated virtual orbitals as well as natural orbitals in the atomic basis so that these can be conveniently employed in post-Hartree–Fock calculations and also used for analysis.

We employed our code to investigate the performance of MP2FNOs for the calculation of correlation energies and ground-state first-order properties, such as dipole and quadrupole moments, electric field gradient at the nuclei, and parity violation energy shifts. As model systems, we considered species containing elements from the first row up to and including the superheavy element tennessine.

We have found that although MP2FNOs are always capable of recovering more correlation energy than their canonical counterparts for a given truncation, this advantage is slightly diminished for the heaviest systems considered, containing astatine and tennessine. Despite that, it is generally found that MP2FNOs can reduce virtual spaces to about 50% of their original size without significant errors in the energy.

Among the properties considered, a truncation of about 50% of the original virtual space has also been shown to provide values that are nearly converged to the results without truncation. That said, different properties exhibit very different convergence behavior; for valence properties, such as the electric dipole moment, MP2FNOs show a fairly smooth convergence to the reference values, whereas for the electric field gradient and, in particular, the parity violation energy shifts for which regions close to the nuclei are important (and thus, higher-lying virtuals are more important in the correlation treatment), significant variations on the calculated values are found for virtual spaces smaller than 50% of the original virtual space.

We have found that for EFGs, correlating only valence electrons provides a pragmatic solution that recovers the smooth convergence seen for valence properties by removing difficult to converge, individually large but in total nearly canceling, contributions from the core electrons. Whether such a strategy can also work for the PV energy shifts remains to be investigated.

As a final point and perspective, we note that improvement of the efficiency of the current scheme is well possible by implementing efficient approximate schemes, such as Cholesky decomposition and Laplace transforms, to generate the MP2 1RDM. Work along these lines is in progress and should enable treatment of larger systems in the future.

SUPPLEMENTARY MATERIAL

See the [supplementary material](#) for further details on the comparison of Hamiltonians for the HTs molecule, the influence of core correlation functions on the correlation energies and expectation values for the HCl molecule, the convergence of EFG for iodine in HI, and the fraction of MP2 and CCSD correlation energies

recovered with different FNO truncations for the hydrogen halide series.

ACKNOWLEDGMENTS

We acknowledge funding from projects Labex CaPPA (Grant No. ANR-11-LABX-0005-01) and ComprIXS (Grant Nos. ANR-19-CE29-0019 and DFG JA 2329/6-1), the I-SITE ULNE project OVERSEE and MESONM International Associated Laboratory (LAI) (Grant No. ANR-16-IDEX-0004), and support from the French national supercomputing facilities (Grant Nos. DARI A0090801859 and A0110801859).

This research used resources of the Oak Ridge Leadership Computing Facility, which is a DOE Office of Science User Facility supported under Contract No. DE-AC05-00OR22725.

AUTHOR DECLARATIONS

Conflict of Interest

The authors have no conflicts to disclose.

Author Contributions

Xiang Yuan: Investigation (lead); Methodology (equal); Software (equal); Writing – original draft (lead); Writing – review & editing (equal). **Lucas Visscher:** Conceptualization (equal); Investigation (equal); Methodology (equal); Resources (lead); Software (lead); Supervision (equal); Writing – original draft (supporting); Writing – review & editing (equal). **André Severo Pereira Gomes:** Conceptualization (equal); Data curation (equal); Funding acquisition (lead); Methodology (equal); Resources (lead); Software (equal); Supervision (equal); Writing – original draft (supporting); Writing – review & editing (equal).

DATA AVAILABILITY

The data that support the findings of this study are openly available in the Zenodo repository at <https://doi.org/10.5281/zenodo.5939520>.

REFERENCES

- 1E. Acher, Y. Hacene Cherkaski, T. Dumas, C. Tamain, D. Guillaumont, N. Boubals, G. Javierre, C. Hennig, P. L. Solari, and M.-C. Charbonnel, *Inorg. Chem.* **55**, 5558 (2016).
- 2A. Leoncini, J. Huskens, and W. Verboom, *Chem. Soc. Rev.* **46**, 7229 (2017).
- 3X. Sun, H. Luo, and S. Dai, *Chem. Rev.* **112**, 2100 (2012).
- 4C. Berger, C. Marie, D. Guillaumont, C. Tamain, T. Dumas, T. Dirks, N. Boubals, E. Acher, M. Laszczyk, and L. Berthon, *Inorg. Chem.* **59**, 1823 (2020).
- 5J. M. Gogolski and M. P. Jensen, *Sep. Sci. Technol.* **56**, 2775 (2020).
- 6C. Berger, E. Moreau, C. Marie, D. Guillaumont, A. Beillard, and L. Berthon, “Extraction of uranium(VI) and plutonium(IV) by new tri alkylcarbamides,” *Solvent Extr. Ion Exch.* **40**(3), 290–311 (2021).
- 7C. A. Gould, K. R. McClain, D. Reta, J. G. C. Kragoskow, D. A. Marchiori, E. Lachman, E.-S. Choi, J. G. Analytis, R. D. Britt, N. F. Chilton, B. G. Harvey, and J. R. Long, *Science* **375**, 198 (2022).
- 8K. Burke, *J. Chem. Phys.* **136**, 150901 (2012).
- 9R. J. Bartlett, V. F. Lotrich, and I. V. Schweigert, *J. Chem. Phys.* **123**, 062205 (2005).

- ¹⁰S. Kervazo, F. Réal, F. Virot, A. Severo Pereira Gomes, and V. Vallet, *Inorg. Chem.* **58**, 14507 (2019).
- ¹¹L. E. Aebbersold and A. K. Wilson, *J. Phys. Chem. A* **125**, 7029 (2021).
- ¹²F. Aquino, N. Govind, and J. Autschbach, *J. Chem. Theory Comput.* **6**, 2669 (2010).
- ¹³A. Sunaga and T. Saue, *Mol. Phys.* **119**, e1974592 (2021).
- ¹⁴T. Helgaker, J. Gauss, P. Jørgensen, and J. Olsen, *J. Chem. Phys.* **106**, 6430 (1997).
- ¹⁵K. L. Bak, J. Gauss, P. Jørgensen, J. Olsen, T. Helgaker, and J. F. Stanton, *J. Chem. Phys.* **114**, 6548 (2001).
- ¹⁶J. Almlöf, *Chem. Phys. Lett.* **181**, 319 (1991).
- ¹⁷M. Häser, “Møller-Plesset (MP2) perturbation theory for large molecules,” *Theoret. Chim. Acta* **87**, 147–173 (1993).
- ¹⁸E. J. Baerends, D. E. Ellis, and P. Ros, *Chem. Phys.* **2**, 41 (1973).
- ¹⁹M. Feyereisen, G. Fitzgerald, and A. Komornicki, *Chem. Phys. Lett.* **208**, 359 (1993).
- ²⁰K. G. Dyall and K. Faegri, Jr., *Introduction to Relativistic Quantum Chemistry* (Oxford University Press, 2007).
- ²¹M. Reiher and A. Wolf, *Relativistic Quantum Chemistry* (Wiley, 2014).
- ²²T. Saue and L. Visscher, *Computational Methods in Lanthanide and Actinide Chemistry* (John Wiley & Sons, 2015), pp. 55–87.
- ²³E. R. Batista, R. L. Martin, and P. Yang, *Computational Methods in Lanthanide and Actinide Chemistry* (John Wiley & Sons, 2015), pp. 375–400.
- ²⁴X. Cao and A. Weigand, *Computational Methods in Lanthanide and Actinide Chemistry* (John Wiley & Sons, 2015), pp. 147–179.
- ²⁵L. Visscher, O. Visser, P. J. C. Aerts, H. Merenga, and W. C. Nieuwpoort, *Comput. Phys. Commun.* **81**, 120 (1994).
- ²⁶T. Saue, R. Bast, A. S. P. Gomes, H. J. Aa. Jensen, L. Visscher, I. A. Aucar, R. Di Remigio, K. G. Dyall, E. Eliav, E. Fasshauer, T. Fleig, L. Halbert, E. D. Hedegård, B. Helmich-Paris, M. Iliáš, C. R. Jacob, S. Knecht, J. K. Laerdahl, M. L. Vidal, M. K. Nayak, M. Olejniczak, J. M. H. Olsen, M. Pernpointner, B. Senjean, A. Shee, A. Sunaga, and J. N. P. van Stralen, *J. Chem. Phys.* **152**, 204104 (2020).
- ²⁷L. Belpassi, M. De Santis, H. M. Quiney, F. Tarantelli, and L. Storchi, *J. Chem. Phys.* **152**, 164118 (2020).
- ²⁸M. Repisky, S. Komorovsky, M. Kadek, L. Konecny, U. Ekström, E. Malkin, M. Kaupp, K. Ruud, O. L. Malkina, and V. G. Malkin, *J. Chem. Phys.* **152**, 184101 (2020).
- ²⁹W. Kutzelnigg and W. Liu, *J. Chem. Phys.* **123**, 241102 (2005).
- ³⁰H. J. Aa. Jensen, “Douglas–Kroll the easy way,” in Conference on Relativistic Effects in Heavy Elements - REHE, Mülheim, Germany, April 2005, available at <https://doi.org/10.6084/m9.figshare.12046158>.
- ³¹W. Liu and D. Peng, *J. Chem. Phys.* **125**, 044102 (2006).
- ³²M. Iliáš and T. Saue, *J. Chem. Phys.* **126**, 064102 (2007).
- ³³D. Peng, W. Liu, Y. Xiao, and L. Cheng, *J. Chem. Phys.* **127**, 104106 (2007).
- ³⁴W. Liu and D. Peng, *J. Chem. Phys.* **131**, 031104 (2009).
- ³⁵J. Liu, Y. Shen, A. Asthana, and L. Cheng, *J. Chem. Phys.* **148**, 034106 (2018).
- ³⁶J. Liu and L. Cheng, *J. Chem. Phys.* **148**, 144108 (2018).
- ³⁷L. Cheng, *J. Chem. Phys.* **151**, 104103 (2019).
- ³⁸A. Asthana, J. Liu, and L. Cheng, *J. Chem. Phys.* **150**, 074102 (2019).
- ³⁹J. Sikkema, L. Visscher, T. Saue, and M. Iliáš, *J. Chem. Phys.* **131**, 124116 (2009).
- ⁴⁰K. Faegri and T. Saue, *J. Chem. Phys.* **115**, 2456 (2001).
- ⁴¹A. S. Pereira Gomes and L. Visscher, *Chem. Phys. Lett.* **399**, 1 (2004).
- ⁴²C. Thierfelder, P. Schwerdtfeger, A. Koers, A. Borschevsky, and B. Fricke, *Phys. Rev. A* **80**, 022501 (2009).
- ⁴³V. Pershina, *Challenges and Advances in Computational Chemistry and Physics* (Springer, The Netherlands, 2010), pp. 451–520.
- ⁴⁴J. Autschbach, N. Govind, R. Atta-Fynn, E. J. Bylaska, J. W. Weare, and W. A. de Jong, *Computational Methods in Lanthanide and Actinide Chemistry* (John Wiley & Sons, 2015), pp. 299–342.
- ⁴⁵L. Halbert, M. L. Vidal, A. Shee, S. Coriani, and A. Severo Pereira Gomes, *J. Chem. Theory Comput.* **17**, 3583 (2021).
- ⁴⁶J. Sucher, *Phys. Rev. A* **22**, 348 (1980).
- ⁴⁷J. V. Pototschnig, A. Papadopoulos, D. I. Lyakh, M. Repisky, L. Halbert, A. Severo Pereira Gomes, H. J. Aa. Jensen, and L. Visscher, *J. Chem. Theory Comput.* **17**, 5509 (2021).
- ⁴⁸D. I. Lyakh, *Int. J. Quantum Chem.* **119**, e25926 (2019).
- ⁴⁹B. Helmich-Paris, M. Repisky, and L. Visscher, *J. Chem. Phys.* **145**, 014107 (2016); [arXiv:1606.06498](https://arxiv.org/abs/1606.06498).
- ⁵⁰L. Visscher, P. J. C. Aerts, and O. Visser, *The Effects of Relativity in Atoms, Molecules, and the Solid State* (Springer, 1991), pp. 197–205.
- ⁵¹L. Belpassi, F. Tarantelli, A. Sgamellotti, and H. M. Quiney, *J. Chem. Phys.* **122**, 184109 (2005).
- ⁵²P.-O. Löwdin, *Phys. Rev.* **97**, 1474 (1955).
- ⁵³E. R. Davidson, *Rev. Mod. Phys.* **44**, 451 (1972).
- ⁵⁴T. L. Barr and E. R. Davidson, *Phys. Rev. A* **1**, 644 (1970).
- ⁵⁵C. Sosa, J. Geertsen, G. W. Trucks, R. J. Bartlett, and J. A. Franz, *Chem. Phys. Lett.* **159**, 148 (1989).
- ⁵⁶A. G. Taube and R. J. Bartlett, *Collect. Czech. Chem. Commun.* **70**, 837 (2005).
- ⁵⁷H. J. Aa. Jensen, P. Jørgensen, H. Ågren, and J. Olsen, *J. Chem. Phys.* **88**, 3834 (1988).
- ⁵⁸H. J. Aa. Jensen, P. Jørgensen, H. Ågren, and J. Olsen, *J. Chem. Phys.* **89**, 5354 (1988).
- ⁵⁹A. G. Taube and R. J. Bartlett, *J. Chem. Phys.* **128**, 164101 (2008).
- ⁶⁰P. Verma, L. Huntington, M. P. Coons, Y. Kawashima, T. Yamazaki, and A. Zaribafiyani, *J. Chem. Phys.* **155**, 034110 (2021).
- ⁶¹M. S. Gordon, M. W. Schmidt, G. M. Chaban, K. R. Glaesemann, W. J. Stevens, and C. Gonzalez, *J. Chem. Phys.* **110**, 4199 (1999).
- ⁶²S. Chamoli, K. Surjuse, M. K. Nayak, and A. K. Dutta, *J. Chem. Phys.* **156**, 204120 (2022).
- ⁶³J. N. P. van Stralen, L. Visscher, C. V. Larsen, and H. J. Aa. Jensen, *Chem. Phys.* **311**, 81 (2005).
- ⁶⁴H. A. Kramers, *Proc. R. Acad. Sci. Amsterdam* **33**, 959 (1930).
- ⁶⁵L. Visscher, *Chem. Phys. Lett.* **253**, 20 (1996).
- ⁶⁶T. Saue and H. J. Aa. Jensen, *J. Chem. Phys.* **111**, 6211 (1999).
- ⁶⁷ReSpect, a relativistic DFT program; see <http://www.respectprogram.org>.
- ⁶⁸M. Yoshimine, *J. Comput. Phys.* **11**, 449 (1973).
- ⁶⁹A. Shee, L. Visscher, and T. Saue, *J. Chem. Phys.* **145**, 184107 (2016).
- ⁷⁰H. J. Aa. Jensen, R. Bast, A. S. P. Gomes, T. Saue, L. Visscher, I. A. Aucar, V. Bakken, C. Chibueze, J. Creutzberg, K. G. Dyall, S. Dubillard, U. Ekström, E. Eliav, T. Enevoldsen, E. Fasshauer, T. Fleig, O. Fossgaard, L. Halbert, E. D. Hedegård, T. Helgaker, B. Helmich-Paris, J. Henriksson, M. van Horn, M. Iliáš, C. R. Jacob, S. Knecht, S. Komorovsky, O. Kullie, J. K. Laerdahl, C. V. Larsen, Y. S. Lee, N. H. List, H. S. Nataraj, M. K. Nayak, P. Norman, G. Olejniczak, J. Olsen, J. M. H. Olsen, A. Papadopoulos, Y. C. Park, J. K. Pedersen, M. Pernpointner, J. V. Pototschnig, R. Di Remigio, M. Repisky, K. Ruud, P. Salek, B. Schimmelpennig, B. Senjean, A. Shee, J. Sikkema, A. Sunaga, A. J. Thorvaldsen, J. Thyssen, J. van Stralen, M. L. Vidal, S. Villaume, O. Visser, T. Winther, S. Yamamoto, and X. Yuan, *Dirac22*, 2022.
- ⁷¹DIRAC, a relativistic *ab initio* electronic structure program, Release DIRAC21, Written by R. Bast, A. S. P. Gomes, T. Saue, L. Visscher, H. J. Aa. Jensen, I. A. Aucar, V. Bakken, K. G. Dyall, S. Dubillard, U. Ekström, E. Eliav, T. Enevoldsen, E. Fasshauer, T. Fleig, O. Fossgaard, L. Halbert, E. D. Hedegård, T. Helgaker, B. Helmich-Paris, J. Henriksson, M. Iliáš, Ch. R. Jacob, S. Knecht, S. Komorovsky, O. Kullie, J. K. Laerdahl, C. V. Larsen, Y. S. Lee, N. H. List, H. S. Nataraj, M. K. Nayak, P. Norman, G. Olejniczak, J. Olsen, J. M. H. Olsen, A. Papadopoulos, Y. C. Park, J. K. Pedersen, M. Pernpointner, J. V. Pototschnig, R. Di Remigio, M. Repisky, K. Ruud, P. Salek, B. Schimmelpennig, B. Senjean, A. Shee, J. Sikkema, A. Sunaga, A. J. Thorvaldsen, J. Thyssen, J. van Stralen, M. L. Vidal, S. Villaume, O. Visser, T. Winther, and S. Yamamoto, see <http://www.diracprogram.org>, 2021.
- ⁷²D. I. Lyakh, “ExaTENSOR, a basic numerical tensor algebra library for distributed heterogeneous HPC platforms,” <https://github.com/ORNL-QCI/ExaTENSOR>, 2022; last accessed 2 June 2022.
- ⁷³K. G. Dyall, *Theor. Chem. Acc.* **108**, 335 (2002).
- ⁷⁴K. G. Dyall, *Theor. Chem. Acc.* **115**, 441 (2006).
- ⁷⁵K. G. Dyall, *Theor. Chem. Acc.* **131**, 1172 (2012).
- ⁷⁶T. H. Dunning, *J. Chem. Phys.* **90**, 1007 (1989).

- ⁷⁷R. A. Kendall, T. H. Dunning, and R. J. Harrison, *J. Chem. Phys.* **96**, 6796 (1992).
- ⁷⁸D. E. Woon and T. H. Dunning, *J. Chem. Phys.* **98**, 1358 (1993).
- ⁷⁹D. E. Woon and T. H. Dunning, *J. Chem. Phys.* **103**, 4572 (1995).
- ⁸⁰K. A. Peterson and T. H. Dunning, *J. Chem. Phys.* **117**, 10548 (2002).
- ⁸¹B. A. Hess, C. M. Marian, U. Wahlgren, and O. Gropen, *Chem. Phys. Lett.* **251**, 365 (1996).
- ⁸²C. M. Marian, *Reviews in Computational Chemistry* (John Wiley & Sons, 2001), pp. 99–204.
- ⁸³B. Schimmelpfennig, “AMFI, an atomic mean-field spin-orbit integral program,” University of Stockholm, Stockholm, Sweden, 1999.
- ⁸⁴K. P. Huber and G. Herzberg, *Molecular Spectra and Molecular Structure. IV. Constants of Diatomic Molecules* (Springer, New York, 1979).
- ⁸⁵J. K. Laerdahl and P. Schwerdtfeger, *Phys. Rev. A* **60**, 4439 (1999).
- ⁸⁶X. Yuan, L. Visscher, and A. S. P. Gomes (2022). “Dataset: Assessing MP2 frozen natural orbitals in relativistic correlated electronic structure calculations,” <https://doi.org/10.5281/zenodo.5939520>.
- ⁸⁷A. E. DePrince and C. D. Sherrill, *J. Chem. Theory Comput.* **9**, 2687 (2013).
- ⁸⁸R. J. Le Roy, *J. Quant. Spectrosc. Radiat. Transfer* **186**, 167 (2017).
- ⁸⁹V. Kello, *Mol. Phys.* **89**, 127 (1996).
- ⁹⁰J. Autschbach, S. Zheng, and R. W. Schurko, *Concepts Magn. Reson., Part A* **36A**, 84 (2010).
- ⁹¹S. Larsson and P. Pyykkö, *Chem. Phys.* **101**, 355 (1986).
- ⁹²L. Visscher, T. Enevoldsen, T. Saue, and J. Oddershede, *J. Chem. Phys.* **109**, 9677 (1998).
- ⁹³R. Bast, A. Koers, A. S. P. Gomes, M. Iliaš, L. Visscher, P. Schwerdtfeger, and T. Saue, *Phys. Chem. Chem. Phys.* **13**, 864 (2011).
- ⁹⁴G. Rauhut and P. Schwerdtfeger, *Phys. Rev. A* **103**, 042819 (2021).
- ⁹⁵R. Berger and M. Quack, *J. Chem. Phys.* **112**, 3148 (2000).

Part III

Applications on molecules containing heavy elements

Papers of application works

7.1 Paper I: Reassessing the potential of TlCl for laser cooling experiments via four-component correlated electronic structure calculations

I proposed the initial idea, carried out all calculations, and wrote the manuscript.

Journal of Chemical Physics, 157, 074313, 2022

Reproduced from *Journal of Chemical Physics* with the permission of AIP Publishing.

Copyright 2022 AIP Publishing LLC.

Reassessing the potential of TlCl for laser cooling experiments via four-component correlated electronic structure calculations

Cite as: J. Chem. Phys. 157, 074313 (2022); doi: 10.1063/5.0092620

Submitted: 23 March 2022 • Accepted: 27 July 2022 •

Published Online: 19 August 2022



View Online



Export Citation



CrossMark

Xiang Yuan^{1,2,a)}  and André Severo Pereira Gomes^{1,b)} 

AFFILIATIONS

¹ Université de Lille, CNRS, UMR 8523 - PhLAM - Physique des Lasers, Atomes et Molécules, F-59000 Lille, France

² Department of Chemistry and Pharmaceutical Science, Faculty of Science, Vrije Universiteit Amsterdam, de Boelelaan 1083, 1081 HV Amsterdam, The Netherlands

^{a)} Author to whom correspondence should be addressed: xiang.yuan@univ-lille.fr

^{b)} Electronic mail: andre.gomes@univ-lille.fr

ABSTRACT

Following the interest in the experimental realization of laser cooling for thallium fluoride (TlF), determining the potential of thallium chloride (TlCl) as a candidate for laser cooling experiments has recently received attention from a theoretical perspective [Yuan *et al.*, J. Chem. Phys. 149, 094306 (2018)]. From these *ab initio* electronic structure calculations, it appeared that the cooling process, which would proceed from transitions between $a^3\Pi_0^+$ and $X^1\Sigma_0^+$ states, had as a potential bottleneck the long lifetime (6.04 μ s) of the excited state $a^3\Pi_0^+$, that would make it very difficult to experimentally control the slowing zone. In this work, we revisit the electronic structure of TlCl by employing four-component Multireference Configuration Interaction (MRCI) and Polarization Propagator (PP) calculations and investigate the effect of such approaches on the computed transition dipole moments between $a^3\Pi_0^+$ and $a^3\Pi_1$ excited states of TlCl and TlF (the latter serving as a benchmark between theory and experiment). Whenever possible, MRCI and PP results have been cross-validated by four-component equation of motion coupled-cluster calculations. We find from these different correlated approaches that a coherent picture emerges in which the results of TlF are extremely close to the experimental values, whereas for TlCl the four-component calculations now predict a significantly shorter lifetime (between 109 and 175 ns) for the $a^3\Pi_0^+$ than prior estimates. As a consequence, TlCl would exhibit rather different, more favorable cooling dynamics. By numerically calculating the rate equation, we provide evidence that TlCl may have similar cooling capabilities to TlF. Our analysis also indicates the potential advantages of boosting stimulated radiation in optical cycles to improve cooling efficiency.

Published under an exclusive license by AIP Publishing. <https://doi.org/10.1063/5.0092620>

I. INTRODUCTION

The realization of high-precision measurements on atoms and molecules to verify violation of time-reversal symmetry, for instance, the appearance of an electron electric dipole moment (eEDM), has become a valuable tool in the search for new physics outside the standard model. This is an alternative method to directly look for new particles in collider experiments, which are currently predicted to require energies on the TeV scale.

To enable such fundamental physics research on atoms and molecules, unprecedented levels of precision in high-precision experiments are essential. Laser cooling technology provides an

effective means of reducing noise in atomic and molecular spectroscopy, but while widespread for atoms, the cooling of molecules is more challenging. Rosa¹ had outlined the three conditions for molecular candidates in laser cooling: (1) strong one-photon transition, (2) highly diagonal Franck-Condon factors (FCFs), and (3) no intervening electronic state.

Since Shuman, Barry, and DeMille² first reported the cooling of the SrF molecule, three diatomic molecules (CaF,³ YO,⁴ and YbF⁵) have been successfully cooled. It is interesting to note that, out of these four successfully cooled systems, three contain atoms for which relativistic effects, such as spin-orbit coupling, play an important role in the resulting molecular electronic structure. By

lifting degeneracies and relaxing selection rules, relativity affects both the energies of electronic states and the associated transition moments. These changes, in turn, provide additional challenges to the design of cooling schemes in comparison to species in the upper rows of the periodic table. Therefore, in this context, simulations based upon relativistic correlated electronic structure calculations, which can achieve rather high accuracy for small, symmetric systems, are particularly interesting as a way to pre-screen candidates for experiments.

Among the species containing heavy elements, thallium halides (TlX) make up an interesting class of systems. TlF is an ideal candidate for the measurement of P- and T-violating interactions^{6–8} because of its high mass and polarizability. Hunter *et al.*⁹ proposed the use of spin-forbidden transition $a^3\Pi_1-X^1\Sigma_0^+$ to set up cooling optical cycling for TlF, leading different groups to investigate its spectroscopic properties experimentally.^{10,11} More recently, the CeNTREX collaboration¹² has been conducting experiments with ²⁰⁵TlF molecular beams.

The transition used for optical cycling in TlF occurs at 271.7 nm, reflecting the fact that the target $a^3\Pi_1$ excited state is rather high in energy compared to the ground state, potentially making this species less advantageous from an experimental perspective than species in which the target excited states are lower, such as in heavier TlX species. However, the calculations of Zou and Liu¹³ on TlBr, TlI, and TlAt have shown that the potential wells of the target $a^3\Pi$ excited states are not sufficiently aligned with that of the ground state to satisfy condition (2). This leaves TlCl as the only remaining candidate in this series.

In a recent investigation of the electronic structure of TlCl, Yuan *et al.*¹⁴ arrived at the conclusion that the $a^3\Pi_0^+-X^1\Sigma_0^+$ transition would meet the aforementioned conditions for optical cycling. However, their calculated radiative lifetime for the $a^3\Pi_0^+$ state was of about 6 μ s, which not only is too long for current experimental conditions but also at odds with the prior theoretical work by Li *et al.*,¹⁵ which found the $a^3\Pi_0^+$ lifetime to be of about 800 ns. Interestingly, in these two investigations, the final spin-orbit coupled electronic states had been obtained from scalar relativistic correlated calculations, whose spin-free states are subsequently coupled via spin-orbit configuration interaction (SOC) calculations.

Thus, the first objective of this work is to revisit the TlCl system by employing more sophisticated relativistic correlated electronic structure methods, in order to resolve the discrepancies in radiative lifetimes described in the literature. With that, our second goal is to address whether or not TlCl can be a system of interest for laser cooling experiments. Given the lack of experimental data on radiative lifetimes for TlCl, we shall also verify the performance of our theoretical approaches with respect to the experimental results of the TlF system.

As it is known in the literature,^{16–20} SOC calculations can be very sensitive to the number of electronic spin-free states entering the SOC calculation and whether a contracted or uncontracted CI is employed. Because of that, we consider it of interest to attack this problem from a different perspective, with spin-orbit coupling (SOC) interactions being accounted for at the mean-field level by using a four-component-based Hamiltonian. That is to be followed by a treatment of electronic correlation on a spinor basis, employing the multireference configuration interaction (MRCI) method as well as benchmark calculations with the relativistic Equation of Motion

Coupled-Cluster singles doubles (EOM-CCSD)²¹ and the Polarization Propagator (PP)²² approaches, in order to cross-validate the MRCI calculations for ground, excited, and transition properties.

This paper is organized as follows: The details of the *ab initio* calculations are described in Sec. II. The computational results and the corresponding cooling scheme are presented and discussed in Sec. III. Finally, a brief summary is presented in Sec. IV.

II. COMPUTATIONAL DETAILS

The *ab initio* calculations on the electronic states of TlF and TlCl have been performed with the DIRAC19²³ and DIRAC22²⁴ releases as well as with a publicly available development snapshot (commit hash *e0617189*) of the DIRAC relativistic electronic structure package.²⁵ In all calculations, we employed the four-component Dirac-Coulomb (DC) Hamiltonian with the usual approximation of the (SS|SS) integrals by a Coulombic correction.²⁶ The uncontracted Dyall basis sets *aaenZ*²⁷ were employed for Tl atom, and the correlation-consistent basis set *aug-cc-pVnZ*^{28,29} was employed for the halogens. In both cases, *n* is the basis sets cardinal number (*n* = 2, 3, and 4 for double-, triple-, and quadruple-zeta, respectively). As a shorthand notation, in the following, we shall refer to the different basis sets as *nZ*.

The molecular axis is placed along the *z*-axis with the center of mass at the origin, with the positive direction being from Tl to X. For permanent dipole moments (PDM), we used the following bond lengths (in Å) corresponding to the experimental equilibrium distances: 2.0844 ($X^1\Sigma_0^+$, TlF), 2.049 ($a^3\Pi_0^+$, TlF), 2.0745 ($a^3\Pi_1$, TlF), 2.485 ($X^1\Sigma_0^+$, TlCl), 2.472 ($a^3\Pi_0^+$, TlCl), and 2.485 ($a^3\Pi_1$, TlCl). Since the PDM of a linear molecule is the first derivative of the energy with respect to the electric field along the molecular *z*-axis, in the complete basis set (CBS) limit, the ground state PDMs are obtained via an expression analogous to that for the total energy,³⁰ that is,

$$\mu_{\text{CBS}} = \mu_n - \alpha \exp^{-(n-1)} - \beta \exp^{-(n-1)^2} \quad (1)$$

for which results from 2Z, 3Z, and 4Z basis sets calculations are needed. We note that for excited states, the CBS results are extrapolated based on 3Z and 4Z results with the formula^{20,31}

$$E_{\text{CBS}}(\mathbf{R}) = \frac{4^3 E_4(\mathbf{R}) - 3^3 E_3(\mathbf{R})}{4^3 - 3^3}. \quad (2)$$

In this study, we focused on the transitions of $a^3\Pi_1-X^1\Sigma_0^+$ and $a^3\Pi_0^+-X^1\Sigma_0^+$ ($\Omega = 0$ states) of TlF and TlCl. The PDMs and the transition dipole moments (TDMs) were obtained with the MRCI method as implemented in the KRCI module^{32,33} (we note the KRCI module employed in our calculations does not support the use of two-component Hamiltonians). In the MRCI calculations, the base configuration space is defined as (8,8) corresponding to the 6s, 6p, and 7s orbital of Tl and 2(3)p orbitals of halogen. The detailed Generalized Active Spaces (GAS) used in these KRCI calculations, including the number of configurations—as well as the GAS setups for additional calculations aiming to verify the robustness of transition moment values with respect to active space—are presented in the [supplementary material](#).

We have also carried out calculations of excitation energies, PDMs, and TDMs with the four-component CCSD,^{34,35} EOM-CCSD,³⁶ and PP^{37,38} methods. The analytic calculation of excited state expectation values is currently not possible for both methods in their implementations in DIRAC. Due to that, we obtained excited state dipole moments through finite field calculations. In these, the component of the dipole moment operator is individually taken as the perturbations (with strengths of ± 0.0005 a.u.) and is included at the Hartree-Fock step corresponding to an orbital-relaxed picture. We note that for the EOM-CCSD implementation, the transition dipole moments are also not currently available. In contrast, for PP, these are available and will be compared to those obtained with MRCI. For EOM-CCSD and PP, we explored different correlation

spaces, in order to verify the effect of truncation: we consider occupied orbitals with energies higher than -10 or -20 a.u. and virtual orbitals with energies up to and including 20 or 100 a.u.

The data, figures, and scripts associated with this paper all can be obtained as [supplementary material](#) in the Zenodo repository.³⁹

III. RESULT AND DISCUSSION

A. Permanent dipole moment

We present in [Table I](#) the PDMs and vertical excitation energies (T_v) for MRCI, EOM-CCSD, and PP, alongside the SOCI calculations from the literature^{14,40} and the experimental results.¹⁰

TABLE I. Computed permanent dipole moments (in Debye) and vertical excitation energies (T_v , in cm^{-1}) for the different states under consideration for TIF and TlCl.

Molecule	State	Method	2Z		3Z		4Z		CBS		SOCI ^{14,40}		Expt.	
			PDM	T_v	PDM	T_v	PDM	T_v	PDM	T_v	PDM	T_v	PDM	T_e^a
TIF	$X^1\Sigma_0^+$	MRCI	-4.16	0	-3.88	0	-3.79	0	-3.74	0	-3.67	0		
		CCSD ^b	-4.37	0	-4.32	0								
		CCSD ^c	-4.33	0	-4.29	0								
		CCSD ^{c,d}		0	-4.30	0								
	$a^3\Pi_0^+$	MRCI	-3.15	36 825	-2.81	34 695	-2.76	33 708	-2.74	32 990	-1.46	37 025		35 164
		EOM ^b	-2.67	34 790	-2.69	3 082								
		EOM ^d				35 148								
		PP		31 592		32 414								
		PP ^e		32 185		32 524								
	$a^3\Pi_1$	MRCI	-2.90	40 070	-2.47	37 921	-2.46	36 507	-2.47	35 474	-1.26	38 535	-2.28	3 664
		EOM ^b	-2.45	36 475	-2.47	36 782								
		EOM ^d				36 851								
		PP		32 920		33 719								
		PP ^e		33 513		33 820								
	$X^1\Sigma_0^+$	MRCI	-4.60	0	-4.46	0	-4.42	0	-4.4	0	-4.32	0		
CCSD ^b		-4.66	0	-4.65	0									
CCSD ^c		-4.63	0	-4.64	0									
CCSD ^{c,d}		-4.66	0	-4.64	0									
TlCl	$a^3\Pi_0^+$	MRCI	-2.43	31 130	-2.19	31 630	-2.13	31 813	-2.1	31 947	-2.08	31 438		31 054
		EOM ^b	-1.78	31 095	-1.80	31 182								
		EOM ^d		31 246		31 232								
		PP		30 801		31 338								
		PP ^d		31 072		31 380								
	$a^3\Pi_1^f$	MRCI	-1.83	33 366	-1.51	34 594	-1.48	34 711	-1.47	34 797	-1.74	32 526		
		EOM ^b	-1.45	32 369	-1.29	32 426								
		EOM ^d		32 500		32 467								

^aExperimental adiabatic excitation energy value.

^bFinite-field calculations, equivalent to an orbital-relaxed formulation.

^cAnalytic gradient calculation, employing an orbital-unrelaxed formulation.³⁵

^dCorrelation space: -10 a.u. to 100 a.u.

^eCorrelation space: -20 a.u. to 100 a.u.

^f $a^3\Pi_1$ state of TlCl is not a bound state.

We find that EOM-CCSD results are rather insensitive to the increase in the correlating space (from -10 to 20 a.u. to -20 to 100 a.u.) for both the $2Z$ and $3Z$ (changes are less than 100 cm^{-1}), whereas, for PP, there are more significant changes for the $2Z$ set (1000 cm^{-1}), but these fall largely in line with the EOM-CCSD results for the $3Z$ basis sets. With that, by considering the $3Z$ basis set results in the following discussion, the same semi-quantitative trends apply for both correlating spaces, and for convenience (and unless otherwise noted), we shall refer to the smaller orbital space (-10 to 20 a.u.) results.

For the MRCI PDMs, our results indicate an asymptotic convergence as a function of the basis set level for all states under consideration. This translates into a decrease in the magnitude of dipole moments for all states of TIF and TlCl at the CBS level compared to the results obtained with the smaller basis sets. Furthermore, the magnitudes of the dipole moments of the excited states are smaller than those of the ground states, and the magnitudes of the PDMs for TIF are all smaller than those for TlCl. In all of our results, the PDMs possess a negative sign, meaning that a decrease in magnitude correlates with a build-up in electronic density surrounding the Tl atom as the quality of the basis set is enhanced.

The MRCI results are consistent with the coupled-cluster results (due to computational resource limitations, we were unable to perform EOM calculations with $4Z$ bases, and thus only present results for $2Z$ and $3Z$ bases); the differences in PDMs between the two approaches are typically, in absolute value, between 0.3 and 0.5 D for all states considered. It is interesting to note that variations across approaches tend to be lower for $3Z$ bases than for $2Z$ bases, with the coupled-cluster findings deviating less than MRCI ones when shifting from $2Z$ to $3Z$; hence, we expect that our $3Z$ results can serve as a semiquantitative comparison, and give us with confidence that our $4Z$ and CBS MRCI results are reliable.

For the coupled-cluster ground states for which we can also calculate PDMs analytically, we observe that the finite-field and analytic derivative results are very close (differences around 0.03 – 0.04 D), indicating that (a) orbital relaxation is not particularly important for such species and (b) the finite-field results for the various electronic states are reliable. We furthermore reuse the results from the finite-field calculations to evaluate the α_{zz} components of the polarizability, which are listed in Table S3 in the [supplementary material](#) and find that the value of TlCl (191 a.u.) is almost twice as large as that of TIF (110 a.u.). These results suggest that, in comparison to TIF, TlCl is more easily polarized by the external electric field, which in turn provides more favorable conditions for experiments testing P-T violation.

Finally, we see that for the ground state, the SOCI results of Yuan *et al.*¹⁴ and our MRCI results compare rather well. For excited states, the situation is different, particularly for the $a^3\Pi_1$ state, as we observe significant differences between methods for both TIF and TlCl.

In comparison to the experiment, the PDM measurements of the $a^3\Pi_1$ state of TIF by Clayburn *et al.*,¹⁰ which yielded a value of $-2.28(7)$ D, are in very good agreement with our MRCI $4Z$ (-2.46 D) or CBS (-2.47 D) results, as well as our EOM-CCSD $3Z$ results (-2.47 D). From that, and the very similar MRCI and CCSD results for TlCl, we expect that our calculations do provide a good estimate of the experimental value. We believe future high-resolution PDM

measurements for more states would be highly desirable as a test, and possible confirmation, of our results.

Concerning the vertical excitation energies (T_v) for TIF, we observe significant variations with the basis set size for MRCI, which result in decreasing excitation energies as the basis set quality is improved (roughly a 2000 cm^{-1} decrease when passing from $2Z$ to $3Z$ for both $^3\Pi$ states, and nearly 1000 cm^{-1} when passing from $3Z$ to $4Z$, and another 1000 cm^{-1} when passing from $4Z$ to CBS). This tendency is qualitatively the same in the EOM-CCSD calculations, although the changes are somewhat smaller (about 300 – 400 cm^{-1} from $2Z$ to $3Z$).

On the other hand, for MRCI results on TlCl, we see significantly smaller fluctuations with changing basis sets (less than 1000 cm^{-1} between $2Z$ and CBS values), with increasing excitation energies as basis sets are improved. As for TIF, EOM-CCSD trends mirror those of MRCI, and energy changes with respect to basis sets are again less significant than those for MRCI.

In contrast to MRCI and EOM-CCSD, PP results for all excited states demonstrate an increase in excitation energies with improving basis set size, with changes between $2Z$ and $3Z$ of around 1000 cm^{-1} for the smaller correlating space, but around 300 cm^{-1} for the larger correlating space. It is interesting to observe that the $3Z$ PP excitation energy for both molecules is generally lower but not dissimilar to the MRCI CBS values, though this may be due to fortuitous error cancellations.

However, for TlCl, it appears that all three correlated techniques exhibit much more similar performance, and, in particular, PP results are much closer to EOM and MRCI ones.

We see that for both species, the T_v EOM-CCSD results are very much in line with the experimental T_e values (given the nature of the excited states, the calculated T_v values should in effect be quite close to the T_e ones), and since MRCI energies tend to closely follow the EOM-CCSD ones, we consider MRCI energies to reliably reflect the experimental excitation energies.

The difference between SOCI and the current four-component derived excitation energies for TIF is striking, with SOCI overestimating the four-component results by 2000 to 3000 cm^{-1} , depending on the excited state. Taken together (a) the strongly underestimated magnitude of the excited state dipole moment with respect to the experiment and (b) the rather good agreement for calculated ground-state dipole moments, it would appear that the SOCI calculations of Liu *et al.*⁴⁰ are somewhat unbalanced in their descriptions of the excited states, with respect to the ground state. Interestingly, for TlCl, the four-component excited state energies, as well as the ground and excited state dipole moments, agree pretty well with the SOCI estimates. This shows that any problems with SOCI calculations are not so much in the description of the different electronic states of TlCl, but rather in the transition properties, to which we will now shift our attention.

B. Transition properties

Our results for TDMs, obtained at bond lengths corresponding to the experimental excited states' equilibrium distances, are found in Table II. Unlike excited state properties, CBS values cannot be estimated for TDMs; hence, we chose to focus on MRCI TDM data obtained with $4Z$ basis sets.

TABLE II. Computed transition dipole moments at R_e and the corresponding lifetimes.

TIF	Transition	TDM(D)	lifetime(ns)	Reference
	$a^3\Pi_1-X^1\Sigma_0^+$	0.837	91	MRCI
	$a^3\Pi_1-X^1\Sigma_0^+$	0.673	153	PP ^a
	$a^3\Pi_1-X^1\Sigma_0^+$	0.634	172	PP ^b
	$a^3\Pi_1-X^1\Sigma_0^+$		99(9)	Exp ⁹
	$a^3\Pi_1-a^3\Pi_0^+$	0.114		MRCI
	$a^3\Pi_1-a^3\Pi_0^-$	0.072		MRCI
	$a^3\Pi_0^+-X^1\Sigma_0^+$	0.518	278	MRCI
	$a^3\Pi_0^+-X^1\Sigma_0^+$	0.651	176	PP ^a
TlCl				
	$a^3\Pi_0^+-X^1\Sigma_0^+$	0.767	175	MRCI
	$a^3\Pi_0^+-X^1\Sigma_0^+$	0.896	128	PP ^a
	$a^3\Pi_0^+-X^1\Sigma_0^+$	0.928	119	PP ^b
	$a^3\Pi_0^+-X^1\Sigma_0^+$	0.130	6040	Reference 14
	$a^3\Pi_0^+-X^1\Sigma_0^+$		808	Reference 15
	$a^3\Pi_1-X^1\Sigma_0^+$	0.946		MRCI
	$a^3\Pi_1-X^1\Sigma_0^+$	0.800		Reference 14

^aCorrelation space: -10 to 20 a.u.^bCorrelation space: -20 to 100 a.u.

Before discussing these results, we have carried out a number of MRCI calculations with different GAS definitions (employing 3Z basis sets due to constraints on computational resources). Our aim with these was to investigate whether or not TDM values vary significantly upon including configurations correlating outer core electrons (the 5d orbitals of Tl) and increasing the virtual space to include higher-lying virtuals (i.e., those with energies up to and including 30 a.u.), than those we were able to consider in the 4Z calculations.

From our results, found in the supplementary information (Tables S4 and S5 and Fig. S1), we first observe that core-correlating configurations tend to increase the TDMs, but not so drastically. This decrease is more significant (around -0.13 D) for calculations employing the larger virtual space than for those employing the smaller virtual space (around -0.07 D). Consequently, the outer-core correlation has an impact on the calculated lifetimes: these change from 163 to 137 ns for the calculations with smaller virtual space and from 145 to 109 ns for the calculations with larger virtual space.

At the same time, we observe that core-correlating configurations tend to increase excitation energies, making them move away from the experimental value. As was the case for the TDMs, this effect is more pronounced for the calculations with the larger virtual space (+2333 cm^{-1}) than with the smaller virtual space (+862 cm^{-1}). By inspecting Fig. S1, we observe that the presence of core-correlating configurations tends to preferentially stabilize the ground state with respect to the excited state.

We note the 3Z results are in agreement with the trend observed for the comparable 4Z calculations. With this and the effect of core correlating configurations in mind, we consider our valence 4Z calculations can provide, respectively, a lower bound for the TDMs and an upper bound for the lifetimes in TlCl.

As EOM TDMs are not yet accessible, we present TDMs values derived from 4Z PP calculations; based on their similarity to EOM and MRCI results for TlCl, we anticipate that PP calculations provide sufficiently accurate results to serve as cross-validation of MRCI results, though somewhat less so for TIF. As for the case of transition energies, we have also assessed the effect of the correlation space truncation on the PP TDMs between the ground and $a^3\Pi_1$ state of TIF, and the ground and $a^3\Pi_0^+$ excited state of TlCl. We find that the results do not vary substantially, which we take as a further indication that, for these systems, the TDM values are not very sensitive to the truncation of the orbital space.

We find that for different transitions in TIF, the MRCI and PP results are indeed quite close to each other, differing by less than 0.1 D for the transitions from the ground to each of the Ω components of the Π states. We note that, for the transition to the $a^3\Pi_0^+$ state, the PP TDM is larger than the MRCI one, whereas the reverse is true for the transition to the $a^3\Pi_1$ state.

As for TIF, for TlCl the difference between MRCI and PP is slightly larger than 0.1 D for the transition from the ground state to the $a^3\Pi_0^+$ state, and the PP value is again larger than the MRCI one. We note here that the PP results are, on the other hand, quite similar to the largest 3Z MRCI calculations, including core-correlating configuration. This could be a further indication that the actual lifetimes could indeed be somewhat lower than the 175 ns obtained from the valence 4Z MRCI calculations since, in the PP calculations, the 5d Tl electrons are also correlated.

The good agreement between these two four-component techniques for both molecules, with results differing by no more than 25%, makes us confident in the capability of MRCI to generate sufficiently accurate TDMs for a reliable assessment of lifetimes, as discussed below.

Comparing our current results for TlCl to those in the literature, we observe first that for the transition from ground to the $a^3\Pi_1$ state, our results differ slightly more than 0.1 D from those of Yuan *et al.*¹⁴ Second, we see that the SOCI TDMs of $a^3\Pi_0^+$ are strongly underestimated, differing from ours by nearly 0.7 D.

The TDMs of $a^3\Pi_0^+$ and $a^3\Pi_1$ of TlCl are slightly larger than the corresponding MRCI and PP ones for TIF, something which is consistent with our understanding that TlCl should have somewhat stronger spin-orbit coupling effects than TIF, whereby further weakening the selection rules making the spin forbidden transition $a^3\Pi-X^1\Sigma^+$ in comparison to TIF.

As the differences in computed TDMs are already illuminating, a more direct comparison to the experiment is provided by the lifetimes presented in Table II. From the TDMs, we evaluate the Einstein coefficients from¹⁴

$$A_{v'v''} = 2.142 \times 10^{10} \times \text{TDM}^2 \times q_{v'v''} \times \Delta E^3 \quad (3)$$

(where the energy difference ΔE and the TDMs are given in a.u. and $A_{v'v''}$ in s^{-1}), while the radiative lifetimes are obtained using

$$\tau_{v'} = \frac{1}{\sum_{v''} A_{v'v''}}. \quad (4)$$

The vibrational energy levels and the corresponding Franck-Condon factors ($q_{v'v''}$) are taken from available experiments^{9,41} ($a^3\Pi_1$ state of TIF) and prior calculations^{14,40} ($a^3\Pi_0^+$ state of both TIF and TlCl). The detailed Einstein coefficients

$A_{v'v''}$ and vibrational branching $R_{v'v''}$ of transitions are listed in the [supplementary material](#).

Given that SOCI PDMs and four-component PDMs for the ground states of TIF and TlCl match quite well, we consider this method (combining ground-state vibrational wavefunctions derived from SOCI potential energy curves and four-component TDMs at the MRCI or PP level) to be reliable.

For TIF, the computed lifetime of the $a^3\Pi_1$ state is 91 and 153 ns for MRCI and PP, respectively, and the former is closer to the experimental value 99(9) ns. For TlCl, the 6.04 μ s lifetime of the $a^3\Pi_0^+$ state calculated by Yuan *et al.*¹⁴ would correspond to a huge challenge under current cooling experimental condition. However, we see that on the basis of the current four-component calculations without including outer-core correlation, lifetimes for the $a^3\Pi_0^+$ state would correspond to 175 ns (MRCI) and 128 ns (PP), respectively, which are both much shorter than the previous value, and as discussed above with the inclusion of outer-core correlation, the tendency is for lifetimes to further decrease. From these results, we, therefore, conclude that TlCl should be a much more favorable system for the experimental realization of laser cooling than previously thought.

Given the small deviation between the theoretical and experimental lifetimes for the MRCI $a^3\Pi_1$ state of TIF and the systematic agreement between four-component approaches for TDMs, we thus consider the lifetime of $a^3\Pi_0^+$ state of TlCl 175 ns to be a more accurate (upper bound) estimate than the previous estimation by Yuan *et al.*¹⁴ and shall use this new calculated lifetime in the following assessment of a proposed cooling scheme.

C. Simulation of laser cooling

As the cooling efficiency and the corresponding length of the slowing region are dependent on the lifetimes, compared to the results of Yuan *et al.*,¹⁴ the new lifetime value for the $a^3\Pi_0^+$ state of TlCl will translate into a different cooling dynamics and, as a result, will alleviate the technical difficulties associated with setting up the experiment. Despite the changes in TDMs, the optical cycling scheme for TIF and TlCl, shown in [Fig. 1](#), will still closely follow

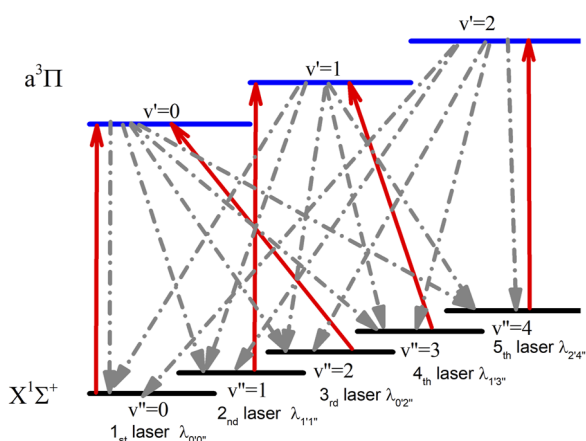


FIG. 1. The proposed cooling scheme for TIF and TlCl. The excited states are $a^3\Pi_1$ and $a^3\Pi_0^+$ for TIF and TlCl, respectively. The dashed gray lines are spontaneous decays and the solid red lines are laser-driven transitions.

TABLE III. The wavelength (nm) of lasers used in the cooling process is represented by [Fig. 1](#).

Laser	TIF	TlCl
1st: $\lambda_{0''}$	272	319
2nd: $\lambda_{1''}$	273	320
3rd: $\lambda_{0''}$	279	325
4th: $\lambda_{1''}$	280	326
5th: $\lambda_{2''}$	281	327

the one originally proposed by Yuan *et al.*,¹⁴ which, for the sake of completeness, is outlined below.

The main pump laser is set at the $a^3\Pi(v' = 0) - X^1\Sigma_0^+(v'' = 0)$ transition, with a wavelength $\lambda_{0''}$: 272 nm (TIF) and 319 nm (TlCl). Four additional lasers are used to repump the population of vibrationally excited states. For clarity, we refer to these lasers as follows: $\lambda_{0''}$ is the first laser, $\lambda_{1''}$ is the second laser, $\lambda_{0''}$ is the third laser, $\lambda_{1''}$ is the fourth laser, and $\lambda_{2''}$ is the fifth laser. All the wavelengths of the lasers are listed in [Table III](#):

To discuss the cooling process in more detail, we solve a rate equation to count the number of photons scattered during the cooling process,⁴²

$$\frac{d\mathbf{P}}{dt} = \mathbf{M}\mathbf{P}, \quad (5)$$

where \mathbf{P} is a vector holding N vibrational levels in ascending order of energy and \mathbf{M} is an $N \times N$ matrix containing various Einstein coefficients.

Before simulating the population dynamics, it is necessary to determine the effect of the vibrational decay process on the $X^1\Sigma_0^+$ ground state. Here, we compute the ratio $\frac{A_{0'0''}}{A_{1'0''}}$ of the Einstein coefficient between electronic [$A_{0'0''}(v' = 0) \rightarrow (v'' = 0)$] and vibrational [$A_{1'0''}(v' = 1) \rightarrow (v'' = 0)$] relaxation. The vibrational transition dipole moment (vTDM) matrix elements over vibrational wave functions of $X^1\Sigma_0^+$ state had been computed with the Molcas³¹ vibrot module,

$$v\text{TDM}_{1'0''} = \int \phi_{(v''=1)} R \phi_{(v''=0)} dR. \quad (6)$$

The ratios for TIF and TlCl are 1.8×10^7 and 3.0×10^7 , respectively. These are similar to the value of 2.5×10^7 for SrF.⁴² Such a large ratio indicates that the vibrational relaxation is very weak; thus, we chose to exclude it in the subsequent simulation model.

Explicitly, the rate equation has the form

$$\begin{aligned} \frac{dP_i}{dt} = & - \sum_{j=1}^{j=i-1} A_{ij} P_i - \sum_{j=1}^{j=i-1} B_{ij} \rho(\omega_{ij}) P_i \\ & - \sum_{j=i+1}^{j=N} B_{ji} \rho(\omega_{ij}) P_i + \sum_{j=i+1}^{j=N} A_{ji} P_j \\ & + \sum_{j=1}^{j=i-1} B_{ji} \rho(\omega_{ji}) P_j + \sum_{j=i+1}^{j=N} B_{ji} \rho(\omega_{ji}) P_j. \end{aligned} \quad (7)$$

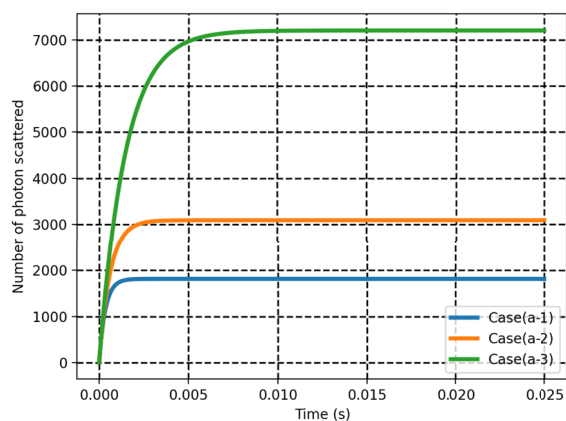
Here, A_{mn} , B_{ij} , and B_{ji} are spontaneous emission, stimulated emission, and absorption coefficients, respectively. $\rho(\omega_{ij})$ is the spectral energy density at frequency ω_{ij} .

After numerically solving Eq. (7), the average number of scattered photons is evaluated by multiplying the obtained population in the excited state of the optical cycle by its total radiation rate $A_{ij} + B_{ij}$. The stimulated coefficients B are proportional to A , with

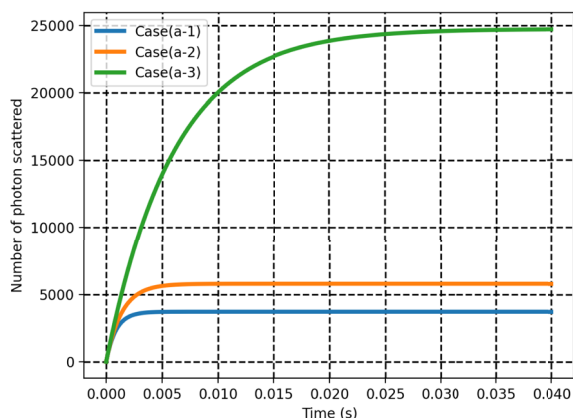
$$B_{ij} = B_{ji} = \frac{\pi^2 c^3}{h\omega_{ij}^3} A_{ij}, \quad (8)$$

where h is the Planck constant and c is the speed of light.

In these simulations, we use three different laser configurations: Case (a-1) includes three lasers: $\lambda_{0'0''}$, $\lambda_{1'1''}$, and $\lambda_{0'2''}$; case (a-2) has an additional laser $\lambda_{1'3''}$; and case (a-3) includes each of the five lasers. The simulation results are plotted in Fig. 2. The population is initially in $X^1\Sigma_0^+$ ($v'' = 0$) state.



(a) TIF



(b) TICl

FIG. 2. The number of scattered photons for TIF and TICl with different laser configurations. Case (a-1) has first three laser: $\lambda_{0'0''}$, $\lambda_{1'1''}$, and $\lambda_{0'2''}$. Case (a-2) includes case (a-1) plus the fourth laser $\lambda_{1'3''}$. Case (a-3) includes case (a-2) plus the fifth laser $\lambda_{2'4''}$.

The two molecules show similar dynamics: TIF reaches the limit faster than TICl, as the rate of its spontaneous radiation is nearly double that of TICl, while TICl scatters more photons than TIF does throughout the cooling process. In this model, TIF absorbs roughly 7300 photons when five lasers are utilized, whereas TICl absorbs 25 000 photons.

A simple equation

$$N_{tot} = \frac{1}{1 - \sum_{i=0}^{i=4} R_{0'i''}} \quad (9)$$

could be used to qualitatively estimate the total photon absorption/emission cycles.⁴³ It is straightforward to see N_{tot} is sensitive to the vibrational branching, particularly on the non-diagonal element of Franck–Condon factors, such as ($v' = 0$) \rightarrow ($v'' = 1, 2, 3, \dots$ etc.). Such sensitivity is also evident in the large difference between the configurations of five and four lasers.

From the above discussion, we have that a smaller number of scattered photons implies the need for a larger number of cooling lasers. This number is, in turn, dependent on the magnitude of non-diagonal FCFs. It would, therefore, be of interest, in order to provide the best theoretical estimates for the number of scattered photons, to calculate non-diagonal FCFs at a high level of theory, for instance, by including triple and higher excitations to the CI or coupled cluster wavefunctions, considering non-adiabatic corrections, or both.

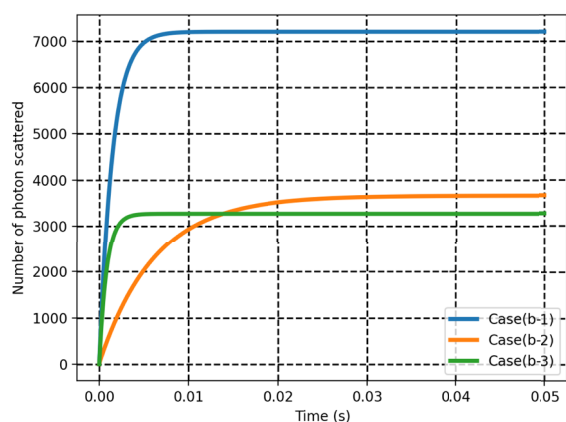
Due to limitations in both computational resources and the availability of computer implementations, it is outside the scope of this work to investigate such aspects. Before attempting to do so, however, it would be useful to have reliable experimental data on vibrational branching measurements in order to determine how much computations must be improved to bridge the gap between theory and experiment for TICl.

In addition, as reported by Norcia *et al.*,⁴⁴ introducing stimulated emission is a potentially efficient method for laser cooling. Consequently, we also examine the effect of stimulated radiation by varying the spectral energy density $\rho(\omega_{ij})$ of the simulation that employs five lasers. The $\rho(\omega_{ij})$ in case (b-1) and case (b-2) are 10^{-12} J/(m³ s Hz) and 10^{-13} J/(m³ s Hz), respectively. In case (b-3), we remove the stimulated radiation terms in the equation and keep the same $\rho(\omega_{ij})$ as for case (b-1). The results are displayed in Fig. 3. The large difference in both photon numbers and scattering rates between case (b-1) and case (b-3) shows that the simulations are significantly affected by stimulated radiation.

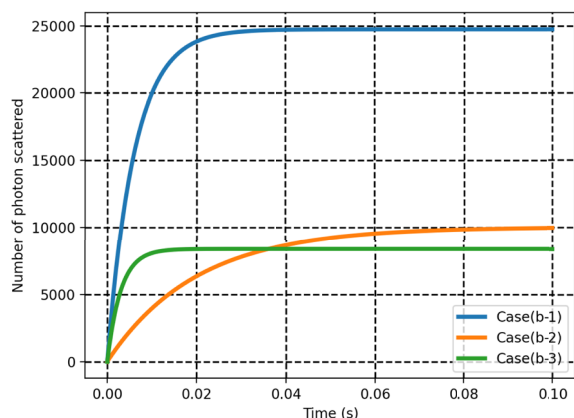
By comparing case (b-1) and case (b-2), we find that increasing the higher spectral energy density results in absorbing more photons. For instance, TICl could scatter 25 000 photons in 0.04 s under $\rho(\omega_{ij}) = 10^{-12}$ J/(m³ s Hz), but only 10 000 in 0.08 s under $\rho(\omega_{ij}) = 10^{-13}$ J/(m³ s Hz). In conclusion, enhancing stimulated radiation is an effective strategy for strengthening the cooling dynamics, including the total number of scattered photons and the scattering rate.

IV. CONCLUSION

Through four-component multi-reference configuration interaction (MRCI), equation of motion coupled-cluster (EOM-CC), and polarization propagator (PP) calculations, we investigated the permanent dipole moments (PDMs) of the ground and low-lying



(a) TIF



(b) TlCl

FIG. 3. The cooling simulation at different levels of stimulated radiation. Case (b-1): spectral energy density $\rho(\omega_{ij})$ is 10^{-12} J/(m³ s Hz); case (b-2): $\rho(\omega_{ij})$ is 10^{-13} J/(m³ s Hz); case (b-3): $\rho(\omega_{ij})$ is 10^{-12} J/(m³ s Hz) but the stimulated radiation coefficients B_{ij} is set as 0.

excited states of TIF and TlCl molecules as well as the transition dipole moments (TDMs) between these electronic states. Our primary objective is to extract, from the TDMs, the excited state lifetimes that will allow us to determine whether or not the TlCl species is a suitable choice for laser cooling experiments.

After cross-validating the four-component MRCI results with the other two methods, we applied it to derive a PDM of -2.47 D and a lifetime of 91 ns for the $a^3\Pi_1$ state of TIF, which are comparable to the experimental results of $-2.28(7)$ D and 99(9) ns, respectively.

For TlCl, we obtained from our four-component MRCI calculations a lifetime of 175 ns for the $a^3\Pi_0^+$ state. This value is much shorter than a recent theoretical estimation of 6.04 μ s by Yuan *et al.*¹⁴

from SOCI calculations. Our results point to the strong underestimation by the SOCI method of the TDMs as the main factor behind such a discrepancy, as the SOCI ground and excited state energies and PDMs for TlCl closely match the four-component values.

We have done a comprehensive population simulation with the new lifetime by solving the rate equation, and we find that TlCl exhibits comparable cooling dynamics to TIF. Moreover, our simulations reveal that the vibrational branching of weak transitions driven by non-diagonal elements of Franck–Condon factors may play a significant role in cooling efficiency. We believe that a highly precise experiment measuring the Franck–Condon factors of $a^3\Pi_0^+ - X^1\Sigma_0^+$ transition of TlCl could provide useful information for pinpointing the deficiencies of current theoretical models.

Finally, we investigate the effect of stimulated radiation on the cooling process. We show that stimulated radiation is significant and that raising the spectral energy density is one approach to enhance the cooling efficiency.

SUPPLEMENTARY MATERIAL

See the [supplementary material](#) for further details on the Generalized Active Spaces (GAS) setup and tests using different MRCI models, the Einstein coefficients and the vibrational branching used in the cooling simulation, and the ZZ component of the polarizability of TIF and TlCl evaluated with finite-field methods.

ACKNOWLEDGMENTS

We thank Valérie Vallet for critical reading of the manuscript. We acknowledge funding from projects ComRIXS (Grant Nos. ANR-19-CE29-0019 and DFG JA 2329/6-1), Labex CaPPA (Grant No. ANR-11-LABX-0005-01), and the I-SITE ULNE project OVERSEE and MESONM International Associated Laboratory (LAI) (Grant No. ANR-16-IDEX-0004) and support from the French national supercomputing facilities (Grant Nos. DARI A0090801859 and A0110801859).

AUTHOR DECLARATIONS

Conflict of Interest

The authors have no conflicts to disclose.

Author Contributions

Xiang Yuan: Conceptualization (lead); Data curation (lead); Formal analysis (lead); Investigation (lead); Methodology (lead); Software (lead); Writing – original draft (lead); Writing – review & editing (equal). **André Severo Pereira Gomes:** Funding acquisition (lead); Investigation (supporting); Software (supporting); Supervision (lead); Writing – original draft (supporting); Writing – review & editing (equal).

DATA AVAILABILITY

The data that support the findings of this study are openly available in the Zenodo repository at <http://doi.org/zenodo.org/record/6376250>, Ref. 39.

REFERENCES

- ¹M. D. Rosa, *Eur. Phys. J. D* **31**, 395 (2004).
- ²E. S. Shuman, J. F. Barry, and D. DeMille, *Nature* **467**, 820 (2010).
- ³S. Truppe, H. J. Williams, M. Hambach, L. Caldwell, N. J. Fitch, E. A. Hinds, B. E. Sauer, and M. R. Tarbutt, *Nat. Phys.* **13**, 1173 (2017).
- ⁴M. T. Hummon, M. Yeo, B. K. Stuhl, A. L. Collopy, Y. Xia, and J. Ye, *Phys. Rev. Lett.* **110**, 143001 (2013).
- ⁵J. Lim, J. R. Almond, M. A. Trigatzis, J. A. Devlin, N. J. Fitch, B. E. Sauer, M. R. Tarbutt, and E. A. Hinds, *Phys. Rev. Lett.* **120**, 123201 (2018).
- ⁶E. A. Hinds and P. G. H. Sandars, *Phys. Rev. A* **21**, 480 (1980).
- ⁷P. G. H. Sandars, *Phys. Rev. Lett.* **19**, 1396 (1967).
- ⁸M. Hubert and T. Fleig, *arXiv:2203.04618* (2022).
- ⁹L. R. Hunter, S. K. Peck, A. S. Greenspon, S. S. Alam, and D. DeMille, *Phys. Rev. A* **85**, 012511 (2012).
- ¹⁰N. B. Clayburn, T. H. Wright, E. B. Norrgard, D. DeMille, and L. R. Hunter, *Phys. Rev. A* **102**, 052802 (2020).
- ¹¹G. Meijer and B. G. Sartakov, *Phys. Rev. A* **101**, 042506 (2020).
- ¹²O. Grasdijk, O. Timgren, J. Kastelic, T. Wright, S. Lamoreaux, D. DeMille, K. Wenz, M. Aitken, T. Zelevinsky, T. Winick, and D. Kawall, *Quantum Sci. Technol.* **6**, 044007 (2021).
- ¹³W. Zou and W. Liu, *J. Comput. Chem.* **30**, 524–539 (2009).
- ¹⁴X. Yuan, S. Yin, Y. Shen, Y. Liu, Y. Lian, H.-F. Xu, and B. Yan, *J. Chem. Phys.* **149**, 094306 (2018).
- ¹⁵Y. Li, H. P. Liebermann, G. Hirsch, and R. J. Buenker, *J. Mol. Spectrosc.* **165**, 219 (1994).
- ¹⁶V. Vallet, L. Maron, C. Teichtel, and J.-P. Flament, *J. Chem. Phys.* **113**, 1391 (2000).
- ¹⁷A. Weigand, X. Cao, V. Vallet, J.-P. Flament, and M. Dolg, *J. Phys. Chem. A* **113**, 11509 (2009).
- ¹⁸C. Danilo, V. Vallet, J.-P. Flament, and U. Wahlgren, *Phys. Chem. Chem. Phys.* **12**, 1116 (2010).
- ¹⁹A. S. Pereira Gomes, F. Réal, N. Galland, C. Angeli, R. Cimraglia, and V. Vallet, *Phys. Chem. Chem. Phys.* **16**, 9238 (2014).
- ²⁰Š. Kervazo, F. Réal, F. Virot, A. Severo Pereira Gomes, and V. Vallet, *Inorg. Chem.* **58**, 14507 (2019).
- ²¹R. J. Bartlett, *WIREs Comput. Mol. Sci.* **2**, 126 (2012).
- ²²A. Dreuw and M. Wormit, *WIREs Comput. Mol. Sci.* **5**, 82 (2015).
- ²³DIRAC, a relativistic *ab initio* electronic structure program, Release DIRAC19, written by A. S. P. Gomes, T. Saue, L. Visscher, H. J. Aa. Jensen, and R. Bast, with contributions from I. A. Aucar, V. Bakken, K. G. Dyall, S. Dubillard, U. Ekström, E. Eliav, T. Enevoldsen, E. Faßhauer, T. Fleig, O. Fossgaard, L. Halbert, E. D. Hedegård, T. Helgaker, B. Helmich-Paris, J. Henriksson, M. Iliáš, C. R. Jacob, S. Knecht, S. Komorovský, O. Kullie, J. K. Lærdahl, C. V. Larsen, Y. S. Lee, H. S. Nataraj, M. K. Nayak, P. Norman, G. Olejniczak, J. Olsen, J. M. H. Olsen, Y. C. Park, J. K. Pedersen, M. Pernpointner, R. di Remigio, K. Ruud, P. Salek, B. Schimmelpennig, B. Senjean, A. Shee, J. Sikkema, A. J. Thorvaldsen, J. Thyssen, J. van Stralen, M. L. Vidal, S. Villaume, O. Visser, T. Winther, and S. Yamamoto, see <http://www.diracprogram.org>, 2019.
- ²⁴DIRAC, a relativistic *ab initio* electronic structure program, Release DIRAC22, written by H. J. A. Jensen, R. Bast, A. S. P. Gomes, T. Saue, and L. Visscher, with contributions from I. A. Aucar, V. Bakken, C. Chibueze, J. Creutzberg, K. G. Dyall, S. Dubillard, U. Ekström, E. Eliav, T. Enevoldsen, E. Faßhauer, T. Fleig, O. Fossgaard, L. Halbert, E. D. Hedegård, T. Helgaker, B. Helmich-Paris, J. Henriksson, M. van Horn, M. Iliáš, C. R. Jacob, S. Knecht, S. Komorovský, O. Kullie, J. K. Lærdahl, C. V. Larsen, Y. S. Lee, N. H. List, H. S. Nataraj, M. K. Nayak, P. Norman, G. Olejniczak, J. Olsen, J. M. H. Olsen, A. Papadopoulos, Y. C. Park, J. K. Pedersen, M. Pernpointner, J. V. Pototschnig, R. di Remigio, M. Repisky, K. Ruud, P. Salek, B. Schimmelpennig, B. Senjean, A. Shee, J. Sikkema, A. Sunaga, A. J. Thorvaldsen, J. Thyssen, J. van Stralen, M. L. Vidal, S. Villaume, O. Visser, T. Winther, S. Yamamoto, and X. Yuan, see <http://www.diracprogram.org>, 2022.
- ²⁵T. Saue, R. Bast, A. S. P. Gomes, H. J. A. Jensen, L. Visscher, I. A. Aucar, R. Di Remigio, K. G. Dyall, E. Eliav, E. Faßhauer *et al.*, *J. Chem. Phys.* **152**, 204104 (2020).
- ²⁶L. Visscher, *Theor. Chem. Acc.* **98**, 68 (1997).
- ²⁷K. G. Dyall, *Theor. Chem. Acc.* **115**, 441 (2006).
- ²⁸R. A. Kendall, T. H. Dunning, Jr, and R. J. Harrison, *J. Chem. Phys.* **96**, 6796 (1992).
- ²⁹D. E. Woon and T. H. Dunning, Jr, *J. Chem. Phys.* **98**, 1358 (1993).
- ³⁰D. Deng, Y. Lian, and W. Zou, *Chem. Phys. Lett.* **688**, 33 (2017).
- ³¹F. Aquilante, J. Autschbach, A. Baiardi, S. Battaglia, V. A. Borin, L. F. Chibotaru, I. Conti, L. De Vico, M. Delcey, I. Fdez Galván *et al.*, *J. Chem. Phys.* **152**, 214117 (2020).
- ³²S. Knecht, H. J. A. Jensen, and T. Fleig, *J. Chem. Phys.* **132**, 014108 (2010).
- ³³T. Fleig, J. Olsen, and L. Visscher, *J. Chem. Phys.* **119**, 2963 (2003).
- ³⁴L. Visscher, T. J. Lee, and K. G. Dyall, *J. Chem. Phys.* **105**, 8769 (1996).
- ³⁵A. Shee, L. Visscher, and T. Saue, *J. Chem. Phys.* **145**, 184107 (2016).
- ³⁶A. Shee, T. Saue, L. Visscher, and A. Severo Pereira Gomes, *J. Chem. Phys.* **149**, 174113 (2018).
- ³⁷M. Pernpointner, *J. Chem. Phys.* **140**, 084108 (2014).
- ³⁸M. Pernpointner, L. Visscher, and A. B. Trofimov, *J. Chem. Theory Comput.* **14**, 1510 (2018).
- ³⁹X. Yuan and A. S. P. Gomes (2022). “Dataset: Reassessing the potential of TlCl for laser cooling experiments via four-component correlated electronic structure calculations,” Zenodo. <https://doi.org/10.5281/zenodo.6376250>
- ⁴⁰Y. Liu, X. Yuan, L. Xiao, H. Xu, and B. Yan, *J. Quant. Spectrosc. Radiat.* **243**, 106817 (2020).
- ⁴¹E. Tiemann, *Mol. Phys.* **65**, 359 (1988).
- ⁴²J. H. V. Nguyen, C. R. Viteri, E. G. Hohenstein, C. D. Sherrill, K. R. Brown, and B. Odom, *New J. Phys.* **13**, 063023 (2011).
- ⁴³M. Fu, H. Ma, J. Cao, and W. Bian, *J. Chem. Phys.* **146**, 134309 (2017).
- ⁴⁴M. A. Norcia, J. R. K. Cline, J. P. Bartolotta, M. J. Holland, and J. K. Thompson, *New J. Phys.* **20**, 023021 (2018).

7.2 Paper II: Final-state-resolved mutual neutralization in $I^+ - I^-$ collisions










I carried out the MRCI calculations for the potential energy curves and transition dipole moment and participated in writing the manuscript.

Physical Review A., 106, 012812, 2022

Reproduced from *Physical Review A.* under CC-BY

Copyright 2022 APS Publishing.

Final-state-resolved mutual neutralization in $I^+ - I^-$ collisions

Mathias Poline ^{1,*} Xiang Yuan ^{2,3} Sylvain Badin ^{2,4} MingChao Ji ¹ Stefan Rosén,¹ Suvasthika Indrajith ¹
Richard D. Thomas ¹ Henning T. Schmidt ¹ Henning Zettergren ¹ Andre Severo Pereira Gomes ²
and Nicolas Sisourat^{4,*}

¹*Department of Physics, Stockholm University, Stockholm SE-10691, Sweden*

²*Université de Lille, CNRS, UMR 8523, Physique des Lasers, Atomes et Molécules, F-59000 Lille, France*

³*Department of Chemistry and Pharmaceutical Science, Faculty of Science, Vrije Universiteit Amsterdam, de Boelelaan 1083, 1081 HV Amsterdam, Netherlands*

⁴*Sorbonne Université, CNRS, Laboratoire de Chimie Physique Matière et Rayonnement, UMR 7614, F-75005 Paris, France*



(Received 11 February 2022; accepted 27 June 2022; published 18 July 2022)

We have studied the mutual neutralization reaction of atomic iodine ions (i.e., $I^+ + I^- \rightarrow I + I$) in a cryogenic double electrostatic ion-beam storage-ring apparatus. Our results show that the reaction forms iodine atoms either in the ground-state configuration ($I(5p^5\ ^2P^\circ)$, $\sim 40\%$) or with one atom in an electronically excited state ($I(6s\ ^2[2])$, $\sim 60\%$), with no significant variation over the branching ratios in the studied collision-energy range (0.1–0.8 eV). We estimate the total charge-transfer cross section to be of the order of 10^{-13} cm^2 at 0.1 eV collision energy. *Ab initio* relativistic electronic structure calculations of the potential-energy curves of I_2 suggest that the reaction takes place at short internuclear distances. The results are discussed in view of their importance for applications in electric thrusters.

DOI: [10.1103/PhysRevA.106.012812](https://doi.org/10.1103/PhysRevA.106.012812)

I. INTRODUCTION

Electric thrusters for space vehicles have been used across the world since the 1960s. Since then, they have been deployed on hundreds of satellites and space exploration probes [1,2]. Thanks to the recent increase in available power on spacecraft [1], the full potential of electric propulsion is now achievable. This is demonstrated by the emergence of all-electric communication satellites and projects requiring the deployment of large constellations of small electric-powered satellites [1–3] (see also [4] and references therein).

The basic physical principles of electric thrusters are the following: a plasma is formed by ionizing the propellant, and the ions created are accelerated by electromagnetic fields. The ejection of the accelerated ions produces a thrust to the spacecraft through the conservation of momentum. The efficiency of these systems depends strongly on the total ion density formed in the plasma. An efficient propellant should therefore have high atomic mass and be easy to ionize in order to yield high ion fluxes and exert a large force on the spacecraft. Xenon is currently the propellant of choice (see, e.g., [5] and references therein), owing to its high atomic mass and fairly low ionization potential. However, xenon is rare, is

expensive, and must be stored either in high-pressure tanks or at cryogenic temperatures, significantly impacting the usable volume in satellites.

The iodine molecule is an interesting candidate to replace xenon [6–9] since it also has high atomic mass and low ionization potential. In contrast to xenon, iodine is cheap and exists in the solid state at standard pressure and temperature. These properties result in a storage density of iodine that is 3 times higher than that of xenon under equivalent conditions. In an iodine plasma thruster, the electric energy is used to ionize the iodine molecules to form the plasma. In addition to this ionization, some energy is also inevitably dissipated in other processes, leading to various atomic and molecular iodine species, both neutral and charged. Only ions can be accelerated electrically to participate in the propulsion. However, various reactions taking place in the volume of the plasma can lead to the neutralization of the species, thus causing substantial power loss. Currently, no data are available on these processes, thus impeding the description and modeling of such thrusters.

As a first step to address these issues, we have studied a key reaction in iodine plasmas [10], the mutual-neutralization (MN) reaction of atomic iodine ions:



where E_K is the kinetic energy released in the process. Recent modeling suggested that this reaction is important to the performance of thrusters [10]. However, the model relies on input from experimental studies that are associated with large uncertainties regarding the actual MN collision partners and the related rates in iodine plasmas [11]. Furthermore, the atoms formed in MN collisions can undergo further reactions [6], whose rates may depend strongly on the final states of the

*Corresponding authors: mathias.poline@fysik.su.se;
nicolas.sisourat@sorbonne-universite.fr

Published by the American Physical Society under the terms of the [Creative Commons Attribution 4.0 International](https://creativecommons.org/licenses/by/4.0/) license. Further distribution of this work must maintain attribution to the author(s) and the published article's title, journal citation, and DOI. Funded by [Bibsam](https://www.bibsam.com/).

reaction products. The present study is therefore needed to improve the modeling of iodine plasma.

In MN reactions, the kinetic energy released E_K is related to the initial- and final-state distributions of the atoms. By measuring E_K , the branching ratios of the different channels in this reaction were determined at collision energies of ~ 0.1 and ~ 0.8 eV. Our results show that (i) the reaction leads to two different sets of product pairs, either a pair of atoms in the ground-state configuration or a pair in which one atom is in its ground state while the other is in the $6s^2[2]$ excited state; (ii) these pairs have a population of roughly 40%/60% with no significant dependence on the collision energy in the studied range; and (iii) the total charge-transfer cross section is of the order of 10^{-13} cm² at 0.1-eV collision energy. Furthermore, insights into the electron dynamics taking place during the collision are provided by potential-energy curves for I₂, which we have calculated by means of multireference *ab initio* relativistic electronic structure methods. These suggest that the relevant curve crossings leading to the observed final states occur at short internuclear distances.

The outline of this article is as follows: in Sec. II, we briefly describe the theoretical and experimental methods employed to study the mutual neutralization reactions of iodine ions. In Sec. III, the *ab initio* potential-energy curves of I₂ are discussed, and the experimental branching ratios for the different channels in this reaction are reported. The article ends with a summary of this work (Sec. IV).

II. METHODS

A. Theory

The *ab initio* calculations of the electronic states of I₂ were performed with the DIRAC19 release [12] and with a development version (hash 1E798E5) of the DIRAC relativistic electronic structure package [13]. In all calculations we employed the four-component Dirac-Coulomb Hamiltonian, which accounts for scalar and spin-orbit effects at the mean-field level. We employed an uncontracted triple-zeta quality basis set, including three diffuse functions (t-aug-dyall.v3z [14]), in order to accurately compute the Rydberg and ion-pair (IP) states.

The ground and electronically excited states considered here were obtained with the multireference configuration interaction (MRCI) method, as implemented in the KRCI module [15] of DIRAC. In the reference configuration for MRCI we employed 10 electrons distributed over 12 spinors. It includes the valence $\sigma_{1/2}$, $\pi_{1/2}$, $\pi_{3/2}$, $\pi_{1/2}^*$, $\pi_{3/2}^*$, and $\sigma_{1/2}^*$ molecular spinors arising from the p^5 manifold of each atom and ensures a qualitatively correct dissociation behavior for large internuclear distances. We calculated 109 single-point energies within the range of 1.9–10 Å for the potential-energy curves (PECs) and 63 molecular states in total for the $\Omega = 0_g, 0_u, 1_g, 1_u, 2_g,$ and 2_u symmetries. Spectroscopic constants for the different (bound) electronic states have been derived from the calculated PECs with the LEVEL [16] program.

Our electronic structure calculations account for spin-orbit coupling from the outset, with systems possessing linear symmetry. Thus, instead of employing the commonly used *LS*-coupling notation to characterize the symmetry of the

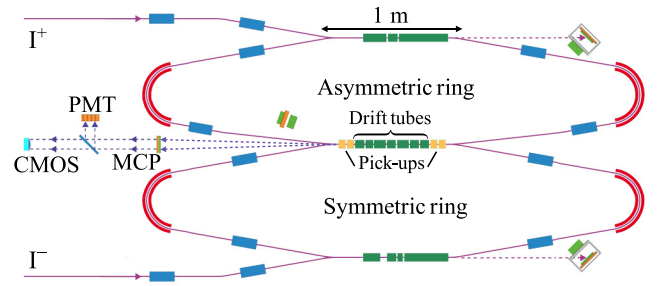


FIG. 1. Schematic of the double electrostatic ion-beam storage ring DESIREE. I⁺ and I[−] ion beams are created from two different ion sources (see text) and injected into the two rings. In the merged section (drift tubes), the ions interact, and the resulting neutrals are detected by means of a three-dimensional imaging detector consisting of a microchannel plate and phosphor screen based detector (MCP), a CMOS camera, and a PMT.

molecular electronic states, we label them by the value of the projection of the total electronic angular momentum along the internuclear axis Ω . For example, the first $\Omega = 0_g^+$ state corresponds to the $^1\Sigma_g^+$ ground state (for further details on how the DIRAC code handles the attribution of such quantities see Ref. [13]).

B. Experimental details

The experiments were carried out at the double electrostatic ion-beam storage-ring facility Double ElectroStatic Ion Ring Experiment (DESIREE) (Stockholm University, Sweden), an ultrahigh-vacuum device operated at cryogenic temperatures of about 13 K. This experimental setup was described previously by Thomas *et al.* [17] (design and technical description), Schmidt *et al.* [18] (first commissioning), and Eklund *et al.* [19] (first mutual neutralization experiment) and is only briefly discussed here.

Positive iodine ions were produced from pure iodine in an electron cyclotron resonance (ECR) ion source, and negative iodine ions were produced from magnesium iodide compounds in a cesium sputtering source. Bending magnets at the exit of the sources were employed to select the ions of interest, after which the two oppositely charged ion beams of ¹²⁷I were accelerated and injected into the two storage rings.

As shown in Fig. 1, the two rings share a common section in which interactions between the two species may occur. Pickup electrodes, located at the entrance and exit of this merged section, measure the beam positions and were used to optimize the overlap of the two ion beams. The collision energy $E_{c.m.}$ of the reaction was then fine-tuned through the biasing of drift tubes. This applied voltage decelerates (accelerates) the negative (positive) ions to the desired velocities in a small section of this merged region (the biased region), allowing us to constrain the region of low-collision-energy interactions (here chosen to be approximately 16 cm long).

A microchannel-plate (MCP) detector [20] located 1.5 m from this biased region was used to detect the neutralized particles arising from mutual neutralization events and residual gas collisions. Each of these events produced light spots on a phosphor screen located behind the MCP. The resulting

TABLE I. Experimental parameters used during the data acquisitions. They include the energies E_i and currents I_i of the positive (A) and negative (B) ion beams, the potentials applied to the interaction region U , and the center-of-mass collision energy obtained $E_{c.m.}$.

Data set	E_A (keV)	E_B (keV)	I_A (nA)	I_B (nA)	U (V)	$E_{c.m.}$ (eV)
1	13	12	3	8	500	0.07 ± 0.01
2	35	30	15	30	1275	0.10 ± 0.02
3	35	30	15	30	1060	0.80 ± 0.10

photons are guided via optics to a complementary metal oxide semiconductor (CMOS) camera and a multianode photomultiplier tube (PMT), which record the positions and relative arrival times of the particles. The PMT signal-processing system can detect events with an arrival-time difference up to 200 ns. In the unbiased region of the merged section, the relative velocity of the two ions is such that the arrival-time differences are well outside this time window. Thus, these events do not interfere with the data from reactions occurring in the biased region.

C. Branching-ratio calculations

For an MN event occurring at a distance L from the detector, the separation between two neutral particles formed in the reaction, as recorded by the detection system, is given by

$$r = \sqrt{r_{\parallel}^2 + r_{\perp}^2} \approx \sqrt{\frac{2(E_K + E_{c.m.})}{\mu}} \frac{L}{v}, \quad (2)$$

where r_{\parallel} is the projected transverse distance, recorded by the camera, $r_{\perp} \approx v\Delta t$ is an approximation of the third dimensional component (v is the average velocity of the reactants), and μ is the reduced mass of the ions. Here, $E_{c.m.}$ is the center-of-mass kinetic energy before the interaction, and E_K is the kinetic energy released in the specific reaction channel.

This particular three-dimensional imaging technique of two particles was first introduced by Amitay and Zajfman [21] for the study of the dissociative recombination reaction [22–24] but has since been employed for a number of MN systems, such as Li^+/D^- [19,25], Mg^+/D^- [26], and O^+/O^- [27,28]. The resulting spectrum represents a distribution of the final-state center-of-mass kinetic energy over the longitudinal extension of the interaction region and the collision-energy spread. By simulating these distributions using the Monte Carlo method and fitting them to the data, the branching ratios can be extracted [19,29]. They are corrected for the energy-dependent efficiency related to the angular acceptance of the detectors (for more details see Ref. [28]).

Table I shows the experimental parameters used during the three experimental runs: In the first run, data were acquired using slower ion beams in order to investigate the low kinetic-energy release E_K channels in detail; in the other two runs, data were acquired with the aim of measuring the final-state distributions of all energetically open channels at two different collision energies.

In order to maximize the range of product kinetic energies that could be detected and obtain satisfying rates, higher beam energies and currents were used in the two later data sets, resulting in larger background contributions. These mainly arise from collisions between stored ions and residual-gas

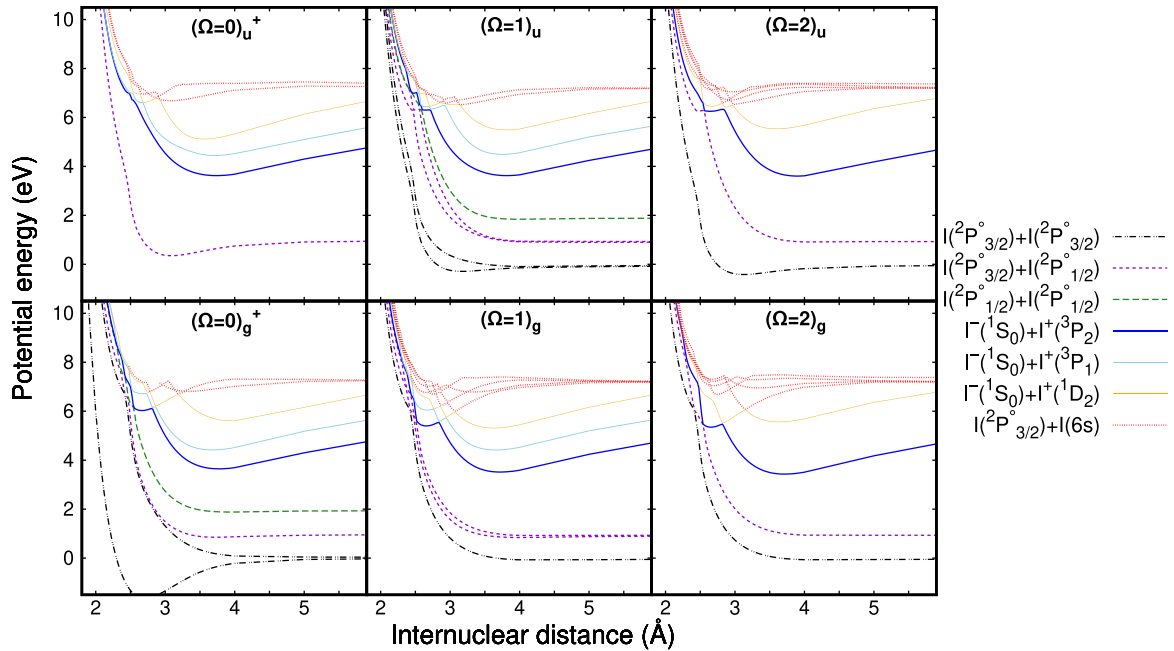


FIG. 2. MRCI PECs of 51 electronic states (including Rydberg and IP) of I_2 , classified in terms of the projection of the total electronic angular momentum Ω . Twelve $(\Omega = 0)_g^-$ and $(\Omega = 0)_u^-$ states are not shown here since there is no $\text{I}^+(^3P_2) + \text{I}^-(^1S_0)$ state with this symmetry. The energies (in eV) have been scaled so that the zero corresponds to twice the energy of the $^2P_{3/2}$ ground state of the isolated iodine atom. See Table III for the energies of the different asymptotes. Detailed views of the PECs at short internuclear distances are shown in Fig. 5 in the Appendix.

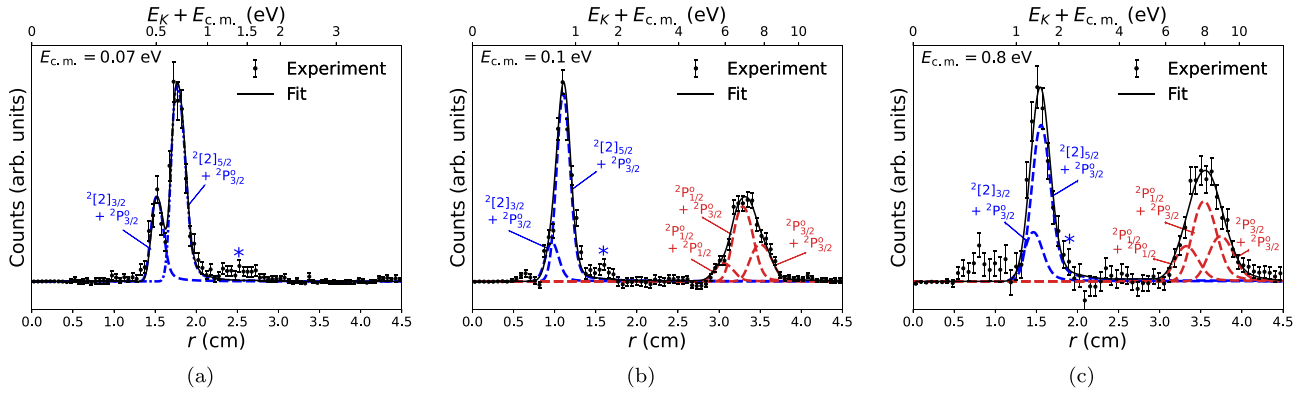


FIG. 3. Yields of neutral pairs as a function of the separation r between the products at center-of-mass collision energies of (a) 0.07 eV, (b) 0.1 eV, and (c) 0.8 eV. The top scale shows the corresponding center-of-mass kinetic energy after the reaction [Eq. (2)]. The solid line results from a fit of the simulated distributions of ground-state–excited-state pairs [blue line; Eq. (3)] and ground-state-configuration pairs [red line; Eq. (4)]. The asterisks indicate contributions from metastable cations (not included in the fit). The background has been subtracted (see Fig. 6 in the Appendix for original spectra).

molecules as well as false coincidences. The majority of the background could be filtered out by excluding events for which the center-of-mass position of the two products on the imaging detector was outside a 5-mm range. However, a non-negligible number of events remained after this selection, in particular for measurements with low signal to background ratio. The filtered-out events were then used as a model for this remaining background and were subsequently subtracted from the spectra. For more details see the Appendix.

D. Reaction cross-section estimate

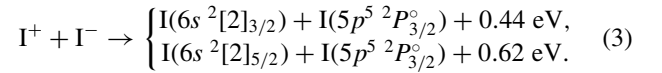
In order to extract MN reaction cross sections, it is necessary to determine the spatial distributions of the interacting particle beams. Currently, a method to derive this overlap (form factor) with high precision is not available at DESIREE. Additionally, it may vary between different experiments since the storing of merged beams requires adjusting the ion optics based on the mass ratio and energies of the two ions. The cross section may therefore be only roughly estimated based on the observed rates relative to other previously studied systems with known cross sections and is subject to large uncertainties. However, given the absence of any experimental or theoretical estimate for this particular collision system, we have made such an evaluation, which is presented in the results section.

III. RESULTS AND DISCUSSION

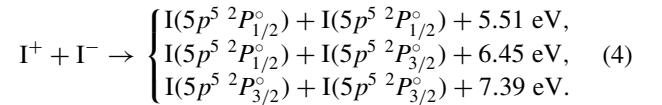
A. Theoretical results

In order to get insights into the MN dynamics, we report the potential-energy curves of I_2 in Fig. 2 (a detailed discussion of these curves is given in the Appendix). At the collision energies investigated in this work, electronic processes take place mainly around the avoided crossings. Assuming the system starts in the lowest ion-pair state [i.e., $I^+(^3P_2) + I(^1S_0)$; blue curve in Fig. 2], one can, in principle, study the paths to a given final state for each symmetry. Since the asymptotic energy of the ion-pair state lies above the neutral excited-state–ground-state pair, the reaction may result in

the formation of an electronically excited iodine atom, i.e.,



As there are too many avoided crossings between the states, an appropriate simulation of the collision dynamics is necessary to study the pathway to these channels. However, the path to the lowest states of I_2 is fairly simple: For all symmetries the lowest ion-pair state exhibits first an avoided crossing with the curves corresponding to $I(^2P_{3/2}^\circ) + I(6s)$ (here shown in red) at an internuclear distance between 2.5 and 3 Å. At shorter internuclear distances, these curves can cross the ground-state-configuration curves, resulting in the following channels:



Therefore, the simplest path to the lowest states of I_2 is through a highly excited state followed by a deexcitation of the excited iodine atom at closer distances between the collision partners.

We note that avoided crossings between the lowest ion-pair state and these excited-state–ground-state pair states also occur at larger internuclear distances (~ 23 Å). However, using a Landau-Zener approach and the Olson semiempirical model (see [30], Eq. (13)), we estimate that the electronic couplings at these avoided crossings are negligible. The dynamics of the reaction are therefore expected to take place at the avoided crossings presented in Fig. 2, for which more advanced modeling is necessary, as the current approach is not applicable to nonisolated crossings occurring at short internuclear distances.

B. Experimental results

The yields of neutral pairs as a function of the separation r between the products for the three acquired data sets (see Table I) are shown in Figs. 3(a), 3(b), and 3(c). As different

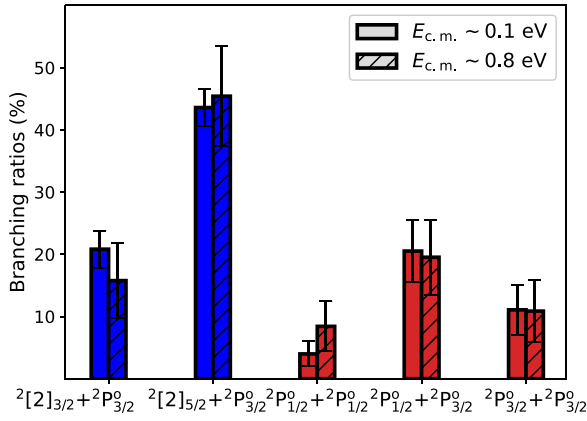


FIG. 4. Branching ratios of the mutual neutralization of I^+ with I^- at the two measured collision energies.

beam energies and collision energies were used for the different data sets, the measured separations then correspond to different final kinetic energies [see Eq. (2)], as highlighted in the top scales of Fig. 3, and hence different final states [Eqs. (3) and (4)]

For the first spectrum [Fig. 3(a)], at (0.07 ± 0.01) -eV collision energy, slower ion beams were used in order to resolve the channels resulting in iodine in the $6s^2[2]$ excited state. Thus, the separations correspond to kinetic energies only up to 3 eV. The two channels [Eq. (3)], corresponding to the spin-orbit splitting of this excited state, can be clearly distinguished in the spectrum, with the $J = 5/2$ state found to dominate. In the second data set [Fig. 3(b)], a similar collision energy was achieved, namely, 0.10 ± 0.02 eV. The same two peaks [from Fig. 3(a)] are then located at lower separations (around 1 cm) due to the higher beam energies used but are no longer resolved. However, an additional peak appears at larger separations, corresponding to pairs of iodine atoms in the ground-state configuration [Eq. (4)]. Since the broadening of the distributions scales with kinetic energy, the individual J -state pairs are not resolved, but the width of the peak indicates that contributions from all three channels are present.

The observed rate for this measurement was found to be commensurate with the O^+/O^- collision system previously studied at DESIREE [28], for which the cross section is well known [27]. We therefore estimate the cross section to be in the range of 10^{-13} cm² (± 1 order of magnitude) at this collision energy (~ 0.1 eV).

In the third measurement [Fig. 3(c)], the same beam energies as in Fig. 3(b) were used, but the drift tubes were biased to yield a slightly higher collision energy, i.e., 0.80 ± 0.10 eV. This results in a lower count rate due to the expected $1/E_{c.m.}$ cross section dependence on the collision energy, as well as additional broadening and a shift in the separations. However, the two main peaks are still fully resolved and within the detectable range.

For the three spectra, the results from the fits of the simulated distributions are shown as solid black lines, with the individual distributions shown by colored lines: blue for the excited-state–ground-state pairs and red for the different ground-state-configuration pairs. While the peaks are found to become broader as the collision energy increases, the relative

TABLE II. Experimental branching ratios of the different channels at collision energies of 0.1 and 0.8 eV.

Product channel	E_K (eV)	Expt., 0.1 eV	Expt., 0.8 eV
$^2[2]_{3/2} + ^2P_{3/2}^o$	0.44	21% \pm 3%	16% \pm 6%
$^2[2]_{5/2} + ^2P_{3/2}^o$	0.62	44% \pm 3%	45% \pm 8%
$^2P_{1/2}^o + ^2P_{1/2}^o$	5.51	4% \pm 2%	8% \pm 4%
$^2P_{1/2}^o + ^2P_{3/2}^o$	6.45	20% \pm 5%	20% \pm 6%
$^2P_{3/2}^o + ^2P_{3/2}^o$	7.39	11% \pm 4%	11% \pm 5%
$^2[2] + ^2P^o$	~ 0.5 eV	65% \pm 1%	61% \pm 3%
$^2P^o + ^2P^o$	~ 6.5 eV	35% \pm 1%	39% \pm 3%

intensities appear to be mostly unchanged. In addition, two small features appear to not correspond to any of the channels: One at short separations, below the lower energetic channels, is believed to be an artifact of the background model used. The second one, around 1.5 eV, is likely to be a contribution from the first fine-structure state of the cation, namely, $I^+(^3P_0)$. Since the state is about 0.8 eV above the ground state, it can be expected to be populated to some degree when produced in an ECR source. The observed peak positions (marked with an asterisk in the spectra) are found to correspond to the channels of Eq. (3) with this additional energy. In the higher-collision-energy measurement [Fig. 3(c)], the peak is not observed as it cannot be resolved from the main peak. Storage of up to 20 s did not reveal any change in the signal, suggesting that the metastable level lives for a longer time. This can be explained by the necessity of a quadrupole transition ($\Delta J = 2$) for decay to the ground state.

Based on the fits, the branching ratios were extracted, with the lower-collision-energy measurement ($E_{c.m.} \sim 0.07$ eV) used to determine the relative intensity of the two excited channels at 0.1-eV collision energy. This is motivated as the branching ratios are not expected to change drastically over such a small range of collision energies. The results are presented in Fig. 4, with the full details presented in Table II.

All energetically open channels are found to be populated to some extent, with the $^2[2]_{5/2} + ^2P_{3/2}^o$ channel found to dominate at the measured collision energies. For the ground-state-configuration pairs, $^2P_{1/2}^o + ^2P_{3/2}^o$ is favored, while a lower population is observed for the $J = 1/2$ pair compared to the $J = 3/2$ pair. As the individual channels are not fully resolved, the branching ratios have rather large uncertainties, as indicated by the error bars. The two main peaks are, however, clearly separated, and thus, their total branching ratios can be determined directly by evaluating the area under the respective peaks. The uncertainties are then given by the counting statistics and the error in the background. These smaller errors are shown in the last two rows of Table II. The results show that the branching ratios do not differ significantly for the two energies considered.

IV. SUMMARY

In this work, we have studied the mutual neutralization of I^+ with I^- , using *ab initio* relativistic electronic structure calculations and merged beam techniques at the double electrostatic ion-beam storage ring DESIREE. We have measured

TABLE III. Dissociation relationships of I_2 . The molecular state is identified by the projection of total electronic angular momentum Ω . The number of states for each symmetry of the Ω state is given in parentheses.

Dissociation limits	Molecular states	Energy level (eV)	
		MRCI (this work)	Expt. [35]
$^2P_{3/2}^\circ + ^2P_{3/2}^\circ$	$2_g(1), 1_g(1), 0_g(2), 2_u(1), 1_u(2), 0_u(2)$	0	0
$^2P_{1/2}^\circ + ^2P_{3/2}^\circ$	$2_g(1), 1_g(2), 0_g(2), 2_u(1), 1_u(2), 0_u(2)$	1.04	0.943
$^2P_{1/2}^\circ + ^2P_{1/2}^\circ$	$0_g(1), 1_u(1), 0_u(1)$	1.99	1.885
$^2[2]_{5/2} + ^2P_{3/2}^\circ$	$2_g(3), 1_g(4), 0_g(4), 2_u(3), 1_u(4), 0_u(4)$	6.629	6.774
$^2[2]_{3/2} + ^2P_{3/2}^\circ$	$2_g(2), 1_g(3), 0_g(4), 2_u(2), 1_u(3), 0_u(4)$	7.248	6.954

the branching ratios of the different channels using product-imaging methods combining position and timing information. Our results show that the reaction forms either high-kinetic-energy iodine neutral pairs in the ground-state configuration or slow neutral pairs with one iodine atom in the $6s^2[2]$ excited state, through avoided crossings at short internuclear distances. Experimentally, these two channels were found to have a population of about 40%/60%, with no significant dependence on the collision energy in the studied range (0.1–0.8 eV) and with an observed rate commensurate with a previously studied system [28] (cross section of $\sim 10^{-13}$ cm² at 0.1-eV collision energy). These results are relevant to the modeling and diagnostics of low-temperature iodine plasmas [31], which are promising candidates as propellants for electric space propulsion. Data on recombination processes are essential to model these plasmas, as these reactions can have substantial effects on the efficiency and ignition time of engines [32]. Furthermore, the atoms formed after MN can undergo further reactions. For example, in [6,10] the authors consider atomic iodine excitation and ionization by electron impact as well as surface recombination. However, they used data that were obtained for iodine in the ground electronic state. The cross sections of these reactions are expected to be different for electronic excited states of iodine. Knowledge of the final-state distribution of the MN reaction, as provided in the present study, is therefore essential to obtain a more accurate description of iodine plasmas. The results discussed here will be combined with theoretical calculations in order to

TABLE IV. Spectroscopic constants of the lowest four bound Ω states of I_2 .

State	T_e (cm ⁻¹)	R_e (Å)	ω_e (cm ⁻¹)	Method
$X 0_g^+$	0	2.717	236.4	MRCI (this work)
	0	2.651	215.9	CASPT2 [34]
	0	2.666	214.5	Exp. [36]
$A 2_u$	10119	3.124	117.7	MRCI (this work)
		3.014	124.0	CASPT2 [34]
	10042	3.073	108.3	Expt. [36]
$A 1_u$	11162	3.173	92.0	MRCI (this work)
		3.040	114.6	CASPT2 [34]
	10907	3.114	93.0	Exp. [36]
$B 0_u^+$	15915	3.089	112.6	MRCI (this work)
		2.991	135.3	CASPT2 [34]
	15769	3.025	125.7	Expt. [36]

develop and improve the accuracy in modeling mutual neutralization reactions involving iodine species, efforts which will be extended to include more complex reactions involving molecular ions.

ACKNOWLEDGMENTS

X.Y. and A.S.P.G. acknowledge funding from projects Labex CaPPA (Grant No. ANR-11-LABX-0005-01) and CompRIXS (Grants No. ANR-19-CE29-0019 and No. DFG JA 2329/6-1), the I-SITE ULNE project OVERSEE, and MESONM International Associated Laboratory (LAI; Grant No. ANR-16-IDEX-0004) and support from the French national supercomputing facilities (Grant No. DARI A0090801859). This work was performed at the Swedish National Infrastructure, DESIREE (Swedish Research Council Contracts No. 2017-00621 and No. 2021-00155), and the authors thank the staff of DESIREE for their crucial contributions. This work is part of the project ‘‘Probing charge- and mass- transfer reactions on the atomic level,’’ supported by the Knut and Alice Wallenberg Foundation (Grant No. 2018.0028), and is based upon work from COST Action (CA18212)-Molecular Dynamics in the GAS phase (MD-GAS), supported by COST (European Cooperation in Science and Technology). H.T.S. and H.Z. acknowledge funding from

TABLE V. Spectroscopic constants of the ion-pair states of I_2 . Experimental values (taken from [36] and references therein) are given in parentheses.

State	T_e (cm ⁻¹)	R_e (Å)	Dissociation limits
$D' 2_g$	40764 (40388)	3.712 (3.594)	$^3P_2 + ^1S_0$
$\beta 1_g$	41438 (40821)	3.721 (3.607)	$^3P_2 + ^1S_0$
$D 0_u^+$	42314 (41026)	3.737 (3.584)	$^3P_2 + ^1S_0$
$E 0_g^+$	42499 (41411)	3.773 (3.647)	$^3P_2 + ^1S_0$
$\gamma 1_u$	42315 (41621)	3.814 (3.683)	$^3P_2 + ^1S_0$
$\delta 2_u$	42162 (41787)	3.900 (3.787)	$^3P_2 + ^1S_0$
$f 0_g^+$	47971 (47026)	3.692 (3.574)	$^3P_0 + ^1S_0$
$g 0_g^-$	48717 (47086)	3.672 (3.572)	$^3P_1 + ^1S_0$
$F 0_u^+$	48961 (47217)	3.712 (3.600)	$^3P_0 + ^1S_0$
$G 1_g$	48694 (47559)	3.654 (3.549)	$^3P_1 + ^1S_0$
$H 1_u$	49327 (48280)	3.749 (3.653)	$^3P_1 + ^1S_0$
$h 0_u^-$	49467 (48646)	3.899 (3.780)	$^3P_1 + ^1S_0$
$F' 0_u^+$	54363 (51706)	3.557 (3.479)	$^1D_2 + ^1S_0$
1_g	55934 (53216)	3.623 (3.522)	$^1D_2 + ^1S_0$
$f' 0_g^+$	58306 (55409)	3.963 (3.825)	$^1D_2 + ^1S_0$

the Swedish Research Council (Contracts No. 2018-04092 and No. 2020-03437). This material is based upon work supported by the Air Force Office of Scientific Research under Award No. FA9550-19-1-7012 (R.D.T.). The authors thank A. Schmidt-May for analysis code development. N.S. thanks A. Bourdon and J.-P. Booth for fruitful discussions and Plas@par for financial support.

APPENDIX

Table III lists the five lowest dissociation limits of I_2 . When considering spin-orbital coupling, there are three valence channels for $I(5p^5) + I(5p^5)$, ${}^2P_{3/2}^\circ + {}^2P_{3/2}^\circ$, ${}^2P_{1/2}^\circ + {}^2P_{3/2}^\circ$, and ${}^2P_{1/2}^\circ + {}^2P_{1/2}^\circ$, as well as two Rydberg channels for $I(5p^46s^1) + I(5p^5)$, ${}^2[2]_{5/2} + {}^2P_{3/2}^\circ$ and ${}^2[2]_{3/2} + {}^2P_{3/2}^\circ$. The corresponding energy gaps of ${}^2P_{3/2}^\circ - {}^2P_{1/2}^\circ$ and ${}^2[2]_{5/2} - {}^2P_{3/2}^\circ$ are 1.0 and 6.63 eV, which are in reasonable agreement with experimental values of 0.94 and 6.77 eV, respectively. On the other hand, for the separation of the 6s Rydberg state ${}^2[2]_{3/2} - {}^2[2]_{5/2}$, the computed value of 0.62 eV is higher than the available experimental value of 0.18 eV.

1. Valence states

There are a total of 22 valence states corresponding to the lowest three dissociation limits, and as can be seen from Fig. 2 (see Fig. 5 for detailed views of the MRCI PECs), most of the molecular states are either repulsive states or quasibound states except for four states: $X\ 0_g^+$, $A\ 2_u$, $A\ 1_u$, and $B\ 0_u^+$, which are consistent with experimental results. The spectroscopic constants of these four states, including equilibrium distance R_e , adiabatic excitation energy T_e , and vibrational constant ω_e , are compared to experimental data

and recent complete active space with second-order perturbation theory correction (CASPT2) results in Table IV. It can be seen from Table IV that our calculations predict T_e rather well, showing average errors no larger than 200 cm^{-1} . For the equilibrium distance, the difference between MRCI and the experimental value is nearly identical to those of CASPT2.

Apart from these valence excited states, we also observe several Rydberg states at energies around 56 000, 61 000, and 67 000 cm^{-1} . We note R_e of such Rydberg states are around 2.66 Å, which is close to R_e of ground-state $X^2\Pi_{3/2g}$ of I_2^+ [33]. So they may belong to a Rydberg series, which converges on the ionization energy threshold associated with the ground state of I_2^+ .

2. Ion-pair states

The ion-pair states exhibit dominantly a repulsive Coulomb character. We also fit the corresponding spectroscopic constants of the bound states by LEVEL according to the PECs. The result for T_e and R_e are collected in Table V for comparison.

The total of 18 IP states correspond to four different atomic states of I^+ : 3P_2 , 3P_1 , 3P_0 , and 1D_2 . There is a systematic difference for R_e . The computed R_e values are larger than the experimental ones by about 0.1 Å. For the adiabatic excitation energy, the deviations show a pattern indicated in the CASPT2 calculation [34]; that is, the difference in R_e between gerade states is smaller than that of the ungerade states.

3. Background subtraction

The experimental distributions prior to background subtraction are shown in Fig. 6. This signal corresponds to

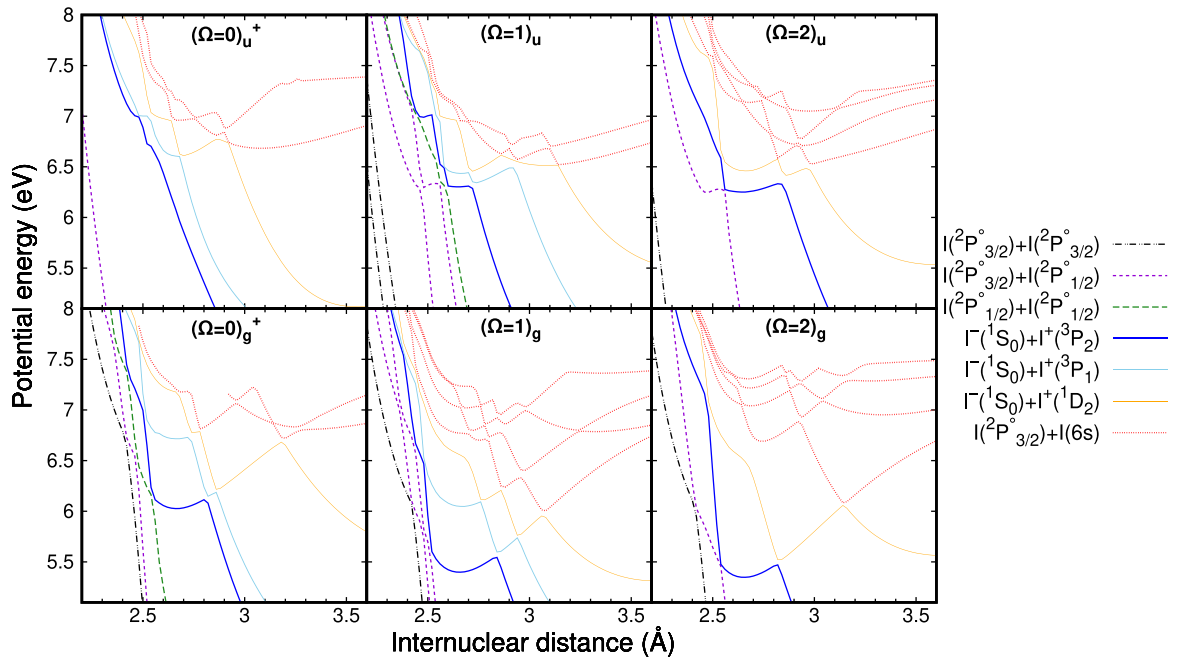


FIG. 5. Detailed views of the MRCI PECs of the electronic states of I_2 at short internuclear distances. Note that the energy for the highest state of symmetry 0_g^+ could not be computed below 2.9 Å within the implementation of our method, as seen in the bottom left panel.

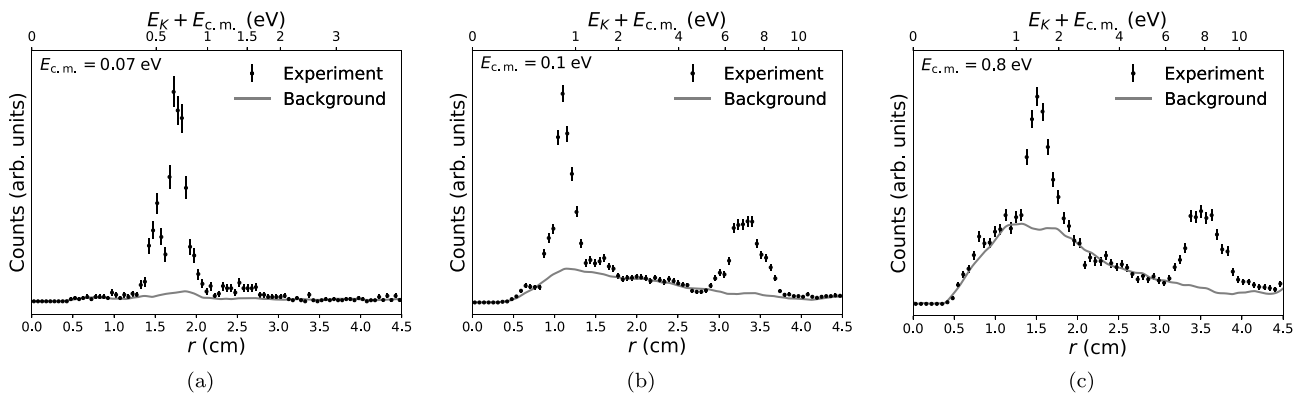


FIG. 6. Spectra from Fig. 3 prior to background subtraction. The background model, which is based on the excluded events in the data analysis, as described in Sec. A3, was fitted to the data and is shown here as a solid gray line.

the data for which the center-of-mass of the two particles is within a 5-mm radius and contains both MN events and background. Outside this radius, the signal should contain only background. Assuming the center-of-mass distribution of the background is random, this signal may be used as a model for the background. An initial fit was first made with

this model based on the data ranges in which no signal is expected to be present [i.e., where r deviates from the simulated distributions of Eqs. (3) and (4)] and is shown as a gray line in Fig. 6. This background model was then subtracted to yield the background-corrected spectra presented in Fig. 3.

- [1] S. Mazouffre, *Plasma Sources Sci. Technol.* **25**, 033002 (2016).
- [2] I. Levchenko, S. Xu, G. Teel, D. Mariotti, M. L. R. Walker, and M. Keidar, *Nat. Commun.* **9**, 879 (2018).
- [3] E. Y. Choueiri, *J. Propul. Power* **20**, 193 (2004).
- [4] R. Lucken, Ph.D. thesis, Université Paris Saclay, 2019.
- [5] V. Croes, A. Tavant, R. Lucken, R. Martorelli, T. Lafleur, A. Bourdon, and P. Chabert, *Phys. Plasmas* **25**, 063522 (2018).
- [6] P. Grondein, T. Lafleur, P. Chabert, and A. Aanesland, *Phys. Plasmas* **23**, 033514 (2016).
- [7] K. Holste, W. Gärtner, D. Zschätzsch, S. Scharmann, P. Köhler, P. Dietz, and P. J. Klar, *Eur. Phys. J. D* **72**, 9 (2018).
- [8] B. D. Prince, D. J. Levandier, and R. J. Bemish, in *Proceedings of the 53rd AIAA/SAE/ASEE Joint Propulsion Conference* (AIAA Press, Atlanta GA, 2017).
- [9] P. Dietz, W. Gärtner, Q. Koch, P. E. Köhler, Y. Teng, P. R. Schreiner, K. Holste, and P. J. Klar, *Plasma Sources Sci. Technol.* **28**, 084001 (2019).
- [10] D. Levko and L. L. Raja, *J. Appl. Phys.* **130**, 173302 (2021).
- [11] T. H. Y. Yeung, *Proc. Phys. Soc.* **71**, 341 (1958).
- [12] A. S. P. Gomes, T. Saue, L. Visscher, H. J. A. Jensen, R. Bast, I. A. Aucar, V. Bakken, K. G. Dyall, S. Dubillard, U. Ekström, E. Eliav, T. Enevoldsen, E. Faßhauer, T. Fleig, O. Fossgaard, L. Halbert, E. D. Hedegård, T. Helgaker, B. Helmich-Paris, and S. Yamamoto, DIRAC19, version 19.0, Zenodo, <https://doi.org/10.5281/zenodo.3572669>.
- [13] T. Saue *et al.*, *J. Chem. Phys.* **152**, 204104 (2020).
- [14] K. G. Dyall, *Theor. Chem. Acc.* **115**, 441 (2006).
- [15] T. Fleig, J. Olsen, and L. Visscher, *J. Chem. Phys.* **119**, 2963 (2003).
- [16] R. J. Le Roy, *J. Quantun Spectrosc. Radiat. Transfer* **186**, 167 (2017).
- [17] R. D. Thomas *et al.*, *Rev. Sci. Instrum.* **82**, 065112 (2011).
- [18] H. T. Schmidt *et al.*, *Rev. Sci. Instrum.* **84**, 055115 (2013).
- [19] G. Eklund, J. Grumer, S. Rosén, M. C. Ji, N. Punnakayathil, A. Källberg, A. Simonsson, R. D. Thomas, M. H. Stockett, P. Reinhed, P. Löfgren, M. Björkhage, M. Blom, P. S. Barklem, H. Cederquist, H. Zettergren, and H. T. Schmidt, *Phys. Rev. A* **102**, 012823 (2020).
- [20] S. Rosén, H. T. Schmidt, P. Reinhed, D. Fischer, R. D. Thomas, H. Cederquist, L. Liljeby, L. Bagge, S. Leontein, and M. Blom, *Rev. Sci. Instrum.* **78**, 113301 (2007).
- [21] Z. Amitay and D. Zajfman, *Rev. Sci. Instrum.* **68**, 1387 (1997).
- [22] D. Zajfman, Z. Amitay, M. Lange, U. Hechtfisher, L. Knoll, D. Schwalm, R. Wester, A. Wolf, and X. Urbain, *Phys. Rev. Lett.* **79**, 1829 (1997).
- [23] Z. Amitay, A. Baer, M. Dahan, J. Levin, Z. Vager, D. Zajfman, L. Knoll, M. Lange, D. Schwalm, R. Wester, A. Wolf, I. F. Schneider, and A. Suzor-Weiner, *Phys. Rev. A* **60**, 3769 (1999).
- [24] R. D. Thomas, *Mass Spectrom. Rev.* **27**, 485 (2008).
- [25] T. Launoy, J. Loreau, A. Dochain, J. Liévin, N. Vaeck, and X. Urbain, *Astrophys. J.* **883**, 85 (2019).
- [26] J. Grumer, G. Eklund, A. M. Amarsi, P. S. Barklem, S. Rosén, M. C. Ji, A. Simonsson, H. Cederquist, H. Zettergren, and H. T. Schmidt, *Phys. Rev. Lett.* **128**, 033401 (2022).
- [27] N. de Ruelle, A. Dochain, T. Launoy, R. F. Nascimento, M. Kaminska, M. H. Stockett, N. Vaeck, H. T. Schmidt, H. Cederquist, and X. Urbain, *Phys. Rev. Lett.* **121**, 083401 (2018).
- [28] M. Poline, A. Dochain, S. Rosén, J. Grumer, M. Ji, G. Eklund, A. Simonsson, P. Reinhed, M. Blom, N. S. Shuman, S. G. Ard, A. A. Viggiano, M. Larsson, H. Cederquist, H. T. Schmidt, H. Zettergren, X. Urbain, P. S. Barklem, and R. D. Thomas, *Phys. Chem. Chem. Phys.* **23**, 24607 (2021).
- [29] G. Eklund, J. Grumer, P. S. Barklem, S. Rosén, M. C. Ji, A. Simonsson, R. D. Thomas, H. Cederquist, H. Zettergren, and H. T. Schmidt, *Phys. Rev. A* **103**, 032814 (2021).

- [30] R. E. Olson, J. R. Peterson, and J. Moseley, *J. Chem. Phys.* **53**, 3391 (1970).
- [31] L. L. Alves, A. Bogaerts, V. Guerra, and M. M. Turner, *Plasma Sources Sci. Technol.* **27**, 023002 (2018).
- [32] S. Williams, A. Midey, S. Arnold, P. Bench, A. A. Viggiano, R. Morris, L. Maurice, and C. Carter, in *Proceedings of the 9th International Space Planes and Hypersonic Systems and Technologies Conference* (AIAA Press, Norfolk, VA, 2012).
- [33] L.-H. Deng, Y.-Y. Zhu, C.-L. Li, and Y.-Q. Chen, *J. Chem. Phys.* **137**, 054308 (2012).
- [34] V. A. Alekseev, *Opt. Spectrosc.* **116**, 329 (2014).
- [35] A. Kramida, Yu. Ralchenko, J. Reader, and NIST ASD Team, NIST Atomic Spectra Database (version 5.9), National Institute of Standards and Technology, <https://doi.org/10.18434/T4W30F>.
- [36] S. Lukashov, A. Petrov, and A. Pravilov, *The Iodine Molecule* (Springer, Cham, 2018).

7.3 Paper III: Theoretical study of the $I^+ - I^-$ mutual neutralization reaction






I participated in writing the manuscript.

Physical Review A., 107, 022808, 2023

Reproduced from *Physical Review A.* with the permission of APS Publishing.

Copyright 2023 APS Publishing.

Theoretical study of the $I^+ + I^-$ mutual neutralization reaction

Sylvain Badin ^{1,2} Xiang Yuan ^{1,3} Pierre-Louis Bourgeois ²
 Andre Severo Pereira Gomes ¹ and Nicolas Sisourat ^{2,*}

¹Univ. Lille, CNRS, UMR 8523-PhLAM-Physique des Lasers Atomes et Molécules, F-59000 Lille, France

²Sorbonne Université, CNRS, Laboratoire de Chimie Physique Matière et Rayonnement, UMR 7614, F-75005 Paris, France

³Department of Chemistry and Pharmaceutical Science, Faculty of Science, Vrije Universiteit Amsterdam, de Boelelaan 1083, 1081 HV Amsterdam, The Netherlands



(Received 8 November 2022; accepted 25 January 2023; published 13 February 2023)

We have computed the cross sections of the mutual neutralization reaction between I^+ and I^- for a collision energy varying from 0.001 eV to 50 eV. These cross sections were obtained using the adiabatic potential energy curves of the I_2 system computed with a direct relativistic multireference configuration interaction method and a semiclassical approach (i.e., Landau-Zener surface hopping). We report the cross sections towards the following neutral states: $I(^2P_{3/2}) + I(^2P_{3/2})$, $I(^2P_{3/2}) + I(^2P_{1/2})$, $I(^2P_{1/2}) + I(^2P_{1/2})$, and $I(5p^46s) + I(^2P_{3/2})$. We also discuss the cross sections towards the following two excited ionic states: $I^-(^1S_0) + I^+(^3P_0)$ and $I^-(^1S_0) + I^+(^3D_2)$. The results of these calculations are in qualitative accordance with recent experimental measurements conducted in the Double ElectroStatic Ion Ring ExpERiment (DESIREE) in Stockholm. These results can be used to model iodine plasma kinetics and thus to improve our understanding of the latter.

DOI: [10.1103/PhysRevA.107.022808](https://doi.org/10.1103/PhysRevA.107.022808)

I. INTRODUCTION

The mutual neutralization (MN) of two oppositely charged ions is a central reaction taking place in electronegative plasmas. The latter are found in, e.g., the lower ionosphere [1], flames [2], interstellar medium [3,4], and in excimer lasers [5]. As such, MN reactions have been investigated in various systems (see, e.g., Ref. [6] and references therein).

Iodine plasma is one example of an electronegative plasma. Interest in iodine plasma has been renewed recently since it is a promising candidate to be used in electric propulsion systems, notably for satellites (see, e.g., Refs. [7,8] and references therein).

Very recently, the MN reaction between I^+ and I^- ions has been studied experimentally by Poline *et al.* [9] at the Double ElectroStatic Ion Ring ExpERiment (DESIREE) facility: the branching ratios for the different channels were measured at two collision energies, 0.1 eV and 0.8 eV. This work showed that the MN reaction forms iodine atoms either in their ground state or with one atom in an electronically excited state. These two classes of states were found to be populated with nearly equal proportions with no dependence on the collision energy. The total cross sections at these collision energies were estimated, but with fairly large uncertainties.

There are currently no accurate absolute cross sections published for the MN reaction between I^+ and I^- ions, which impedes the modeling of iodine plasma. Investigating such a collision system is a difficult task since iodine has a strong spin-orbit coupling, and moreover, the potential energy curves of I_2 exhibit multiple and overlapping avoided crossings, where the MN reaction can take place. The aim of

the present work is to provide estimates of these cross sections in a broad range of collision energies. For that, we have employed a combination of *ab initio* relativistic electronic structure calculations and the Landau-Zener surface hopping (LZSH) method to compute the relevant cross sections. Our calculations are then compared to the recent experiments of Poline *et al.* [9].

This paper is organized as follows. In the next section we briefly outline the methods used in the present work. Section III is devoted to the discussion of the theoretical results of this work and their comparison with the experimental results obtained recently by Poline *et al.* [9] at the DESIREE double ion ring. The conclusions are reported in Sec. IV. Atomic units are used throughout, unless explicitly indicated otherwise.

II. METHODS

A. Potential energy curves

The potential energy curves used in this work, shown in Fig. 1, were already presented in Poline *et al.* [9]. They have been obtained with the multireference configuration interaction (MRCI) method, as implemented in the Kramers restricted configuration interaction (KRCI) module [10] of the DIRAC relativistic electronic structure package [11]. Such calculations have been carried out with the DIRAC19 [12] release as well as with the development version identified by hash 1e798e5. We employed triple-zeta quality basis sets [13] supplemented by diffuse functions so that Rydberg and ion-pair (IPr) states could be accurately represented. The exponents for the diffuse functions (listed in Table III of the Appendix) were automatically generated by DIRAC as even-tempered sequences based on the most diffuse exponents of the dyall.v3z basis. The reference wave function consisted of the set of

*Nicolas.sisourat@sorbonne-universite.fr

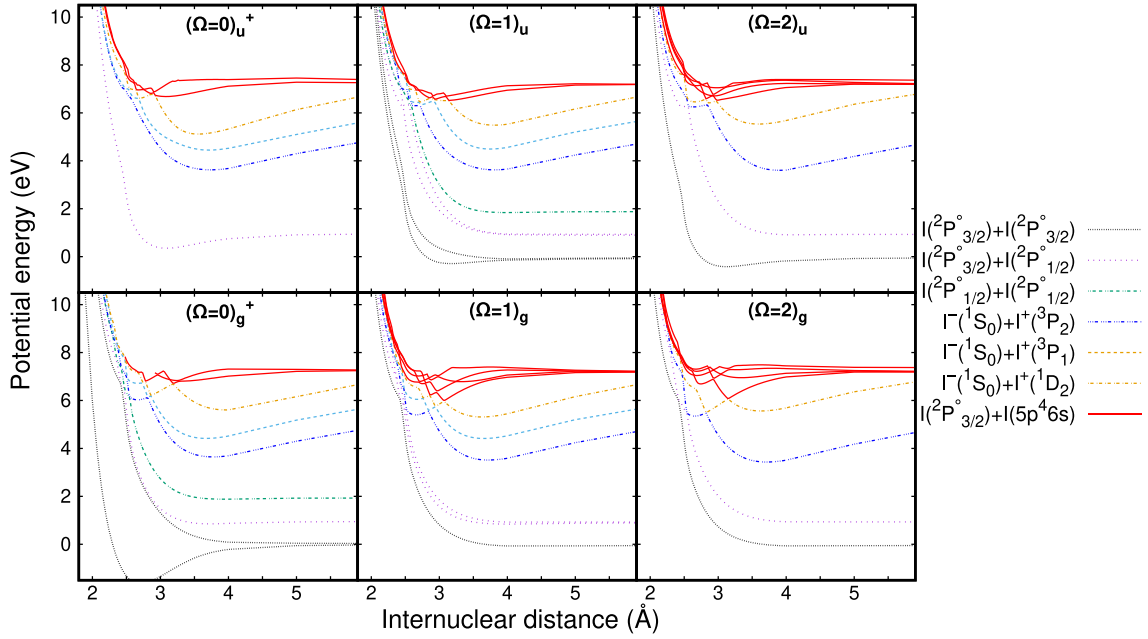


FIG. 1. Potential energy curves of 51 electronic states of I_2 computed with relativistic MRCI (reconstructed from the data from Poline *et al.* [9]). Only the states of the symmetries that correlate with the $I^-(^1S_0) + I^+(^3P_2)$ reactants state are displayed here.

determinants spanned by the p^5 manifold of each of the iodine atoms (thus representing 10 electrons in 12 spinors). For further information, readers can consult the computational details section of Poline *et al.* [9].

It should be noted that we computed the potential energy curves for states with projection of total electronic angular momentum $\Omega = 0, 1, 2$ but not for states with $\Omega > 2$ since the $I^-(^1S_0) + I^+(^3P_2)$ reactant state does not correlate with such states. Indeed, the $I^-(^1S_0) + I^+(^3P_2)$ state correlates with states having the following angular momenta [14]: the double degenerate $(\Omega = 1)_g$, $(\Omega = 1)_u$, $(\Omega = 2)_g$, and $(\Omega = 2)_u$, and the singly degenerate $(\Omega = 0)_g^+$ and $(\Omega = 0)_u^+$.

Furthermore, for implementation reasons the KRCI module does not take into account the $+/-$ symmetry and thus is not able to differentiate directly the $+$ and the $-$ states. In order to do that, we also computed the dipole transition moments between the $(\Omega = 0)_g$ and the $(\Omega = 0)_u$ states. Knowing that the lowest $(\Omega = 0)_g$ state is of $+$ symmetry and that the lowest $(\Omega = 0)_u$ state is of $-$ symmetry [14], we were able to rebuild the potential energy curves of the $(\Omega = 0)_g^+$ and $(\Omega = 0)_u^+$ states using the selection rule stating that the dipole transition between a $+$ and a $-$ state is forbidden [15]. The list of the computed states and their asymptotic energies are reported in Table I.

B. Landau-Zener surface hopping

An accurate description of MN reactions at low collision energies requires, in principle, a fully quantum mechanical approach for the nuclear dynamics. However, in the current system, such a sophisticated approach is out of reach from a computational point of view: nonadiabatic couplings are not implemented in the KRCI module of the DIRAC package. Moreover, the potential energy curves of I_2 exhibit multiple and overlapping avoided crossings such that a diabaticization

procedure would be a tedious and challenging task. To overcome this difficulty, in this work we employ the LZSH method [17] to obtain the cross sections of the $I^+ + I^-$ mutual neutralization reaction.

LZSH is a probabilistic, semiclassical method in which the system is moving classically along the potential energy curves. The nonadiabatic interactions are considered only at the vicinity of avoided crossings [18,19]. The list of the avoided crossings considered in this work is given in Table IV of the Appendix. Note that, as previously mentioned in Poline *et al.* [9], we estimated the electronic couplings at large-distance ($R > 7 \text{ \AA}$) crossings between the ion-pair states and the $I(5p^46s) + I(^2P_{1/2})$ states. These couplings have been shown to be negligible (see below).

The LZSH method can be described as follows: The system starts at a distance R_0 on the curve corresponding to the reactants [i.e., the curves which correlate with the $I^-(^1S_0) + I^+(^3P_2)$ ion pair state], R_0 being larger than the internuclear distances of all avoided crossings [in this work, $R_0 = 12$ atomic units (a.u.)]. The system then moves along this curve while it has sufficient kinetic energy and until it reaches an avoided crossing. At this point there is a probability $P_{\alpha \rightarrow \beta}^{LZ}$ [given by the Landau-Zener formula [20–22], Eq. (1)] that the system hops from its starting state (named α) to the other state involved in the avoided crossing (named β), if its kinetic energy is sufficient. We have

$$P_{\alpha \rightarrow \beta}^{LZ} = \exp\left(-\frac{\pi}{2v} \sqrt{\frac{\Delta V_{\alpha\beta}^3}{\frac{d^2}{dR^2}(\Delta V_{\alpha\beta})}}\right), \quad (1)$$

where v is the relative radial velocity of the two nuclei at the crossing and $\Delta V_{\alpha\beta}$ is the energy difference between the two adiabatic potential energy curves at the avoided crossing. v is

TABLE I. Asymptotic energies of the I₂ states employed in this work. The molecular states are identified by the projection of the total electronic angular momentum (Ω). The number of states for each Ω symmetry are given in parentheses. The last four states of this table correspond to ion-pair states.

Dissociation limits	Molecular states	Asymptotic energy (eV)	
		MRCI (this work)	Exp [16]
² P _{3/2} + ² P _{3/2}	2 _g (1), 1 _g (1), 0 _g ⁺ (2), 2 _u (1), 1 _u (2), 0 _u ⁻ (2)	0	0
² P _{1/2} + ² P _{3/2}	2 _g (1), 1 _g (2), 0 _g ⁺ (1), 0 _g ⁻ (1), 2 _u (1), 1 _u (2), 0 _u ⁺ (1), 0 _u ⁻ (1),	1.04	0.943
² P _{1/2} + ² P _{1/2}	0 _g ⁺ (1), 1 _u (1), 0 _u ⁻ (1)	1.99	1.885
² [2] _{5/2} + ² P _{3/2}	2 _g (3), 1 _g (4), 0 _g ⁺ (2), 0 _g ⁻ (2), 2 _u (3), 1 _u (4), 0 _u ⁺ (2), 0 _u ⁻ (2)	7.23	6.774
² [2] _{3/2} + ² P _{3/2}	2 _g (2), 1 _g (3), 0 _g ⁺ (2), 0 _g ⁻ (2), 2 _u (2), 1 _u (3), 0 _u ⁺ (2), 0 _u ⁻ (2)	7.41	6.954
¹ S ₀ + ³ P ₂	2 _g (1), 1 _g (1), 0 _g ⁺ (1), 2 _u (1), 1 _u (1), 0 _u ⁺ (1)	7.24	7.392
¹ S ₀ + ³ P ₁	1 _g (1), 0 _g ⁻ (1), 1 _u (1), 0 _u ⁻ (1)	8.13	8.191
¹ S ₀ + ³ P ₀	0 _g ⁺ (1), 0 _u ⁺ (1)	8.22	8.271
¹ S ₀ + ¹ D ₂	2 _g (1), 1 _g (1), 0 _g ⁺ (1), 2 _u (1), 1 _u (1), 0 _u ⁺ (1)	9.00	9.094

simply obtained by energy conservation,

$$v = \sqrt{\frac{2[E_m - V_{\text{eff},\alpha}(R)]}{\mu}}, \quad (2)$$

with μ being the reduced mass of the system (for I₂, $\mu = 115666$ a.u.). $V_{\text{eff},\alpha}(R)$ is the effective adiabatic potential energy of the state α at the internuclear distance R ,

$$V_{\text{eff},\alpha}(l, R) = V_{\alpha}(R) + \frac{l(l+1)}{2\mu R^2}. \quad (3)$$

E_m is the mechanical energy of the system,

$$E_m = E_{\text{coll}} + V_{\text{asymp}} \quad (4)$$

where E_{coll} is the collision energy in the center of mass frame and V_{asymp} is the energy of the I⁻(¹S₀) + I⁺(³P₂) reactant state at $R \rightarrow +\infty$.

When the kinetic energy of the system reaches 0, the system turns back, and when it reaches R_0 again, the trajectory ends. By computing a sufficiently high number of trajectories, we can compute a reaction probability P_f towards each of the possible product states f :

$$P_f = \frac{N_f}{N_{\text{tot}}}, \quad (5)$$

where N_f is the number of trajectories which ended in the product state f and N_{tot} is the total number of trajectories. In this work we used $N_{\text{tot}} = 400$. We found that using a higher value of N_{tot} has no significant impact on the results.

The cross sections towards each product state are then obtained by integrating the P_f over the angular momentum l [23],

$$\sigma_f^X(E_{\text{coll}}) = \frac{\pi}{2\mu E_{\text{coll}}} \sum_{l=0}^{l=+\infty} (2l+1)P_f(E_{\text{coll}}, l), \quad (6)$$

where X denotes a given symmetry state of the I₂ potential energy curves.

Practically, the sum in Eq. (6) stops (at a value $l = l_{\text{max}}$) when the rotational barrier becomes too important for the system to reach the farthest avoided crossing involving the

reactant state. We have

$$l_{\text{max}} = -\frac{1}{2} + \sqrt{\frac{1}{4} - \frac{\mu R_c^2}{2}(4V(R_c) - V_{\text{asymp}} - E_{\text{coll}})}, \quad (7)$$

where R_c and $V(R_c)$ are the internuclear distance and the adiabatic energy of the reactant state at this avoided crossing.

This approach is used for each of the symmetries considered in this work (see Sec. II A), and the reaction cross sections towards each state are then obtained by averaging over all symmetries, taking into account their multiplicity, hence

$$\sigma_f(E_{\text{coll}}) = \frac{\sum_{X \in \text{symmetries}} m_X \sigma_f^X(E_{\text{coll}})}{\sum_{X \in \text{symmetries}} m_X}, \quad (8)$$

with m_X being the multiplicity of the symmetry X and σ_f^X the reaction cross section towards the state α for the symmetry X obtained with Eq. (6).

At large distance ($R > 7 \text{ \AA}$), the avoided crossings between the ion-pair states and the I(⁵p⁴6s) + I(²P_{1/2}) states are not described by the MRCI calculations presented in Sec. II A. For the avoided crossings between the ion pair states I⁻(¹S₀) + I⁺(³P₂), I⁻(¹S₀) + I⁺(³P₁) and the I(⁵p⁴6s) + I(²P_{1/2}) states we used a semiempirical model to estimate the electronic couplings (see Olson *et al.* [24], Eq. (13), using $\frac{v^2}{2} = 3.059 \text{ eV}$ [25]). We obtained coupling values that are less than 8.10^{-5} a.u.. These avoided crossings take place at sufficiently large distances for the semiempirical model to be valid. However, the avoided crossings between the ion pair states I⁻(¹S₀) + I⁺(¹D₂) and the I(⁵p⁴6s) + I(²P_{1/2}) states take place at shorter distances and thus were described by computing the potential energy curves of the system (using the same method as the one described in Sec. II A), with 21 points with an internuclear distance varying from 7 to 8 Å. We obtained coupling values that are less than 6×10^{-5} a.u.. Including these avoided crossings in our calculation was shown to have no significant effect on the results (less than 0.2% difference on the cross sections).

C. Empirical correction to the asymptotic energies

When comparing the asymptotic energies obtained with the MRCI method and the experimental values (see Table I), we noticed that the MRCI asymptotic energies of the neutral

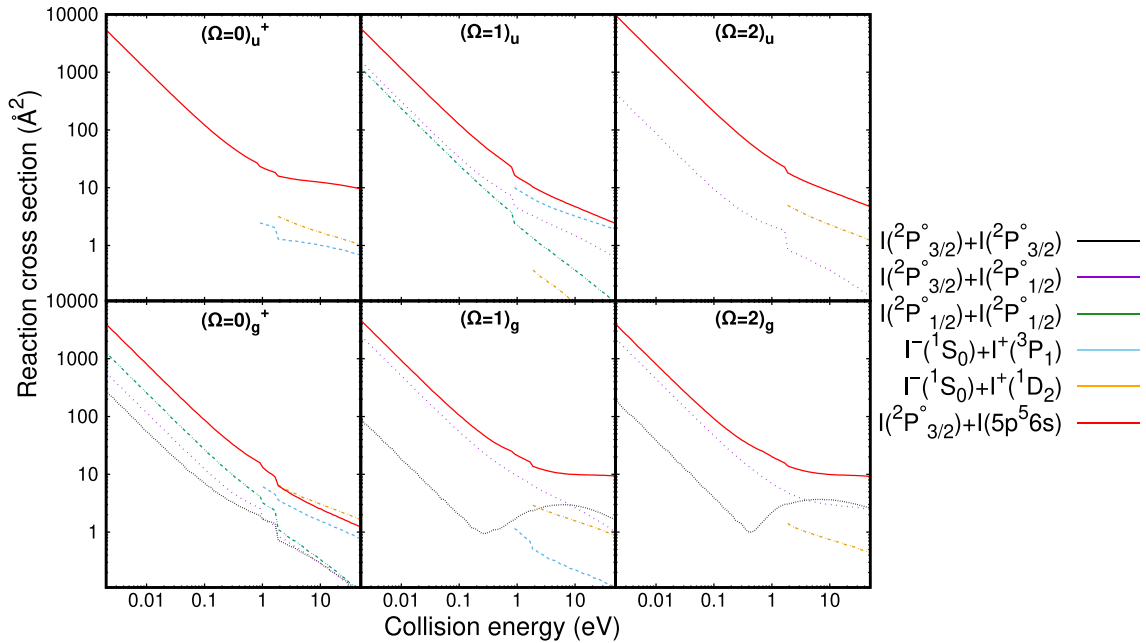


FIG. 2. Cross sections for the reactions between I^+ and I^- for the six symmetries correlating with the $I^-(^1S_0) + I^+(^3P_2)$ reactants state.

states are overestimated while the MRCI asymptotic energy of the ion pair states is underestimated. For the three lowest neutral product states and the excited ion pair products, the difference between the asymptotic energies of the reactant and product states are satisfactory within the MRCI method (between 3% and 12% of error). However, the differences of asymptotic energy between the reactant and the $5p^46s$ states [$I(^2[2]_{3/2}) + I(^2P_{5/2})$ and $I(^2[2]_{3/2}) + I(^2P_{3/2})$ states] are not well reproduced. The path towards the $I(^2[2]_{3/2}) + I(^2P_{5/2})$ state is open only by 0.01 eV in the MRCI calculation while it should be open with an asymptotic energy difference of 0.62 eV, and the path towards the $I(^2[2]_{3/2}) + I(^2P_{3/2})$ state is closed while it should be open with an asymptotic energy difference of 0.44 eV. To correct for this qualitative and quantitative failure, we decided to increase artificially the asymptotic energy of the ion pair states by a quantity ϵ in order to reproduce the experimental asymptotic energy difference between the $I(^2[2]_{3/2}) + I(^2P_{5/2})$ and the $I^-(^1S_0) + I^+(^3P_2)$. The value of ϵ is 0.61 eV. This is the only departure from the underlying *ab initio* energy curves in our work.

III. RESULTS AND DISCUSSION

Using the potential energy curves presented in Sec. II A, we applied the LZSH method for each of the symmetries considered here (see Sec. II A). We thus obtained the reaction cross sections towards the following neutral product states: $I(^2P_{3/2}) + I(^2P_{3/2})$, $I(^2P_{3/2}) + I(^2P_{1/2})$, $I(^2P_{1/2}) + I(^2P_{1/2})$, and $I(5p^46s) + I(^2P_{1/2})$.

Here, we did not try to differentiate the different substates constituting the $I(5p^46s)$ configuration obtained with the MRCI method, since the energy difference between some of these substates is below 0.2 eV [16]. We lack extensive benchmark studies between MRCI and other approaches such as those based on coupled cluster wave functions for the iodine systems. However, from recent examples in the literature

[26–28] in which a comparison of methods has been made on an equal footing (same basis set and Hamiltonian), we see that among different correlated approaches, the corresponding electronic state energies can differ by values which are similar to, or higher than, the differences among substates seen here.

We also obtained the reaction cross sections towards the two lowest-energy excited ion-pair states $I^-(^1S_0) + I^+(^3P_1)$ and $I^-(^1S_0) + I^+(^1D_2)$. The evolution of these reaction cross sections with respect to the collision energy is shown in Fig. 2 and the total symmetrized reaction cross sections, obtained with Eq. (8), are shown in Fig. 3.

At collision energies lower than 0.1 eV the cross sections towards the neutral product states follow an asymptotic behavior proportional to the inverse of the collision energy. At these energies, for all symmetries, the most abundant product is the neutral $I(5p^46s) + I(^2P_{1/2})$ product, followed by

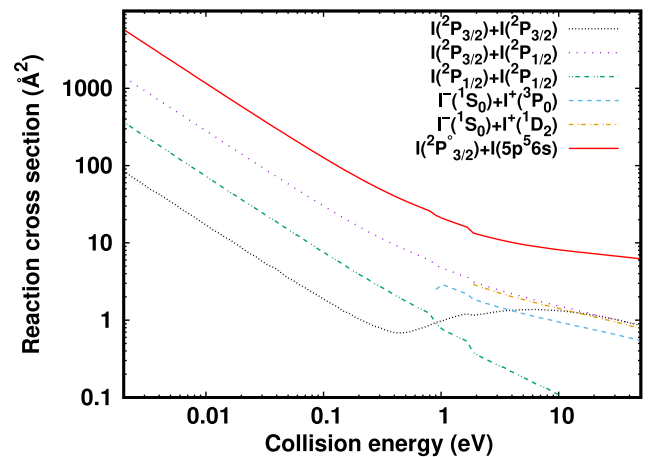


FIG. 3. Total (symmetry averaged) cross sections for the $I^+ + I^- \rightarrow 2I$ and $I^+ + I^- \rightarrow (I^+)^* + I^-$ reactions.

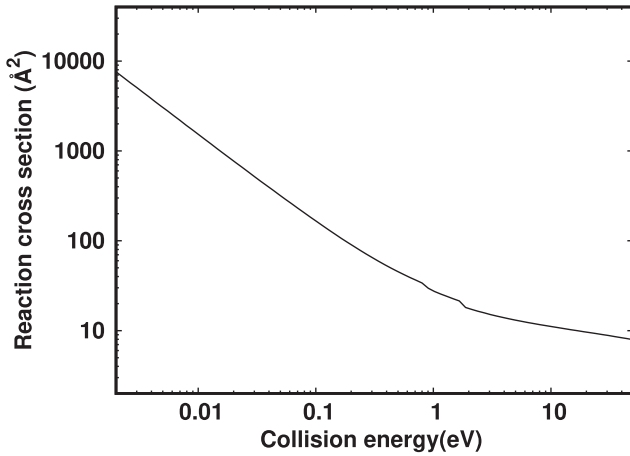


FIG. 4. Total (symmetry averaged) cross section for mutual neutralization cross section between I⁺ and I⁻.

the three lowest-energy neutral products I(²P_{3/2}) + I(²P_{3/2}), I(²P_{3/2}) + I(²P_{1/2}), and I(²P_{1/2}) + I(²P_{1/2}), in this order.

At collision energies higher than 0.3 eV the cross sections towards the I(²P_{3/2}) + I(²P_{3/2}) state increase up to the collision energy of 10 eV, while the cross sections towards the

I(²P_{1/2}) + I(²P_{3/2}) and I(5p⁴6s) + I(²P_{1/2}) states decrease at a slower rate than for the collision energies below 0.1 eV. At collision energies higher than 0.1 eV the cross sections towards the I(²P_{1/2}) + I(²P_{1/2}) state continue to decrease as the inverse of the collision energy, so it becomes negligible compared to the other cross sections.

The reaction cross sections towards the I⁻(¹S₀) + I⁺(³P₁) and I⁻(¹S₀) + I⁺(¹D₂) ion pair states have energy thresholds of, respectively, 0.26 eV and 1.1 eV. The values of these cross sections after their threshold are of the same order of magnitude as the one of the I(²P_{1/2}) + I(²P_{3/2}) state.

The total of the neutralization cross sections (sum of the cross sections toward all neutral states) is shown in Fig. 4. It decreases as the inverse of the collision energy up to 0.1 eV and then decreases at a slower rate. The two discontinuities at 0.26 eV and 1.1 eV correspond to the energy thresholds of the reactions producing the two excited ion pairs.

In 2021, Poline *et al.* [9] conducted an experiment at the double ion storage ring DESIREE in Stockholm. They were able to measure the branching ratios towards each of the neutral product states—more specifically, they obtained the ratio (denoted by R_σ) between the I(5p⁴6s) + I(²P_{1/2}) states and the I(²P_{3/2}) + I(²P_{3/2}), I(²P_{3/2}) + I(²P_{1/2}), and I(²P_{1/2}) + I(²P_{1/2}) states, for collision energy of 0.1 and 0.8 eV. We therefore have R_σ as

$$R_\sigma = \frac{\sigma[I(^2P_{3/2}) + I(^2P_{3/2})] + \sigma[I(^2P_{3/2}) + I(^2P_{1/2})] + \sigma[I(^2P_{1/2}) + I(^2P_{1/2})]}{\sigma[I(5p^46s) + I(^2P_{1/2})] + \sigma[I(^2P_{3/2}) + I(^2P_{3/2})] + \sigma[I(^2P_{3/2}) + I(^2P_{1/2})] + \sigma[I(^2P_{1/2}) + I(^2P_{1/2})]} \quad (9)$$

We can directly obtain this ratio from our calculations. The comparison between the theoretical ratio and the measurements is shown in Fig. 5. Our results show that this branching ratio does not vary significantly with respect to the collision energy, with values between 22% and 27%. The measured and computed ratio are of the same order of magnitude. However, the LZSH-based model underestimates this ratio by a factor of 1.5.

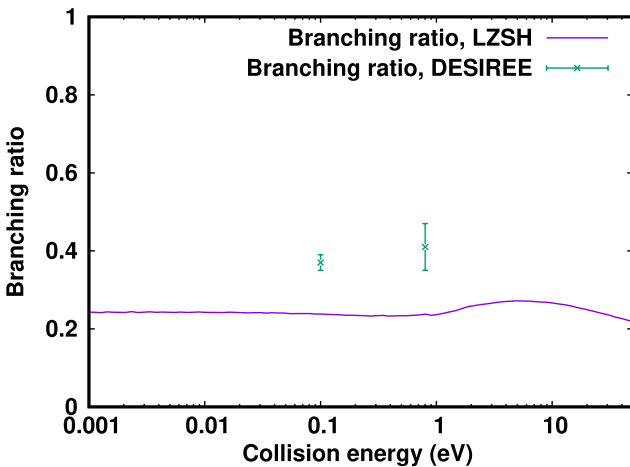


FIG. 5. Comparison of the R_σ ratios, computed with the LZSH method and measured by Poline *et al.* [9].

Moreover, our model gives a semiquantitative agreement for the prediction of the ratios between the cross sections of the I(²P_{3/2}) + I(²P_{3/2}), I(²P_{3/2}) + I(²P_{1/2}), and I(²P_{1/2}) + I(²P_{1/2}) states. These ratios, in comparison with those obtained by Poline *et al.* [9], are displayed in Table II.

Poline *et al.* [9] were also able to estimate the absolute neutralization cross section, at a collision energy of 0.1 eV, to be in the range of 10^{3±1} Å². Our results displayed in Fig. 4 (165 Å² at 0.1 eV) agree with this estimation.

The disagreement between the experiments at DESIREE and our results may be attributed to the semiclassical approach employed in this work. However, given the complexity of the studied collisional system and the lack of data on the considered MN reaction, such semiquantitative estimates represent a significant step toward a better modeling, and thus understanding, of iodine plasma.

TABLE II. Ratios of the cross sections between the three lowest neutral product states, obtained with the LZSH method and experimentally by Poline *et al.* [9] at collision energy of 0.1 and 0.8 eV.

Product channel	0.1 eV		0.8 eV	
	LZSH	exp.	LZSH	exp.
I(² P _{3/2}) + I(² P _{3/2})	5%	31%	12%	28%
I(² P _{3/2}) + I(² P _{1/2})	76%	57%	76%	51%
I(² P _{1/2}) + I(² P _{1/2})	19%	11%	13%	21%

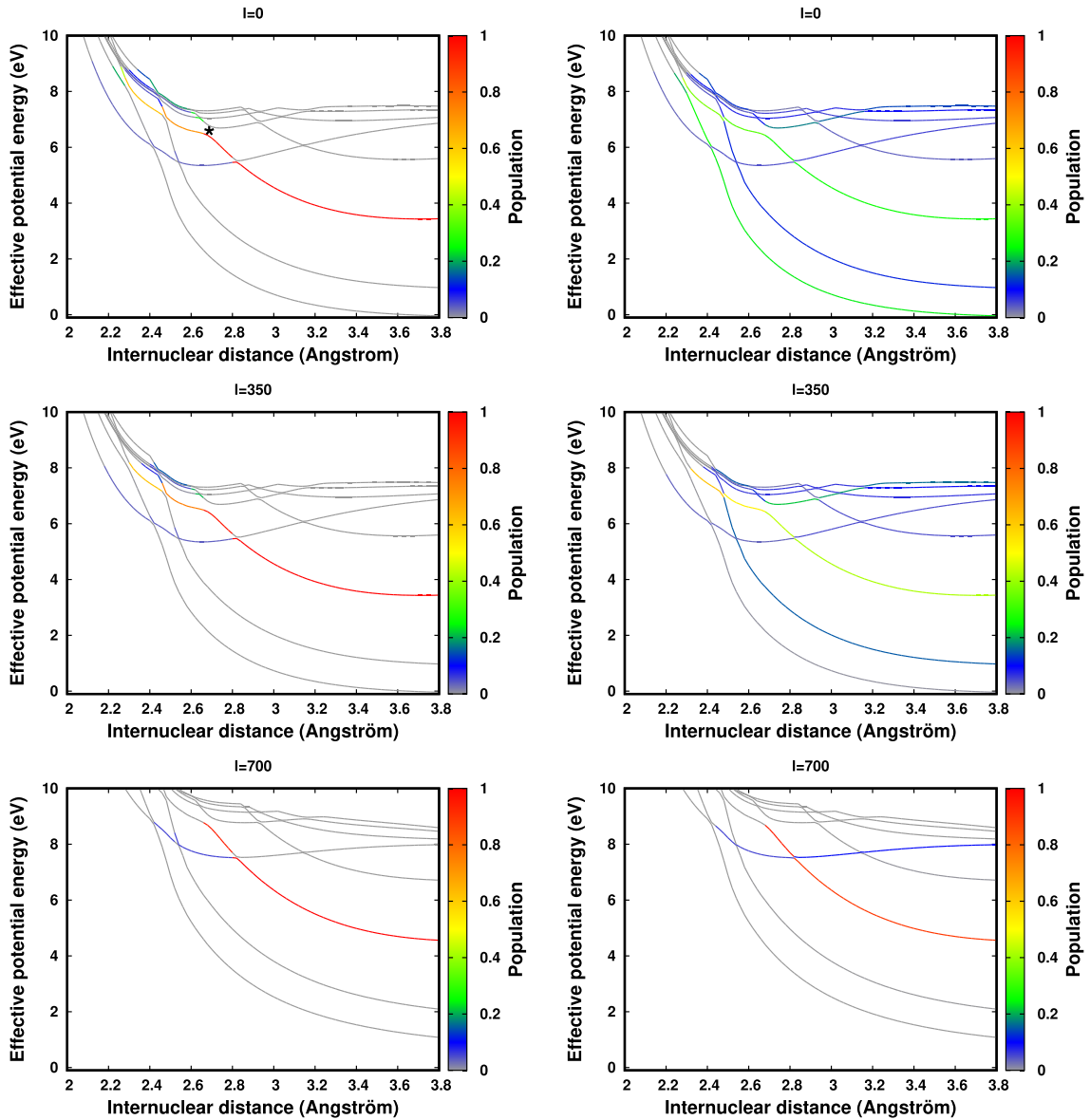


FIG. 6. Effective potential energy curves of the first eight states of the $(\Omega = 2)_g$ symmetry for three different values of angular momentum. The population $n_{\alpha}^{\leftarrow}(R)$ [$n_{\alpha}^{\rightarrow}(R)$] is displayed with a color scheme in the left (right) panel. At $t = 0$, the population is 1 in the lowest ion-pair state (the third state in energy order) and 0 in all the other states

In order to gain more insight into the dynamics of the MN reaction, we investigate which avoided crossings contribute the most to the reactivity. We computed statistically the population on each state as a function of time [$n_{\alpha}(t)$],

$$n_{\alpha}(t) = \frac{N_{\alpha}(t)}{N_{\text{traj}}}, \quad (10)$$

where $N_{\alpha}(t)$ is the number of trajectories on the state α at the time t . Since the time does not appear explicitly in the method described in Sec. II B, we computed it *a posteriori* by integrating Newton's law of motion [see Eq. (11), with r_i, r_j being two adjacent points of the potential energy surface and v being the speed of the system]. The time is set arbitrarily at 0 when a trajectory starts at R_0 . N_{traj} is the total number of

computed trajectories.

$$\begin{aligned} \Delta t_{ji} &= \frac{\sqrt{2\mu}}{B} (\sqrt{E_m - V(r_j)} - \sqrt{E_m - V(r_i)}) \text{ if } R \text{ decreases} \\ \Delta t_{ij} &= \frac{\sqrt{2\mu}}{B} (\sqrt{E_m - V(r_i)} - \sqrt{E_m - V(r_j)}) \text{ if } R \text{ increases,} \end{aligned} \quad (11)$$

with $\Delta t_{lk} = t(r_l) - t(r_k)$ and $B = [V(r_j) - V(r_i)]/(r_j - r_i)$.

For each of the symmetries considered in this work we computed $N_{\text{traj}} = 10\,000$ trajectories, for a collision energy of 0.9 eV and three different values of the angular momentum l ($l = 0, l = 350$, and $l = 700$). The populations obtained with these trajectories are then computed using Eq. (10) for each of the electronic states considered in this work. The population on each of the first eight electronic states of the $(\Omega = 2)_g$ symmetry are displayed in Fig. 6. For clarity we choose to

TABLE III. Diffuse exponents used in the electronic structure calculations for the iodine atom. These were added to the dyall.v3z basis set.

Primitive type	Exponents
s	0.0395300
	0.0175618
	0.0078021
p	0.0285513
	0.0112589
	0.0044398
d	0.0773620
	0.0321000
	0.0133193
f	0.1159934
	0.0331410
	0.0094689

represent separately the population $n_{\alpha}^{\leftarrow}(R)$ coming from the part of the trajectories with decreasing values of R (before reaching the closest approach distance) and the population $n_{\alpha}^{\rightarrow}(R)$ coming from the part of the trajectories with increasing values of R (after reaching the closest approach distance), which are given by

$$n_{\alpha}^{\leftarrow}(R) = \frac{N_{\alpha}^{\leftarrow}(R)}{N_{\text{tot}}} \quad \text{and} \quad n_{\alpha}^{\rightarrow}(R) = \frac{N_{\alpha}^{\rightarrow}(R)}{N_{\text{tot}}}, \quad (12)$$

with $N_{\alpha}^{\leftarrow}(R)$ [$N_{\alpha}^{\rightarrow}(R)$] being the number of trajectories crossing the internuclear distance R before (after) reaching the closest approach distance. In Fig. 6, $n_{\alpha}^{\leftarrow}(R)$ [$n_{\alpha}^{\rightarrow}(R)$] is shown in the left (right) panel of the figure using a color scheme traced on the effective potential energy curves [see Eq. (3)] of the $(\Omega = 2)_g$ symmetry.

At the first avoided crossing reached by the system (at 2.8 Å), it mainly has a diabatic behavior with approximately 90% of the population transferred to the higher energy state. This behavior is observed for the majority of the avoided crossings of the system, with the important exception of the crossing between the fourth and fifth states (in increasing energy order) at 2.7 Å (marked with a star in Fig. 6). For this crossing we mainly observe an adiabatic behavior, but still with an important percentage of the population (about 30%) transferred to the higher energy state. This intermediate behavior is directly responsible for the reactivity towards the I^{*} states, and indirectly responsible for the reactivity towards the lowest energy states through the avoided crossings between the third and fourth states at 2.5 Å and between the second and third states at 2.3 Å. The path towards the lowest energy states is the first to be screened by the rotational barrier. A chemical reaction towards those states is thus only possible for collisions with a low impact parameter (the link between the impact parameter b and the angular momentum l is given by $l = \sqrt{2\mu E_{\text{coll}}} \times b$ [23]).

The reactions towards the I($5p^46s$) + I($^2P_{3/2}$) states are still possible at higher values of l , which explains the higher reactivity towards those states (see Fig. 5). The populations were also computed for the other symmetries. We did not find any major difference in the behavior of the

TABLE IV. List of the avoided crossings considered in this work. For each avoided crossing we give its internuclear distance and the index of the two electronic states concerned by this crossing. The electronic states indexes are given by their energetic order (starting from zero for the lowest energy state of each symmetry)

Symmetry	Lower state	Higher state	R (Å)
$(\Omega = 0)_g^+$	3	4	2,30
	2	3	2,36
	5	6	2,36
	4	5	2,39
	1	2	2,42
	3	4	2,42
	2	3	2,46
	5	6	2,48
	4	5	2,51
	3	4	2,54
	2	3	2,66
	5	6	2,74
	6	7	2,78
	4	5	2,82
	5	6	2,86
7	8	2,96	
7	8	3,15	
6	7	3,18	
7	8	3,28	
$(\Omega = 0)_u^+$	4	5	2,42
	3	4	2,48
	1	2	2,48
	2	3	2,54
	1	2	2,58
	4	5	2,62
	3	4	2,64
	2	3	2,68
	4	5	2,76
	3	4	2,86
4	5	2,90	
3	4	2,92	
$(\Omega = 1)_g$	5	6	2,24
	4	5	2,26
	6	7	2,29
	3	4	2,31
	2	3	2,33
	5	6	2,34
	1	2	2,35
	4	5	2,37
	3	4	2,38
	0	1	2,42
	6	7	2,42
	5	6	2,44
	2	3	2,44
	4	5	2,46
	1	2	2,48
3	4	2,48	
2	3	2,53	
7	8	2,67	
6	7	2,70	
5	6	2,71	
4	5	2,76	
8	9	2,77	
7	8	2,78	

TABLE IV. (Continued)

Symmetry	Lower state	Higher state	R (Å)
	6	7	2,80
	3	4	2,84
	8	9	2,85
	5	6	2,86
	7	8	2,87
	4	5	2,94
	6	7	2,96
	8	9	2,99
	5	6	3,06
	7	8	3,25
$(\Omega = 1)_u$	6	7	2,34
	5	6	2,36
	3	5	2,42
	2	3	2,46
	6	8	2,46
	6	7	2,50
	5	6	2,52
	4	5	2,54
	7	9	2,54
	6	7	2,56
	3	4	2,56
	5	6	2,58
	4	5	2,60
	9	10	2,64
	7	8	2,64
	6	7	2,70
	8	9	2,70
	7	8	2,86
	8	9	2,90
	6	8	2,92
	9	10	3,06
	8	9	3,10
	7	8	3,14
$(\Omega = 2)_g$	2	6	2,24
	3	4	2,24
	1	2	2,30
	6	7	2,42
	0	1	2,42
	4	6	2,44
	3	4	2,46
	1	2	2,54
	6	7	2,61
	2	3	2,49
	5	6	2,62
	4	5	2,64
	3	4	2,68
	2	3	2,82
	6	7	2,86
	5	6	2,88
	4	5	2,94
	6	7	2,94
	5	6	3,04
	3	4	3,14
	6	7	3,16
$(\Omega = 2)_u$	3	4	2,48
	6	7	2,50
	5	6	2,50

TABLE IV. (Continued)

Symmetry	Lower state	Higher state	R (Å)
	4	5	2,51
	3	4	2,52
	2	3	2,55
	1	2	2,56
	4	5	2,64
	6	7	2,70
	5	7	2,74
	4	5	2,78
	3	4	2,82
	2	3	2,84
	6	7	2,86
	4	5	2,90
	5	6	2,92
	4	5	2,94
	3	4	2,98
	6	7	3,15

populations between the $(\Omega = 2)_g$ symmetry and the other symmetries.

IV. CONCLUSION

As a first step towards the generation of accurate models for the reactivity in iodine plasmas, in this work we have investigated a computational protocol, combining four-component multireference CI calculations for the I_2 system to obtain potential energy curves and the semiclassical Landau-Zener surface hopping method to treat nuclear dynamics, to obtain theoretical cross sections of the mutual neutralization reaction between I^+ and I^- for collision energies varying from 0.001 eV to 50 eV.

Our results agree qualitatively with the recent experimental measurements performed at the double ion ring DESIREE facility in the overlapping collision energy range. Furthermore, our work provides absolute cross sections over a broad range of collision energy. Our results show that the total cross section decrease from 1000 \AA^2 at 0.001 eV collision energy to about 10 \AA^2 at 10 eV impact energy. Moreover, the branching ratios towards the different final states do not vary significantly with respect to the collision energy. We also studied the dynamics of this mutual neutralization reaction.

The data and insights provided in this work will allow to model, beyond the current state of the art, the chemistry taking place in iodine plasma, which is particularly relevant for electric space propulsion.

ACKNOWLEDGMENTS

S.B. thanks the École normale supérieure Paris-Saclay for the PhD scholarship. X.Y. and A.S.P.G. acknowledge funding from projects CompRIXS (No. ANR-19-CE29-0019 and No. DFG JA 2329/6-1), Labex CaPPA (No. ANR-11-LABX-0005-01), and the I-SITE ULNE project OVERSEE and MESONM International Associated Laboratory (LAI) (No. ANR-16-IDEX-0004), and support from the French national supercomputing facilities (Grants No. DARI A0090801859 and No. A0110801859). P.L.B. and N.S. thank Institut

Physique des Infinis for financial support. S.B., P.L.B., and N.S. thank the members of the DESIREE facility for their warm welcome. The authors would also like to thank A. Bourdon, J.-P. Booth, and B. Esteves for their interest in our work.

APPENDIX

The diffuse functions used to describe accurately Rydberg and ion-pair states are given in Table III. Table IV reports the list of the avoided crossings considered in this work.

-
- [1] N. S. Shuman, D. E. Hunton, and A. A. Viggiano, *Chem. Rev.* **115**, 4542 (2015).
- [2] A. B. Fialkov, *Prog. Energy Combust. Sci.* **23**, 399 (1997).
- [3] D. Smith, N. G. Adams, and M. J. Church, *Planet. Space Sci.* **24**, 697 (1976).
- [4] D. Smith, *Chem. Rev.* **92**, 1473 (1992).
- [5] W. L. Morgan, J. N. Bardsley, J. Lin, and B. L. Whitten, *Phys. Rev. A* **26**, 1696 (1982).
- [6] Å. Larson, J. Hörnquist, P. Hedvall, and A. E. Orel, *J. Chem. Phys.* **151**, 214305 (2019).
- [7] D. Rafalskyi, J. M. Martínez, L. Habl, E. Zorzoli Rossi, P. Proynov, A. Boré, T. Baret, A. Poyet, T. Lafleur, S. Dudin, and A. Aanesland, *Nature (London)* **599**, 411 (2021).
- [8] B. Esteves, F. Marmuse, C. Drag, A. Bourdon, A. Alvarez Laguna, and P. Chabert, *Plasma Sources Sci. Technol.* **31**, 085007 (2022).
- [9] M. Poline, X. Yuan, S. Badin, M. C. Ji, S. Rosén, S. Indrajith, R. D. Thomas, H. T. Schmidt, H. Zettergren, A. S. P. Gomes, and N. Sisourat, *Phys. Rev. A* **106**, 012812 (2022).
- [10] T. Fleig, J. Olsen, and L. Visscher, *J. Chem. Phys.* **119**, 2963 (2003).
- [11] T. Saue, R. Bast, A. S. P. Gomes, H. J. A. Jensen, L. Visscher, I. A. Aucar, R. D. Remigio, K. G. Dyall, E. Eliav, E. Fasshauer, T. Fleig, L. Halbert, E. D. Hedegård, B. Helmich-Paris, M. Iliaš, C. R. Jacob, S. Knecht, J. K. Laerdahl, M. L. Vidal, M. K. Nayak *et al.*, *J. Chem. Phys.* **152**, 204104 (2020).
- [12] A. S. P. Gomes, T. Saue, L. Visscher, H. J. A. Jensen, R. Bast, I. A. Aucar, V. Bakken, K. G. Dyall, S. Dubillard, U. Ekström, E. Eliav, T. Enevoldsen, E. Faßhauer, T. Fleig, O. Fossgaard, L. Halbert, E. D. Hedegård, T. Helgaker, B. Helmich-Paris, J. Henriksson *et al.*, “DIRAC19” (2019).
- [13] K. G. Dyall, *Theor. Chem. Acc.* **115**, 441 (2006).
- [14] S. Lukashov, A. Petrov, and A. Pravilov, The iodine molecule: Insights into intra- and intermolecular perturbation in diatomic molecules (2018).
- [15] C. N. Banwell, *Fundamentals of Molecular Spectroscopy*, 3rd ed. (McGraw-Hill, London, 1983).
- [16] A. Kramida, Yu. Ralchenko, J. Reader, and NIST ASD Team, (2019), NIST Atomic Spectra Database (ver. 5.7.1), [Online]. Available: <https://physics.nist.gov/asd> [2020, September 30]. National Institute of Standards and Technology, Gaithersburg, MD.
- [17] A. K. Belyaev, C. Lasser, and G. Trigila, *J. Chem. Phys.* **140**, 224108 (2014).
- [18] M. Desouter-Lecomte, Y. Justum, and X. Chapuisat, in *Introduction la Théorie Quantique: Concepts, Pratiques et Applications* (2017).
- [19] E. Wigner and E. E. Witmer, in *World Scientific Series in 20th Century Chemistry* (World Scientific, Singapore, 2000), Vol. 8, pp. 287–311.
- [20] C. Zener, *Proc. R. Soc. London, Ser. A* **137**, 696 (1932).
- [21] A. K. Belyaev and O. V. Lebedev, *Phys. Rev. A* **84**, 014701 (2011).
- [22] O. V. Ivakhnenko, S. N. Shevchenko, and F. Nori, *Phys. Rep.* **995**, 1 (2023).
- [23] M. S. Child, *Molecular Collision Theory* (Academic, London, 1974).
- [24] R. E. Olson, J. R. Peterson, and J. Moseley, *J. Chem. Phys.* **53**, 3391 (1970).
- [25] R. J. Peláez, C. Blondel, C. Delsart, and C. Drag, *J. Phys. B: At., Mol. Opt. Phys.* **42**, 125001 (2009).
- [26] X. Yuan and A. S. Pereira Gomes, *J. Chem. Phys.* **157**, 074313 (2022).
- [27] J. V. Pototschnig, K. G. Dyall, L. Visscher, and A. S. P. Gomes, *Phys. Chem. Chem. Phys.* **23**, 22330 (2021).
- [28] M. Denis, M. S. Nørby, H. J. A. Jensen, A. S. P. Gomes, M. K. Nayak, S. Knecht, and T. Fleig, *New J. Phys.* **17**, 043005 (2015).

Summary and Conclusion

In this thesis, we have investigated two aspects of relativistic quantum chemistry calculations on molecules: the methodological development of relativistic coupled cluster response theory and the application of established methods to the electronic structure of molecules containing heavy elements

Chapter 3 details the implementation of frequency-dependent linear response properties, drawing upon two distinct relativistic coupled cluster wave function models, namely CC-CC and CC-CI. We validated our approach by examining three diverse categories of molecular properties including the purely electric property (frequency (in)dependent) polarizability, purely magnetic property (indirect spin-spin coupling constant), and electric-magnetic mixed property (optical rotation). The validation is done by reproducing the results obtained by other programs such as DALTON and CFOUR using a non-relativistic Hamiltonian. Furthermore, the utilization of complex algebra enables us to extend the frequency from real to complex numbers for the evaluation of the damped linear response function. This is associated with the absorption cross-section in the theoretical simulation of the spectroscopy.

In Chapter 4, we further implemented the frequency-dependent quadratic response and two-photon absorption (TPA) grounded in the relativistic equation-of-motion coupled cluster model to study nonlinear molecular properties. Parallel to Chapter 3, we test two different types of properties - the purely electric property (first hyperpolarizability), and the mixed electric-magnetic property (Verdet constant). We validated our code by exactly reproducing the EOM quadratic response results obtained by DALTON. Given DALTON's absence of an EOM-type two-photon absorption, we compared our EOM-based TPA to that of the CC-QR module in DALTON. We found a discrepancy of approximately

3%, which aligns with the magnitude of variation noted in quadratic response properties.

In Chapter 5, we reimplemented EOM-CC energy including ionization potential (IP), electron affinity (EA), and excitation energy (EE) on the ExaCorr module. We have so far performed very basic calculations to validate our code. In these tests, the new EOM codes reproduce the RELCCSD results very well. We are optimistic to be able to show the number of applications of this code in the near future.

All three implementations mentioned above are based on the new coupled cluster module ExaCorr in the DIRAC program. ExaCorr is designed to be able to exploit a large number of GPU-accelerated nodes, found in supercomputer architectures. While the lack of symmetry implementation is a drawback for small symmetric systems, the large-scale parallelization compensates for this limitation, especially for sizable systems under the C_1 symmetry.

However, the high cost of the coupled cluster method still poses significant challenges to carrying out investigations on large systems even utilizing the ExaCorr. To further improve the efficiency of this code, in Chapter 6, we implemented the MP2 frozen natural orbitals (FNOs) to replace the Hartree-Fock orbitals before performing CC calculations. We showcase the performance on both correlation energy and the expectation value of ground state including electric dipole and quadrupole moment, the electric gradient at the nuclei, and parity-violating energy difference. We found that using MP2FNOs can accelerate the convergence of the correlation energy and molecular properties. This allows for reliable estimates using just half the size of the full virtual orbital space.

In Chapter 7, we applied the existing relativistic quantum chemistry models including EOM-CC, multi-reference configuration interaction (MRCI), and Polarization Propagator (PP) to obtain the electronic structure (like potential energy curves) and molecular properties such as transition dipole moment as accurate as possible. While these applications belong to different physics topics -the work of TlCl towards molecular laser cooling and fundamental physics, and the work of I_2 is used in the analysis of the atomic collision in plasma physics, the relativistic effect and electron correlation both show their significance.

In conclusion, the development and application work both showcase that

for molecular property calculation, particularly for molecules containing heavy elements, it is necessary to develop and apply methods that can deal with relativistic effects and electron correlation on an equal footing. The relativistic (EOM) coupled cluster and response theory forms a good team for the frequency (in)dependent molecular property calculation.

As a perspective, most current implementation work in this thesis relies on the single-code tensor operation library TAL-SH, which is limited by the capacity of a single node. Naturally, in the near future, we should extend all the code including response properties, and EOM energy to use a library suited for distributed memory computing architectures, such as the ExaTENSOR. Once that is carried out, we can combine the code with other developed methods such as the quantum embedding approach[113] to investigate the large molecules we could not compute before for both response properties and energy. We are working towards this goal.

Moreover, the high cost remains a dark cloud above the performance of the coupled cluster method on calculating large systems. Extending the current relativistic MP2FNOs by introducing the effect of excited states is a promising approach to accomplish the reduced-scaling calculation of coupled cluster response theory. To advance towards this goal we have implemented in ExaCorr the CIS and CIS(D) methods[114], which can help in this direction, both as tools to generate natural transition orbitals[115] and as a low-order scaling alternative to EOM-CCSD for obtaining excited state energies.

Finally, our current frequency domain response code is based upon time-dependent perturbation theory. This makes it unsuitable to obtain the response of molecules to strong perturbations. To address this, we aim to develop real-time relativistic coupled cluster models, leveraging the components of the existing program. With that, we will have a toolset to investigate molecular properties across the periodic table in different regimes (linear/nonlinear, strong/weak perturbations, short/long process timescales).

Bibliography

- (1) King, D. M.; Liddle, S. T. Progress in molecular uranium-nitride chemistry. *Coordin. Chem. Rev* **2014**, 266-267, 2–15, DOI: 10.1016/j.ccr.2013.06.013.
- (2) Loiseau, T.; Mihalcea, I.; Henry, N.; Volkringer, C. The crystal chemistry of uranium carboxylates. *Coordin. Chem. Rev* **2014**, 266-267, 69–109, DOI: 10.1016/j.ccr.2013.08.038.
- (3) Yang, W.; Parker, T. G.; Sun, Z.-M. Structural chemistry of uranium phosphonates. *Coordin. Chem. Rev* **2015**, 303, 86–109, DOI: 10.1016/j.ccr.2015.05.010.
- (4) Liddle, S. T. The Renaissance of Non-Aqueous Uranium Chemistry. *Angew. Chem. Int. Ed.* **2015**, 54, 8604–8641, DOI: 10.1002/anie.201412168.
- (5) Clark, D. L.; Hobart, D. E.; Neu, M. P. Actinide Carbonyl Complexes and Their Importance in Actinide Environmental Chemistry. *Chem. Rev.* **1995**, 95, 25–48, DOI: 10.1021/cr00033a002.
- (6) Hartline, D. R.; Meyer, K. From Chemical Curiosities and Trophic Molecules to Uranium-Based Catalysis: Developments for Uranium Catalysis as a New Facet in Molecular Uranium Chemistry. *JACS Au* **2021**, 1, 698–709, DOI: 10.1021/jacsau.1c00082.
- (7) Fox, A. R.; Bart, S. C.; Meyer, K.; Cummins, C. C. Towards uranium catalysts. *Nature* **2008**, 455, 341–349, DOI: 10.1038/nature07372.
- (8) Vodyanitskii, Y. N. Chemical aspects of uranium behavior in soils: A review. *Eurasian Soil Sc.* **2011**, 44, 862–873, DOI: 10.1134/S1064229311080163.
- (9) Sénéchal, K.; Toupet, L.; Ledoux, I.; Zyss, J.; Le Bozec, H.; Maury, O. First lanthanide dipolar complexes for second-order nonlinear optics. *Chem. Commun.* **2004**, 2180–2181, DOI: 10.1039/B407073A.
- (10) Law, G.-L.; Wong, K.-L.; Lau, K.-K.; Lap, S.-t.; Tanner, P. A.; Kuo, F.; Wong, W.-T. Nonlinear optical activity in dipolar organic–lanthanide complexes. *J. Mater. Chem.* **2010**, 20, 4074, DOI: 10.1039/b926376d.

- (11) Andraud, C.; Maury, O. Lanthanide Complexes for Nonlinear Optics: From Fundamental Aspects to Applications. *Eur. J. Inorg. Chem.* **2009**, *2009*, 4357–4371, DOI: 10.1002/ejic.200900534.
- (12) Tancrez, N.; Feuvrie, C.; Ledoux, I.; Zyss, J.; Toupet, L.; Le Bozec, H.; Maury, O. Lanthanide Complexes for Second Order Nonlinear Optics: Evidence for the Direct Contribution of f Electrons to the Quadratic Hyperpolarizability. *J. Am. Chem. Soc.* **2005**, *127*, 13474–13475, DOI: 10.1021/ja054065j.
- (13) Sénéchal-David, K. et al. Synthesis, Structural Studies, Theoretical Calculations, and Linear and Nonlinear Optical Properties of Terpyridyl Lanthanide Complexes: New Evidence for the Contribution of f Electrons to the NLO Activity. *J. Am. Chem. Soc.* **2006**, *128*, 12243–12255, DOI: 10.1021/ja063586j.
- (14) Valore, A. et al. Fluorinated β -Diketonate Diglyme Lanthanide Complexes as New Second-Order Nonlinear Optical Chromophores: The Role of f Electrons in the Dipolar and Octupolar Contribution to Quadratic Hyperpolarizability. *J. Am. Chem. Soc.* **2010**, *132*, 4966–4970, DOI: 10.1021/ja101081q.
- (15) Klepov, V. V.; Serezhkina, L. B.; Vologzhanina, A. V.; Pushkin, D. V.; Sergeeva, O. A.; Stefanovich, S. Y.; Serezhkin, V. N. Tris(acrylato)uranylates as a scaffold for NLO materials. *Inorg. Chem. Commun.* **2014**, *46*, 5–8, DOI: 10.1016/j.inoche.2014.04.024.
- (16) Wang, S.; Alekseev, E. V.; Ling, J.; Liu, G.; Depmeier, W.; Albrecht-Schmitt, T. E. Polarity and Chirality in Uranyl Borates: Insights into Understanding the Vitrification of Nuclear Waste and the Development of Nonlinear Optical Materials. *Chem. Mater.* **2010**, *22*, 2155–2163, DOI: 10.1021/cm9037796.
- (17) Barker, T. J.; Denning, R. G.; Thorne, J. R. G. Applications of two-photon spectroscopy to inorganic compounds. 2. Spectrum and electronic structure of cesium uranyl nitrate, $\text{CsUO}_2(\text{NO}_3)_3$. *Inorg. Chem.* **1992**, *31*, 1344–1353, DOI: 10.1021/ic00034a011.
- (18) Serezhkin, V. N.; Grigoriev, M. S.; Abdulmyanov, A. R.; Fedoseev, A. M.; Savchenkov, A. V.; Stefanovich, S. Y.; Serezhkina, L. B. Syntheses, Crystal Structures, and Nonlinear Optical Activity of $\text{Cs}_2\text{Ba}[\text{AnO}_2(\text{C}_2\text{H}_5\text{COO})_3]_4$ (An = U, Np, Pu) and Unprecedented Octanuclear Complex Units in $\text{KR}_2(\text{H}_2\text{O})_8[\text{UO}_2(\text{C}_2\text{H}_5\text{COO})_3]_5$ (R = Sr, Ba). *Inorg. Chem.* **2017**, *56*, 7151–7160, DOI: 10.1021/acs.inorgchem.7b00809.

- (19) Żuk, M.; Podgórski, R.; Ruszczyńska, A.; Ciach, T.; Majkowska-Pilip, A.; Bilewicz, A.; Krysiński, P. Multifunctional Nanoparticles Based on Iron Oxide and Gold-198 Designed for Magnetic Hyperthermia and Radionuclide Therapy as a Potential Tool for Combined HER2-Positive Cancer Treatment. *Pharmaceutics* **2022**, *14*, 1680, DOI: 10.3390/pharmaceutics14081680.
- (20) Takeda, M.; Shibuya, H.; Inoue, T. The Efficacy of Gold-198 Grain Mold Therapy for Mucosal Carcinomas of the Oral Cavity. *Acta Oncologica* **1996**, *35*, 463–467, DOI: 10.3109/02841869609109923.
- (21) Schiff, L. I. Measurability of Nuclear Electric Dipole Moments. *Phys. Rev.* **1963**, *132*, 2194–2200, DOI: 10.1103/PhysRev.132.2194.
- (22) Safronova, M. S.; Budker, D.; DeMille, D.; Kimball, D. F. J.; Derevianko, A.; Clark, C. W. Search for new physics with atoms and molecules. *Rev. Mod. Phys.* **2018**, *90*, 025008, DOI: 10.1103/RevModPhys.90.025008.
- (23) Chupp, T. E.; Fierlinger, P.; Ramsey-Musolf, M. J.; Singh, J. T. Electric dipole moments of atoms, molecules, nuclei, and particles. *Rev. Mod. Phys.* **2019**, *91*, 015001, DOI: 10.1103/RevModPhys.91.015001.
- (24) Arrowsmith-Kron, G. et al. Opportunities for Fundamental Physics Research with Radioactive Molecules, en, arXiv:2302.02165 [nucl-ex, physics:nucl-th, physics:physics], 2023.
- (25) Rosa, M. D. Laser-cooling molecules: Concept, candidates, and supporting hyperfine-resolved measurements of rotational lines in the A-X(0,0) band of CaH. *Eur. Phys. J. D* **2004**, *31*, 395–402, DOI: 10.1140/epjd/e2004-00167-2.
- (26) Ivanov, M. V.; Jagau, T.-C.; Zhu, G.-Z.; Hudson, E. R.; Krylov, A. I. In search of molecular ions for optical cycling: a difficult road. *Phys. Chem. Chem. Phys.* **2020**, *22*, 17075–17090, DOI: 10.1039/D0CP02921A.
- (27) Christiansen, O.; Jørgensen, P.; Hattig, C. Response functions from Fourier component variational perturbation theory applied to a time-averaged quasienergy. *Int. J. Quantum. Chem* **1998**, *68*, 52.
- (28) Cronstrand, P.; Luo, Y.; Ågren, H. In *Advances in Quantum Chemistry*; Elsevier: 2005; Vol. 50, pp 1–21, DOI: 10.1016/S0065-3276(05)50001-7.
- (29) Helgaker, T.; Coriani, S.; Jørgensen, P.; Kristensen, K.; Olsen, J.; Ruud, K. Recent Advances in Wave Function-Based Methods of Molecular-Property Calculations. *Chem. Rev.* **2012**, *112*, 543–631, DOI: 10.1021/cr2002239.

- (30) Norman, P.; Ruud, K.; Saue, T., *Principles and practices of molecular properties: theory, modeling and simulations*, First edition; John Wiley & Sons: Hoboken, NJ, 2018.
- (31) Dreuw, A.; Head-Gordon, M. Single-Reference ab Initio Methods for the Calculation of Excited States of Large Molecules. *Chem. Rev.* **2005**, *105*, 4009–4037, DOI: 10.1021/cr0505627.
- (32) Adamo, C.; Jacquemin, D. The calculations of excited-state properties with Time-Dependent Density Functional Theory. *Chem. Soc. Rev.* **2013**, *42*, 845–856, DOI: 10.1039/C2CS35394F.
- (33) Laurent, A. D.; Jacquemin, D. TD-DFT benchmarks: A review. *Int. J. Quantum Chem* **2013**, *113*, 2019–2039, DOI: 10.1002/qua.24438.
- (34) Ikäläinen, S.; Lantto, P.; Vaara, J. Fully Relativistic Calculations of Faraday and Nuclear Spin-Induced Optical Rotation in Xenon. *J. Chem. Theory Comput.* **2012**, *8*, 91–98, DOI: 10.1021/ct200636m.
- (35) Kervazo, S.; Réal, F.; Virot, F.; Severo Pereira Gomes, A.; Vallet, V. Accurate Predictions of Volatile Plutonium Thermodynamic Properties. *Inorg. Chem.* **2019**, *58*, 14507–14521, DOI: 10.1021/acs.inorgchem.9b02096.
- (36) Sunaga, A.; Saue, T. Towards highly accurate calculations of parity violation in chiral molecules: relativistic coupled-cluster theory including QED-effects. *Mol. Phys.* **2021**, *119*, e1974592, DOI: 10.1080/00268976.2021.1974592.
- (37) Bartlett, R. J.; Musiał, M. Coupled-cluster theory in quantum chemistry. *Rev. Mod. Phys.* **2007**, *79*, 291–352, DOI: 10.1103/RevModPhys.79.291.
- (38) Wang, F. In *Handbook of Relativistic Quantum Chemistry*, Liu, W., Ed.; Springer Berlin Heidelberg: Berlin, Heidelberg, 2017, pp 797–823, DOI: 10.1007/978-3-642-40766-6_33.
- (39) Krylov, A. I. Equation-of-Motion Coupled-Cluster Methods for Open-Shell and Electronically Excited Species: The Hitchhiker’s Guide to Fock Space. *Annu. Rev. Phys. Chem.* **2008**, *59*, 433–462, DOI: 10.1146/annurev.physchem.59.032607.093602.
- (40) Bartlett, R. J. Coupled-cluster theory and its equation-of-motion extensions. *WIREs Comput Mol Sci* **2012**, *2*, 126–138, DOI: 10.1002/wcms.76.
- (41) Crawford, T. D.; Schaefer, H. F. In *Reviews in computational chemistry*, 2007; Vol. 14.
- (42) Shavitt, I.; Bartlett, R. J., *Many-body methods in chemistry and physics: MBPT and coupled-cluster theory*; Cambridge molecular science, OCLC: ocn297147115; Cambridge University Press: Cambridge ; New York, 2009.

- (43) Lyakh, D. I.; Musiał, M.; Lotrich, V. F.; Bartlett, R. J. Multireference Nature of Chemistry: The Coupled-Cluster View. *Chem. Rev.* **2012**, *112*, 182–243, DOI: 10.1021/cr2001417.
- (44) Sneskov, K.; Christiansen, O. Excited state coupled cluster methods: Excited state coupled cluster methods. *WIREs Comput Mol Sci* **2012**, *2*, 566–584, DOI: 10.1002/wcms.99.
- (45) Liu, J.; Cheng, L. Relativistic coupled-cluster and equation-of-motion coupled-cluster methods. *WIREs Comput Mol Sci* **2021**, *11*, DOI: 10.1002/wcms.1536.
- (46) Sverdrup Ofstad, B.; Aurbakken, E.; Sigmundson Schøyen, Ø.; Kristiansen, H. E.; Kvaal, S.; Pedersen, T. B. Time-dependent coupled-cluster theory. *WIREs Comput Mol Sci* **2023**, e1666, DOI: 10.1002/wcms.1666.
- (47) Calvin, J. A.; Peng, C.; Rishi, V.; Kumar, A.; Valeev, E. F. Many-Body Quantum Chemistry on Massively Parallel Computers. *Chem. Rev.* **2021**, *121*, 1203–1231, DOI: 10.1021/acs.chemrev.0c00006.
- (48) Kobayashi, R.; Rendell, A. P. A direct coupled cluster algorithm for massively parallel computers. *Chem. Phys. Lett* **1997**, *265*, 1–11, DOI: 10.1016/S0009-2614(96)01387-5.
- (49) Wang, M.; May, A. J.; Knowles, P. J. Parallel programming interface for distributed data. *Computer Physics Communications* **2009**, *180*, 2673–2679, DOI: 10.1016/j.cpc.2009.05.002.
- (50) Kuš, T.; Lotrich, V. F.; Bartlett, R. J. Parallel implementation of the equation-of-motion coupled-cluster singles and doubles method and application for radical adducts of cytosine. *J. Chem. Phys* **2009**, *130*, 124122, DOI: 10.1063/1.3091293.
- (51) Asadchev, A.; Gordon, M. S. Fast and Flexible Coupled Cluster Implementation. *J. Chem. Theory Comput.* **2013**, *9*, 3385–3392, DOI: 10.1021/ct400054m.
- (52) Peng, C.; Calvin, J. A.; Pavošević, F.; Zhang, J.; Valeev, E. F. Massively Parallel Implementation of Explicitly Correlated Coupled-Cluster Singles and Doubles Using TiledArray Framework. *J. Phys. Chem. A* **2016**, *120*, 10231–10244, DOI: 10.1021/acs.jpca.6b10150.
- (53) Olivares-Amaya, R.; Watson, M. A.; Edgar, R. G.; Vogt, L.; Shao, Y.; Aspuru-Guzik, A. Accelerating Correlated Quantum Chemistry Calculations Using Graphical Processing Units and a Mixed Precision Matrix Multiplication Library. *J. Chem. Theory Comput.* **2010**, *6*, 135–144, DOI: 10.1021/ct900543q.

- (54) DePrince, A. E.; Hammond, J. R. Coupled Cluster Theory on Graphics Processing Units I. The Coupled Cluster Doubles Method. *J. Chem. Theory Comput.* **2011**, *7*, 1287–1295, DOI: 10.1021/ct100584w.
- (55) Lyakh, D. I. An efficient tensor transpose algorithm for multicore CPU, Intel Xeon Phi, and NVidia Tesla GPU. *Computer Physics Communications* **2015**, *189*, 84–91, DOI: 10.1016/j.cpc.2014.12.013.
- (56) Ma, W.; Krishnamoorthy, S.; Villa, O.; Kowalski, K. GPU-Based Implementations of the Noniterative Regularized-CCSD(T) Corrections: Applications to Strongly Correlated Systems. *J. Chem. Theory Comput.* **2011**, *7*, 1316–1327, DOI: 10.1021/ct1007247.
- (57) Kaliman, I. A.; Krylov, A. I. New algorithm for tensor contractions on multi-core CPUs, GPUs, and accelerators enables CCSD and EOM-CCSD calculations with over 1000 basis functions on a single compute node. *J. Comput. Chem.* **2017**, *38*, 842–853, DOI: 10.1002/jcc.24713.
- (58) Pototschnig, J. V.; Papadopoulos, A.; Lyakh, D. I.; Repisky, M.; Halbert, L.; Severo Pereira Gomes, A.; Jensen, H. J. A.; Visscher, L. Implementation of Relativistic Coupled Cluster Theory for Massively Parallel GPU-Accelerated Computing Architectures. *J. Chem. Theory Comput.* **2021**, acs.jctc.1c00260, DOI: 10.1021/acs.jctc.1c00260.
- (59) Lyakh, D. I. Domain-specific virtual processors as a portable programming and execution model for parallel computational workloads on modern heterogeneous high-performance computing architectures. *Int J Quantum Chem* **2019**, *119*, e25926, DOI: 10.1002/qua.25926.
- (60) Liakos, D. G.; Sparta, M.; Kesharwani, M. K.; Martin, J. M. L.; Neese, F. Exploring the Accuracy Limits of Local Pair Natural Orbital Coupled-Cluster Theory. *J. Chem. Theory Comput.* **2015**, *11*, 1525–1539, DOI: 10.1021/ct501129s.
- (61) Riplinger, C.; Pinski, P.; Becker, U.; Valeev, E. F.; Neese, F. Sparse maps—A systematic infrastructure for reduced-scaling electronic structure methods. II. Linear scaling domain based pair natural orbital coupled cluster theory. *J. Chem. Phys.* **2016**, *144*, 024109, DOI: 10.1063/1.4939030.
- (62) Riplinger, C.; Neese, F. An efficient and near linear scaling pair natural orbital based local coupled cluster method. *J. Chem. Phys.* **2013**, *138*, 034106, DOI: 10.1063/1.4773581.
- (63) Crawford, T. D.; Kumar, A.; Bazanté, A. P.; Di Remigio, R. Reduced-scaling coupled cluster response theory: Challenges and opportunities. *WIREs Comput Mol Sci* **2019**, *9*, DOI: 10.1002/wcms.1406.

- (64) D’Cunha, R.; Crawford, T. D. PNO++: Perturbed Pair Natural Orbitals for Coupled Cluster Linear Response Theory. *J. Chem. Theory Comput.* **2021**, *17*, 290–301, DOI: 10.1021/acs.jctc.0c01086.
- (65) Epifanovsky, E.; Zuev, D.; Feng, X.; Khistyayev, K.; Shao, Y.; Krylov, A. I. General implementation of the resolution-of-the-identity and Cholesky representations of electron repulsion integrals within coupled-cluster and equation-of-motion methods: Theory and benchmarks. *J. Chem. Phys.* **2013**, *139*, 134105, DOI: 10.1063/1.4820484.
- (66) Schütz, M.; Manby, F. R. Linear scaling local coupled cluster theory with density fitting. Part I: 4-external integrals. *Phys. Chem. Chem. Phys.* **2003**, *5*, 3349–3358, DOI: 10.1039/B304550A.
- (67) Hohenstein, E. G.; Fales, B. S.; Parrish, R. M.; Martínez, T. J. Rank-reduced coupled-cluster. III. Tensor hypercontraction of the doubles amplitudes. *J. Chem. Phys.* **2022**, *156*, 054102, DOI: 10.1063/5.0077770.
- (68) DePrince, A. E.; Sherrill, C. D. Accuracy and Efficiency of Coupled-Cluster Theory Using Density Fitting/Cholesky Decomposition, Frozen Natural Orbitals, and a t_1 -Transformed Hamiltonian. *J. Chem. Theory Comput.* **2013**, *9*, 2687–2696, DOI: 10.1021/ct400250u.
- (69) Peng, C.; Calvin, J. A.; Valeev, E. F. Coupled-cluster singles, doubles and perturbative triples with density fitting approximation for massively parallel heterogeneous platforms. *Int J Quantum Chem* **2019**, *119*, DOI: 10.1002/qua.25894.
- (70) Bozkaya, U.; Sherrill, C. D. Analytic energy gradients for the coupled-cluster singles and doubles with perturbative triples method with the density-fitting approximation. *J. Chem. Phys.* **2017**, *147*, 044104, DOI: 10.1063/1.4994918.
- (71) DIRAC, a relativistic ab initio electronic structure program, Release DIRAC23 (2023), written by R. Bast, A. S. P. Gomes, T. Saue and L. Visscher and H. J. Aa. Jensen, with contributions from I. A. Aucar, V. Bakken, C. Chibueze, J. Creutzberg, K. G. Dyall, S. Dubillard, U. Ekström, E. Eliav, T. Enevoldsen, E. Faßhauer, T. Fleig, O. Fossgaard, L. Halbert, E. D. Hedegård, T. Helgaker, B. Helmich-Paris, J. Henriksson, M. van Horn, M. Iliaš, Ch. R. Jacob, S. Knecht, S. Komorovský, O. Kullie, J. K. Lærdahl, C. V. Larsen, Y. S. Lee, N. H. List, H. S. Nataraj, M. K. Nayak, P. Norman, A. Nyvang, G. Olejniczak, J. Olsen, J. M. H. Olsen, A. Papadopoulos, Y. C. Park, J. K. Pedersen, M. Pernpointner, J. V. Pototschnig, R. di Remigio, M. Repisky, K. Ruud, P. Sałek, B. Schimmelpfennig, B. Senjean, A. Shee, J. Sikkema, A. Sunaga, A. J. Thorvaldsen, J. Thyssen, J. van Stralen, M. L. Vidal, S. Villaume, O. Visser, T. Winther, S. Yamamoto and X. Yuan (available at

- <https://doi.org/10.5281/zenodo.7670749>, see also <https://www.diracprogram.org>).
- (72) Saue, T.; Bast, R.; Gomes, A. S. P.; Jensen, H. J. A.; Visscher, L.; Aucar, I. A.; Di Remigio, R.; Dyall, K. G.; Eliav, E.; Fasshauer, E., et al. The DIRAC code for relativistic molecular calculations. *J. Chem. Phys* **2020**, *152*, 204104.
- (73) Born, M.; Oppenheimer, R. Zur Quantentheorie der Molekeln. *Annalen der Physik* **1927**, *389*, 457–484, DOI: 10.1002/andp.19273892002.
- (74) Saue, T. Relativistic Hamiltonians for Chemistry: A Primer. *ChemPhysChem* **2011**, *12*, 3077–3094, DOI: 10.1002/cphc.201100682.
- (75) Dyall, K. G.; Fægri, K., *Introduction to relativistic quantum chemistry*; Oxford University Press: New York, 2007.
- (76) Foldy, L. L.; Wouthuysen, S. A. On the Dirac Theory of Spin 1/2 Particles and Its Non-Relativistic Limit. *Phys. Rev.* **1950**, *78*, 29–36, DOI: 10.1103/PhysRev.78.29.
- (77) Douglas, M.; Kroll, N. K. Quantum Electrodynamical Corrections to the Fine Structure of Helium. *ANNALS OF PHYSICS* **1974**, *82*, 89.
- (78) Nakajima, T.; Hirao, K. The Douglas–Kroll–Hess Approach. *Chem. Rev.* **2012**, *112*, 385–402, DOI: 10.1021/cr200040s.
- (79) Buenker, R. J.; Chandra, P.; Hess, B. A. Matrix representation of the relativistic kinetic energy operator: Two-component variational procedure for the treatment of many-electron atoms and molecules. *Chem. Phys.* **1984**, *84*, 1–9, DOI: 10.1016/0301-0104(84)80001-4.
- (80) Chang, C.; Pelissier, M.; Durand, P. Regular Two-Component Pauli-Like Effective Hamiltonians in Dirac Theory. *Phys. Scr.* **1986**, *34*, 394–404, DOI: 10.1088/0031-8949/34/5/007.
- (81) Lenthe, E. V.; Baerends, E. J.; Snijders, J. G. Relativistic regular two-component Hamiltonians. *J. Chem. Phys* **1993**, *99*, 4597–4610, DOI: 10.1063/1.466059.
- (82) Van Lenthe, E.; Baerends, E. J.; Snijders, J. G. Relativistic total energy using regular approximations. *J. Chem. Phys* **1994**, *101*, 9783–9792, DOI: 10.1063/1.467943.
- (83) Iliáš, M.; Aa. Jensen, H. J.; Kellö, V.; Roos, B. O.; Urban, M. Theoretical study of PbO and the PbO anion. *Chem. Phys. Lett* **2005**, *408*, 210–215, DOI: 10.1016/j.cpllett.2005.04.027.

- (84) Iliáš, M.; Saue, T. An infinite-order two-component relativistic Hamiltonian by a simple one-step transformation. *J. Chem. Phys.* **2007**, *126*, 064102, DOI: 10.1063/1.2436882.
- (85) Liu, W.; Peng, D. Infinite-order quasirelativistic density functional method based on the exact matrix quasirelativistic theory. *J. Chem. Phys.* **2006**, *125*, 044102, DOI: 10.1063/1.2222365.
- (86) Kutzelnigg, W.; Liu*, W. Quasirelativistic theory I. Theory in terms of a quasi-relativistic operator. *Mol. Phys.* **2006**, *104*, 2225–2240, DOI: 10.1080/00268970600662481.
- (87) Kutzelnigg, W. Effective Hamiltonians for degenerate and quasidegenerate direct perturbation theory of relativistic effects. *The Journal of Chemical Physics* **1999**, *110*, 8283–8294, DOI: 10.1063/1.478739.
- (88) Sikkema, J.; Visscher, L.; Saue, T.; Iliáš, M. The molecular mean-field approach for correlated relativistic calculations. *The Journal of Chemical Physics* **2009**, *131*, 124116, DOI: 10.1063/1.3239505.
- (89) Kellø, V.; Sadlej, A. J. Picture change and calculations of expectation values in approximate relativistic theories. *Int. J. Quant. Chem.* **1998**, *68*, 159–174, DOI: 10.1002/(SICI)1097-461X(1998)68:3<159::AID-QUA3>3.0.CO;2-U.
- (90) Helgaker, T.; Jørgensen, P.; Olsen, J., *Molecular electronic-structure theory*; Wiley: Chichester ; New York, 2000.
- (91) Stanton, R. E.; Havriliak, S. Kinetic balance: A partial solution to the problem of variational safety in Dirac calculations. *J. Chem. Phys.* **1984**, *81*, 1910–1918, DOI: 10.1063/1.447865.
- (92) Pawłowski, F.; Olsen, J.; Jørgensen, P. Molecular response properties from a Hermitian eigenvalue equation for a time-periodic Hamiltonian. *J. Chem. Phys.* **2015**, *142*, 114109, DOI: 10.1063/1.4913364.
- (93) Szalay, P. G.; Müller, T.; Gidofalvi, G.; Lischka, H.; Shepard, R. Multiconfiguration Self-Consistent Field and Multireference Configuration Interaction Methods and Applications. *Chem. Rev.* **2012**, *112*, 108–181, DOI: 10.1021/cr200137a.
- (94) Bartlett, R. J. Many-body perturbation theory and coupled cluster theory for electron correlation in molecules. *Annual review of physical chemistry* **1981**, *32*, 359–401.
- (95) Langhoff, S. R.; Davidson, E. R. Configuration interaction calculations on the nitrogen molecule. *Int. J. Quantum Chem.* **1974**, *8*, 61–72, DOI: 10.1002/qua.560080106.

- (96) Marie, A.; Kossoski, F.; Loos, P.-F. Variational coupled cluster for ground and excited states. *J. Chem. Phys* **2021**, *155*, 104105, DOI: 10.1063/5.0060698.
- (97) Koch, H.; Jensen, H. J. A.; Jørgensen, P.; Helgaker, T.; Scuseria, G. E.; Schaefer, H. F. Coupled cluster energy derivatives. Analytic Hessian for the closed-shell coupled cluster singles and doubles wave function: Theory and applications. *J. Chem. Phys* **1990**, *92*, 4924–4940, DOI: 10.1063/1.457710.
- (98) Raghavachari, K.; Trucks, G. W.; Pople, J. A.; Head-Gordon, M. A fifth-order perturbation comparison of electron correlation theories. *Chem. Phys. Lett* **1989**, *157*, 479–483, DOI: 10.1016/S0009-2614(89)87395-6.
- (99) Salek, P.; Vahtras, O.; Helgaker, T.; Ågren, H. Density-functional theory of linear and nonlinear time-dependent molecular properties. *J. Chem. Phys* **2002**, *117*, 9630–9645, DOI: 10.1063/1.1516805.
- (100) Koch, H.; Jørgensen, P. Coupled cluster response functions. *J. Chem. Phys* **1990**, *93*, 3333–3344, DOI: 10.1063/1.458814.
- (101) Coriani, S.; Pawłowski, F.; Olsen, J.; Jørgensen, P. Molecular response properties in equation of motion coupled cluster theory: A time-dependent perspective. *J. Chem. Phys* **2016**, *144*, 024102, DOI: 10.1063/1.4939183.
- (102) Shee, A.; Visscher, L.; Saue, T. Analytic one-electron properties at the 4-component relativistic coupled cluster level with inclusion of spin-orbit coupling. *J. Chem. Phys* **2016**, *145*, 184107, DOI: 10.1063/1.4966643.
- (103) Shee, A.; Saue, T.; Visscher, L.; Severo Pereira Gomes, A. Equation-of-motion coupled-cluster theory based on the 4-component Dirac–Coulomb(–Gaunt) Hamiltonian. Energies for single electron detachment, attachment, and electronically excited states. *J. Chem. Phys.* **2018**, *149*, 174113, DOI: 10.1063/1.5053846.
- (104) Davidson, E. R. The iterative calculation of a few of the lowest eigenvalues and corresponding eigenvectors of large real-symmetric matrices. *Journal of Computational Physics* **1975**, *17*, 87–94, DOI: 10.1016/0021-9991(75)90065-0.
- (105) David Sherrill, C.; Schaefer, H. F. In *Advances in Quantum Chemistry*; Elsevier: 1999; Vol. 34, pp 143–269, DOI: 10.1016/S0065-3276(08)60532-8.

- (106) Bouchafra, Y.; Shee, A.; Réal, F.; Vallet, V.; Severo Pereira Gomes, A. Predictive Simulations of Ionization Energies of Solvated Halide Ions with Relativistic Embedded Equation of Motion Coupled Cluster Theory. *Phys. Rev. Lett.* **2018**, *121*, 266001, DOI: 10.1103/PhysRevLett.121.266001.
- (107) Opoku, R. A.; Toubin, C.; Gomes, A. S. P. Simulating core electron binding energies of halogenated species adsorbed on ice surfaces and in solution *via* relativistic quantum embedding calculations. *Phys. Chem. Chem. Phys.* **2022**, *24*, 14390–14407, DOI: 10.1039/D1CP05836C.
- (108) Severo Pereira Gomes, A.; Jacob, C. R. Quantum-chemical embedding methods for treating local electronic excitations in complex chemical systems. *Annu. Rep. Prog. Chem., Sect. C: Phys. Chem.* **2012**, *108*, 222, DOI: 10.1039/c2pc90007f.
- (109) Wesolowski, T. A.; Shedge, S.; Zhou, X. Frozen-Density Embedding Strategy for Multilevel Simulations of Electronic Structure. *Chem. Rev.* **2015**, *115*, 5891–5928, DOI: 10.1021/cr500502v.
- (110) Jacob, C. R.; Neugebauer, J. Subsystem density-functional theory: Subsystem density-functional theory. *WIREs Comput Mol Sci* **2014**, *4*, 325–362, DOI: 10.1002/wcms.1175.
- (111) Misael, W. A.; Gomes, A. S. P. Core excitations and ionizations of uranyl in $\text{Cs}_2\text{UO}_2\text{Cl}_4$ from relativistic embedded damped response time-dependent density functional theory and equation of motion coupled cluster calculations, en, arXiv:2302.07223 [physics], 2023.
- (112) Surjuse, K.; Chamoli, S.; Nayak, M. K.; Dutta, A. K. A low-cost four-component relativistic equation of motion coupled cluster method based on frozen natural spinors: Theory, implementation, and benchmark. *J. Chem. Phys.* **2022**, *157*, 204106, DOI: 10.1063/5.0125868.
- (113) De Santis, M.; Sorbelli, D.; Vallet, V.; Gomes, A. S. P.; Storchi, L.; Belpassi, L. Frozen-Density Embedding for Including Environmental Effects in the Dirac-Kohn–Sham Theory: An Implementation Based on Density Fitting and Prototyping Techniques. *J. Chem. Theory Comput.* **2022**, *18*, 5992–6009, DOI: 10.1021/acs.jctc.2c00499.
- (114) Yuan, X.; Lejeune, T.; Gomes, A. S. P. *in preparation* **2023**.
- (115) Höfener, S.; Klopper, W. Natural transition orbitals for the calculation of correlation and excitation energies. *Chem. Phys. Lett.* **2017**, *679*, 52–59, DOI: 10.1016/j.cpllett.2017.04.083.

Appendix **A**

Supplemental information of Chapter
3

Supplementary information: Formulation and Implementation of frequency-dependent linear response properties with Relativistic Coupled-Cluster theory for GPU-accelerated computer architectures

Xiang Yuan,^{*,†,‡} Loïc Halbert,^{*,†} Johann Pototschnig,[‡] Anastasios Papadopoulos,[‡] Sonia Coriani,^{*,¶} Lucas Visscher,^{*,‡} and André Severo Pereira Gomes^{*,†}

[†]*Univ. Lille, CNRS, UMR 8523 - PhLAM - Physique des Lasers Atomes et Molécules, F-59000 Lille, France*

[‡]*Department of Chemistry and Pharmaceutical Sciences, Faculty of Science, Vrije Universiteit Amsterdam, 1081 HV Amsterdam, The Netherlands*

[¶]*DTU Chemistry – Department of Chemistry, Technical University of Denmark, DK-2800 Kongens Lyngby, Denmark*

E-mail: xiang.yuan@univ-lille.fr; loic.halbert@univ-lille.fr; soco@kemi.dtu.dk; l.visscher@vu.nl;
andre.gomes@univ-lille.fr

Working equations for CCSD linear response

In what follows a, b, c, \dots will indicate particle lines, i, j, k, \dots hole lines, and p, q, r, s, \dots general indexes.¹ In all equations below we use Einstein notation. Furthermore we define

- P as a permutation operator, with : $P_{-pq}f(\dots pq\dots) = f(\dots pq\dots) - f(\dots qp\dots)$;
- $X_q^p = \langle p|X|q\rangle$ are matrix elements of property operator X ;
- $V_{rs}^{pq} = \langle pq||rs\rangle$ are antisymmetrized two-electron integrals, and $f_q^p = \langle p|f|q\rangle$ Fock matrix elements;
- λ denotes ground-state CC Lagrange multipliers, and is therefore equivalent to $\bar{\mathbf{t}}^{(0)}$, and we have $\langle\Lambda| = \langle R| + \sum_{\mu} \lambda_{\mu} \langle\mu| e^{-T_0} = \langle R| + \sum_{\mu} \lambda_{\mu} \langle\bar{\mu}| \equiv \langle R| + \sum_{\mu} \bar{t}_{\mu}^{(0)} \langle\bar{\mu}|$
- \mathbf{r} and \mathbf{l} denote, depending on context, (trial) vectors associated to the solution of right and left-hand EOMCC or response equations.

Linear response

The ξ^X vector is defined as²

$$\xi_{\mu}^X = \langle\bar{\mu}|X|\text{CC}\rangle \quad (1)$$

and the programmable expressions for its elements are given by:

$$\xi_i^{Xa} = +X_i^a + X_e^a t_i^e - X_i^m t_m^a - (X_e^m t_i^e) t_m^a + X_e^m t_{im}^{ae} \quad (2)$$

$$\xi_{ij}^{Xab} = +P_{-ab} X_f^b t_{ij}^{af} - P_{-ij} X_j^m t_{im}^{ab} - P_{-ij} (X_e^m t_i^e) t_{mj}^{ab} - P_{-ab} (X_f^m t_m^a) t_{ij}^{fb} \quad (3)$$

The η^X vector is defined as²

$$\eta_{\mu}^X = \langle\Lambda|[X, \hat{\tau}_{\mu}]|\text{CC}\rangle \quad (4)$$

and the programmable expressions for its elements are given by

$$\begin{aligned}\eta^{Xi}_a = & X_a^i + X_a^e \lambda_e^i - X_m^i \lambda_a^m - X_a^m t_m^e \lambda_e^i - X_e^i t_m^e \lambda_a^m - \frac{1}{2} (t_{mn}^{fe} \lambda_{fe}^{mi}) X_a^n \\ & - \frac{1}{2} (t_{nm}^{fe} \lambda_{fa}^{nm}) X_e^i\end{aligned}\quad (5)$$

$$\begin{aligned}\eta^{Xij}_{ab} = & + P_{-ij} P_{-ab} \lambda_a^i X_b^j + P_{-ab} \lambda_{ae}^{ij} X_b^e - P_{-ij} \lambda_{ab}^{im} X_m^j - P_{-ab} (t_m^e \lambda_{ae}^{ij}) X_b^m \\ & - P_{-ij} (t_m^e \lambda_{ab}^{im}) X_e^j\end{aligned}\quad (6)$$

whereas the elements of the $\text{EOM} \boldsymbol{\eta}$ vector³ are

$$\text{EOM} \eta^{Xi}_a = + \eta^{Xi}_a + \lambda_{ab}^{ij} \xi^{Xb}_j \quad (7)$$

The CC Hessian (\mathbf{F}) is defined as²

$$F_{\mu\nu} = \langle \Lambda | [[H_0, \hat{\tau}_\mu], \hat{\tau}_\nu] | \text{CC} \rangle \quad (8)$$

and the programmable expressions for the matrix elements for its contraction with a response vector $\overset{x}{t}$, $\left(\overset{x}{t} F\right)$ are given by

$$\begin{aligned}\left(\overset{x}{t} F\right)_c^k = & + V_{ca}^{ki} \overset{x}{t}_i^a - \lambda_c^i \mathcal{F}_a^k \overset{x}{t}_i^a - \lambda_a^k \mathcal{F}_c^i \overset{x}{t}_i^a + \lambda_e^k \mathcal{W}_{ca}^{ei} \overset{x}{t}_i^a - \lambda_c^m \mathcal{W}_{ma}^{ki} \overset{x}{t}_i^a - \lambda_a^m \mathcal{W}_{mc}^{ik} \overset{x}{t}_i^a + \lambda_e^i \mathcal{W}_{ac}^{ek} \overset{x}{t}_i^a \\ & - \frac{1}{2} \lambda_c^i V_{ab}^{kj} \overset{x}{t}_{ij}^{ab} - \frac{1}{2} \lambda_a^k V_{cb}^{ij} \overset{x}{t}_{ij}^{ab} + \lambda_a^i V_{bc}^{jk} \overset{x}{t}_{ij}^{ab} - \lambda_{ae}^{mk} \mathcal{W}_{mc}^{ie} \overset{x}{t}_i^a - \lambda_{ec}^{im} \mathcal{W}_{am}^{ek} \overset{x}{t}_i^a + \frac{1}{2} \lambda_{ef}^{ki} \mathcal{W}_{ca}^{ef} \overset{x}{t}_i^a \\ & + \frac{1}{2} \lambda_{ca}^{mn} \mathcal{W}_{mn}^{ki} \overset{x}{t}_i^a - \frac{1}{2} (\lambda_{ec}^{mn} t_{mn}^{ef}) V_{fa}^{ki} \overset{x}{t}_i^a - \frac{1}{2} (\lambda_{ef}^{mk} t_{mn}^{ef}) V_{ca}^{ni} \overset{x}{t}_i^a - \frac{1}{2} (\lambda_{ea}^{mn} t_{mn}^{ef}) V_{fc}^{ik} \overset{x}{t}_i^a \\ & - \frac{1}{2} (\lambda_{ef}^{mi} t_{mn}^{ef}) V_{ac}^{nk} \overset{x}{t}_i^a - \frac{1}{2} \lambda_{ac}^{ij} \mathcal{F}_b^k \overset{x}{t}_{ij}^{ab} - \frac{1}{2} \lambda_{ab}^{ik} \mathcal{F}_c^j \overset{x}{t}_{ij}^{ab} - \lambda_{eb}^{ik} \mathcal{W}_{ac}^{ej} \overset{x}{t}_{ij}^{ab} + \lambda_{ac}^{mj} \mathcal{W}_{mb}^{ik} \overset{x}{t}_{ij}^{ab} \\ & - \frac{1}{4} \lambda_{ec}^{ij} \mathcal{W}_{ab}^{ek} \overset{x}{t}_{ij}^{ab} + \frac{1}{4} \lambda_{ab}^{mk} \mathcal{W}_{mc}^{ij} \overset{x}{t}_{ij}^{ab} + \frac{1}{2} \lambda_{ae}^{ij} \mathcal{W}_{bc}^{ek} \overset{x}{t}_{ij}^{ab} - \frac{1}{2} \lambda_{ab}^{im} \mathcal{W}_{mc}^{jk} \overset{x}{t}_{ij}^{ab}\end{aligned}\quad (9)$$

$$\begin{aligned}
\left(\begin{smallmatrix} x \\ tF \end{smallmatrix}\right)_{cd}^{kl} = & + P_{-cd}P_{-kl}\lambda_c^k V_{da}^{li} \overset{x}{t_i^a} - P_{-kl}\lambda_a^k V_{cd}^{il} \overset{x}{t_i^a} - P_{-cd}\lambda_c^i V_{ad}^{kl} \overset{x}{t_i^a} - P_{-kl}\lambda_{cd}^{ki} \mathcal{F}_a^l \overset{x}{t_i^a} - P_{-cd}\lambda_{ca}^{kl} \mathcal{F}_d^i \overset{x}{t_i^a} \\
& + P_{-cd}\lambda_{ce}^{kl} \mathcal{W}_{da}^{ei} \overset{x}{t_i^a} - P_{-kl}\lambda_{cd}^{km} \mathcal{W}_{ma}^{li} \overset{x}{t_i^a} + P_{-cd}P_{-kl}\lambda_{ca}^{ml} \mathcal{W}_{md}^{ki} \overset{x}{t_i^a} + \lambda_{cd}^{mi} \mathcal{W}_{ma}^{kl} \overset{x}{t_i^a} \\
& - P_{-cd}P_{-kl}\lambda_{ed}^{ki} \mathcal{W}_{ca}^{el} \overset{x}{t_i^a} - \lambda_{ea}^{kl} \mathcal{W}_{cd}^{ei} \overset{x}{t_i^a} - \frac{1}{2}P_{-cd}\lambda_{ca}^{kl} V_{db}^{ij} \overset{x}{t_{ij}^{ab}} - \frac{1}{2}P_{-kl}\lambda_{cd}^{ki} V_{ab}^{lj} \overset{x}{t_{ij}^{ab}} + \frac{1}{4}\lambda_{cd}^{ij} V_{ab}^{kl} \overset{x}{t_{ij}^{ab}} \\
& + \frac{1}{4}\lambda_{ab}^{kl} V_{cd}^{ij} \overset{x}{t_{ij}^{ab}} + P_{-kl}P_{-cd}\lambda_{cb}^{kj} V_{da}^{li} \overset{x}{t_{ij}^{ab}} - \frac{1}{2}P_{-kl}\lambda_{ab}^{ik} V_{cd}^{jl} \overset{x}{t_{ij}^{ab}} - \frac{1}{2}P_{-cd}\lambda_{ac}^{ij} V_{bd}^{kl} \overset{x}{t_{ij}^{ab}} \quad (10)
\end{aligned}$$

EOM-EE σ -Vectors and intermediates

The programmable expressions for the elements for the EOM-EE right $R\sigma$ and left $L\sigma$ vectors are given by:

$$R\sigma_i^a = \mathcal{F}_e^a r_i^e - \mathcal{F}_i^m r_m^a + \mathcal{F}_e^m r_{mi}^{ea} + \mathcal{W}_{ma}^{ei} r_m^e + \frac{1}{2}\mathcal{W}_{ef}^{am} r_{im}^{ef} + \frac{1}{2}\mathcal{W}_{ie}^{mn} r_{mn}^{ea} \quad (11)$$

$$\begin{aligned}
R\sigma_{ij}^{ab} = & - P_{-ab}\mathcal{W}_{ij}^{mb} r_m^a + P_{-ij}\mathcal{W}_{ej}^{ab} r_i^e + P_{-ab}(\mathcal{W}_{fe}^{bm} r_m^e) t_{ij}^{af} - P_{-ij}(\mathcal{W}_{je}^{nm} r_m^e) t_{in}^{ab} \\
& + P_{-ab}\mathcal{F}_e^b r_{ij}^{ae} - P_{-ij}\mathcal{F}_j^m r_{im}^{ab} + \frac{1}{2}\mathcal{W}_{ij}^{mn} r_{mn}^{ab} + P_{-ab}P_{-ij}\mathcal{W}_{ej}^{mb} r_{im}^{ae} \\
& - P_{-ab}\frac{1}{2}(V_{fe}^{nm} r_{mn}^{ea}) t_{ij}^{fb} - P_{-ij}\frac{1}{2}(V_{fe}^{nm} r_{im}^{fe}) t_{jn}^{ba} + \frac{1}{2}\mathcal{W}_{ef}^{ab} r_{ij}^{ef} \quad (12)
\end{aligned}$$

$$L\sigma_a^i = l_e^i \mathcal{F}_a^e - l_a^m \mathcal{F}_m^i + \frac{1}{2}l_{ef}^{im} \mathcal{W}_{am}^{ef} - \frac{1}{2}l_{ae}^{mn} \mathcal{W}_{mn}^{ie} - G_e^f \mathcal{W}_{fa}^{ei} - G_m^n \mathcal{W}_{na}^{mi} + l_e^m \mathcal{W}_{am}^{ie} \quad (13)$$

$$\begin{aligned}
L\sigma_{ab}^{ij} = & P_{-ab}l_{ae}^{ij} \mathcal{F}_b^e - P_{-ij}l_{ab}^{im} \mathcal{F}_m^j + \frac{1}{2}l_{ab}^{mn} \mathcal{W}_{mn}^{ij} + P_{-ij}P_{-ab}l_{ae}^{im} \mathcal{W}_{bm}^{je} + P_{-ab}V_{ae}^{ij} G_b^e - l_a^m \mathcal{W}_{mb}^{ij} \\
& - P_{-ij}V_{ab}^{im} G_m^j + P_{-ij}l_e^i V_{ab}^{ej} + P_{-ij}P_{-ab}l_a^i \mathcal{F}_b^j + \frac{1}{2}l_{ef}^{ij} \mathcal{W}_{am}^{ef} \quad (14)
\end{aligned}$$

The programmable expressions for the elements of the intermediates \mathcal{F} , \mathcal{W} used above are given by:

$$\mathcal{F}_m^i = f_m^i + f_e^i t_m^e + V_{me}^{in} t_n^e + \frac{1}{2} V_{ef}^{in} \tau_{mn}^{ef} \quad (15)$$

$$\mathcal{F}_e^a = f_e^a - f_a^m t_m^e + V_{fa}^{me} t_m^f - \frac{1}{2} V_{af}^{mn} \tau_{mn}^{ef} \quad (16)$$

$$\mathcal{F}_e^m = f_e^m + V_{ef}^{mn} t_n^f \quad (17)$$

$$\mathcal{W}_{mn}^{ij} = V_{mn}^{ij} + P_{-mn} V_{en}^{ij} t_m^e + \frac{1}{2} V_{ef}^{ij} \tau_{mn}^{ef} \quad (18)$$

$$\mathcal{W}_{ej}^{mb} = V_{ej}^{mb} + V_{ef}^{mb} t_j^f - V_{ej}^{mn} t_n^b - V_{ef}^{mn} (t_{jn}^{fb} + t_j^f t_n^b) \quad (19)$$

$$\begin{aligned} \mathcal{W}_{mn}^{ie} = & V_{mn}^{ie} + \mathcal{F}_f^i t_{mn}^{ef} - \mathcal{W}_{mn}^{io} t_o^e + \frac{1}{2} V_{fg}^{ie} \tau_{mn}^{fg} \\ & + P_{-mn} \bar{W}_{fn}^{ie} t_m^f + P_{-mn} V_{mf}^{io} t_n^e \end{aligned} \quad (20)$$

$$\begin{aligned} \mathcal{W}_{am}^{ef} = & V_{am}^{ef} + P_{-ef} V_{ag}^{en} t_{mn}^{gf} \\ & + \mathcal{W}_{ag}^{ef} t_m^g + \mathcal{F}_a^n t_{mn}^{ef} + \frac{1}{2} V_{am}^{no} \tau_{no}^{ef} - P_{-ef} \bar{W}_{am}^{nf} t_n^e \end{aligned} \quad (21)$$

$$\mathcal{W}_{ab}^{ef} = V_{ab}^{ef} - P_{-ef} V_{ab}^{mf} t_m^e + \frac{1}{2} V_{ab}^{mn} \tau_{mn}^{ef} \quad (22)$$

$$\bar{W}_{ej}^{mb} = V_{ej}^{mb} - V_{ef}^{mn} t_{nj}^{bf} \quad (23)$$

$$\mathcal{W}_{ie}^{mn} = V_{ie}^{mn} + t_i^f V_{fe}^{mn} \quad (24)$$

$$\mathcal{W}_{ef}^{am} = V_{ef}^{am} - V_{ef}^{nm} t_n^a \quad (25)$$

$$G_a^e = -\frac{1}{2} l_{af}^{mn} t_{mn}^{ef} \quad (26)$$

$$G_m^i = \frac{1}{2} l_{ef}^{in} t_{mn}^{ef} \quad (27)$$

$$\tau_{ij}^{ab} = t_{ij}^{ab} + \frac{1}{2} P_{-ab} P_{-ij} t_i^a t_j^b \quad (28)$$

Davidson scheme for solving first-order response equation

Due to the extremely large dimension of $\bar{\mathbf{H}}$ in practical calculations, solving the response equations to obtain the perturbed amplitudes calls for the use of iterative procedures,^{4,5} since directly inverting $(\bar{\mathbf{H}} - \omega_k \mathbf{I})$ in the full single and double excitation space is not feasible in all but the simplest cases. In this work we have opted to follow the scheme outlined by Olsen et al.⁶, with adjustments due to the fact that $\bar{\mathbf{H}}$ is non-symmetric, so that a common framework for solving both linear systems and eigenvalue equations can be put in place.

To this end, we have reimplemented and generalized the Davidson solver code outlined by Shee et al.⁷, so that all matrix/vector operations are now expressed in terms of tensor operations, involving the tensor datatypes available in the GPU-accelerated tensor operation frameworks used in ExaCorr.⁸ In doing so, we have conserved the features previously implemented for the solution of eigenvalue equations (multi-root solutions, root-following, etc), and added the ability to solve right-hand side and left-hand side linear systems (though for linear response we will only make use of the right-hand side solutions).

The iterative solver workflow for the solution of linear systems therefore consists of the following steps, which are summarized in figure 1:

1. Choose an orthonormal vector as the initial guess for the trial vector space $\{\mathbf{b}\}$ where $\mathbf{t} = \mathbf{b}\beta'$ (note that \mathbf{t} and \mathbf{b} are TAL-SH tensors and β' is a Fortran array). By default, we start with pivoted unit trial vectors (see below for details);
2. Construct the reduced subspace matrix \mathbf{G}' and column vector \mathbf{C}' by projecting the $\mathbf{G} = (\bar{\mathbf{H}} - \omega_k \mathbf{I})$ matrix $\bar{\mathbf{H}}$ and property gradient vector $\mathbf{C} = \xi^Y$ onto the current trial vector space $\{\mathbf{b}_i, i = 1, \dots, L\}$, respectively. The $\bar{\mathbf{H}}\mathbf{b}$ products are obtained with the EOM-EE σ -vector routines;

$$\mathbf{G}\mathbf{t}^Y = -\xi^Y \implies \mathbf{b}^\dagger \mathbf{G}\mathbf{b}\beta' = \mathbf{b}^\dagger \mathbf{C} \implies \mathbf{G}'\beta' = \mathbf{C}' \quad (29)$$

3. Evaluate the residual vector (\mathbf{r}^k) and preconditioner (\mathbf{p}^k)

$$\mathbf{r}^k = (\boldsymbol{\sigma} - \omega_k \mathbf{b}) \boldsymbol{\beta}' - \mathbf{C}$$

$$\mathbf{p}^k = (\omega_k - \bar{H}_{||})^{-1}$$

the latter being utilized to improve convergence;⁹ compute the norm of \mathbf{r}^k and compare it to the threshold defined by the user ;

4. If the norm of \mathbf{r}^k exceeds the threshold, it indicates that the calculation has not converged. In this case, we construct the correction vector $\boldsymbol{\epsilon}^k = \mathbf{p}^k \mathbf{r}^k$ and orthonormalize it to the existing trial vector using a modified Gram-Schmidt procedure, in order to generate the new trial vectors \mathbf{b}^k , adding it to $\{\mathbf{b}_i, i = 1, \dots, L, L_k\}$. Using the newly generated trial vectors, repeat step 2 until the norm of the residual vector becomes smaller than the threshold;
5. Once the norm of the error vector falls below the threshold, it indicates that the calculation has converged. At this point, the Davidson routine stops, and the final solution vector is obtained from \mathbf{b} and $\boldsymbol{\beta}'$ as a TAL-SH tensor, which is subsequently used to calculate the response function of interest.

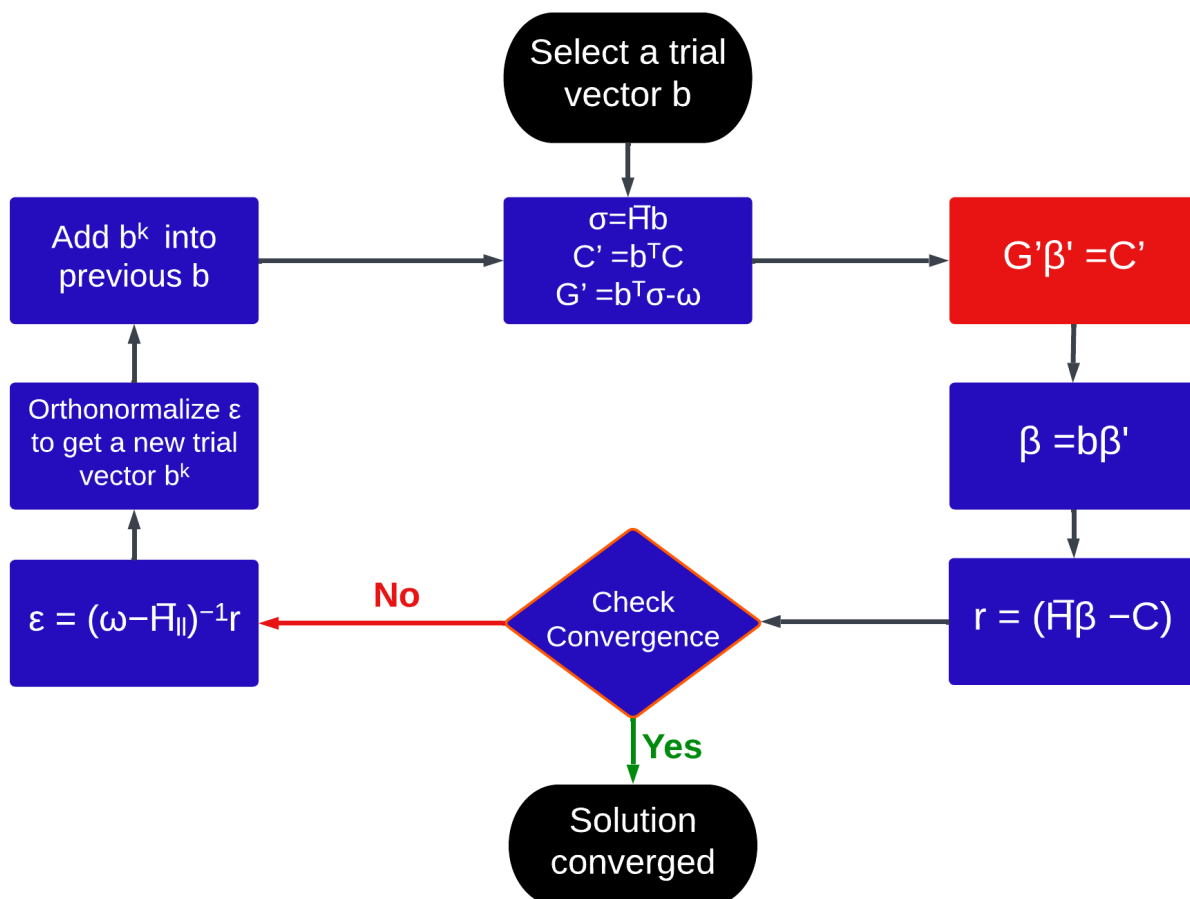


Figure 1: Workflow of the Davidson scheme for solving response equations. The operations performed within the black boxes are independent from the Davidson loop. The tasks in the blue boxes are implemented using TAL-SH tensors. The solution of the linear system in the subspace, indicated by the red box, employs Fortran arrays.

Frequency dependent polarizability of IIB atoms

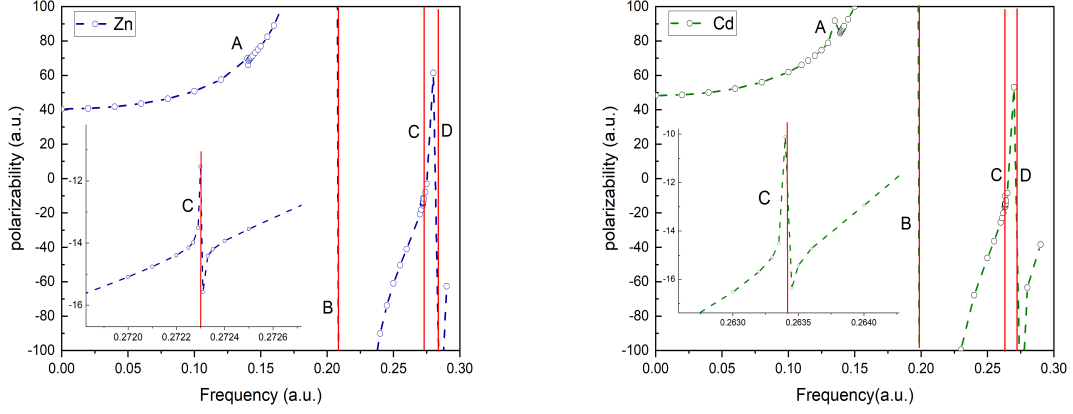


Figure 2: Frequency dependent polarizability of Zn and Cd.

Table 1: Number of iterations for solving response equations with different frequencies

Frequency (a.u.)	Zn	Cd	Hg
0.0	15	14	13
0.05	18	16	14
X ^a	49	39	52
X ^b	39	36	41

^a Frequency close to the **B** transition: For **Zn**: 0.213 a.u.; For **Cd**: 0.203 a.u.; For **Hg**: 0.25 a.u;

^b : With damping factor $\gamma = 0.01$ a.u.

Comparison between LRCC with DIRAC and Dalton

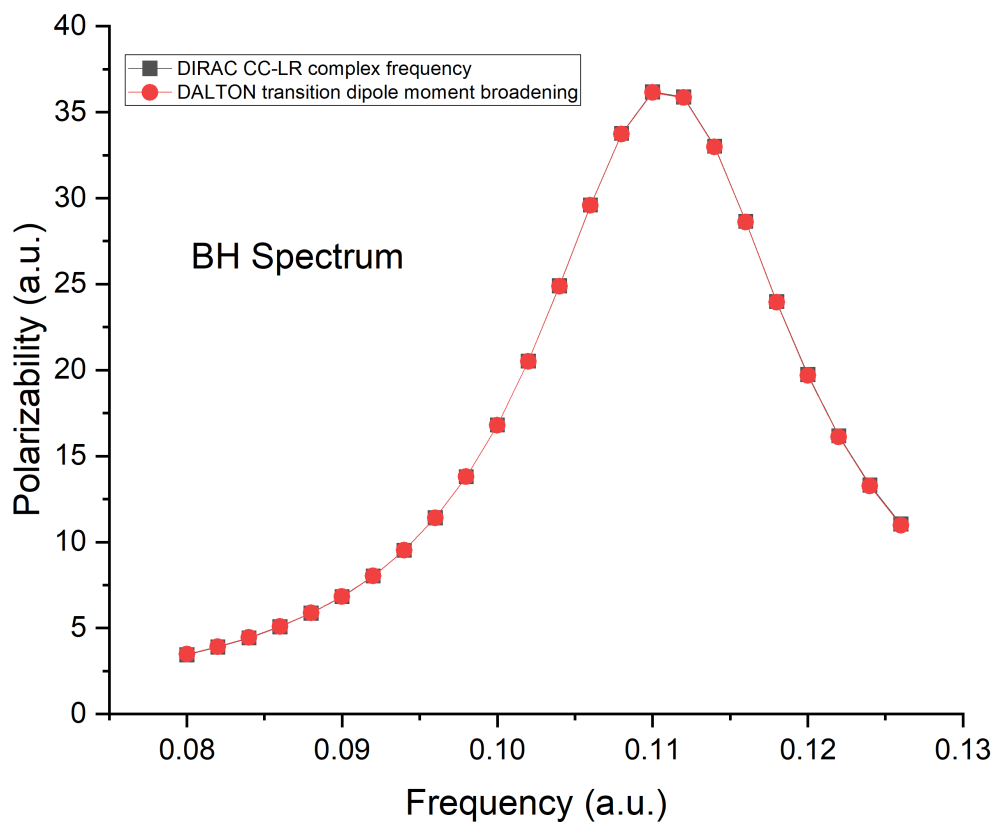


Figure 3: Comparison of LR-CC damped response results obtained with DIRAC with the Levy-Leblond Hamiltonian and standard LR-CC results obtained with Dalton, to which a Lorentzian broadening $L = \frac{1}{1+(\frac{\omega-\omega_0}{\gamma/2})^2}$, with the same γ used in the LR-CC damped response calculations has been applied.

Excitation energy of I₂

We present the results of excitation energy of I₂ for B³Π₀₊ and C¹Π₁ states. We use the RELCCSD module to perform the calculations, where all occupied and virtual orbitals are correlated. The Complete basis set(CBS) results are extrapolated by TZ and QZ values with the formula:

$$E_{CBS} = \frac{4^3 E_{QZ} - 3^3 E_{TZ}}{4^3 - 3^3}$$

Table 2: EOM-CCSD Excitation energy of I₂ for B³Π₀₊ and C¹Π₁ states

	B ³ Π ₀₊		C ¹ Π ₁	
	eV	nm	eV	nm
aug-DZ	2.28	544	2.54	487
aug-TZ	2.38	520	2.59	478
aug-QZ	2.41	514	2.61	475
CBS	2.43	510	2.62	473
Exp	2.34	530	2.51	495

Indirect spin-spin couplings

We present here the results for the Indirect spin-spin coupling J for the hydrogen halides.

Table 3: Isotropic and anisotropic spin-spin coupling J (Hz) for HX(X=F, Cl, Br, I)

Models	$^1\text{HF}^{19}$	$^1\text{HCl}^{35}$	$^1\text{HBr}^{79}$	$^1\text{HI}^{127}$
Isotropic				
NR-HF	560.2324	33.1722	32.6909	-2.1729
NR-B3LYP	377.5294	23.2295	-5.6679	
NR-CC-CI	458.5500	36.9018	92.9897	
NR-CC-CC	457.6892	36.6414	90.5146	
NR-CC-CC ^a	457.6715	36.6414	90.5144	
X2C-HF	559.7091	32.0803	-13.6915	-201.2263
X2C-B3LYP	375.7986	22.3179	-35.3065	-138.7448
X2C-CC-CI	457.7350	36.4102	71.9471	8.4426
X2C-CC-CC	456.8450	36.1321	68.7287	1.8104
DC-HF	559.3715	31.9899	-14.6151	-203.2970
Anisotropic				
NR-HF	28.8305	70.3046	489.1606	672.0842
NR-B3LYP	71.7803	59.0412	393.8655	
NR-CC-CI	-42.4747	42.8696	304.9419	
NR-CC-CC	-39.4953	43.7373	310.8541	
X2C-HF	29.2373	70.9774	508.9765	739.8355
X2C-B3LYP	72.9026	59.3847	394.2909	486.5593
X2C-CC-CI	-41.3592	43.4599	322.0869	466.6810
X2C-CC-CC	-38.3627	44.3369	328.3281	475.1557
DC-HF	29.3720	71.0300	509.5169	740.8219

^a Calculations were performed using the CFOUR program

Table 4: Difference in the linear response contribution to the spin-spin coupling constant K_{HX} between CC-CI and CC-CC ($\Delta K^{\text{LR}} = K^{\text{LR}}(\text{CC-CI}) - K^{\text{LR}}(\text{CC-CC})$, in a. u.) for the HX(X=F, Cl, Br, I) systems, broken down into the xx, yy, zz components. Apart from the absolute values, we also provide the difference per correlated electron ($\Delta K_e^{\text{LR}} = \Delta K^{\text{LR}}/N_e$, with $N_e = 10, 18, 36$ and 54 across the series)

	System	Hamiltonian	components		
			zz	xx	yy
ΔK^{LR}	HF	NR	-0.0277	0.0456	0.0456
		X2C	-0.0273	0.0465	0.0465
	HCl	NR	-0.0751	0.1298	0.1298
		X2C	-0.0724	0.1347	0.1347
	HBr	NR	-0.1351	0.4097	0.4097
		X2C	-0.0860	0.4834	0.4834
HI	X2C	0.1130	1.0875	1.0875	
ΔK_e^{LR}	HF	NR	-0.0028	0.0046	0.0046
		X2C	-0.0027	0.0046	0.0046
	HCl	NR	-0.0042	0.0072	0.0072
		X2C	-0.0040	0.0075	0.0075
	HBr	NR	-0.0038	0.0114	0.0114
		X2C	-0.0024	0.0134	0.0134
HI	X2C	0.0021	0.0201	0.0201	

Table 5: Isotropic and anisotropic indirect spin-spin coupling (J_{iso} and J_{aniso} in Hz) for the isolated H_2Se subsystem taken at the geometry of the supermolecule, (J_{iso}^{super} and J_{aniso}^{super} in Hz) for the H_2Se subsystem in $\text{H}_2\text{Se-H}_2\text{O}$, and the shifts (ΔJ , in Hz) for the isolated ("ME") H_2Se molecules in the presence of H_2O

Models	J_{iso}	J_{iso}^{super}	$\Delta J_{iso}^{\text{ME}}$	J_{aniso}	J_{aniso}^{super}	$\Delta J_{aniso}^{\text{ME}}$
			$^1\text{H}_b\text{-H}^1$			
HF ^a	-17.1157	-18.4466	-1.3309	43.4044	42.9922	-0.4122
HF	-16.3598	-17.6472	-1.2874	43.5591	43.1654	-0.3937
BLYP	-7.4945	-7.8597	-0.3652	41.2526	40.9022	-0.3504
B3LYP	-8.1176	-8.5639	-0.4463	41.2997	40.9395	-0.3602
CC-CI	-9.8335	-10.2246	-0.3911	39.9376	39.5455	-0.3921
CC-CC	-10.2487	-10.6565	-0.4078	40.1031	39.7072	-0.3959
			$^1\text{H-}^{34}\text{Se}$			
HF ^a	93.6021	93.6042	0.0021	302.0356	300.7717	-1.2639
HF	55.2216	56.1003	0.8787	349.7842	346.5116	-3.2726
BLYP	-24.8033	-21.2742	3.5291	263.5003	261.1415	-2.3588
B3LYP	-7.0856	-4.0854	3.002	267.6406	265.3991	-2.2415
CC-CI	68.1164	70.0653	1.9489	213.7819	212.0822	-1.6998
CC-CC	67.4464	69.4103	1.9639	218.0737	216.3287	-1.7450

^a Nonrelativistic calculation with the Levy-Leblond Hamiltonian

Optical rotation

Table 6: Optical rotation Test of H_2S_2 using uncontracted basis set

Method	G Tensor	Optical rotation
CC(X2C)	-0.10732	-271.1273
CC(X2C, virtual to 100 a.u.)	-0.10757	-271.7746
CC(LEVY-LEBLOND)	-0.10029	-253.3778
CC(DALTON)	-0.10029	-253.3856

Table 7: Optical rotation (a.u.) of Hydrogen peroxide series (H_2Y_2) with a frequency corresponding to the sodium D-line (589.29 nm, 0.077319 a.u.) calculated with X2C and LEVY-LEBLOND Hamiltonian

Method	H_2O_2	H_2S_2	H_2Se_2	H_2Te_2
HF(LEVY-LEBLOND)	-93.2588	-124.5926	-205.8141	-93.6808
HF(X2C)	-93.0240	-136.7733	-22.3730	2007.9020
B3LYP(LEVY-LEBLOND)	-172.7622	-295.4117	-1098.4716	-18269
B3LYP(X2C)	-173.8253	-320.9461	-1418.7842	4075
CC(LEVY-LEBLOND)	-181.5585	-253.3779	-386.6950	-263.5968
CC(X2C)	-182.4976	-271.1273	-1906.1708	218.8335

Table 8: Excitation energy (a.u.) of the first ten states of H₂Se₂ and H₂Te₂ from nonrelativistic calculations

State	TDHF	CIS	B3LYP	CC
H ₂ Se ₂				
Singlet state				
1	0.1083	0.1120	0.0889	0.1016
2	0.1624	0.1646	0.1343	0.1478
3	0.2024	0.2035	0.1668	0.1796
4	0.2214	0.2233	0.1919	0.2061
5	0.2407	0.2489	0.2077	0.2283
Triplet state				
1	0.0719	0.0820	0.0661	0.0812
2	0.0954	0.1311	0.1121	0.1309
3	0.1315	0.1461	0.1510	0.1561
4	0.1798	0.1841	0.1576	0.1703
5	0.1900	0.1958	0.1764	0.1901
Singlet-Triplet Splitting				
1	0.0364	0.0300	0.0228	0.0203
2	0.0671	0.0335	0.0222	0.0169
3	0.0709	0.0574	0.0158	0.0235
4	0.0416	0.0392	0.0343	0.0359
5	0.0507	0.0531	0.0313	0.0383
H ₂ Te ₂				
Singlet state				
1	0.0957	0.0989	0.0777	0.0898
2	0.1402	0.1421	0.1158	0.1292
3	0.1814	0.1829	0.1497	0.1611
4	0.1898	0.1923	0.1638	0.1760
5	0.1994	0.2171	0.1816	0.1999
Triplet state				
1	0.0635	0.0725	0.0584	0.0721
2	0.0924	0.1141	0.0968	0.1143
3	0.1138	0.1296	0.1320	0.1367
4	0.1530	0.1590	0.1388	0.1498
5	0.1532	0.1599	0.1453	0.1565
Singlet-Triplet Splitting				
1	0.0322	0.0264	0.0193	0.0177
2	0.0478	0.0279	0.0190	0.0149
3	0.0676	0.0532	0.0178	0.0244
4	0.0368	0.0333	0.0250	0.0262
5	0.0462	0.0572	0.0363	0.0434

CPU vs GPU Benchmarks

We provide below an assessment of the difference in performance between RelCCSD, CPU and GPU-based execution of EOM-EE and response equation of Hg atoms with the same correlation orbital space and basis set indicated in the manuscript: 12 occupied and 102 virtual spinors.

These calculations have all been carried out in a single node of the TGCC BULL Irene/Joliot Curie (partition V100L), consisting of a Intel(R) Xeon(R) Gold 6240 CPU @ 2.60GHz (72 cores and 386 Gb of RAM per node) and one NVIDIA Tesla V100-PCIE-32GB GPU. To make the comparison only dependent upon the GPU usage, we have set the number of OpenMP threads to 1 in all runs, and toggle between CPU and GPU usage for the same executable. Both ExaCorr and the standalone code were compiled with GCC 11.1.0, CUDA 11.7 and Openblas 0.3.15 as available in the computer center.

To examine this in greater detail, we focus on the single evaluation of the EOM-EE sigma vector, which is central to the procedure of solving the response equations (as well as in the determination of EOM eigenvalues and eigenvectors). We have done so with a stand-alone program that sets up, for a given problem size (number of occupied and virtual spinors), the necessary variables (1-/2-body integral tensors, EOM-CC intermediates, T amplitudes and a single trial vector) and executes a single instance of the production EOM-EE sigma vector code 10 times over, while collecting at each evaluation the elapsed walltime. The results for these evaluations is presented in table 9. As is the case with ExaCorr, the stand-alone program does not carry out I/O to disk, with all aforementioned tensors being always present in RAM.

From these results, we observe speedups of at least a factor of 6 for smaller problem sizes (which are comparable to the setup for the valence-only calculation on the Hg atom described in the paper), though in absolute terms sigma vector evaluation is rather quick for both CPU and GPU execution. For larger problem sizes, we observe somewhat larger speedups for the GPU code.

Table 9: Timings (in seconds) for benchmark evaluations of the EOM-EE sigma vector code used by the response equation solver using CPU and GPU (and the speedup for the GPU case) for different problem sizes (number of occupied \mathbf{O} and virtual \mathbf{V} spinors), as well as a model metric for the cost \mathbf{C} of the evaluation (calculated as the formal O^2V^4 scaling). For convenience, a scaled cost (\mathbf{SC} , obtained by scaling all \mathbf{C} values by the smallest one) is also provided.

\mathbf{O}	\mathbf{V}	time (s)			Cost metric	
		CPU	GPU	speedup	\mathbf{C}	\mathbf{SC}
10	102	6	1	6	1.08E+10	1.0
10	130	13	2	6	2.86E+10	2.6
10	160	26	5	6	6.55E+10	6.1
10	200	58	10	6	1.60E+11	14.8
20	102	20	2	9	4.33E+10	4.0
20	130	43	4	10	1.14E+11	10.6
20	160	85	8	10	2.62E+11	24.2
20	200	183	16	12	6.40E+11	59.1
30	102	48	5	10	9.74E+10	9.0
30	130	103	8	13	2.57E+11	23.7
30	160	203	14	15	5.90E+11	54.5
30	200	429	25	17	1.44E+12	133.0
40	102	96	8	12	1.73E+11	16.0
40	130	203	13	15	4.57E+11	42.2
40	160	395	21	19	1.05E+12	96.9
40	200	821	37	22	2.56E+12	236.5

The difference in performance reported on table 9 can also be visualized in terms of the scaling plot, shown in figure 4, which presents the increase execution time with respect to the increase in problem size, here taken to be the **SC** cost metric presented above. From the figure we see for both CPU and GPU code execution time grows in a fairly linear manner (in log scale) with increased problem size.

We note the slope for the CPU case is somewhat larger than for the GPU code, which could indicate the increase in speedup with problem size could come at least in part from a less optimized CPU implementation as opposed to being purely a gain in performance of the GPU code with increased problem size, but at this stage we have not explored the matter further. We were unable to increase the problem size beyond those shown due to the amount of RAM available on the node.

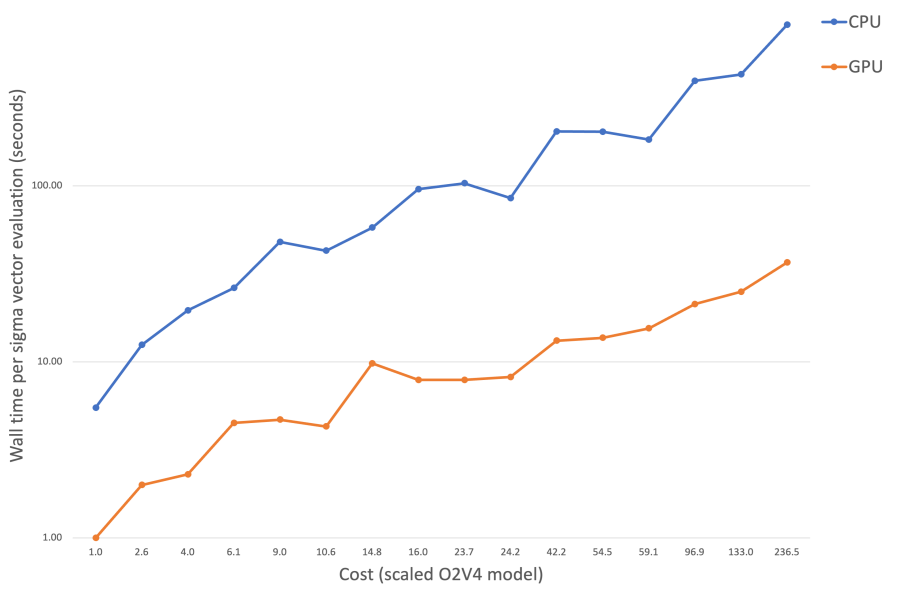


Figure 4: Scaling of sigma vector evaluation for benchmark calculations employing CPU and GPU offloading for increased problem size (on the basis of the scaled cost measure, see table 9).

Beyond assessing the performance of the code for sigma vector evaluation, we present in table 10 a comparison of the CPU and GPU performance for the solution of the linear response functions to determine the XX, YY and ZZ components of the dipole polarizability for the mercury atom. This comparison provides a picture closer to the actual code use in

production.

Our results indicate that GPU offloading remains advantageous in practice as a means to speed up our calculations. However, we see that for the tests carried out the speedup in the total time to solution in each of these code sections is not as significant as for the sigma vector evaluation itself. This is not unexpected since there are other operations which are less computationally intensive than the sigma vector evaluation (such as trial vector update, orthonormalization and antisymmetrization). That said, as the problem size increased we see an increase of the speedup, in line with what is observed for the sigma vector evaluation.

Table 10: Walltimes (in seconds) for the aggregate time for determination of the XX, YY and ZZ components of the dipole polarizability (LR) for the Hg atom for GPU and CPU execution, as a function of problem size (number of occupied \mathbf{O} and virtual \mathbf{V} spinors). For a direct comparison to the results in table 9, all calculations employed 1 OpenMP thread.

\mathbf{O}	\mathbf{V}	time (s)		speedup
		CPU	GPU	
12	102	773	317	2.4
18	148	5485	1524	3.6
18	180	10879	2606	4.2

ExaCorr vs RELCCSD comparison

We present below a comparison between the ExaCorr and RELCCSD implementations. As response theory is not implemented in RELCCSD, the fairest comparison between codes that can be done is for the solution of the EOM-EE problem for a single excited state, and without making use of double group point symmetry in RELCCSD. Given the very different design decisions (basically a tradeoff between storing data on RAM for ExaCorr and on disk for RELCCSD), we compare only the time to solution for the EOM-EE equations in each case. Our results, shown in table 11, indicate that time to solution between RELCCSD and ExaCorr (GPU) are comparable, though for the small problem size considered here RELCCSD still shows a smaller time to solution.

Table 11: Walltimes (in seconds) for the aggregate time for determination of a single EOM-EE excited state for Hg electron for the Hg atom, employing the RELCCSD and ExaCorr (CPU and GPU) codes, for a given number of occupied **O** and virtual **V** spinors.

O	V	RELCCSD	ExaCorr (CPU)	Exacorr(GPU)
12	102	46	255	115

References

- (1) Crawford, T. D.; Schaefer III, H. F. An introduction to coupled cluster theory for computational chemists. *Rev. comp. chem* **2007**, *14*, 33–136.
- (2) Christiansen, O.; Jørgensen, P.; Hättig, C. Response functions from Fourier component variational perturbation theory applied to a time-averaged quasienergy. *Int. J. Quantum. Chem* **1998**, *68*, 1–52.
- (3) Faber, R.; Coriani, S. Resonant inelastic X-ray scattering and nonresonant X-ray emission spectra from coupled-cluster (damped) response theory. *J. Chem. Theory. Comput* **2018**, *15*, 520–528.
- (4) Davidson, E. R. The iterative calculation of a few of the lowest eigenvalues and corresponding eigenvectors of large real-symmetric matrices. *J. Comput. Phys* **1975**, *17*, 87–94.
- (5) Hirao, K.; Nakatsuji, H. A generalization of the Davidson’s method to large nonsymmetric eigenvalue problems. *J. Comput. Phys* **1982**, *45*, 246–254.
- (6) Olsen, J.; Jensen, H. J. A.; Jørgensen, P. Solution of the large matrix equations which occur in response theory. *J. Comput. Phys* **1988**, *74*, 265–282.
- (7) Shee, A.; Saue, T.; Visscher, L.; Severo Pereira Gomes, A. Equation-of-motion coupled-cluster theory based on the 4-component Dirac–Coulomb (–Gaunt) Hamiltonian. En-

- ergies for single electron detachment, attachment, and electronically excited states. *J. Chem. Phys.* **2018**, *149*, 174113.
- (8) Pototschnig, J. V.; Papadopoulos, A.; Lyakh, D. I.; Repisky, M.; Halbert, L.; Severo Pereira Gomes, A.; Jensen, H. J. A.; Visscher, L. Implementation of Relativistic Coupled Cluster Theory for Massively Parallel GPU-Accelerated Computing Architectures. *J. Chem. Theory Comput.* **2021**, acs.jctc.1c00260.
- (9) Saue, T.; Jensen, H. J. A. Linear response at the 4-component relativistic level: Application to the frequency-dependent dipole polarizabilities of the coinage metal dimers. *J. Chem. Phys.* **2003**, *118*, 522–536.

Appendix **B**

Supplemental information of Chapter
4

Supplementary information:
Frequency-Dependent Quadratic Response
Properties and Two-photon Absorption from
Relativistic Equation-of-Motion Coupled Cluster
Theory

Xiang Yuan,^{*,†,‡} Loïc Halbert,^{*,†} Lucas Visscher,^{*,‡} and André Severo Pereira
Gomes^{*,†}

[†]*Univ. Lille, CNRS, UMR 8523 - PhLAM - Physique des Lasers Atomes et Molécules,
F-59000 Lille, France*

[‡]*Department of Chemistry and Pharmaceutical Sciences, Faculty of Science, Vrije
Universiteit Amsterdam, 1081 HV Amsterdam, The Netherlands*

E-mail: xiang.yuan@univ-lille.fr; loic.halbert@univ-lille.fr; l.visscher@vu.nl;
andre.gomes@univ-lille.fr

Working equations for CCSD EOM quadratic response

In what follows a, b, c, \dots will indicate particle lines, i, j, k, \dots hole lines, and p, q, r, s, \dots general indexes.¹ In all equations below we use Einstein notation. Furthermore, we define

- P as a permutation operator, with : $P_{-pq}f(\dots pq \dots) = f(\dots pq \dots) - f(\dots qp \dots)$;
- $Y_q^p = \langle p|Y|q\rangle$ are matrix elements of property operator Y .

In our implementation the property Jacobian ${}^{EOM}A_{\nu\mu}^Y$ is never formed by itself, instead we always evaluate the product of \bar{t}^X (or L_f) and ${}^{EOM}A_{\nu\mu}^Y$. This product has the same structure as η_μ^Y (Eq. 1, see definition of matrix elements in Yuan et al.²)

$$(\eta_s^Y)' = {}^{EOM} \eta_s^Y - \langle HF | \hat{Y} | HF \rangle \quad (1)$$

$$(\eta_d^Y)' = \eta_d^Y, \quad (2)$$

with the difference of using \bar{t}^X (or L_f) rather than \bar{t}^0 as in linear response.

Also, we reuse the η_μ^Y diagrams and routine by replacing the \bar{t}^0 by \bar{t}^X to define a new intermediate $({}^{XY}\eta')_\mu$:

$$\begin{aligned} ({}^{XY}\eta')_a^i &= Y_a^e (\bar{t}^X)_e^i - Y_m^i (\bar{t}^X)_a^m - Y_a^m (t_m^e (\bar{t}^X)_e^i) - (Y_e^i t_m^e) (\bar{t}^X)_a^m \\ &\quad - 1/2 (t_{mn}^{fe} (\bar{t}^X)_{fe}^{mi}) Y_a^n - 1/2 (t_{nm}^{fe} (\bar{t}^X)_{fa}^{nm}) Y_e^i + (\bar{t}^X)_{ae}^{im} (\xi^Y)_m^e \end{aligned} \quad (3)$$

$$\begin{aligned} ({}^{XY}\eta')_{ab}^{ij} &= P_{-ab} P_{-ij} (\bar{t}^X)_a^i Y_b^j - P_{-ij} (\bar{t}^X)_{ab}^{im} Y_m^j + P_{-ab} (\bar{t}^X)_{ae}^{ij} Y_b^e \\ &\quad - P_{-ij} (t_m^e Y_e^j) (\bar{t}^X)_{ab}^{im} - P_{-ab} (t_m^e Y_b^m) (\bar{t}^X)_{ae}^{ij} \end{aligned} \quad (4)$$

DIRAC revision number

0923e70dd0, fe4351caf9 and 380df6b

Performance of MP2 frozen natural orbitals

We utilize the six notations below to streamline the discussion and represent the corresponding MP2FNO selection scheme.

- FNO(I): threshold of occupation number $1.0d^{-4}$
- FNO(II): threshold of occupation number $1.0d^{-5}$

- FNO(III): threshold of occupation number $1.0d^{-6}$
- FNO(I'): threshold of occupation number $1.0d^{-4}$ plus doubly-degenerate orbitals
- FNO(II'): threshold of occupation number $1.0d^{-5}$ plus doubly-degenerate orbitals
- FNO(III'): threshold of occupation number $1.0d^{-6}$ plus doubly-degenerate orbitals

From Table 1 we note under the standard selection schemes: FNO(I, II, III), the excitation energy of the low-lying states: $(4s4p) {}^3P$ and $(4s4p) {}^1P$ are closed to the canonical orbitals results. On the other hand, for higher states 3S , 1S , 1D , and 3D , the excitation energy are significantly overestimated. Additionally, we note that the sequence of the excited states is incorrect for FNO(I) and FNO(II). For instance, under FNO(II), the 3S state is positioned higher than 1S .

This discrepancy can be traced back to the overestimation of the 5s orbital energy. As illustrated in Table 2 when comparing the recanonicalized orbital energy of FNOs to the original 5s orbital energy (-0.0999 a.u.), the energy value of 5s orbital in FNO(I)(0.2745 a.u.), FNO(II)(0.1640 a.u.), and FNO(III)(-0.0119 a.u.) are all higher. Notably, for FNO(I) and FNO(II), these are so much higher than the energies even become strongly positive.

We now shift our focus to FNO(I'), FNO(II'), and FNO(III'). We observe that the energies of the 3S and 1S states are more accurate. For example, for FNO(I') the error of 1S state is 0.0017 a.u, which is significantly less than the error observed in FNO(I) at 0.1351 a.u. This can be attributed to the fact that we achieve a notable stabilization of the 5s orbital (-0.0932 a.u.) across the FNO(I', II', III') spaces.

However, incorporating doubly-degenerate orbitals with low occupation numbers in the ground state doesn't significantly improve the 1D , and 3D states. We also observe that the degeneracy of the components of $5p_{3/2}$ and $4d_{3/2}$ and $4d_{5/2}$ orbitals in FNO(I', II', III') is sometimes broken with the $|m_j| = 1/2$ orbitals being lower than the others. This issue can likely be attributed to the scheme we employed to include the doubly-degenerate $s_{1/2}$ and

$p_{1/2}$, instead of full shells. This symmetry breaking at the orbital level is then reflected in a poorer description of the high-lying states involving those orbitals.

We note no such thing takes place for the 4p orbitals since these have large enough occupation numbers at the ground state to always be included in the correlation treatment.

Table 1: Performance of MP2FNOs on the excitation energy (a.u.) of eight excited states for Ga^+

Excited state	FNO(I)	FNO(II)	FNO(III)	FNO(I')	FNO(II')	FNO(III')	Canonical	Exp ^a
$(4s4p)^3P_0^u$	0.2310	0.2126	0.2120	0.2117	0.2119	0.2113	0.2112	0.2158
$(4s4p)^3P_1^u$	0.2333	0.2146	0.2140	0.2189	0.2141	0.2135	0.2132	0.2179
$(4s4p)^3P_2^u$	0.2384	0.2188	0.2181	0.2383	0.2187	0.2181	0.2173	0.2221
$(4s4p)^1P_1^u$	0.2657	0.3280	0.3249	0.3543	0.3271	0.3241	0.3221	0.3221
$(4s5s)^3S_1^g$	0.5981	0.6425	0.4915	0.4666	0.4647	0.4645	0.4630	0.4691
$(4s5s)^1S_1^g$	0.5864	0.6414	0.5192	0.4861	0.4838	0.4835	0.4812	0.4860
$(4p^2)^1D_2^{g*}$	0.5918	0.6453	0.5183	0.5469	0.5466	0.5454	0.4914	0.4908
$(4s4d)^3D_1^g$	0.5987	0.6632	0.5439	0.5678	0.5467	0.5460	0.5118	0.5186

^a Results from NIST

* 44% from the configuration 4s4d

Table 2: Orbital energy (a.u.) of lowest 12 virtual orbitals for Ga^+

FNO(I')	FNO(I')	FNO(II)	FNO(II')	FNO(III)	FNO(III')	Canonical	Virtual orbitals
-0.1317	-0.1955	-0.1892	-0.1955	-0.1892	-0.1955	-0.1957	4p _{1/2}
-0.1253	-0.1253	-0.1854	-0.1854	-0.1854	-0.1854	-0.1924	4p _{3/2}
-0.1253	-0.1253	-0.1854	-0.1854	-0.1854	-0.1854	-0.1924	4p _{3/2}
0.2745	-0.0932	0.1640	-0.0932	-0.0119	-0.0932	-0.0999	5s _{1/2}
0.4708	-0.0384	0.1693	-0.0384	0.1270	-0.0384	-0.0659	5p _{1/2}
0.4708	0.0579	0.1693	0.0579	0.1270	0.0579	-0.0654	5p _{3/2}
0.4734	0.1870	0.2745	0.1693	0.1276	0.1270	-0.0654	5p _{3/2}
0.4734	0.4708	0.4708	0.1693	0.1276	0.1270	-0.0566	4d _{3/2}
0.4734	0.4708	0.4708	0.1870	0.1276	0.1276	-0.0566	4d _{3/2}
1.6174	0.4734	0.4734	0.4708	0.1640	0.1276	-0.0565	4d _{5/2}
1.6509	0.4734	0.4734	0.4708	0.1693	0.1276	-0.0565	4d _{5/2}
1.6509	0.4734	0.4734	0.4734	0.1693	0.1693	-0.0565	4d _{5/2}

References

- (1) Crawford, T. D.; Schaefer III, H. F. An introduction to coupled cluster theory for computational chemists. *Rev. comp. chem* **2007**, *14*, 33–136.
- (2) Yuan, X.; Halbert, L.; Pototschnig, J.; Papadopoulos, A.; Coriani, S.; Visscher, L.; Gomes, A. S. P. Formulation and Implementation of Frequency-Dependent Linear Response Properties with Relativistic Coupled Cluster Theory for GPU-accelerated Computer Architectures. 2023; <http://arxiv.org/abs/2307.14296>, arXiv:2307.14296 [physics].

Appendix **C**

Supplemental information of Chapter
6

Supplementary information: Assessing MP2 frozen natural orbitals in relativistic correlated electronic structure calculations

Xiang Yuan,^{1,2, a)} Lucas Visscher,^{2, b)} and André Severo Pereira Gomes^{1, c)}

¹⁾*Université de Lille, CNRS, UMR 8523 - PhLAM - Physique des Lasers, Atomes et Molécules, F-59000 Lille, France.*

²⁾*Department of Chemistry and Pharmaceutical Sciences, Faculty of Science, Vrije Universiteit Amsterdam, de Boelelaan 1083, 1081 HV Amsterdam, The Netherlands.*

^{a)}Electronic mail: xiang.yuan@univ-lille.fr

^{b)}Electronic mail: l.visscher@vu.nl

^{c)}Electronic mail: andre.gomes@univ-lille.fr

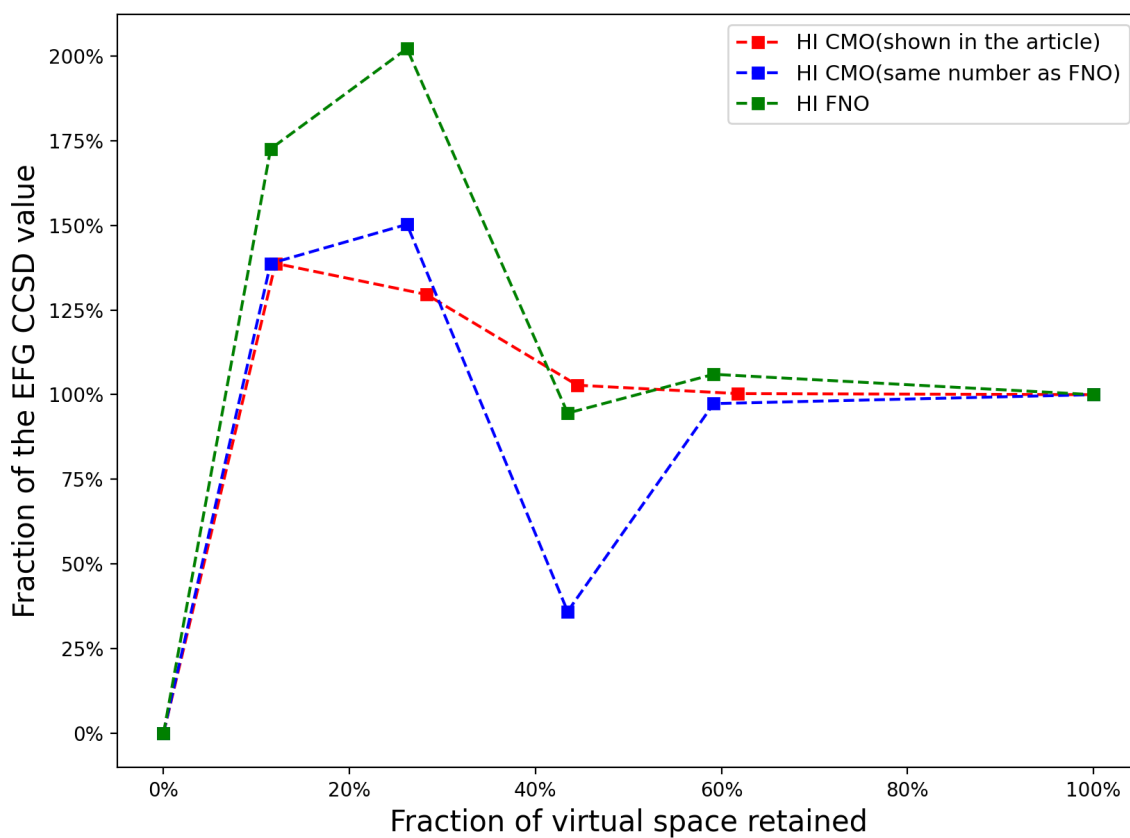


Figure S1: Convergence of the CCSD EFG at the I atom with respect to the size of the virtual orbital space, for the X2C Hamiltonian, comparing FNO and CMO, the latter being truncated at exactly the same number of FNO and approximately respecting atomic shell boundaries as shown in the article body. The X axis indicates the fraction of the virtual space retained, while the Y axis gives the fraction of the correlation energy recovered with respect to the value obtained with the untruncated virtual space.

Table S1: Correlation energy and expectation value using uncontracted aug-cc-pVTZ and aug-cc-pCVTZ basis sets for HCl with full orbital space

MP2 Correlation energy (a.u.)	aug-cc-pVTZ	aug-cc-pCVTZ
All Electrons	-0.33206	-0.51702
Valence Electrons only	-0.20986	-0.21094
CCSD Correlation energy (a.u.)	aug-cc-pVTZ	aug-cc-pCVTZ
All Electrons	-0.34904	-0.53415
Valence Electrons only	-0.22911	-0.23077
CCSD Dipole Moment (a.u.)	aug-cc-pVTZ	aug-cc-pCVTZ
All Electrons	0.73	0.73
Valence Electrons only	0.76	0.77
CCSD Quadupole Moment (a.u.)	aug-cc-pVTZ	aug-cc-pCVTZ
All Electrons	2.74	2.74
Valence Electrons only	2.87	2.87
CCSD Electric field gradient (a.u.)	aug-cc-pVTZ	aug-cc-pCVTZ
All Electrons	3.59	3.56
Valence Electrons only	3.41	3.38

Table S2: Energy and molecular properties of HTs using different Hamiltonians with Hartree-Fock wave functions

Property(a.u.)	DC ^a	DCSSSS ^b	X2C	X2C ^c	X2C spinfree	NONREL
Total energy	-53750.9	-53718.7	-53671.3	-53448.8	-53241.6	-45401.0
HOMO-LUMO gap	0.2669	0.2668	0.2670	0.2694	0.3428	0.3633
Electric Dipole moment	0.992	0.988	0.986	0.955	0.358	-0.074
Electric Quadrupole moment ^d	1566.65	1566.66	1566.68	1566.83	1568.00	1570.81
Electric field gradient ^e	60.1	59.9	59.8	56.5	78.4	21.7

^a Dirac-Coulomb Hamiltonian in which (SSISS) integrals are replaced by an interatomic SS correction.

^b Dirac-Coulomb Hamiltonian with explicitly including (SSISS) type Coulomb integrals.

^c Using Gaussian charge nuclear model.

^d ZZ component.

^e ZZ component on Ts nucleus.

Table S3: The fraction of the MP2 and CCSD correlation energy of hydrogen halides molecules using frozen natural orbitals

Retained Virtual Orbital Space	MP2 Correlation Energy	CCSD Correlation Energy
HF		
0.00%	0.00%	0.00%
11.54%	64.93%	64.33%
32.05%	85.02%	85.09%
64.10%	98.36%	98.46%
82.05%	99.88%	99.89%
100.00%	100.00%	100.00%
HCl		
0.00%	0.00%	0.00%
10.99%	43.08%	44.59%
35.16%	84.80%	85.63%
62.64%	94.91%	95.13%
81.32%	99.39%	99.43%
100.00%	100.00%	100.00%
HBr		
0.00%	0.00%	0.00%
16.13%	57.53%	56.12%
29.68%	77.27%	76.52%
48.39%	92.01%	91.71%
67.74%	98.03%	97.97%
100.00%	100.00%	100.00%
HI		
0.00%	0.00%	0.00%
11.52%	30.97%	31.32%
26.18%	67.66%	66.99%
43.46%	89.49%	89.23%
59.16%	96.74%	96.66%
100.00%	100.00%	100.00%
HAt		
0.00%	0.00%	0.00%
11.76%	35.97%	33.95%
23.90%	63.53%	61.22%
44.85%	87.62%	86.66%
62.87%	96.86%	96.62%
100.00%	100.00%	100.00%
HTs		
0.00%	0.00%	0.00%
10.54%	25.86%	24.22%
23.47%	55.31%	52.89%
42.86%	80.29%	79.00%
59.52%	93.50%	93.08%
100.00%	100.00%	100.00%

Appendix **D**

Supplemental information of Chapter
7

Supplementary information: Reassessing the potential of TICI for laser cooling experiments via four-component correlated electronic structure calculations

Xiang Yuan^{1, 2, a)} and André Severo Pereira Gomes^{1, b)}

¹⁾*Université de Lille, CNRS, UMR 8523 - PhLAM - Physique des Lasers, Atomes et Molécules, F-59000 Lille, France.*

²⁾*Department of Chemistry and Pharmaceutical Science, Faculty of Science, Vrije Universiteit Amsterdam, de Boelelaan 1083, 1081 HV Amsterdam, The Netherlands.*

^{a)}Electronic mail: xiang.yuan@univ-lille.fr

^{b)}Electronic mail: andre.gomes@univ-lille.fr

Table S1: Einstein coefficients $A_{v'v''}$ (in s^{-1}) and vibrational branching $R_{v'v''}$ of the $a^3\Pi_1-X^1\Sigma_0^+$ for TlF

		$v'=0$	$v'=1$	$v'=2$
$v''=0$	$A_{v'v''}$	10907071	4540	116407
	$R_{v'v''}$	0.98836	0.00041	0.01055
$v''=1$	$A_{v'v''}$	8497	10368496	336295
	$R_{v'v''}$	0.00077	0.93956	0.03047
$v''=2$	$A_{v'v''}$	112369	168188	8307317
	$R_{v'v''}$	0.01018	0.01524	0.75278
$v''=3$	$A_{v'v''}$	2946	313347	934001
	$R_{v'v''}$	0.00027	0.02839	0.08464
$v''=4$	$A_{v'v''}$	1889	58348	799012
	$R_{v'v''}$	0.00017	0.00529	0.07240
$v''=5$	$A_{v'v''}$	2723	10286	288217
	$R_{v'v''}$	0.00025	0.00093	0.02612

Table S2: Einstein coefficients $A_{v'v''}$ (in s^{-1}) and vibrational branching $R_{v'v''}$ of the $a^3\Pi_0^+-X^1\Sigma_0^+$ for TlCl

		$v'=0$	$v'=1$	$v'=2$
$v''=0$	$A_{v'v''}$	5644340	10468	58963
	$R_{v'v''}$	0.98565	0.00183	0.01030
$v''=1$	$A_{v'v''}$	3017	5206414	313698
	$R_{v'v''}$	0.00053	0.90918	0.05478
$v''=2$	$A_{v'v''}$	76729	107077	3447529
	$R_{v'v''}$	0.0134	0.0187	0.60203
$v''=3$	$A_{v'v''}$	260	288471	427477
	$R_{v'v''}$	0.00005	0.05037	0.07465
$v''=4$	$A_{v'v''}$	2001	19844	780483
	$R_{v'v''}$	0.00035	0.00347	0.13629
$v''=5$	$A_{v'v''}$	56	21714	224278
	$R_{v'v''}$	0.00001	0.00379	0.03916

Table S3: The polarizability of TlF and TlCl at CCSD TZ level with finite field computation

Molecule	ZZ component of Polarizability (a.u)
TlF	110
TlCl	191

I. GAS SETUP OF MRCI

We reduce the number of reference determinants in `space1` and `space2` but correlate more virtual orbitals. The virtual space for the correlating calculations contains orbitals with energies up to and including 5 a.u and 8.4 a.u, respectively. In `space3`, we employ the same configuration as depicted in

the manuscript, but with the `dyall.aae3Z` basis set. In `space4`, we consider the outer-core correlations from the 5d orbitals of Tl. In `space5` and `space6`, we correlate the electrons of 5d(Tl) and 3s(Cl) by allowing single and double excitations, respectively, and additionally correlate more virtual orbitals (that is, those with energies up to and including 30 a.u.). In `space7` and `space8`, we freeze the core orbitals but only include more virtual orbitals to provide the reference.

Table S4: Generalized Active Spaces and occupation constraints for the TICl molecule

GAS(space0_aae4z 2 a.u)	Min_occupation	Max_occupation	Kramers pairs	Total determinants
I	0	8	4	
II	6	8	4	
III	8	8	70	10 442 120
GAS(space1_aae4z 5 a.u)	Min_occupation	Max_occupation	Kramers pairs	Total determinants
I	4	4	2	
II	6	8	5	
III	8	8	167	306 570
GAS(space2_aae4z 8.4 a.u)	Min_occupation	Max_occupation	Kramers pairs	Total determinants
I	4	4	2	
II	6	8	5	
III	8	8	195	410 909
GAS(space3_aae3z 2 a.u)	Min_occupation	Max_occupation	Kramers pairs	Total determinants
I	0	8	4	
II	6	8	4	
III	8	8	70	10 227 291
GAS(space4_aae3z 2 a.u)	Min_occupation	Max_occupation	Kramers pairs	Total determinants
I	11	12	6	
II	16	18	3	
III	18	20	8	
IV	20	20	62	11 525 942
GAS(space5_aae3z 30 a.u)	Min_occupation	Max_occupation	Kramers pairs	Total determinants
I	11	12	6	
II	16	18	3	
III	18	20	8	
IV	20	20	151	61 620 589
GAS(space6_aae3z 30 a.u)	Min_occupation	Max_occupation	Kramers pairs	Total determinants
I	10	12	6	
II	16	18	3	
III	18	20	8	
IV	20	20	151	105 069 249
GAS(space7_aae3z 2 a.u)	Min_occupation	Max_occupation	Kramers pairs	Total determinants
I	12	12	6	
II	16	18	3	
III	18	20	8	
IV	20	20	62	2 176 044
GAS(space8_aae3z 30 a.u)	Min_occupation	Max_occupation	Kramers pairs	Total determinants
I	12	12	6	
II	16	18	3	
III	18	20	8	
IV	20	20	151	11 532 895

Table S5: TICl: The computed transition dipole moments of $a^3\Pi_0^+ - X^1\Sigma_0^+$ at R_e and the corresponding lifetimes

TZ results;	Truncation energy (a.u.)	TDM(D)	lifetime(ns)	Excitation energy(cm^{-1})	Reference	core orbitals
	2	0.795	163	31603	MRCL_space3	no
	2	0.821	153	31821	MRCL_space7	no
	2	0.868	137	32465	MRCL_space4	yes
	30	0.843	145	32110	MRCL_space8	no
	30	0.936	118	33835	MRCL_space5	yes
	30	0.973	109	34443	MRCL_space6	yes
QZ results;						
	2	0.767	175	31813	MRCL_space0	no
	2	0.803	160	35506	MRCL_space1	no
	2	0.804	160	35593	MRCL_space2	no

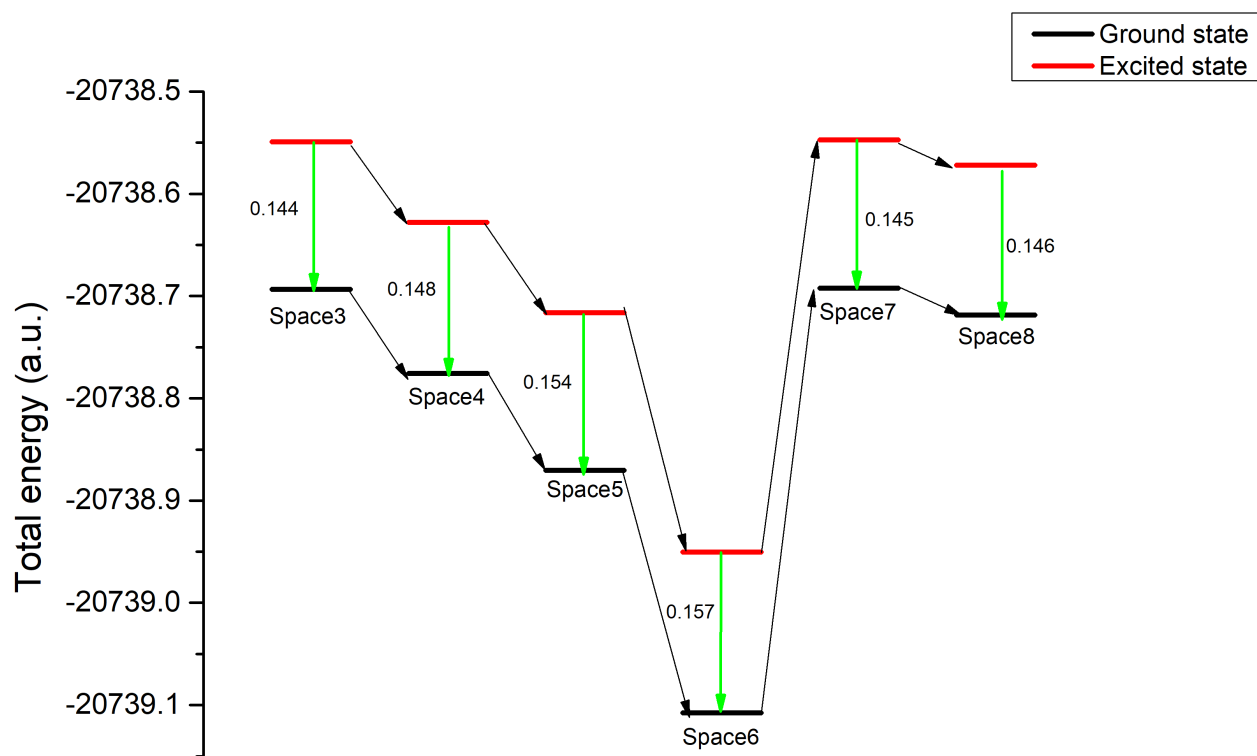


Figure S1: Total energies of ground state $X^1\Sigma_0^+$ and excited state $a^3\Pi_0^+$ for TICl, for the different CI spaces explored.